The effect of free surface on classical ship hydrodynamics using RANSE

—— Resistance, Manoeuvring, Propulsion, Seakeeping and Stability ——

Qiuxin Gao

Submitted in fulfilment of the requirements for the degree of

Doctor of Philosophy

Department of Naval Architecture and Marine Engineering

Universities of Strathclyde and Glasgow

February 2012

Declaration of Author's Right

Acknowledgements

Table of Contents

Abstract

In this research, the Computational Fluid Dynamics (CFD) approach, based on the solution of the Reynolds Averaged Navier-Stokes (RANS) equations is used to study the classical ship hydrodynamic problems, all being affected markedly by the presence of free-surface, namely: ship resistance, propulsion, manoeuvring, seakeeping and stability, the latter focusing on flooding of a damaged ship. In this respect, this thesis represents a marked deviation from classical approaches and a unique contribution to ship dynamics and hydrodynamics.

The RANS equations with SST K-ω two-equation turbulence model and Volume Of Fluid (VOF) formulation were discretised by the finite volume (FV) method and the pressure-coupled governing equations were solved by the SIMPLE algorithm. The geometric reconstruction algorithm was adopted to locate transient free surfaces. The second order upwinding scheme was used for the discretisation of the convection flux and Multi-grid Acceleration was applied to improve convergence.

In addressing ship resistance, grid sensitivity studies were carried out according to the "ITTC guideline of quality" manual. The computed results were verified and validated against available model test data. Additionally, the results of the effects of the turbulence models were investigated by comparing turbulence quantities predicted by SST K-ω and RSM.

In addressing ship propulsion, the propeller was modelled as an actuator disk of equivalent thrust and torque. Distributions of the body force were compared with results from a parametric study and the implementation of the body force approach was validated by model test data.

In addressing ship manoeuvring, numerical PMM simulations of pure sway and yaw motions were performed. The numerical results were benchmarked against physical

experiments. The computed hydrodynamic derivatives were compared with empirical formulae and subsequently implemented in manoeuvring simulations.

In addressing seakeeping, incident waves were generated by a numerical wave maker and the computed results for wave diffraction were validated against physical measurements. Furthermore, RANS simulation for roll decay was undertaken and validated against results from model tests. Finally, a numerical roll tank was established to study the hydrodynamic coefficients of the roll motion in intact and damaged conditions and the corresponding results were compared with available model test data.

In conclusion, systematic studies and ensuing results from numerical simulations of classical ship hydrodynamic problems using RANS demonstrated beyond doubt that CFD could and should play an important role in the design, analysis and evaluation of ship hydrodynamic performance. In addition, they provide unshakeable evidence of the level of capability to make the next important step: rendering CFD a routine "tool" in ship dynamics and hydrodynamics.

Nomenclature

ρ_a Density of air

ρ_w Density of water

Δ Displacement volume

ε Dissipation rate

Δ Laplace operator

μ_a Molecular dynamic viscosity of air

μ_w Molecular dynamic viscosity of water

$\vec{V}$ Velocity vector

r_a Volume fraction of air

r_w Volume fraction of water

ω Angular velocity

Γ Effective viscosity

ν Kinematic viscosity

∂ Partial differential operator

δ Phase angle

σ	Prandtl constant
α	Roll angle
→	Vector
φ	roll angle
μ_T	Turbulence eddy viscosity
A	Amplitude
B	Ship breadth
C	Model constant
C_B	Block coefficient
C_F	Friction resistance coefficient
C_P	Pressure resistance coefficient
C_r	Courant number $V\Delta t/L$
C_R	Residual resistance coefficient
C_T	Total resistance coefficient
Fr	Froude number $V/\sqrt{gL}$
G	Gravity
∇	Hamilton-operator
k	Form factor
K	Turbulence kinetic energy

L   Characteristic length

Lpp   Ship length between perpendiculars

P   Pressure

∂ Partial differential operator

Pe   Peclet number VL/Γ

R   Propeller radius

r   Volume fraction

Re   Reynolds number VL/ν

S   Source of momentum equation

S_W Wetted surface area

T   Ship draft
t   Time
τ_w wall shear stress
u_τ Wall friction velocity $\sqrt{\tau_w/\rho}$

u   longitudinal velocity component

v   lateral velocity component

V   Velocity magnitude

w   vertical velocity component

W   Wake fraction

x   Non dimensional longitudinal coordinate by ship length

y   Non dimensional lateral coordinate by ship length

z Non dimensional vertical coordinate by ship length

K Roll moment coefficient

M Pitch moment coefficient

N Yaw moment coefficient

Y^+ Y plus $\mu_\tau y / \nu$

1 Introduction

It has been a tremendous campaign for CFD research and development in advancing from the earlier computation in a notebook to the large modern mainframes and clusters of today. The intention in this work is not to address all the breakthroughs on the theories and methodologies of CFD but instead to focus on and delve into demonstrating its full potential in the area of ship hydrodynamics.

As a subject, ship hydrodynamics focuses on the study of hydrodynamic forces or loads acting on a sailing or operating ship. Traditionally, and for ease of understanding, it comprises a number of disciplines each addressing specific ship behaviour. The classical ship hydrodynamics normally refer to ship resistance, propulsion, manoeuvring and seakeeping and, in a broader sense, ship stability. The hydrodynamic performance of a ship determines energy efficiency, safety and environmental performance of a ship design, thus, of great engineering significance.

Ship hydrodynamic characteristics are evaluated by model tests, performed in a towing tank or by accredited numerical analysis on a computer. As ship hydrodynamic problems are fraught with non-linearities (e.g., large amplitude motion), viscous and turbulent effects (boundary layer, flow separation, vortex shedding), free surface (green water, wave breaking, dry transom) and scale effects, Computational Fluid Dynamics (CFD) based on RANS method offers integrated and advanced capabilities over simplified numerical approaches, thus offering a vehicle to pursue and achieve real change in enhancing ship hydrodynamic performance.

Moreover, in addition to overcoming modelling limitations concerning a multitude of non-linear transient phenomena involving free-surface and viscous flows, numerical tanks offer a number of advantages over physical model tests, of which the following are worth mentioning:

- Retrievability

This involves the ability to be able to retrieve all of the information (data) whenever they are needed from the data files of the running case without any costs being involved.

- Flexibility:

Allowing ability to change the testing from fresh water to sea water effortlessly.

- Scalability:

The model size and speed are scalable, thus there are no restrictions encountered in numerical simulations.

- Repeatability:

The environmental conditions are repeatable; hence exactly the same incident wave can be generated in two different runs of simulations.

- Safety:

The simulations can be carried out without any health and safety hazards due to the use of electricity and machinery while also eliminating the likelihood of human error.

- Prospect:

Even faster, more efficient and more accurate simulations can be expected in the future with the advances and innovations in computational science and technology.

Starting with ship resistance as one of the oldest topics in the study of ship hydrodynamics, it has recently re-invented itself as one of the hottest topics due to campaigns on energy savings, emission reductions and on maximising cost-

effectiveness. Hence, the need for an integrated or an all-embracing approach to ship dynamics and hydrodynamics.

An accurate determination of ship resistance is not only essential for the prediction of ship speed, but will also affect all other hydrodynamic analysis, like power requirement as well as performance in propulsion, manoeuvring and seakeeping.

The traditional way to determine ship resistance was through towing tank model tests.

The history of ship resistance model test can be traced back to the nineteen century, when William Froude built the first towing tank in the world - Chelston Cross Tank at Torquay - in 1871. Similar techniques of measurements are still applied in towing tanks all over the world today.

Figure 1 Models used by Froude

While the facilities in resistance model testing are steadily advancing, the time and costs involved provide reasons for vigilance on the need to pursue modern physical experiments.

With the rapid advances of high performance computing (HPC) technology, and innovations in the area of numerical methodology with the likes of Computational Fluid Dynamics (CFD), numerical simulation of physical model test, or the numerical towing tank (NTT), is becoming an increasingly attractive option in the analysis and optimisation of ship resistance.

Compared with physical model tests, NTT has an excellent turnaround and an attractive price to performance ratio. Most importantly, the prospect of NTT is so

strong that researchers of ship hydrodynamics cannot afford to miss the opportunity that may be afforded, hence the main fundamental motive of the present work.

The hull-propeller interaction determines the power performance of the propeller(s) behind a ship. It is normally evaluated by propulsion efficiencies, i.e. efficiency of open water, hull efficiency and relative rotative efficiency. The efficiency of propulsion is directly related to the power consumption within the main engine. It is one of most important economic indices within ship and propeller designs. The efficiency of the propulsion system is one of the key topics in shipping technology today. Moreover, propeller cavitation and its characteristics, particularly in affecting ship vibration and acoustic noise, are all essential factors in civil and especially naval ships.

Figure 2 Propeller tests

Traditionally, the self-propulsion tests in towing tank were the only way to assess the efficiency of the propulsion system. Due to scale effects, additional towing forces need to be exerted in order to perform the test at the ship self-propulsion point. The wake fraction and thrust deduction were estimated by the thrust-identity method.

There are two approaches to simulate self-propulsion: one is using propeller modelling, such as body force; the other is by direct simulation of self-propulsion, which is computationally expensive. Although propeller modelling is preferred at the current stage, its implementation needs to be validated and the parametric studies

carried out in order to assess the performance of the model, and to establish solid foundation for future applications.

The performance of a ship's manoeuvring capability is vital at critical moments where the ship needs to complete a manoeuvre suddenly, such as the catastrophic case of the Titanic. Traditionally, model tests were the only means to assess the manoeuvrability of a ship design, in which either a steady test or the Planar Motion Mechanism (PMM) test were used. Steady tests comprise oblique towing and rotating arm tests while Planar Motion Mechanism (PMM) tests are more advanced and transient, like pure sway and pure yaw tests, and are much more expensive and more time-consuming than resistance model tests.

Figure 3 Ship Performing a Turning Circle Manoeuvre

The numerical calculations of ship manoeuvring motions in captive conditions is another potential market of CFD applications. There are similarities between calculations for manoeuvring and calculations for resistance, in that both are considered as static problems with significant viscous or turbulence effects. However, calculations of manoeuvring motions are more challenging. There are many different manoeuvring modes of motion to be simulated and the symmetry condition at centre plane is not applicable in manoeuvring computations. Similar to the flow around a hydrofoil with attacking angles, the vortices and flow separation make the problem physically more complicated to resolve. Benchmarking and validation of the computations of manoeuvring using CFD is the only way leading to successful future applications of CFD technology.

Seakeeping deals with ship motions in waves. Traditionally, it was tackled by a combination of model tests in a wave basin and numerical tools based on simplified methods, such as strip theory.

Figure 4 MARIN seakeeping model test

The facilities in place for seakeeping model testing are approaching cutting edge with state-of-the-art wind-wave-current maker. However, the costs involved also increase exponentially. Thus in tight-budget projects, numerical prediction of seakeeping performance serves as an extremely practical alternative. Although impressive achievements in applying potential codes to seakeeping prediction have been made, there are fundamental difficulties for it to go forward any further, due to reasons such as large amplitude, effect of non-linearities, green water, damping, flooding, scale effect, and coupling with other modes of motion. In such cases, the RANS-based CFD method could serve as a potential lifeline. In this respect, attempts were made in this research to generate waves and study challenging problems involving diffraction and roll decay using the RANS approach as a paving the way to future general seakeeping prediction.

Flooding is an extremely peculiar scenario within damaged ship hydrodynamics. It is considerably tricky to study progressive water ingress and egress experimentally due to the availability of free flowing space within compartments. In contrast, the setup of numerical simulation is generally straightforward, such as draft, opening, roll centre, amplitude, centre of gravity and so on. On this basis, the hydrodynamics of roll motions of a damaged ship was also investigated by the RANS approach.

Figure 5 Estonia

Targeting on solving the above mentioned hydrodynamic problems using CFD, the scientific approach featuring benchmarking and validation studies of ship hydrodynamics is adopted to assess the accuracy and efficiency of all pertinent numerical tanks. In this respect, the structure of the thesis is organised in the following manner: Chapter 2 states the aim of the research; Chapter 3 elaborates on the critical review undertaken to establish state-of-the-art and identify gaps. Chapter 4 describe the mathematical modelling with numerical technology being briefed in Chapter 5. Chapters 6-10 address ship resistance, propulsion, manoeuvring, seakeeping and stability, respectively. Finally, the research is discussed in Chapter 11 leading to key conclusions, as outlined in Chapter 12.

2   Aim and Approach of the Research

The primary aim of this research is to address the analysis of classical ship hydrodynamic problems by using state-of-the-art CFD approach based on the solution of RANS equations. This covers resistance, propulsion, manoeuvring, seakeeping and the special case of flooding of a damaged ship.

The numerical simulations of the flow past a ship hull in the topics of ship hydrodynamics will be carried out with the interest in being able to assist with engineering applications in mind. The accuracy of the computed field variables such as velocity, wave elevation and turbulence stress, and the integral variables such as six-degrees-of-freedom forces will be evaluated by comparing numerical results with data from physical model tests.

The effects of varying the most sensitive parameters and their impact on the results of the calculations will be studied, which includes grid density and turbulence modelling.

For the simulation of self-propulsion performance, propeller modelling by body force will be implemented. A parametric study will be carried out to assess the accuracy and efficiency of the approach.

For the study of seakeeping performance, a digital wave maker will be developed and implemented to evaluate the influence of incident waves on ship hydrodynamics. In addition, roll decay will be simulated to obtain the hydrodynamic coefficients.

For the evaluation of ship manoeuvrability, a numerical PMM facility will be developed and applied to obtain the hydrodynamic derivatives for manoeuvring simulations.

Finally, for the investigation of the effects of flooding on damping and adding mass, numerical roll tank will be established to perform forced roll motions in intact and damaged conditions.

3   Critical Review

The key developments in state-of-the-art of numerical (mainly towing) tanks can be summarised through a series of CFD workshops held since 1980.

The first milestone in the development of numerical towing tank was marked by the first international workshop on numerical prediction of viscous flow around ships, which was held by SSPA-CTU in Gothenburg, Sweden in 1980 [47]. The purpose of the event was to assess the accuracy in ship viscous flows calculation and to find directions for further development. This was to be achieved through analysis of the results obtained by a large number of methods for two well-specified test cases.

Seventeen groups participated. The computational results were sent to organisers, who compiled all the information and presented them in a booklet format suitable for comparison, which was then distributed to the participants during the final meeting in Gothenburg.

Of the seventeen methods in the workshop, sixteen methods were based on the boundary layer approximation, albeit some of these included higher order effects (such as partially parabolic equation methods). Only one method was based on the Reynolds Averaged Navier-Stokes Equations (RANSE). The general conclusion from the workshop was that the boundary layer method computed the flow in the boundary layer reasonably well over the majority of the hull (up to 70% of ship length) but failed completely near the stern. Unfortunately, this is a region of great importance, because the inflow to the propellers needs to be predicted with high accuracy.

The main reason for the failure of the boundary layer methods was that the boundary layer is thick near the stern. The cross flow was strong and thus the cross pressure

gradient could not be neglected anymore. All of these features invalidate the assumptions made in the Prandtl boundary layer theory [72] near the stern and in the ship wake.

The failure of the boundary layer methods in the 1980 workshop prompted the developers to delve into more advanced methods. During the 1980s a large number of RANS methods were developed for the prediction of ship stern flow. Towards the end of the decade a new workshop was organised, which became the second milestone in the development of viscous-flow methods in predicting flow around a ship.

A SSPA-CTU-IIHR workshop was then held in Gothenburg in September of 1990 [48]. In a similar format to the 1980 workshop, the organisers compiled all the computed results and presented them together with the data, then available for both hulls, again in a format suitable for direct comparison. It was immediately obvious that a breakthrough had been made in the ability to predict the stern flow. In contrast to the 1980 event, now all methods but two were of the RANSE method, these being a boundary layer method and a Large Eddy Simulation (LES). Quite encouraging predictions were noted, even for the mystery case where there were no experimental data available beforehand.

However, one particular problem was identified: it was not possible to predict the detailed shape of the velocity contours in the central part of the wake, at the propeller plane. Both test cases involved were for full-bodied hulls (HSVA tankers) and the flow into the propeller plane was strongly influenced by vortices created at the bilge. This causes a hook-like shape within the velocity contours, which was not well predicted by the numerical methods.

The reason for the inability to predict the wake hooks was much debated both at the workshop and in the years to follow. Deng et al [21] showed that an ad hoc reduction of the eddy viscosity, using the K-ε two-equation turbulence model, in the bilge vortex by a factor of 2.5 created an almost perfect prediction of the wake hook. This

could indicate that inadequate turbulence modelling was the main reason for the failure in the wake predictions.

The numerical results obtained by Sotiropoulos and Abdallah [80] were in reasonably good agreement with the experimental data on the two test cases. In their method, primitive variables and collated mesh with compatible pressure boundary condition were applied. The features of pressure and velocity field were captured well. Thus the treatment of the boundary conditions is a key factor in affecting the accuracy of the calculation.

Although remarkable progress had been made to predict the flow around the ship stern in the next ten years, none of the methods were able to predict the free surface effect. As a result, free surface effects were neglected, and the double model was adopted in all numerical approaches.

The third key development was the workshop held in Tokyo in 1994, organised by the Ship Research Institute of Japan (SRI) [43], now the National Maritime Research Institute (NMRI).

The Tokyo workshop was somewhat different from the previous ones in that it focused on the free surface calculation, hence this workshop may be considered as the breakthrough of free surface RANSE calculations. Ten RANSE methods were featured with this capability.

At a Froude number of 0.316, most RANSE, as well as potential methods, predicted the wave profile on the Series 60, CB=0.60 hull. The wave pattern was also reasonably well predicted for up to about y/L=0.2 with the two of the best methods available at the time.

One such method was developed by Farmer, Martinelli and Jameson [25]; while the other was developed by Tahara and Stern [86]. However, moving further away from the hull, all of the methods suffered from considerable damping effects of the waves. No wave pattern could be predicted at a Froude number of 0.16, because all the waves would be damped out.

Farmer et al used a multi-grid acceleration technique to improve the convergence, while Tahara et al applied a large domain and finite-analytic difference method.

Some very good predictions of wake contours for the Hamburg Ship Model Basin (HSVA) tanker were presented by Sotiropoulos and Patel [81], who used a full Reynolds stress turbulence model.

After the Tokyo workshop, the main target of numerical prediction of flow around the ship was then focused on reliable viscous free surface calculation for practical hull forms.

The fourth key development affecting CFD progress was the workshop on CFD in ship hydrodynamics, which was jointly organised by CTU-IIHR-TUHH (Technical University of Hamburg-Harburg) and held in Gothenburg, Sweden in 2000 [49]. The objective was to focus on RANSE calculation with free surfaces, and to introduce modern hull forms as test cases (KRISO VLCC, Korean Container Ship, DTMB 5415). Twenty participating groups presented their papers on the workshop. The participants include not only major ship research institutes (IIHR, HSVA, MARIN, ECN, CTU, SRI, KRISO, INSEAN, DERA and MSU), but also major commercial code companies (FLUENT, CFX, COMET).

For the free surface calculations around the Korean container ship, the wave profile on the hull was quite well predicted, but the first wave crest was most often under-predicted. The best results were obtained by the NEPTUN method, developed by Cura [17], where the level set method was used to model the free surface.

However, the numerical results of the total resistance and its components, friction resistance and pressure resistance, were scattered and some predictions deviated by more than 10% from the experimental data.

The fifth CFD workshop was held in National Maritime Research Institute (NMRI) of Japan in 2005 [34]. The test cases of calculation of oblique towing and wave diffraction were added to this workshop. An effort was made to evaluate the use of

the ITTC Verification and Validation (V&V) procedure for uncertainty analysis in CFD [38].

A total of twenty groups participated in the Workshop, using seventeen different flow codes. The details of each code were collected using a questionnaire to assist in the classification of the numerical methods.

All of the RANS methods computed the flow around the hull using Cartesian coordinates and solved the Reynolds Averaged Navier-Stokes equations for the velocity and pressure with various turbulence models. The turbulence models ranged from zero equation to the Reynolds stress models with the majority using two equation SST k-ω or variants. Surface tracking and surface capture methods were used for the free surface, with the majority using surface capture methods.

Grid generation methods varied considerably with block structured, multi-block structured and block overlapping methods, with the latter predominating. Two of the participants used unstructured methods, and the number of grid points used varied from around 1 million to 10 million with the majority in the range 2-4 million points.

Computed velocity field contours compare quite well with the measured data. The hook-shape for the KVLCC2M was particularly well resolved by the results obtained from the Reynolds stress-based turbulence models and by models that were calibrated for such flows. Comparing with the wave profiles on the hull surface showed that there were good agreement with measured data. All of the methods used captured the wave crests near the hull reasonable well. However, the results from the longitudinal wave cuts show a large dependency on the grid resolution and numerical scheme.

Comparing the results obtained at CFDWS05 with those from Gothenburg 2000, there has been a slight improvement in the variations of prediction of the resistance coefficients (from 5%-8% for Gothenburg 2000 to 4%-7% for CFDWS 2005). However, the average comparison error appears to be around the same value. Predictions of the viscous wake indicate a similar trend with the best results obtained

from Reynolds stress models or those models that are calibrated for such flows. Generally speaking, the predictions on the free surface wave patterns have improved, especially in terms of the resolution of the wave crests downstream of the stern.

The sixth and latest workshop was held in CTU, Gothenburg in 2010 [50]. The test cases were similar but included more calculations of free running conditions than in CFDWS 2005. The computed results were collected and compared on the same test cases. Good agreements were obtained for most of the solvers, e.g. ISIS, FreSCo ICARE, CFDShip-IOWA, PANASSOS, SHIPFLOW, SURF, WAVIS, FLUENT, CFX and STARCD; however, they fail in the resolution of low Froude number wave patterns due to numerical damping. Two particular solvers, ISIS and FreSCo, outperform others with impressive predictions of wave elevation at the Froude number of 0.142 of hull form KVLCC 2. Both of them used the free surface capturing algorithm based on the VOF method with effective interface sharpening techniques [22, 62].

In this research, the general purpose software FLUENT 12.1 was used to calculate ship hydrodynamics. The main feature of the numerical simulation was the RANS approach with VOF modelling of free surface flow. Shear Stress Transportation (SST) k-ω was the default turbulence model used. In the case of resistance calculations with data of turbulence quantities, the Reynolds Stress Model (RSM) was used and compared with SST k-ω on the performance of turbulence prediction. Additionally, a grid sensitivity study was carried out for the selected test case to evaluate numerical uncertainty. Most computations were with free surface, and comparisons were made for the results with and without free surface on ship resistance.

The contents of this thesis will be organised in the following sequence.

Chapter 4 is the mathematical modelling. In this section, the RANS governing equations will be described. The closing turbulence models SST k-ω and VOF formulations outlined, and the boundary conditions briefly defined.

Chapter 5 is the description of numerical discretisation methods. The solutions of pressure-coupled equations and algebraic linear system are also outlined.

Chapter 6 covers the numerical resistance tank. The results of benchmarking and validation of resistance calculations are presented in this section. Uncertainty analysis following the ITTC guideline was carried out and numerical errors are evaluated. Based on the numerical results, model-full scale correlation is studied. Two well known approaches, Froude and Hughes', of data extrapolation from model to full scale are compared and the approach based on numerical wind tunnel to calculate 1+k is implemented.

Chapter 7 is the numerical propulsion tank. The body force method is described and implemented in the study hull-propeller interaction of a container ship. The effects of body force parameters were investigated and the results compared with experimental data.

Chapter 8 presents the results of the numerical manoeuvring tank. Two manoeuvring motions are addressed, which are oscillatory sway and oscillatory yaw. The derivatives with respect to velocity and acceleration are calculated by simulations of oscillatory motions. The results of manoeuvring simulations are then compared with experiment data.

Chapter 9 is the study of numerical seakeeping tank. The wave generation is implemented at the inlet. The computed results of incident wave effect are validated. Comparisons of numerical and physical wave tanks indicate that quality of the numerical wave tank is encouraging. Additionally, roll decay is simulated by RANS method. The numerical results were compared with measured data.

Chapter 10 is the numerical roll tank. The forced roll motions at intact and damage conditions are simulated numerically and the flooding effects on ship hydrodynamics are investigated.

Finally, the results and analysis of the implementation of all numerical tanks are discussed in Chapter 11 leading to a number of conclusions as described in Chapter 12.

4   Mathematical Modelling

When ships sail, no matter whether they are sailing in rough sea or calm river conditions, they will inevitably be subjected to what could be referred to in a generalised manner: the effects of free surface.

In rough sea conditions, we may witness the so called "green water" or the water on deck effect, one of the phenomena free surface exhibits violently, which could result in deck equipment, deck house and cargo damage or indeed the stability of the ship could deteriorate, particularly for damaged vessels, and in the worst case scenario, the ship may capsize.

Even in calm river, we may notice mild yet visible free surface effects. Regular wave patterns are formed beside and behind the ship, called "Kelvin" waves, a first described by Load Kelvin in 1887. The phenomenon was illustrated by a point of moving pressure in wave theory, and in a matter of fact, the ship wave can be treated as the superposition of a variety of pressure sources released from the bow, shoulder, stern, appendages and so on.

Ship waves are steadily generated by a cruising ship while sailing and energy needs to be supplied constantly to sustain these waves. This energy is accounted for through what is called wave resistance. To reduce fuel consumption, decrease oxide emission and protect the environment, naval architects are paying increasingly more attention to the study of wave resistance.

The modelling of the wave requires delicate computational techniques. The interface between gas and liquid is often referred to as free surface. The reason for the "free" designation arises from the large difference between the densities of gas and liquid (e.g., the density ratio for water and air is about 820). A low gas density means that

its inertia could be ignored compared to that of the liquid. In this sense, the liquid moves independently, or freely, with respect to the gas.

It is apparent that the presence of a free or moving boundary results in serious complications for any type of analysis. Ship hydrodynamics becomes increasingly more difficult to address due to the complexity arising from breaking waves, green water, complicated geometry, multiple modes of motions and even cavitation. Thus special techniques should be used to model free surface.

Regardless of the method employed, there are three essential features required to model free surfaces properly:

• A method is needed to describe the shape and location of the surface

• An algorithm is required to evolve the shape and location with time

• Free-surface boundary conditions must be applied at the surface

Earlier free surface models were based on the adaptive grid method by Hirt [36]. The mesh is not fixed and the governing equations are solved on the moving mesh. The free surface is tracked and updated by the fluid velocity at the free surface boundary.

Because one of the boundaries (the free surface) of the computational domain is part of the solution (unknown beforehand) and is moving, the computational mesh is deformed explicitly with time. Therefore, the method to use is the Lagrangian method.

At the free surface boundary, there are kinematic and dynamic boundary conditions imposed.

The kinematic condition states that there is no mass flux across the free surface and the dynamic condition that the forces on both sides of the boundary are in equilibrium.

The advantage of the adaptive grid method is the simplicity in its concept, the amount of saving in computer storage as only the fluid domain needs to be discretised and most importantly allows an easier adaption of the mesh to the ship motion problems. The disadvantage being that remeshing needs to be done at every time step to fit the free surface boundary and may encounter the problems when there are large steepness, overturning and fragmentation of free surface.

Thus, this method is normally used for moderate amplitude of free surface flows with and without ship motions.

Instead of using the Lagrangian method, Euler methods are widely preferred to avoid mesh deformation. There are a few interface capturing techniques available such as Marker-And-Cell (MAC) [32], Volume-of-Fluid (VOF) [35], Level-Set (LS) [69], etc. Amongst them, the VOF method is one of the methods used in most commercial software such as FLUENT, CFX and STARCD etc. Therefore, mathematical modelling based on VOF will be used in this work.

Because the turbulent flow is characterised by a fluctuating velocity field with a continuum spectrum of frequencies up to very high range, it is computationally much more expensive to simulate such flows directly in practical engineering calculations as in direct numerical simulation. Instead, instantaneous governing equations can be time-averaged to remove the small scale, resulting in a modified set of equations that are computationally less expensive to solve (Reynolds averaged). However, the modified equations contain additional unknown variables (Reynolds stress). Turbulence models are used to determine these variables in terms of their known quantities, which are called closure relations.

The origin of the time-averaged Navier-Stokes equations dates back to the late nineteenth century when Reynolds (1895) published results from his research on turbulence. The earliest attempts at developing a mathematical description of the turbulent stresses, which is the core of the closure problem, were performed by Boussinesq (1877) with the introduction of the eddy viscosity concept. Prandtl (1904) introduced the boundary layer theory and developed the concept of mixing-length

model, which prescribed an algebraic relation for the turbulent stress. These early developments were the cornerstone for nearly all subsequent turbulence modelling efforts.

Generally, turbulence models can be divided into the following types: algebraic turbulence models (zero equation turbulence models); one equation turbulence models; two-equation turbulence models; Reynolds stress turbulence models; and large eddy simulation.

Among algebraic turbulence models, two well-known models are Cebeci-Smith [11] and Baldwin-Lomax [5] turbulence models. Cebeci and Smith's model was designed for attached boundary layer, while Baldwin and Lomax proposed a model to define turbulence length scale from the shear layer thickness (suitable for separated flow). These turbulence models can be applied successfully to some physically simple turbulent flows. However, because the turbulence transportation is neglected and mixing length is prescribed, it is not suitable for turbulent flow around complicated geometry such as flow past ship stern and its wake.

As an alternative to the algebraic or mixing length model, a one-equation turbulent model has been developed in an attempt to improve the turbulent flow predictions by solving one additional transport equation. The well known one-equation turbulence model of Spalart and Allmaras [82] solves a modelled transport equation for a quantity that is a modified form of the turbulent kinematic viscosity. The model is successfully being used for aerospace applications involving wall bounded flows. However, these models are criticised for their inability to rapidly accommodate the change in length scale that might be necessary when the flow changes abruptly from wall bounded to a free shear flow (flow around ship stern). Spalart -Allmaras turbulence model is thus effectively a low Reynolds number model, requiring the viscous affected region of the boundary layer to be properly resolved.

In the two-equation turbulence models, two transport equations related to the turbulence characteristic length and speed scale are solved.

Kolmogorov's k-ω model [44] (1942) was the first two-equation turbulence model to involve turbulent kinetic energy and specific dissipation rate while the K-ɛ model developed by Launder and Spalding [51] (1972) is currently the most widely used two-equation turbulence model in engineering problems. The low Reynolds number K-ω model can predict some characteristic quantities of turbulent flow with good accuracy, however, it requires fine mesh to model the flow in the viscous sub-layer.

The eddy viscosity approximation for determining the Reynolds stresses is not a very effective model when it comes to flows with sudden changes in mean strain rate, curved surfaces, secondary motions, rotating and stratified flows, and separated and three-dimensional flows. The eddy viscosity model typically fails to give anything more than qualitative results due to its primary assumptions of the local isotropy and local equilibrium inherent in the model, which inherently assumes that the normal Reynolds stresses are equal, and that the flow history effects on the Reynolds stresses are negligible.

In order to overcome the disadvantages of the eddy viscosity models, the Reynolds stress turbulence models introduce transportation equations for Reynolds stress. However, due to the increased complexity of this class of turbulence models, the Reynolds-stress closure models have not been commonly used. The best-known Reynolds-stress closure model was developed by Launder, Reece and Rodi [52] (1975).

In relation to numerical simulations of turbulence at the highest level, Large Eddy Simulation (LES) ranks second after direct numerical simulation (DNS) as being the most computationally intensive. The primary idea behind LES is only to simulate the larger scales of turbulence that are set by geometry or specific flow conditions and to account for the influence of the neglected smaller scales by use of an alternative model. Since turbulence is known to be more isotropic at smaller scales, it is believed that the usual model assumptions involved in the eddy viscosity models would not matter as long as the grid is sufficiently fine. Since the neglected scales

are roughly proportional to the cell size, a filter is introduced to keep the larger scale and discard (model) smaller scale.

The most well-known Large-Eddy-Simulation models (Subgrid scale models) were developed by Smagorinsky [78] (1963) and Lilly [55] (1966).

The use of LES simulation is still limited due to its requirement for computer resource. It has currently been successfully applied to simpler geometries such as flow around a circular cylinder.

In this research, it should be noted that the SST k-ω, which combines the accuracy of near-wall k-ω and robustness of turbulent core area of k-ε will be used as the default turbulence model unless otherwise noted.

4.1 Governing Equations

The Reynolds averaged Navier-Stokes equations with SST K-ω turbulence model and VOF modelling are written as shown next.

4.1.1 Continuity Equation

$$\nabla \cdot \vec{V} = 0. \tag{1}$$

4.1.2 Momentum Equation

$$\frac{\partial}{\partial t}(\rho\vec{V}) + \nabla \cdot (\rho\vec{V}\vec{V}) = \rho\vec{g} - \nabla P + \nabla \cdot \tau + S \tag{2}$$

4.1.3 Turbulence Model

$$\frac{\partial}{\partial t}(\rho K) + \nabla \cdot (\rho \vec{V} K) = \nabla \cdot (\Gamma_K \nabla K) + G_K - Y_K \tag{3}$$

$$\frac{\partial}{\partial t}(\rho \omega) + \nabla \cdot (\rho \vec{V} \omega) = \nabla \cdot (\Gamma_\omega \nabla \omega) + G_\omega - Y_\omega \tag{4}$$

4.1.4 VOF Equation

$$\frac{\partial}{\partial t}(r_w) + \nabla \cdot (r_w \vec{V}) = 0. \tag{5}$$

$$r_w + r_a = 1 \tag{6}$$

Where:

∇ Hamiltonian or gradient operator

$\vec{V}$ Velocity vector

t Time

$\vec{g}$ Gravity vector

P Pressure

$\tau = \rho(\mu + \mu_t)(\nabla \vec{V} + \nabla \vec{V}^T) - \frac{2}{3}\rho k \delta_{ij}$ Stress tensor

$\rho = r_w \rho_w + r_a \rho_a$ Mixture density

$\mu = r_w \mu_w + r_a \mu_a$ Mixture viscosity

ρ_w and ρ_a Water and air densities

μ_w and μ_a Water and air dynamic viscosities

S	External body force

$$\mu_t = \alpha^* \rho K / \omega$$

$$\alpha^* = \alpha_\infty^* \left(\frac{\alpha_0^* + \mathrm{Re}_t / R_k}{1 + \mathrm{Re}_t / R_k} \right)$$

$$\mathrm{Re}_t = \frac{\rho k}{\mu \omega}$$

$$R_k = 6$$

$$\alpha_0^* = \frac{\beta_i}{3}$$

$$\beta_i = 0.072$$

$$\alpha_\infty^* = 1$$

$$\Gamma_K = \mu + \mu_t / \sigma_K$$

$$\sigma_k = 2.0$$

$$\Gamma_\omega = \mu + \mu_t / \sigma_\omega$$

$$\sigma_\omega = 2.0$$

Both r_w and r_a satisfy the following restriction:

- $0 <= r_w$, $r_a <= 1$

- If r_w , $r_a = 0$, the cell is full of air or water

- If r_w , $r_a = 1$, the cell is full of water or air

- If $0 < r_w$, $r_a < 1$, the cell contains the interface

- If r_w, $r_a = 0.5$, interface capturing condition

In the VOF approach, a assumption for transported quantities is made that the field variables (velocity, pressure, temperature and turbulence quantities) are shared by all phases of fluids. Therefore, only a single set of governing equations is derived.

In a 3D case, there are eight equations to be solved for eight variables, i.e. u, v, w, p, K, ω, r_w, and r_a.

4.2   Boundary Conditions

To solve the controlling equations above, proper boundary conditions need to be imposed.

At the inlet, velocity and other flow variables are specified explicitly. Turbulent quantities are derived from the turbulence intensity and the turbulence viscosity ratio, which are 1% and 1 respectively.

At the outlet, hydrostatic pressure is prescribed.

The outer boundary can be treated as a slip wall where zero shear stresses are imposed. Normally the outer boundary is taken at one ship length away from the centre line so that the blockage coefficient is less than 1% and the blockage effect can be neglected.

Special care was given to the boundary condition on the hull surface.

There are two ways of modelling near wall boundary layer. The first is through the use of the non-slip boundary condition where the viscous sub-layer needs to be well resolved. This requires the use of high fidelity low Reynolds number turbulence model, and Y plus should be below 1, i.e. very fine meshes. The second is through the use of wall function. The first grid point is normally located in Log-law zone,

where Y plus is around 30 so that most turbulence models can be used, and the number of total meshes used can be reduced significantly.

4.3   Wall function

In the method of the wall function, slip velocity is prescribed based on the distance from the wall, normally non-dimensioned as Y plus.

Y plus takes the following form:

$$Y_P^+ = \frac{\rho u_\tau Y_P}{\mu}$$

Y_p is the distance of first grid point to the wall

Where wall friction velocity is defined as

$$u_\tau = \sqrt{\frac{\tau_w}{\rho}}$$

τ_w denotes wall shear stress.

Turbulent flows are significantly affected by the presence of walls, thus the mean velocity field is affected by the no-slip condition that has to be satisfied at the wall. However, the turbulence is also affected by the presence of the wall in non-trivial ways. At very close proximities to the wall, viscous damping reduces the tangential velocity fluctuations, while kinetic blocking reduces the normal fluctuations. Towards the outer part of the near-wall region, however, the turbulence is rapidly augmented by the production of turbulence kinetic energy as a result of the large gradients in mean velocity.

Numerous experiments have shown that the near-wall region can be subdivided into three layers:

The inner most layer, called the viscous sub-layer ($Y^+ <= 5$), where the flow is laminar and molecular viscosity plays a dominant role in momentum, heat and mass transfer.

The outer layer, called the fully turbulent layer ($Y^+ >= 30$), where turbulence plays a major role.

Finally, there is an interim region (buffer zone $5 < Y^+ < 30$) between the viscous sub-layer and the fully turbulent layer, where both the effects of molecular viscosity and turbulence are important.

In the method of the wall function, semi-empirical expression of flow quantities are imposed based on the distance from the wall.

The standard wall function of Launder and Spalding [51] is given below:

The non-dimensional velocity is defined as

$$U_P^* = \frac{U_P}{u_\tau}$$

Based on the experimental and DNS results of flat plate and channel flow, the log law and linear law can be written as follows

Logarithmic law:

$$U_P^* = \frac{1}{\kappa} Ln(E Y_P^+)$$

Where

$\kappa = 0.42$

$E = 9.81$

Linear law:

$$U_P^* = Y_P^+$$

The logarithmic law for the mean velocity is known to be valid when $Y_P^+ > 30$. The upper limit depends on the Reynolds number and may vary from 300 to 500. The linear law is valid for $Y_P^+ < 5$. In the buffer sub-layer, a transition from the linear to the logarithmic law takes place. In the practical usage of wall function, a critical Y_P^+ value of 11.225 is set as an intersection where the switch between linear and logarithmic law occurs.

The wall function is used to provide robust boundary conditions. In momentum equations, boundary conditions are applied to specify shear stress. In turbulent kinetic energy equations, zero normal gradient condition is used and other boundary conditions are used to estimate turbulence production and specific dissipation rate. Specific dissipation rate is specified as below.

$$\omega_P = \frac{u_\tau^3}{\kappa Y_P K_P^2}$$

5 Numerical Methodology

The transport equation of scalar ϕ (u, v, w, K, ω) has the following general form:

$$\frac{\partial}{\partial t}(\rho\phi) + \nabla \cdot (\rho\vec{V}\phi) = \nabla(\Gamma \cdot \nabla\phi) + S \tag{9}$$

The finite volume discretisation of the equation requires the integration of the four terms as shown above in equation (9): time derivative, convection, diffusion, and source (force including pressure). Among the four terms, discretisation of convection involves special treatment, while discretisation of the other three terms is relatively straightforward.

5.1 Discretisation of the time derivative

Second order implicit discretisation is applied to the time derivative in transient problems:

$$\frac{3\phi^{n+1} - 4\phi^n + \phi^{n-1}}{2\Delta t} = f^{n+1}(\phi)$$

5.2 Discretisation of the diffusion terms

The diffusion terms in transport equations are centrally differenced, and are second order accurate.

5.3 Discretisation of the source term

The source term (pressure force etc.) is discretised with central interpolation. In order to improve stability, the source term is linearised in the non-linear case below:

$$S(\phi) = C0 + C1 \cdot \phi$$

If C1 is negative, then it can be dealt with implicitly, which will increase the value of the diagonal element in the coefficient matrix of the algebraic equations; otherwise it is dealt with explicitly.

5.4   Discretisation of the convection term

For the convection term, the finite volume integration of $\nabla \cdot (\rho \vec{V} \phi)$ needs to include the values of the variables on the surface of the cell, for instance $\rho \vec{V}$ and ϕ at faces e
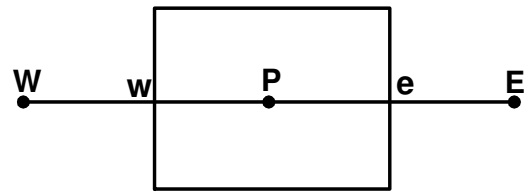
and w of cell P, as shown in the diagram on the RHS. For the interpolation of $\rho \vec{V}$, linear interpolation would be appropriate, however, for the interpolation of ϕ, linear interpolation may result in numerical oscillation, and thus differencing techniques will be described.

5.4.1   Interpolation of variable

Convection tends to cause flow to propagate along the characteristic line. In other words, the downstream characteristic quantities are determined by the upstream characteristic quantities; therefore, upwinding schemes are generally expected for the convection term. A central difference scheme for convection, i.e. a central interpolation of variable, may cause oscillations of the solution, and result in convergence problems. In this research, the second order upwinding interpolation is used.

5.4.1.1   Second order upwinding

When accuracy of the second-order is desired, quantities at the cell surfaces are computed using a linear reconstruction approach. In this approach, higher order accuracy can be achieved at the cell surfaces through a Taylor series expansion of the

cell-centred solution about the cell centroid. The face value ϕ_e for second-order upwinding is computed using the following expression

$$\phi_e = \phi_P + \nabla \phi_P \cdot \vec{ds}_{Pe}$$

Where ϕ_P and $\nabla \phi_P$ are the cell-centred (P) value and its gradient in the upstream cell, and $\vec{ds}_{Pe}$ is the displacement vector from the upstream cell centroid (P) to the surface centroid (e). This formulation requires the determination of the gradient $\nabla \phi$ in each cell, which is computed using the divergence theorem, which in the discrete form, can be written as

$$\nabla \phi = \frac{1}{V} \sum \bar{\phi}_f \vec{A}$$

where

- $\vec{A}$ is the area vector

- The face values $\bar{\phi}_f$ are computed by averaging ϕ from the two cells adjacent to the surface.

5.4.1.2   Interpolation of mass flux

In the derivation of a difference scheme for the scalar transport equations, linear interpolation scheme is widely used. However, when a non-staggered grid is used in a co-located grid layout where all variables are stored at the centre of cell, the linear interpolation for velocity in the continuity equation and for pressure in the momentum equation, leads to odd-even uncoupling, and result in a non-physical pressure field. There are two remedies for this problem: one is to use a staggered mesh, as proposed by Harlow and Welch [32] in their MAC method; and the other is a special interpolation treatment for mass flux as proposed by Rhie and Chow [74].

The main disadvantage of a staggered mesh layout is the consequential increase in the geometrical complexity of having multiple different sets of nodes and control volumes. A co-located mesh is thus more popular in finite volume methods.

5.4.1.3   Rhie and Chow interpolation

Rhie and Chow proposed a remedy to the checker-boarding problem by introducing an indirect interpolation for mass face flux $\rho \vec{V}$. The idea is described below.

The discretised scalar momentum equations have a general algebraic form as follows:

$$a_P \phi_P = \sum_{nb} a_{nb} \phi_{nb} + S \tag{11}$$

where a_P, a_{nb} are coefficients of the algebraic matrix and ϕ_P, ϕ_{nb} are variables of ϕ at the centre of cell P and nb (neighboring cells)

S is the remaining term, including the discretisation of body force, pressure gradient, etc.

For velocity u, the algebraic equation can be written as:

$$u_P = d_P \nabla_x P_P + S_R \tag{12}$$

Where S_R consists of other terms in the u momentum equation.

From this expression, a similar relationship can be applied to face velocity u_e or u_w. The combination with equation (12) obtains a modified face velocity as shown below:

$$u_e = \overline{u}_e - \overline{d}_e (\overline{\nabla}_x P_e - \nabla_x P_e) \tag{13}$$

The over-bars in equation (13) indicates that the quantities on the cell faces are obtained by linear interpolation from equation (12).

It can be seen from the above expression that the pressure values at node P do not cancel out and there is no odd-even decoupling.

By using this interpolation to calculate mass face flux $\rho\bar{v}$, the checker-boarding process can be prevented.

5.5   The discretisation of volume fraction equation

For the discretisation of the volume fraction equation, special treatments are needed. Using the abnormal interpolation method (e.g. second order upwinding) will result in strong numerical diffusion because of the large volume fraction gradient near the interface (it is a discontinuous interface for volume fraction function).

5.5.1   Geometric Reconstruction Method

The earliest method for VOF equation was the Donor-Acceptor method by Hirt and Nicholas [35]. Although the approach is designed to prevent numerical diffusion at the interface, it is of first order accuracy.

The geometric reconstruction method by Young [95] represents the interface between fluids using a piecewise-linear approach. It assumes that the interface has a linear slope within each cell, and uses this linear shape for the calculation of advection of the fluid through the cell face. There are three steps to this approach.

- The first step is calculating the position of the linear interface relative to the centre of each partially-filled cell, based on the information about volume fraction and its derivatives in the cell.

- The second step is calculating the advecting amount of fluid through each face, using computed linear interface representation and information about the normal and tangential velocity distribution on the face.

- The third step is calculating the volume fraction in each cell using the balance of fluxes calculated during the previous step.

In order to avoid numerical diffusion of volume fraction and to keep the interface sharp, geometric interpolation method is used for the equation of volume fraction.

The geometric reconstruction method is an effective algorithm to capture the free surface without any loss of sharpness. For ship hydrodynamic problems the free surface is normally steep at the bow and the stern, therefore the geometric reconstruction method with VOF approach is used in this research.

5.6   Discretisation of the continuity equation

For incompressible fluids, the continuity equation is a constraint on the velocity field. Central difference scheme or linear interpolation can be used to discretise divergence-free constraint. The difficulty of solving the continuity equation is that zero discrete divergence cannot be satisfied for velocity field from the given pressure. In order to satisfy mass conservation law, the pressure needs to be corrected. The correction of the pressure field will result in a correction of the velocity field through the use of momentum equations. Thus, from continuity equation, a Poisson type of pressure governing equation can be derived. This is the general idea of the SIMPLE type algorithms.

5.7   SIMPLE velocity-pressure coupling algorithm

From the discretised momentum equations, the velocity field can be calculated if pressure field is known. However, there is no transport equation for pressure. Therefore, the SIMPLE (Semi-Implicit Method for Pressure Linked Equations) type of algorithm is used.

SIMPLE velocity-pressure coupling method was developed by Patankar and Spalding [70] and has been refined by a number of researchers.

In the SIMPLE method, the pressure equation is derived from a constraint on the solution of the Navier-Stokes equation in order to satisfy continuity.

The discretised mass conservation gives:

$$u_e - u_w + \cdots = 0 \tag{14}$$

The velocity field resulting from the current pressure field does not generally satisfy the mass conservation equation.

The change of velocity is related to the change of pressure through equation (13), as shown next:

$$u_e^{'} = (\overline{d}_E P_E^{'} - \overline{d}_P P_P^{'}) \tag{15}$$

Other terms are neglected because all correction will be zero when convergence is reached.

Inserting equation (15) into equation (14), equation (16) for pressure correction is obtained, which is similar in form to the pressure Poisson equation.

$$a_P P_P^{'} = \sum_{nb} a_{nb} P_{nb}^{'} + m \tag{16}$$

Where:

      m   mass imbalance in control volume

From pressure correction, velocity and pressure could be obtained as follows:

$$P_P = P_P + \omega_P P_P^{'}$$

$$u_P = u_P + u_P^{'}$$

Where:

ω_P is under relaxation (about 0.3) because of approximations made in pressure correction equation. For the velocity, no under relaxation is needed.

Generally, there are four steps in SIMPLE algorithm

- Step 1: Solve the momentum equation by the current pressure

- Step 2: Formulate pressure-correction equation

- Step 3: Solve pressure-correction equation

- Step 4: Correct velocity and pressure

Normally, several internal iterations are needed to reach convergence.

The basic SIMPLE method was initially developed by Patankar and Spalding in 1972. Since then a number of modifications to the coupling method have been made. The variants of SIMPLE are SIMPLEC, SIMPLER and PISO aiming to improve the coupling of the momentum and pressure equations, via minor modifications to the SIMPLE algorithm. In this research, the SIMPLE method is adopted.

5.8   Linear algebraic equation solver

After the finite volume discretisation of the governing equations using the numerical techniques described above, a large sparse set of algebraic equations is generated. Once the solution to the algebraic equation is found, the problem is solved.

Typically, a CFD algorithm will involve repetitive calculations of Poisson pressure equation and other scalar transport equations for momentum, volume fraction, and turbulence. Normally, most of its execution time will be spent in solving these linearised equations, thus the efficiency of the linear solvers determines the efficiency of the solution method as a whole. Therefore, the speed at which the linearised equations are solved is crucial for the overall efficiency of the solver.

Methods for solving linear equations can be divided into two classes, the direct method and the iterative method.

Direct methods such as Gauss elimination and LU factorization are often used for small dense problems. However, for the large sparse problems which are typically encountered in the solution of partial differential equations, iterative methods such as Jacobian method, Gauss-Seidel, SOR (successive over relaxation), Stone method and CG (Conjugate gradient) would be more efficient.

The iterative solvers are fast for small mesh sizes, their rate of convergence decreases with an increasing number of equations. This is mainly due to the fact that these methods are much faster at smoothing the small wavelength components than the long wavelength components of the error. One way to improve their efficiency is through the multi-grid acceleration technique where a PDE is solved on a series of meshes with varying number of mesh points.

There are three basic operators in a multi-grid technique: the smoother, which improves the current estimate of the solution on a given mesh; and the restriction and prolongation operators, which maps a set of equations and provides a solution between a fine and a coarse mesh.

Combining simple iterative method and multi-grid technique reduces the convergence time significantly. In this research, a Gauss-Seidel method with multi-grid acceleration algorithm is used to solve the linear equations system.

5.9 Parallel computing

All numerical calculations are run in parallel mode. The machine used in this research is a High Performance Computing (HPC) cluster with 8*130 (nodes) processors provided by Esteem Systems Ltd in partnership with SUN Microsystems (now Oracle).

The machine has a theoretical peak performance of 13 TeraFlops, equivalent to thirteen thousand billion operations per second.

For a typical resistance calculation of 2M cells with a computational time of 20 seconds, it takes roughly 30 hours of clock time for a machine using 16 cores.

6   Resistance

In this section, the computational results of the steady flow around the hull in forward motion are presented. The predicted velocity, wave and turbulence quantities are compared against available model test data. The uncertainty in the calculations of ship resistance is also addressed.

6.1   Test Case

A Cargo ship (Series 60) was selected for the first numerical analysis. This hull form was widely used as test case of earlier international CFD conferences and as the benchmark test in the calibration of towing tank system. A wide range of data is available thanks to the international collaboration of the experimental studies on this hull form.

The main dimensions are listed in Table 1**: Main dimensions**

Table 1: Main dimensions of Series 60

	model scale	full scale
Lpp [m]	3.048	121.92
B [m]	0.406	16.256
T [m]	0.163	6.502
CB	0.60	0.60
Displacement [m^3]	0.121	7744.0

Wetted surface [m^2]	1.579	2526.4

The main particulars in the model scale correspond to the model produced in IOWA Institute of Hydraulic Research (IIHR), University of IOWA. Resistance test and flow measurements of the model were carried out in the IIHR towing tank.

As we can see from Figure 6 **Series 60 hull form**, Series 60 is a fine hull form with a block coefficient of 0.60. There is no bulbous bow. The parallel middle body is short and the stern has an overhang.
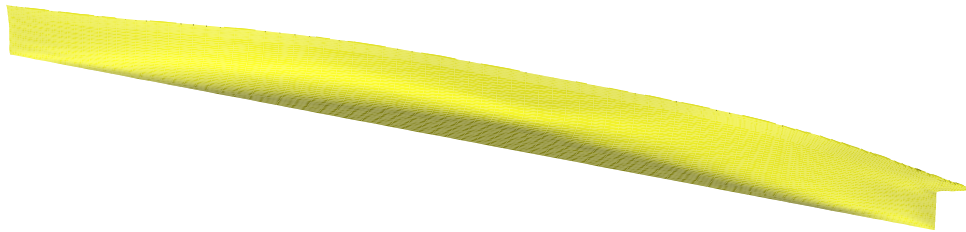
Figure 6 Series 60 hull form

6.2   Boundary Conditions

The computational domain is composed of velocity inlet, pressure outlet, hull surface, outer wall, and top and symmetry planes as shown in Figure 7.
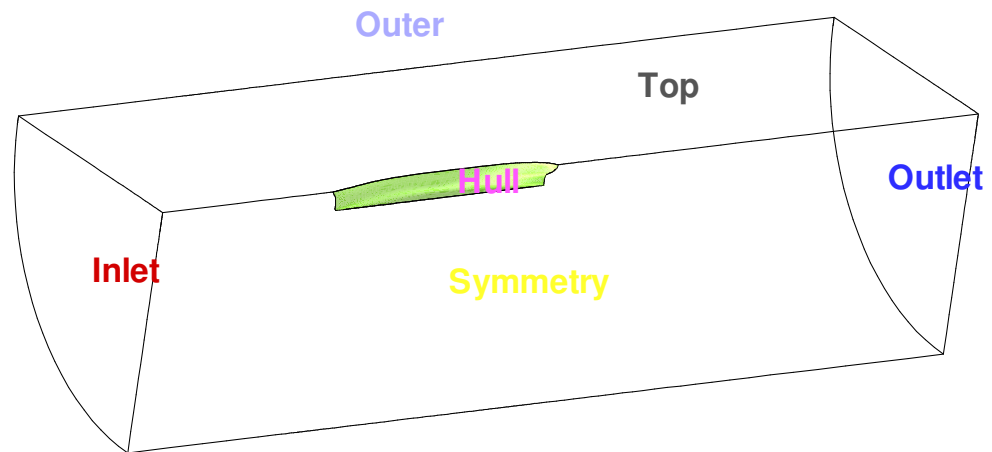
Figure 7 Computational domains

The velocity inlet is located at one ship length in front of the bow where flow variables are specified explicitly.

For a model speed V, the components of velocity (u, v, w) are (V, 0.0, 0.0) respectively. The turbulent quantities are derived from turbulence intensity I and turbulence viscosity ratio, which are 1% and 1 respectively.

Turbulence intensity I is defined as $I = u'/V$

Where:

u' Turbulence fluctuation

I=1%

$u' = IV = 1\%V$

$K = 1.5u'^2 = 1.5 \times 10^{-4} \times V^2$

$\omega = C_u K / \nu$

Where:

C_u Turbulence constant is 0.09

The volume fraction is prescribed based on the draft. For cells above the free surface, r_w is 0. Otherwise, r_w is 1.0.

The outlet is at two ship lengths behind the stern where hydrostatic pressure is given.

The outer boundary is one ship length away from centreline. Slip walls are assigned.

6.3   Meshes

For the calculation of ship resistance, the centre plane is also a symmetry plane. Therefore, only half of the computational domain is meshed.

Special care was given to the number of cells within a wave length, in regards to the wave amplitude and the boundary layer.

Mesh quality is an essential factor in successful numerical simulations. In the boundary layer, the variation or gradient of physical quantities is large. The distribution of the grids should be sufficient enough to reflect the physical phenomena. Another region where fine grids are expected is around the free surface, where either the wave length is short or the wave amplitude is small.

The distance of the first grid from the wall is measured by Y plus. In this test case, all meshes are generated for the use of the wall function. The Y-Plus value is about 50.

Free surface is a unique flow phenomenon of ship hydrodynamics. The computational zone of the free surfaces needs to be carefully meshed. In this research, the following meshing measures are taken.

In the direction of incoming flow, the wave length is estimated as shown next:

The theoretical wave length $\lambda/L=2\pi Fr^2$

Where:

Froude number $\qquad Fr=\dfrac{V}{\sqrt{gL}}$

g $\qquad\qquad\qquad$ Gravity

Around 50 grid points are distributed in a wave length for a base mesh (for grid sensitivity study, other meshes are generated from the base mesh).

In the direction of wave amplitude, estimated free surface height is $CV^2/2g$ from Bernoulli's principle.

Where C is a correction factor, which takes into account waterline entry angle and 3D effects.

V is the ship speed.

In this study, C is 0.5.

Around 20 grid points are distributed evenly in the free surface zone for the base mesh.

The meshes were generated using multi-block techniques by GAMBIT 2.4.6. Six main blocks are created. These are the free surface block, bow block, stern block, middle block from bow to stern, front block from inlet to bow, and after block from stern to outlet. For those involving complex geometry, minor blocks are used within the main block to improve mesh quality.

For the purpose of the uncertainty studies, three meshes with a refining factor of $\sqrt{2}$ were generated. Total cell numbers are 0.25M, 0.71M and 2.0M, respectively.

The side view of mesh topology is shown below
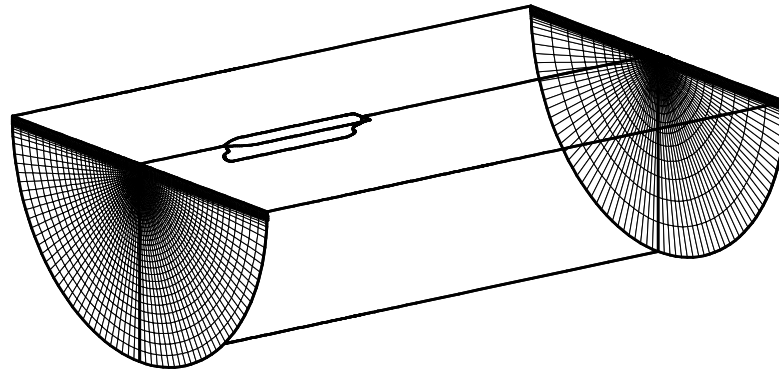
Figure 8 Side view of mesh topology

6.4   Numerical Verification

Grid sensitivity studies were carried out to check the grid dependency of field and integral variables.

For the numerical simulation of flow around the hull with free surface, unsteady formulation of the governing equations are used. Variable time step is chosen to ensure good convergence and high computational efficiency. The time step is determined by the Courant number:

$$C = \frac{udt}{dx} \, .$$

C is 1.0 for all transport equations, except in the case of the VOF equation, where C becomes 0.2.

The model speed is 1.73m/s and the Froude number is 0.316. The total amount of time steps required to reach a convergence is about 8000 and total non-dimensional time based on model speed and length is 4.0.

The computed results by three meshes are presented below.

The wave profiles in Figure 9 show that the comparison between computations and model tests, in which the X axis points towards the stern with its origin at the bow. Axis Z is an upward vertical axis with a factor of 1000 (Non-dimensioned by model length).
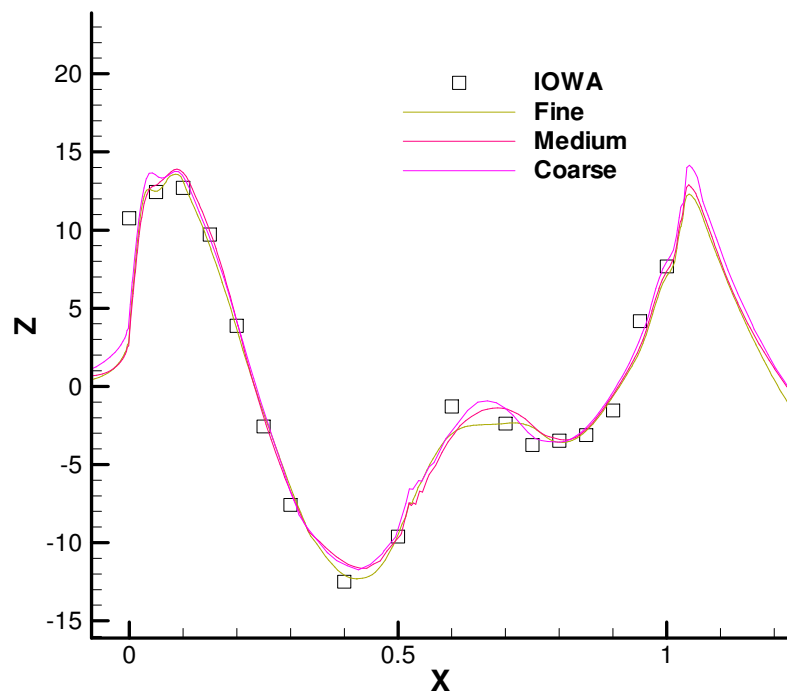
Figure 9 Comparison of wave profiles (Fr=0.316)

Where X is longitudinal coordinates nondimensioned by ship length and Z vertical coordinate with a factor of 1000.

As we can see from Figure 9, the first wave crest is at the bow. The non-dimensional theoretical wave height is $Fr^2/2=0.05$. The computed and measured wave heights are about 30% of the theoretical value. The real wave height is much lower than its theoretical value due to the viscous and 3d effects. We can also see from the plot that the first trough is at x/L=0.4. As we know, the theoretical non-dimensional wave length is $2\pi Fr^2$ or 0.63. The first trough from bow should be located at around x/L=0.32. It is slightly deferred due to changes in the shape of the front body. The second crest is at x/L=0.65, which is close to the wave length of the bow wave, but

its magnitude is much lower. This is due to the effects of the mid-body shape. Another wave crest is seen at the stern, which is of the same magnitude as the bow wave. Overall, the computed crest and trough of wave profile agrees well with the experimental data. The number of cells used in the base mesh is sufficient to capture the features of the wave. The fine mesh gives slightly better prediction than the coarse mesh.

Although three meshes predict similar wave profiles, fine meshes did improve the wave resolution slightly. Therefore, only the wave elevation obtained via the fine mesh is presented.

The comparison of wave elevation between calculation by fine mesh and measurement is given in Figure 10 and Figure 11. The computed and measured near field wave patterns are shown in Figure 10.
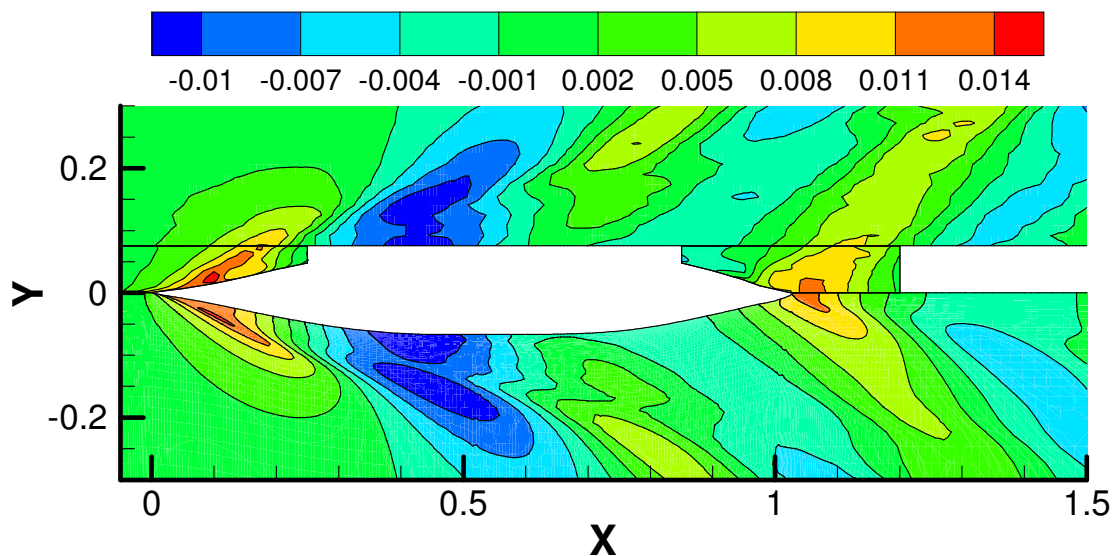
Figure 10 Comparison of wave elevation

(Upper: measurement IOWA, Lower: present calculation)

Where Y is lateral coordinate nondimensioned by ship length.

As we can see from Figure 10, two primary wave arrays are formed from the locations of stagnations at the bow and the stern. The waves travel downstream from there with a wave length of $2\pi Fr^2 L$. There are minor waves generated from the shoulders and these interact with the primary waves. The agreement between present calculations and measurements is extremely satisfactory.

The far field wave patterns are compared in Figure 11. As we can see, measured wave patterns are affected by severe deflection of the tank wall, while the computed results show both the divergent and the transverse waves reasonably well.

It can also be noticed that the predicted wave patterns are smeared far downstream, due to numerical damping. The mesh resolution in the far field is not sufficient enough to resolve the local wave pattern. The mesh size at the outlet is of the scale of the wave length to alleviate boundary reflections.

In most cases, we are only interested in the ship resistance and the near field wave elevation. The predicted accuracy of the far field wave patterns will not have a large influence on the near field wave pattern behaviour. If the far field wave were to be well resolved, the computational domain needs to be further enlarged and the mesh size reduced. The computational cost will increase exponentially tens and hundreds times of the current cost.

If far field wave estimation is needed, potential flow based method or multi-zone approaches such as SHIPFLOW of FLOWTECH and PANASSOS of MARIN could be used.
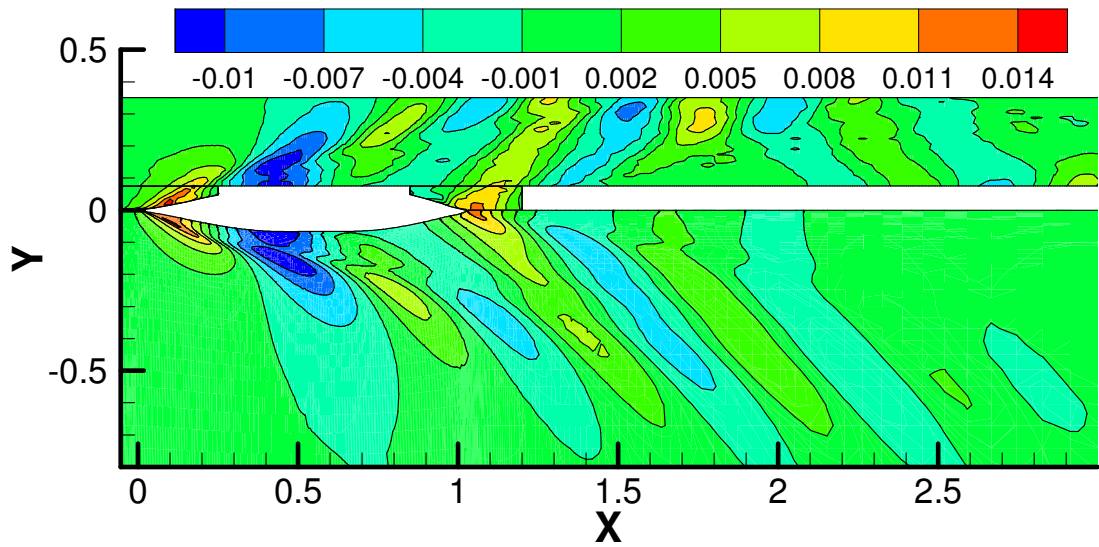
Figure 11: Far field wave pattern

(Upper: measurement, IOWA, Lower: present calculation)

6.5 Uncertainty Analysis

The computational results of the resistance at Froude number 0.316 by three meshes are given in Table 2 and are used for the grid uncertainty study in accordance with the quality manual of ITTC resistance committee [253].

Table 2 Grid convergence study

Grid	Coarse	Medium	Fine	Data
$1000C_T$	5.25	5.20	5.17	5.42
$1000C_P$	1.82	1.77	1.75	1.91(CR)

1000C_F	3.43	3.43	3.42	3.51(ITTC)

The computed and measured pressure resistance and friction resistance coefficients are also shown in Table 2. The comparison indicates that the computed friction resistances by the three meshes are close, but 3% lower than the ITTC correlation line.

The ITTC friction line is given by:

$$C_F = \frac{0.075}{(LOG_{10}Rn - 2)^2}$$

The difference is attributed to the significant transverse flow due to large curvature at the bow and the stern. The ITTC friction line tends to underestimate 3D effects by 2-3% at model Reynolds number.

To compare, we calculated the friction resistance coefficient employing Hughes's line and the ATTC line as shown next.

Hughes line:

$$C_F = \frac{0.066}{(LOG_{10}Rn - 2.03)^2}$$

ATTC line:

$$\frac{0.242}{\sqrt{C_F}} = LOG_{10}(Rn \times C_F)$$

The friction resistance coefficients are 3.13×10^{-3} and 3.40×10^{-3}, respectively via the Hughes line and the ATTC line.

The computed friction resistance coefficient agrees well with the ATTC line but is much higher than that of the Hughes line. Hughes' friction line is roughly 10% lower than ATTC and ITTC lines at model Reynolds number.

The effect of grid resolution on pressure resistance (wave resistance plus viscous pressure resistance) is clearly seen in Table 2. The change in pressure resistance due to mesh is roughly 3-5%. The pressure resistance coefficients converge consistently with increasing grid density. Therefore, we can use the Richardson extrapolation method to obtain the true value of the computed resistance coefficient.

Using computed total resistance in Table 2, we carried out a verification study following the ITTC guideline.

Grid refining factor: $r_G = \sqrt{2}$

The changes of solutions:

$$\varepsilon_{32} = S_3 - S_2 = 0.05 \times 10^{-3}$$

$$\varepsilon_{21} = S_2 - S_1 = 0.03 \times 10^{-3}$$

The ratio of solution changes: $R_k = \varepsilon_{21} / \varepsilon_{32} = 0.6$

Therefore, the monotonic convergence condition $R_k < 1.0$ is satisfied. The generalised Richardson Extrapolation (RE) can be used to estimate numerical errors.

Order of accuracy:

$$P_k = \ln(\varepsilon_{32} / \varepsilon_{21}) / \ln(r_G) = 1.5$$

The error of first order RE estimation:

$$\delta_k = \varepsilon_{21} / (r_G^{P_k} - 1) = 0.044 \times 10^{-3}$$

Correction factor:

$$C_k = (r_G^{P_k} - 1)/(r_G^{P_{kest}} - 1) = 0.68$$

Therefore, the improved estimate of error:

$$\delta_k^* = C_k \delta_k = 0.03 \times 10^{-3}$$

The uncertainty in error estimate:

$$U_k^* = (1 - C_k)\delta_k = 0.014 \times 10^{-3}$$

The corrected solution:

$$S_C^* = 5.14 \times 10^{-3}$$

The results of uncertainty analysis are summarised in Table 3.

Table 3: Verification of total resistance

R_k	P_k	C_k	δ_k^*	U_k^*	S_C^*
0.60	1.5	0.68	0.03×10^{-3}	0.014×10^{-3}	5.14×10^{-3}

The total resistance coefficient from the model test is $D = 5.42 \times 10^{-3}$. We can thus carry out the numerical validation.

The comparison error:

$$E_c = D - S_C = 5.42 \times 10^{-3} - 5.14 \times 10^{-3} = 5\%D$$

The uncertainty of numerical simulation:

$$U_{SN} = U_k^* = 0.2\%D$$

The uncertainty of model test:

$$U_D = 2.5\%D$$

Therefore, the validation uncertainty:

$$U_V = \sqrt{U_{SN}^2 + U_D^2} = 2.51\%D$$

The resulting comparison error is larger than the validation uncertainty: $E_c > U_V$ and thus simulation results are not validated. The simulation seems to underestimate the resistance coefficient. Similar results are obtained in the ITTC report [38]. The validation error was attributed to error in the numerical model (turbulence model) in the ITTC report. However, it was noticed that the stern tube and the propeller hub, which were fitted in the model tests were not simulated in both calculations. When these factors are taken into account, then the computed resistance coefficients agree well with the measurements.

The validation results of total resistance are summarized in Table 4.

Table 4 Validation of total resistance

E%	U_V %	U_D %	U_{SN} %
5.0	2.51	2.50	0.2

To check the computed velocity field, comparisons of the velocity distribution at the propeller plane is shown in Figure 12: Flow field at propeller plane. On the left of the plot is the measured velocity at the propeller plane [60] and on the right is the present calculation. As we can see, the computed contour of the longitudinal velocity and the cross vector generally agrees well with the measurements. There is a slight difference of flow near centre plane, as the flow from the measurement is not symmetric about the centre plane due to the error of model alignments and oscillations of the carriage; it is strictly symmetric in the calculation due to the boundary condition imposed.
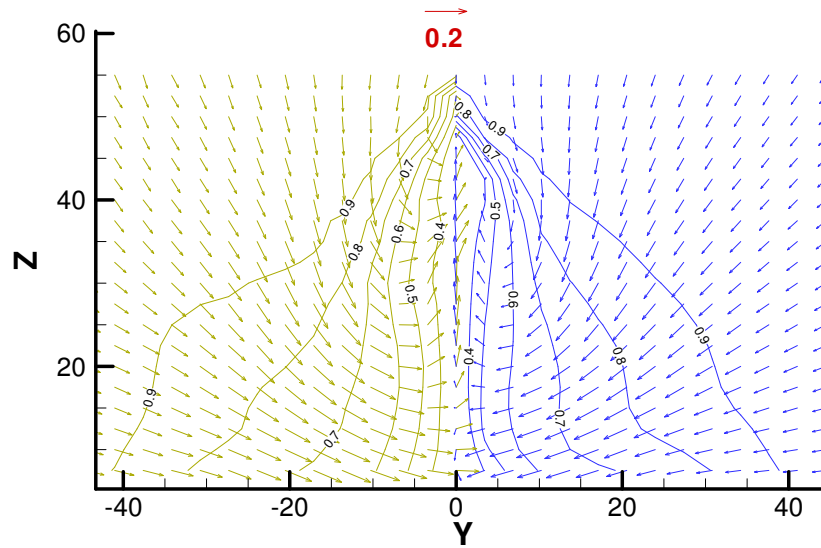
Figure 12: Flow field at propeller plane

(Left: measurement, IOWA, Right: present calculation)

Where Y and Z are lateral and vertical coordinates by ship length with a factor 1000.

6.6   Free Surface Effects

In order to estimate the free surface effects, two approaches are used. One is to compare the results from the double model calculations. The other is to use the Froude and Hughes' methods.

6.6.1   Double Model Calculations

The calculations of flow around the hull without free surface (double model) were carried out using three meshes with the same density as those in the free surface calculations (only removing meshes above the water surface).

The results of the computed resistance are given in Table 5.

Table 5 Grid convergence study

	Coarse	Medium	Fine	Data
$1000C_{TD}$	3.78	3.76	3.76	
$1000C_P$	0.32	0.30	0.30	
$1000C_F$	3.46	3.46	3.46	3.51(ITTC)

As we can see from Table 5, the differences between the computed resistances by the three meshes are small. The grid effects on the resistance coefficients are not significant at double model calculations. As we pointed out, the two areas where mesh resolutions are sensitive are free surface zone and boundary layer. Without free surface, the only area of mesh sensitivity would be the boundary layer. In the case of wall function, the resolution of the boundary layer is improved; therefore, the effect of grid density on the resistance without free surface is relatively small.

We can obtain wave resistance by subtracting double model result from that with free surface.

The wave resistance:

$$C_w = C_T - C_{TD} = 1.38 \times 10^{-3}$$

Where:

C_T and C_{TD} are resistance coefficients with and without free surface and are non-dimensioned by wetted surface area at rest S_w.

$$C_T = R / 0.5\rho V^2 S_w$$
$$C_{TD} = R_D / 0.5\rho V^2 S_w$$

R and R_D are total resistances with and without free surface (double model).

It accounts for 26.8% of the total resistance at Froude number 0.316.

We can also obtain form factor from the results of double model calculations as shown next:

Form factor:

$$1+k = C_{TD} / C_{FITTC} = 1.07$$

The viscous pressure resistance coefficient is kC_F, i.e. 0.24×10^{-3}, or 4.6% the total resistance coefficient.

6.6.2   Froude and Hughes approaches

Wave resistance can be derived from the total resistance by Froude and Hughes approaches.

In Froude's method, residual resistance coefficient is derived from the total resistance coefficient as shown next:

$C_R = C_T - C_F$

It gives a residual resistance coefficient of 1.57×10^{-3}. The residual resistance calculated using Froude approach includes both the wave resistance and viscous-pressure resistance. Viscous-pressure resistance is Reynolds number dependent; it will thus overestimate the wave resistance when it is used in the study of model-ship correlation.

Therefore, Hughes method [79] is more widely applied. In Hughes' method, residual resistance is derived as shown next:

$C_R = C_T - (1+k)C_F$

It gives a residual resistance coefficient of 1.38×10^{-3}, which is the same as that from the double model calculations.

6.6.3 Model-ship correlation

We can obtain ship resistance at full scale using Hughes method as shown next:

Full scale ship resistance coefficient: $C_{Ts} = C_R + (1+k)C_{Fs} = 3.01 \times 10^{-3}$

Where:

C_{Fs} is from the ITTC friction line at full scale.

6.7 Concluding remarks

In conclusion, calculations of flow around Series 60 hull as the benchmarking test for the numerical verification and validation of the computational results were carried out. The grid sensitivity studies were performed using three refining meshes. The computed wave profile, wave pattern and velocity distribution were in good agreement with model tests. The results show a monotonic grid convergence for computed resistance. Comparative computations with and without free surface were also conducted. Wave resistance was derived by double model calculation as well as using Froude and Hughes methods. The wave resistance is 26.8% of the total resistance, which is much larger than the viscous-pressure resistance, 4.6% in this case. The form factor is obtained from the results of the double model calculations and can be used for full scale extrapolation.

6.8 The calculation of flow around DTMB5415

The hull form of Series 60 of a cargo ship was one of relative simplicity due to the absence of bulbous bow and transom. From the 4th ship hydrodynamics workshop,

attentions were turned to modern hull form with bulbous bow and transom. Therefore, benchmarking calculation of flow around DTMB5415 was also made. The main purpose of the test case is to validate the numerical accuracy of flow around the modern hull form and to check the effects of turbulence models by comparison of the turbulence model SST k-ω with the Reynolds Stress Model (RSM).

Model DTMB5415, shown in Figure 13 was conceived as a preliminary design for a Navy surface combatant in 1980. The hull geometry includes both a sonar dome and a transom stern. Propulsion is provided through its twin open-water propellers driven by the shafts supported by struts. The hull form was selected as test case in recent CFD workshops.

Figure 13 Snapshot of the DTMB5415 model

The main dimension and loading conditions are given in Table 6.

Table 6 Principal Dimensions of DTMB5415

Main particulars		Full scale
Length between perpendiculars	LPP (m)	142.0
Length of waterline	LWL (m)	142.18
Maximum beam of waterline	BWL (m)	19.06
Draft	T (m)	6.15

Displacement	Delta (m3)	8424.4
Wetted area w/o rudder	SW (m2)	2972.6
Wetted surface area of rudder	SR (m2)	30.8
Block coefficient (CB)	Delta /(LPPBWL T)	0.507
Midship section coefficient (CM)		0.821
LCB (%LPP), fwd+		-0.683
Vertical Center of Gravity (from keel)	KG (m)	7.5473
Metacentric height	GM (m)	1.95
Moment of Inertia	Kxx/B	0.37
Moment of Inertia	Kyy/LPP, Kzz/LPP	0.25

The model DTMB5415 used in the IIHR model test has a scale ratio of 46.59 with an Lpp of 3.048m.

The model speed is 1.53m/s. Froude and Reynolds numbers are 0.28 and 5.13×10^{6}, respectively.

Model test was performed in free condition. The measured sinkage/Lpp and trim at Froude number 0.28 are: s= -1.92×10^{-3} and t = -0.136°.

In order to compare computed results with measurements, numerical simulations were carried out using sinkage and trim from the model tests.

For the calculations of resistance of a free running ship, there are two approaches. One is unsteady approach solving ship motion equations using computed heave force and pitch moment. The other is steady approach by updating sinkage and trim through iterations. Thus, more computational efforts are required. In this test case, focus is laid on the validation of turbulent quantities, thus the same computational conditions as model test including sinkage and trim are used.

6.8.1 Mesh

The computational domain is similar to that used in the calculations of Series 60. It has a size of 4× Lpp long (1× Lpp from inlet to bow, 2×Lpp from stern to outlet), 2×Lpp wide (in the case of resistance calculation, centre plane is a symmetry plane, hence only half of domain needs to be meshed), and 1×Lpp deep (plus 0.5×Lpp above waterline).

The sketch of the computational domain is shown in Figure 14.
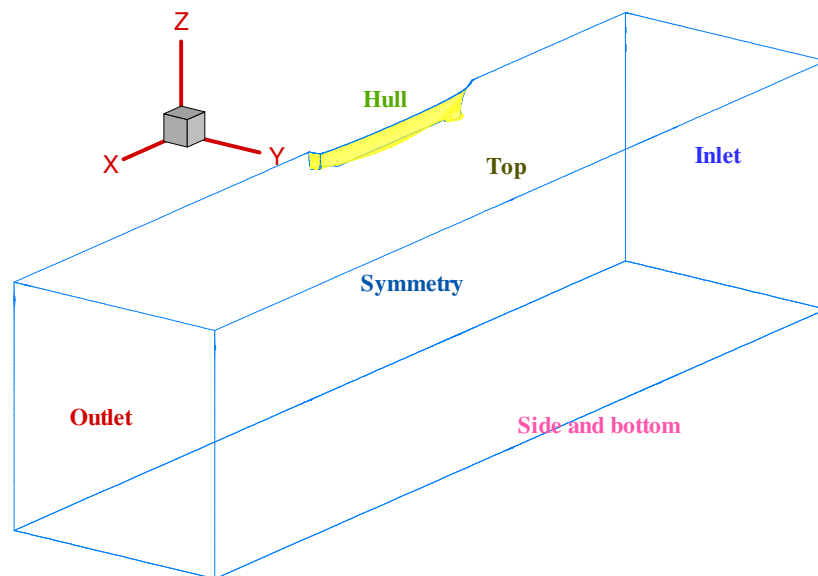
Figure 14 Sketch of computational domain

The structured meshes were generated using GAMBIT. Multi-block technology is applied. Altogether 30 blocks were used to cover free surface, boundary layer and wake. Total cell number is around 2.4M.

The Y plus value at hull surface is around 50. The surface meshes at bow and stern are shown in Figure 15.
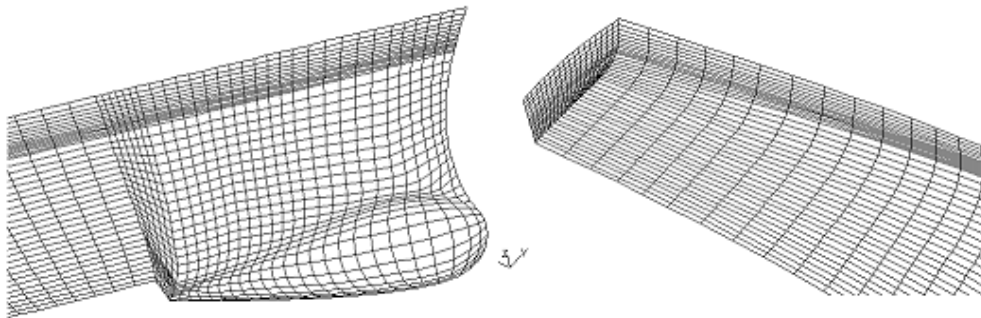
Figure 15 Fore and aft body meshes

A set up similar to that used in the test case of Series 60 is used. Computational results and analysis are given below.

6.8.2   Wave elevation

Three wave cuts at lateral locations y/L=0.082, 0.172 and 0.302 were measured experimentally by Olivieri [67] to provide data for wave validation. The comparisons of present calculation with measurements are given below.

The comparison of wave cuts at y/Lpp=0.082 is shown in Figure 16, where it can be seen that the first crest is located at the bow. The computed and measured first trough is at around x/L=0.25. As we know, the theoretical wave length is roughly 0.5Lpp at

Fr=0.28, therefore, the computed wave length is consistent with theory. Around mid-ship, the wave is flat. No clear wave length can be identified due to the interaction between bulbous bow and mid-body boundary layer. The agreement between calculation and measurement is good with the bow wave slightly overestimated and stern wave underestimated by the numerical calculations.
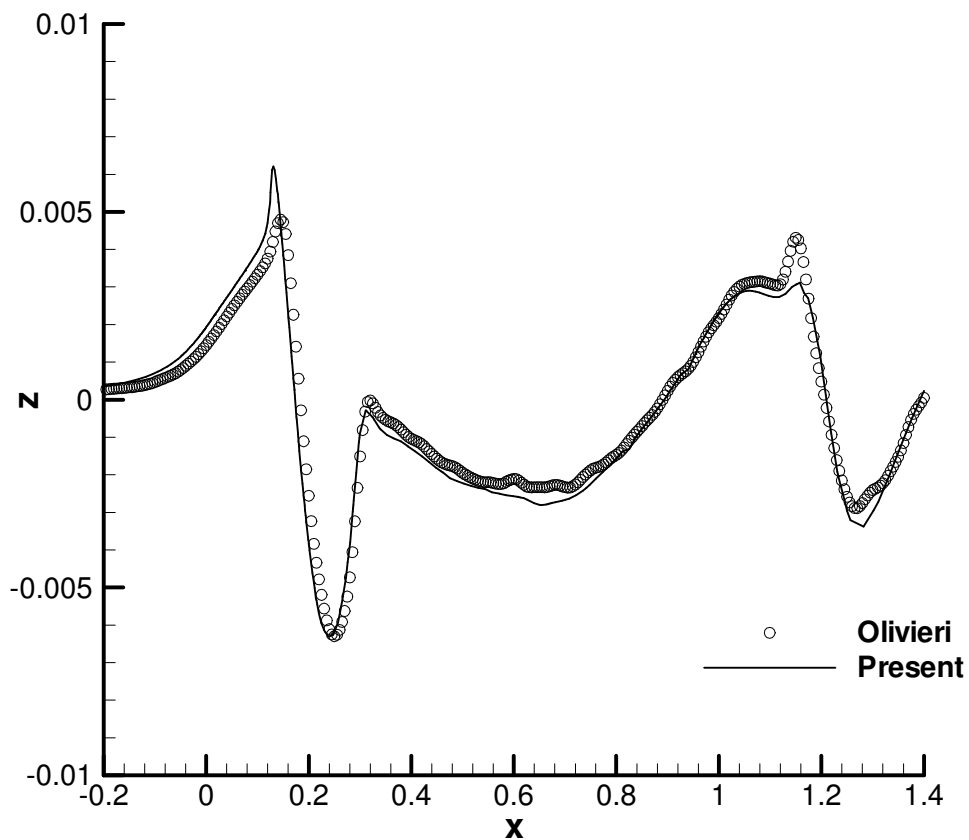
Figure 16 Wave cut, y/LPP = 0.082

Where X and Z are longitudinal and vertical coordinates nondimensioned by ship length

The comparison of wave cuts at y/Lpp=0.172 is shown in Figure 17. It can be seen that the primary wave generated by the bow and the transom travelled both transversely and longitudinally. One clear wave crest and trough can be seen near the

mid-body, which seems to be generated by the front shoulder. However, the wave length is shorter than that implied from theory due to its interaction with the wave from the back shoulder. The agreement between calculation and measurement is good with slight over-prediction by the computed results.
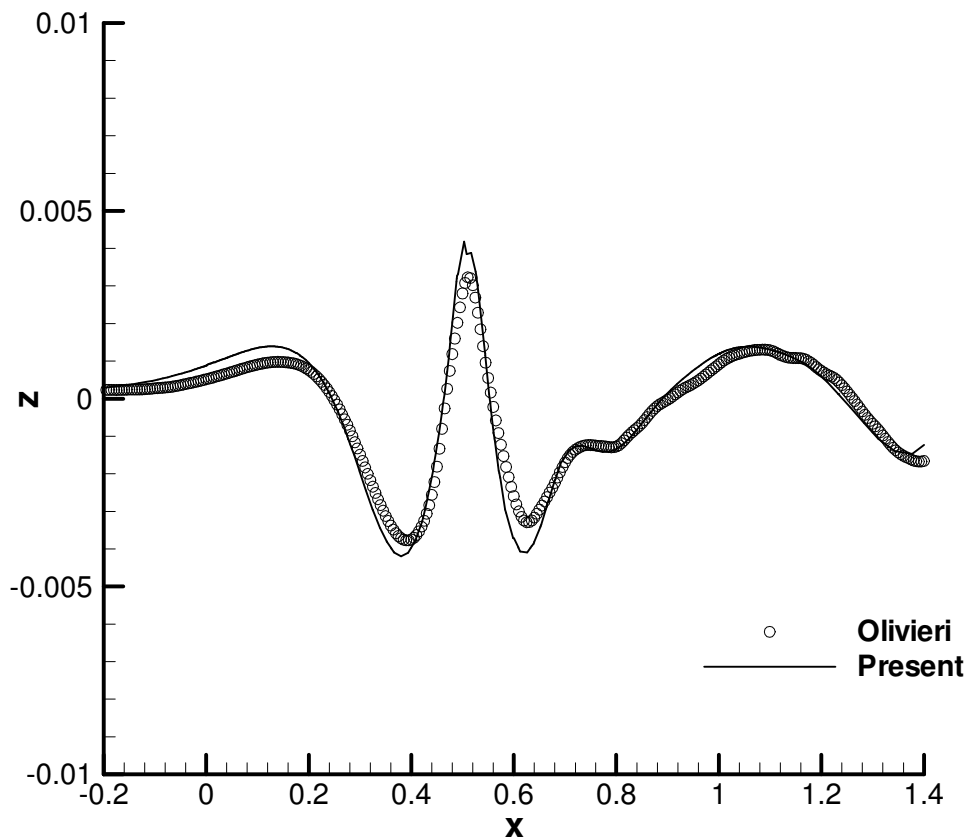
Figure 17 Wave cut, Y =0.172

Where Y is lateral coordinates nondimensioned by ship length

The comparison of wave cuts at y/Lpp=0.302 is shown in Figure 18. It can be seen that the wave is flat when x/Lpp<0.5 due to the characteristic envelop angle 19.28° of the Kelvin wave pattern. One free diverging wave can be seen due to interaction

of the bow and shoulder waves. The wave length is close to its theoretical wave length of 0.5Lpp. The agreement between calculation and measurement is good except for the excessive wave damping in the wake due to insufficient mesh density at the far field.
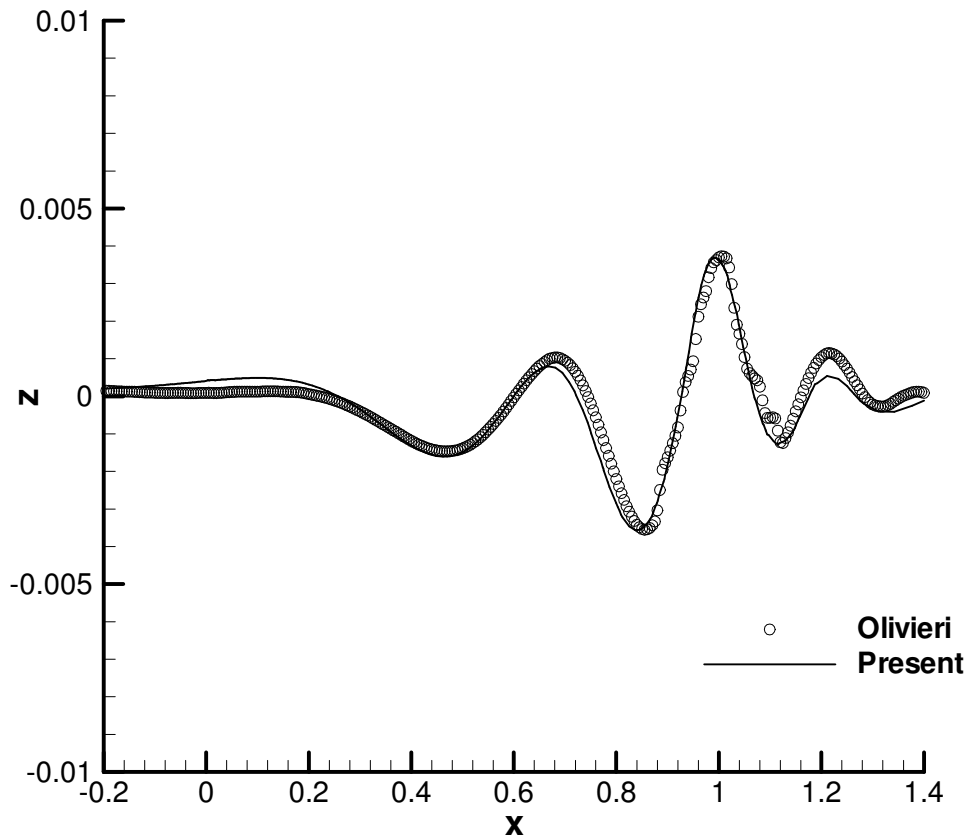
Figure 18 Wave cut, Y = 0.302

The comparison between wave patterns is shown in Figure 19. The computed near field wave elevation coincides with the measured wave. The bow wave, shoulder wave, stern wave and their interaction are well predicted by the present calculations.
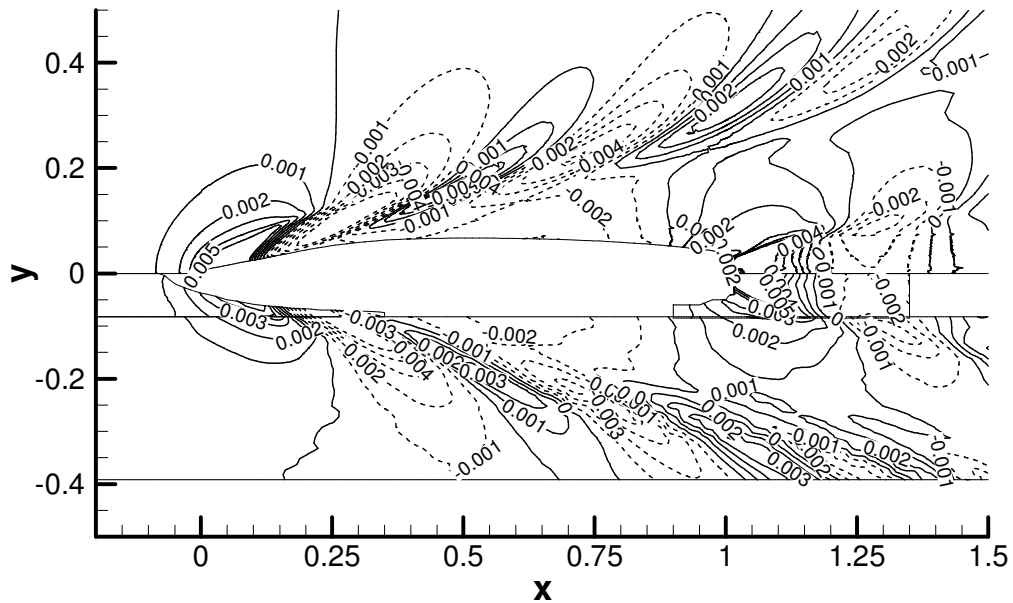
Figure 19 Comparison of wave elevations (Upper: Present, Lower: Olivieri)

6.8.3   Velocity field

The velocity distribution at the propeller plane is important for the analysis of propeller performance. A comparison of nominal wake (axial velocity contours) at the propeller plane is shown in Figure 20 and Figure 21. The computed axial velocity in the inner boundary layer is consistent with the measured one. At the outer boundary layer, agreement is generally good. Some discrepancies can be seen near the centre plane. The differences are attributed to the symmetric boundary condition imposed in the calculation. As we can see from the experiment data, the flow near the centre plane is not strictly symmetric due to errors in model alignment and carriage oscillation. Overall, the velocity contour is well predicted by the present calculation.
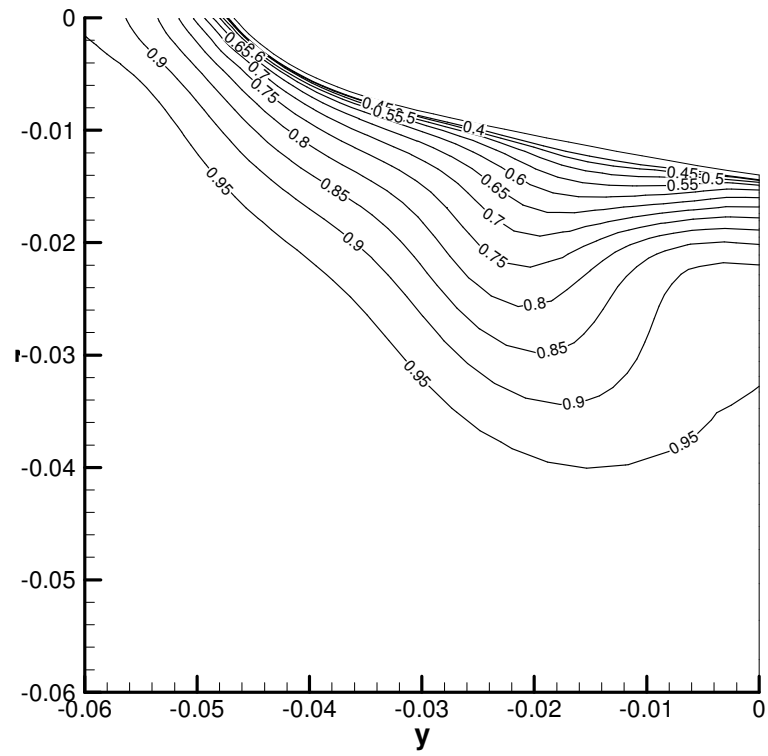
Figure 20 Computed longitudinal velocity contour at 0.935
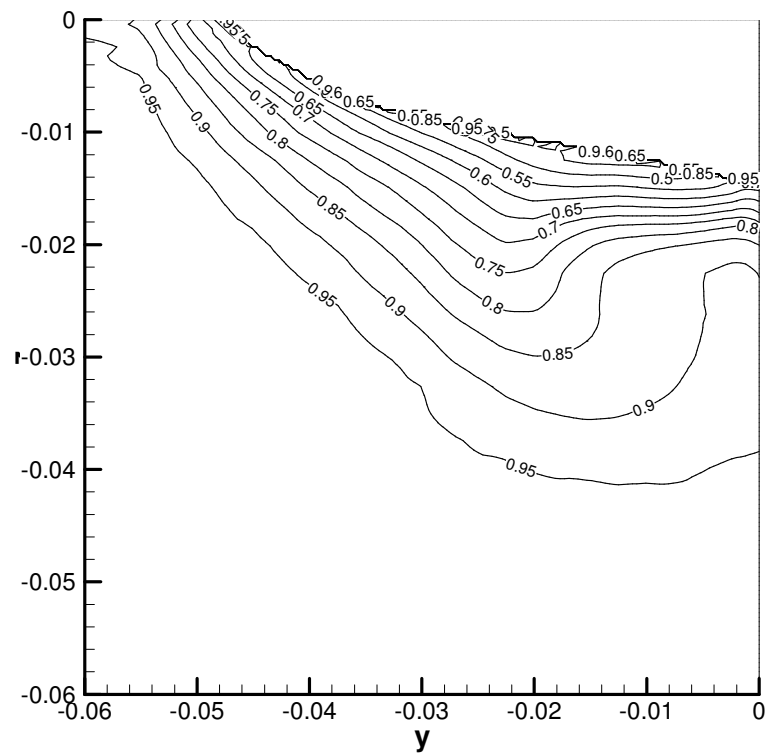
Figure 21 Measured longitudinal velocity contour at 0.935

6.8.4 Turbulence quantities

In this test case, the turbulence quantities from the measurements are available for comparison. The measurements were done by Olivieri [67, 68], therefore, comparisons of turbulence variables were made to assess the accuracy of Shear-Stress Transport (SST) K-ω turbulence model.

The Shear-Stress Transport (SST) K-ω turbulence model was developed by Menter [24] to effectively blend the robust and accurate formulation of the k-ω models in the near wall region with the free stream independence of the k-ε model in the far field. Similar to the standard k-ω turbulence model, SST k-ω model solves two equations of the turbulent kinetic energy and the specific dissipation rate. Therefore, it is computationally economic compared with the Reynolds stress model. The features of the SST k-ω model in incorporating low Reynolds number correction and shear stress transportation, makes it more accurate and reliable for flows with adverse pressure gradient flow, separation and reattachment. However, as the SST k-ω model is based on the Boussinesq hypothesis, the turbulence viscosity becomes an isotropic scalar quantity, which is not strictly true for complex turbulent flows.

SST K-ω is considered one of well-calibrated turbulence models under the Boussinesq hypothesis. Its performance with ship hydrodynamics problems of modern ships was validated against the model test data in this test case.

SST K-ω equations are solved with a second order upwinding difference scheme. The experimental results at longitudinal cut x/L=0.935 are available from model tests and are used to validate the calculations by the SST k-ω turbulent model.

The comparison of turbulent kinetic energy k at location x/Lpp=0.935 is shown in Figure 22 and Figure 23. As we can see, the shape of the turbulent kinetic energy contour bears some similarity to axial velocity contour. Turbulence kinetic energy is lower at the outer layer and higher at inner layer of boundary layer. However, at

areas very close to hull surface, turbulence kinetic energy is diminishing. Normally, the strength of turbulent flow is measured by turbulence intensity, i.e. I.

Turbulence intensity is defined as $I = u'/U = \sqrt{2k/3}/U$

From results of turbulent kinetic energy, we can obtain the range of I: 0<I<0.06 at x/Lpp=0.935. This could be used as a guideline to setup inlet boundary condition of turbulence. Turbulence intensity higher than 1% may result in larger background noise and thus affect the accuracy of the numerical experiment.

The agreement between computed and measured turbulence kinetic energy is acceptable. However, the computed results by SST K-ω tend to overestimate k near the hull surface.

Figure 22 Computed turbulence kinetic energy (x/L=0.935)

Figure 23 Measured turbulent kinetic energy (x/L=0.935)

The comparison of Reynolds stress $\overline{uu}$ at location x/Lpp=0.935 is shown in Figure 24 and Figure 25. As we can see, the shape of turbulent stress $\overline{uu}$ is similar to that of the turbulence kinetic energy. It is lower at the outer layer and higher at the inner boundary layer. When very close to hull surface, $\overline{uu}$ is diminishing. $\overline{uu}$ is proportional to the square of the turbulence intensity I, i.e. $\overline{uu} \propto I^2$ or 2k/3.

From results of $\overline{uu}$, we can obtain the range of $\overline{uu}$: 0<$\overline{uu}$<0.003 at x/Lpp=0.935.

The agreement between the computed and measured turbulence Reynolds stress $\overline{uu}$ is acceptable. However, the change of computed $\overline{uu}$ is not as sharp as that from the data.
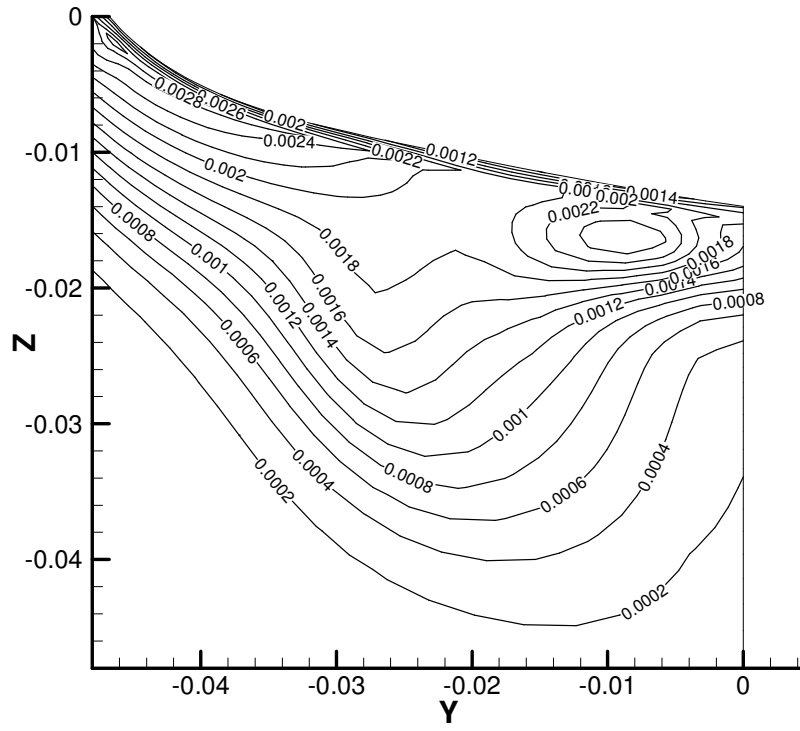
Figure 24 Computed $\overline{uu}$
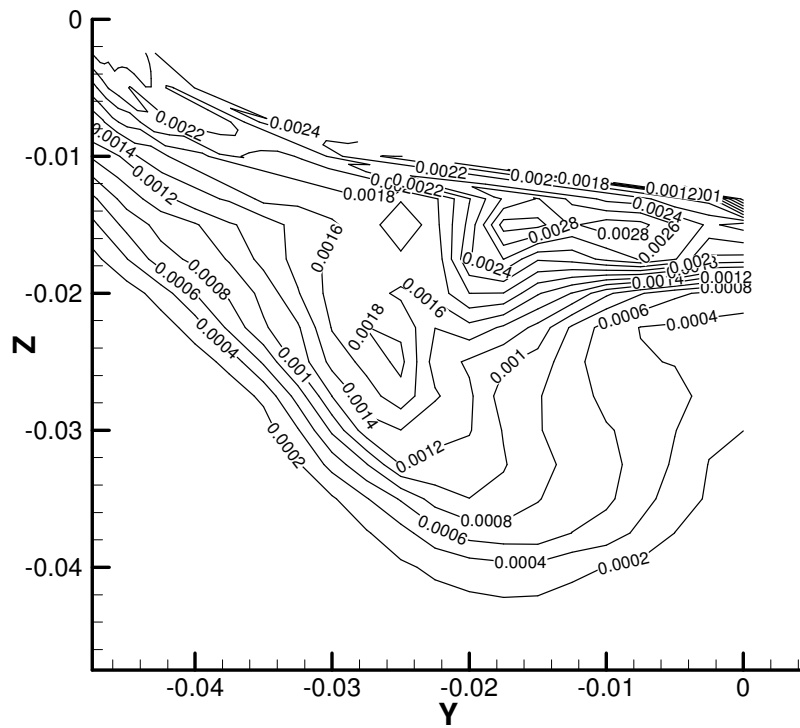
Figure 25 Measured $\overline{uu}$

The comparison of Reynolds stress $\overline{vv}$ at location x/Lpp=0.935 is shown in Figure 26 and Figure 27. The shape of the Reynolds stress $\overline{vv}$ contour is similar to that of the Reynolds stress $\overline{uu}$. It is lower at the outer layer and higher at inner layer of the boundary layer. At very close to hull surface, $\overline{vv}$ is diminishing.

Near the hull surface, the computed Reynolds stress $\overline{vv}$ is close to the computed Reynolds stress $\overline{uu}$ due to the isotropic assumption, while the measured Reynolds stress $\overline{vv}$ is smaller than the measured Reynolds stress $\overline{uu}$. The range of the measured $\overline{vv}$ is: $0<\overline{vv}<0.0015$ while it is $0<\overline{vv}<0.003$ for computed $\overline{vv}$. The blocking effects of wall (directly related to $\overline{vv}$) may be more severe than the effect of damping (directly related to $\overline{uu}$). Therefore, measured $\overline{vv}$ is smaller than measured $\overline{uu}$. However, computed Reynolds stress $\overline{uu}$ and $\overline{vv}$ are proportional to $\partial u/\partial x$ and $\partial v/\partial y$ respectively together with isotropic turbulent viscosity, while the values of $\partial u/\partial x$ and $\partial v/\partial y$ are close. The difference between the computed and the measured $\overline{vv}$ is mainly due to the Bossenesq hypothesis. Comparisons show that turbulence viscosity is actually not a scalar.

Agreement between the computed and the measured $\overline{vv}$ is acceptable in the outer zone. However, computed results overestimate $\overline{vv}$ near the hull surface.
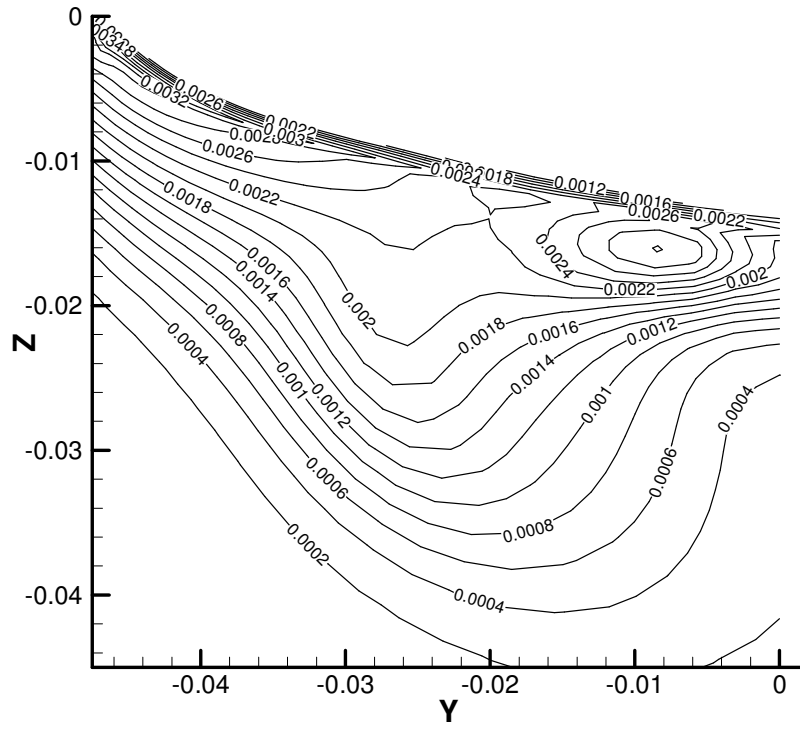
Figure 26 Computed $\overline{vv}$
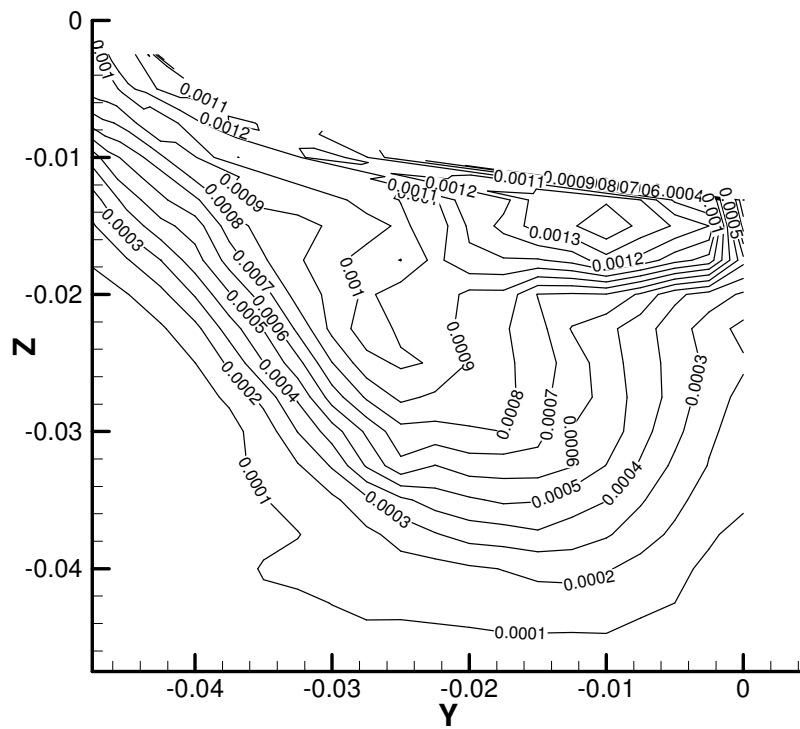
Figure 27 Measured $\overline{vv}$

85

The comparison of Reynolds stress $\overline{ww}$ at location x/Lpp=0.935 is shown in Figure 28 and Figure 29. The shape of the computed and measured Reynolds stress $\overline{ww}$ contours is similar to that of the Reynolds stress $\overline{vv}$. There is high correlation for $\overline{vv}$ and $\overline{ww}$ from both the measurement and its prediction. However, the correlation of $\overline{ww}$ and $\overline{uu}$ is high only for the prediction and not for the measurement. The results indicate that the Bossenesq hypothesis is not valid in this case.

$\overline{ww}$ is lower at the outer layer and higher at inner layer of boundary layer. Very close to the hull surface, $\overline{ww}$ is diminishing.

The range of measured $\overline{ww}$ is: $0<\overline{ww}<0.0015$, while it is $0<\overline{ww}<0.003$ for computed $\overline{ww}$.

Agreement between computed and measured $\overline{ww}$ is acceptable in the outer zone but computed results over predict $\overline{ww}$ near the hull surface.

Figure 28 Computed $\overline{ww}$

Figure 29 Measured $\overline{ww}$

The comparison of the Reynolds stress $\overline{uv}$ at location X=0.935 is shown in Figure 30 and Figure 31. The shape of Reynolds stress $\overline{uv}$ contours differ from Reynolds stress $\overline{uu}$ etc. Near the centre plane, Reynolds stress $\overline{uv}$ is negative while it is positive away from centre plane. Near the hull surface, $\overline{uv}$ is normally positive, unless there are flow separations.

The range of the measured $\overline{uv}$ is: $-0.0003 < \overline{uv} < 0.0005$, while it is $-0.0004 < \overline{uv} < 0.0006$ for the computed $\overline{uv}$. Reynolds stress $\overline{uv}$ is proportional to $\partial u/\partial y + \partial v/\partial x$. As can be seen from the u contour, there is sign change for $\partial u/\partial y$ as shown in $\overline{uv}$ contour. $\partial v/\partial x$ is not a dominating quantity.

The agreement between computed and measured $\overline{uv}$ is acceptable. However, computed results over predict $\overline{uv}$ near the positive centre of contour.

Figure 30 Computed $\overline{uv}$ (X=0.935)
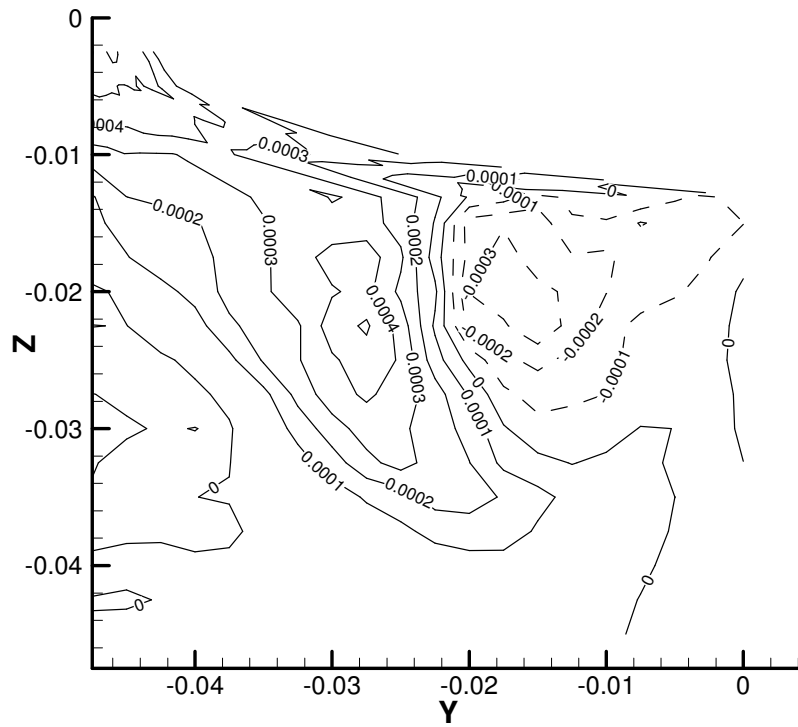
Figure 31 Measured $\overline{uv}$

88

The comparison of the Reynolds stress $\overline{uw}$ at location x/Lpp=0.935 is shown in Figure 32 and Figure 33. The shape of the Reynolds stress $\overline{uw}$ contours is similar to that of the Reynolds stress $\overline{ww}$. It is lower at the outer layer and higher at inner layer of boundary layer. Very close to hull surface, $\overline{uw}$ is diminishing.

The range of the measured $\overline{uw}$ is: $0 < \overline{uw} < 0.0010$, while it is $0 < \overline{uw} < 0.0015$ for the computed $\overline{uw}$. Reynolds stress $\overline{uw}$ is proportional to $\partial u / \partial z + \partial w / \partial x$. $\partial u / \partial z$ is dominantly large while $\partial w / \partial x$ is small. Agreement between computed and measured $\overline{uw}$ is acceptable in the outer zone but computed results over predict $\overline{uw}$ near the hull surface.
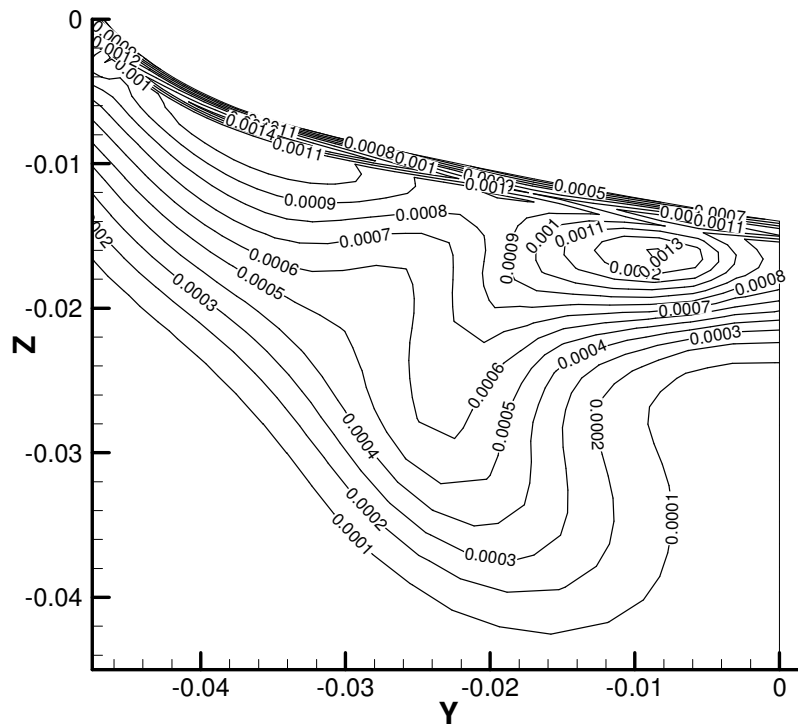
Figure 32 Computed $\overline{uw}$
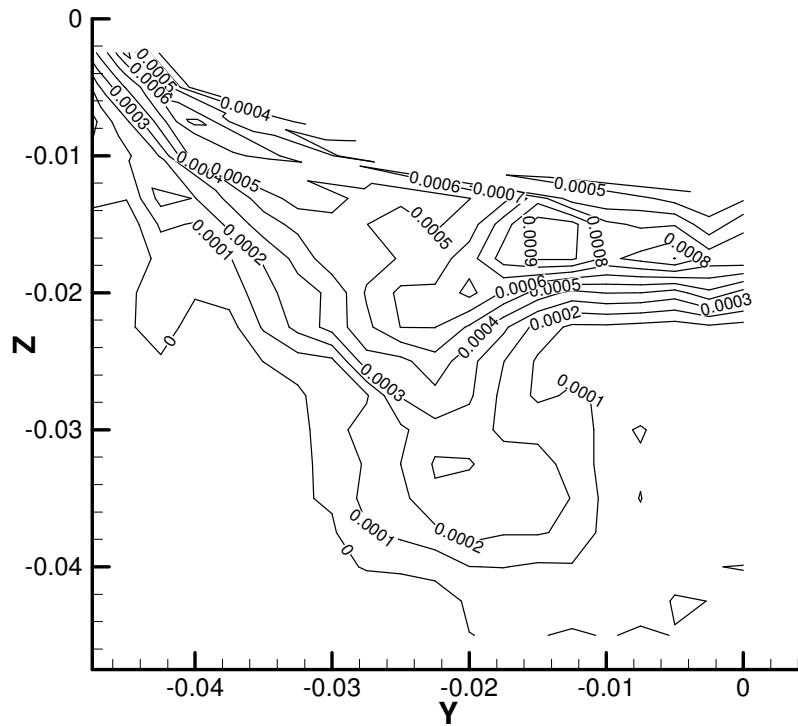
Figure 33 Measured $\overline{uw}$

The comparison of Reynolds stress components show that the overall agreement between the calculations made using SST k-ω and measurement is acceptable. The shape and size of the contours agree well. However, it was noticed that SST k-ω generally overestimates Reynolds stress near the hull surface. Comparison between $\overline{uu}$, $\overline{vv}$ and $\overline{ww}$ shows that the Bossenesq hypothesis is not valid in 3d geometry with large curvature and pressure gradient.

6.8.5   Resistance

The comparison of resistance components is given in Table 7.

The comparison shows that the computed total resistance is 1.95% higher than the measured resistance. The computed frictional resistance coefficient is higher than the

ITTC friction line in this test case because static wetted surface area was used in non-dimensional form. The computed pressure resistance coefficient is close to the measurement if the form factor were taken into account.

Table 7 comparisons of resistances

Parameters		EFD (D)	ITTC	Computed
$C_T \times 10^3$	Value	4.61		4.70
	E%D			-1.95
$C_F \times 10^3$	Value		3.38	3.51
	E%ITTC			-3.85
$C_R \times 10^3$	Value	1.23		1.19
	E%D			3.25

6.9 Calculation by Reynolds Stress Model (RSM)

The Reynolds Stress Model (RSM) abandons the isotropic eddy-viscosity hypothesis and closes the Reynolds-averaged Navier-Stokes equations by solving the transport equations for the Reynolds stresses together with an equation for the dissipation rate. Therefore, seven additional transport equations are solved in 3D. It is of great interest to compare the performance of high-end turbulent models with the measured data of turbulence quantity.

In order to study the effects of the turbulence models on ship hydrodynamics, the calculations of turbulent flow around DTMB 5415 using Reynolds Stress Model

(RSM) were compared with the computed results using SST k-ω and with the data from the model test, taking a particular interest with regards to turbulent shear stress.

The RSM equations are solved with second order upwinding difference scheme. The numerical results at longitudinal cut x/L=0.935 were extracted and compared with the measurements and those from the SST k-ω turbulent model.

The computed turbulent shear stresses by RSM are given in Figures 34-39.
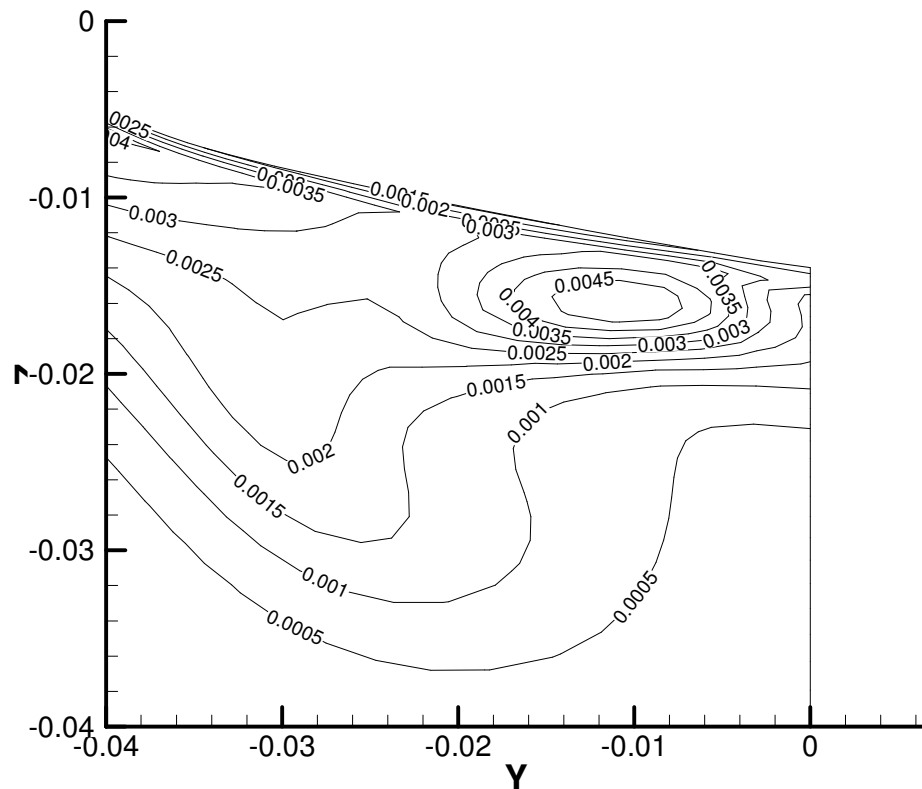
Figure 34 Turbulence kinetic energy by RSM

As can be seen from Figure 34, the computed turbulence kinetic energy by RSM is very close to that obtained via SST K-ω. Slightly higher turbulence kinetic energy was predicted, thus the pressure strain model of RSM may need further calibration in complicated hydrodynamic flows.
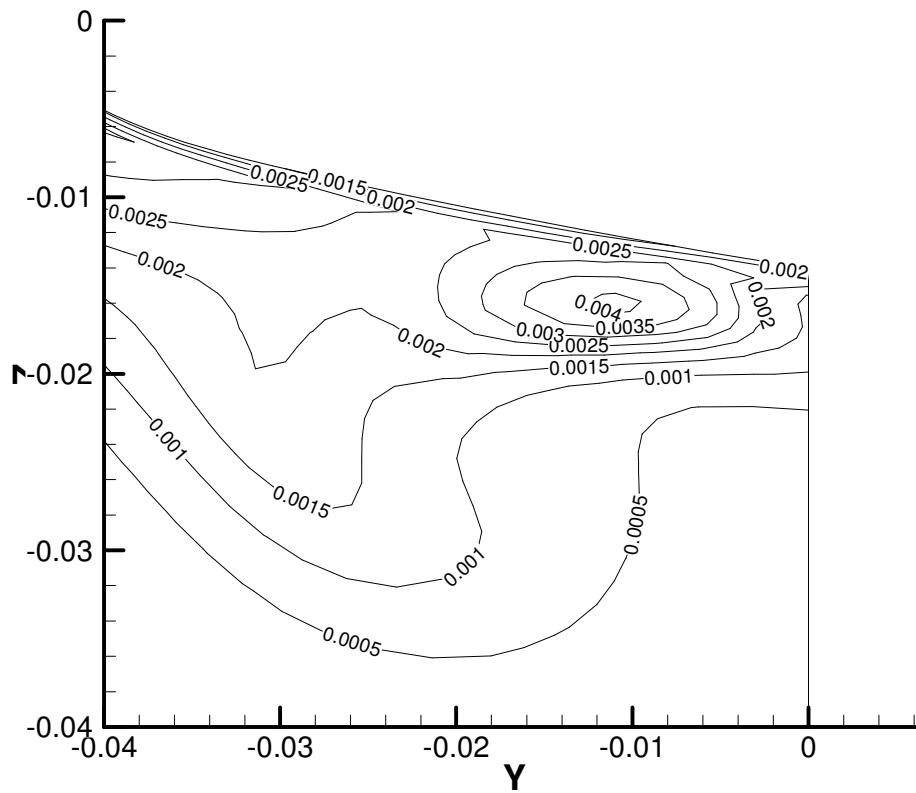
Figure 35 Computed turbulence stress $\overline{uu}$ by RSM

The computed Reynolds stress $\overline{uu}$ by RSM as shown in Figure 35 indicates that it is over predicted near the hull surface although the shape of the contour is similar to both the measurement and calculation obtained via SST K-ω. The range of $\overline{uu}$ by RSM is 0.0-0.004. The over estimation of $\overline{uu}$ will directly result in higher turbulence kinetic energy.
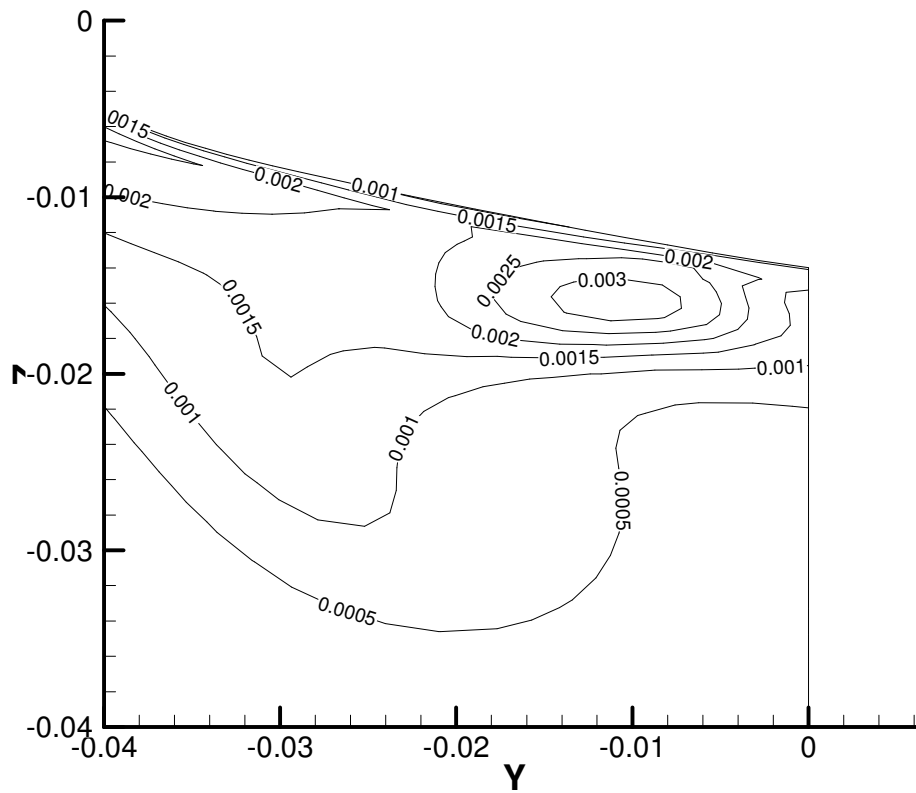
Figure 36 Computed turbulence stress $\overline{vv}$ by RSM

The computed Reynolds stress $\overline{vv}$ by RSM is shown in Figure 36. The magnitude of the predicted $\overline{vv}$ is closer to those obtained by SST k-ω than by physical measurements. The range of $\overline{vv}$ by RSM is 0.0-0.003. It is lower than the computed $\overline{uu}$ but higher than the measurements.
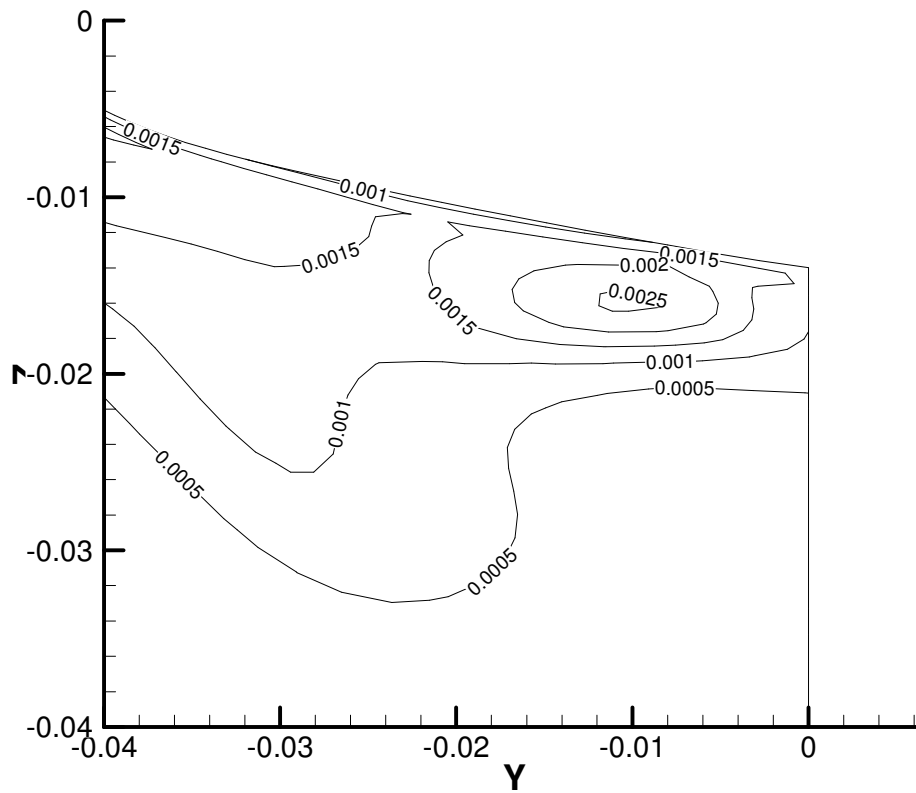
Figure 37 Computed turbulence stress $\overline{ww}$ by RSM

The computed Reynolds stress $\overline{ww}$ by RSM is shown in Figure 37. The magnitude of the predicted $\overline{ww}$ by RSM is close but slightly lower than the computed $\overline{vv}$. The range of $\overline{ww}$ by RSM is 0.0-0.0025. The correlation of the computed $\overline{uu}$, $\overline{vv}$ and $\overline{ww}$ by RSM is very close to the data. However, the magnitude is higher than that of the measurement.
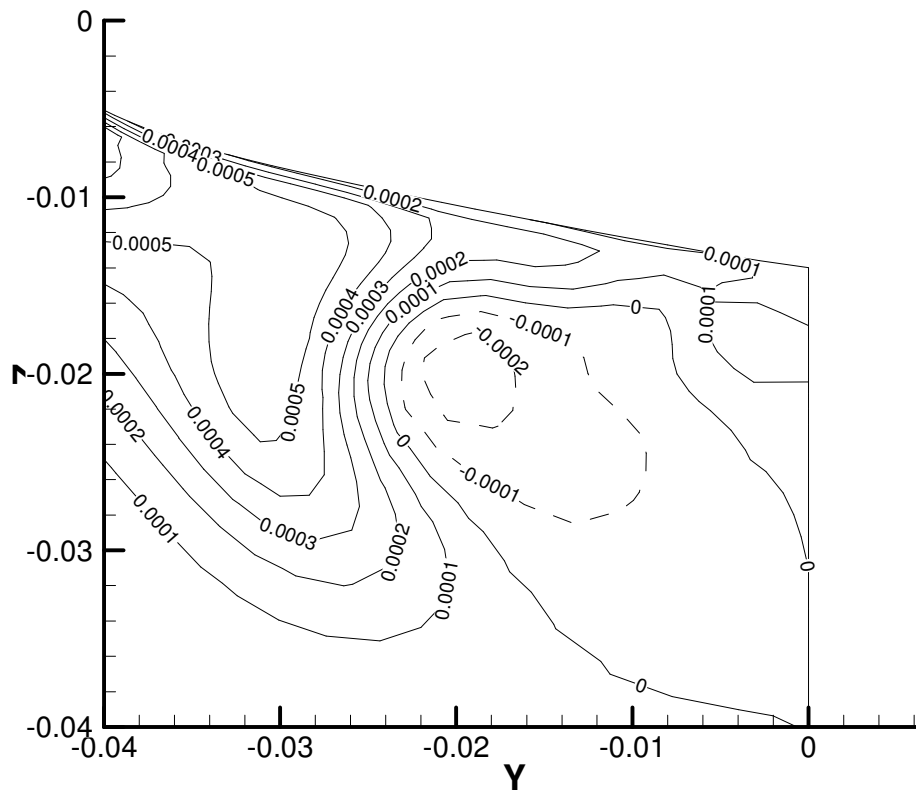
Figure 38 Computed turbulence stress $\overline{uv}$ by RSM

The computed Reynolds stress $\overline{uv}$ by RSM is shown in Figure 38. The magnitude of the predicted $\overline{uv}$ by RSM is pretty close to the data. The range of $\overline{uv}$ by RSM is -0.0002-0.0005. As $\overline{uv}$ is directly related to wall shear stress, the consistency of the predicted $\overline{uv}$ with the measurement is given great weight in considering which turbulence model to use.
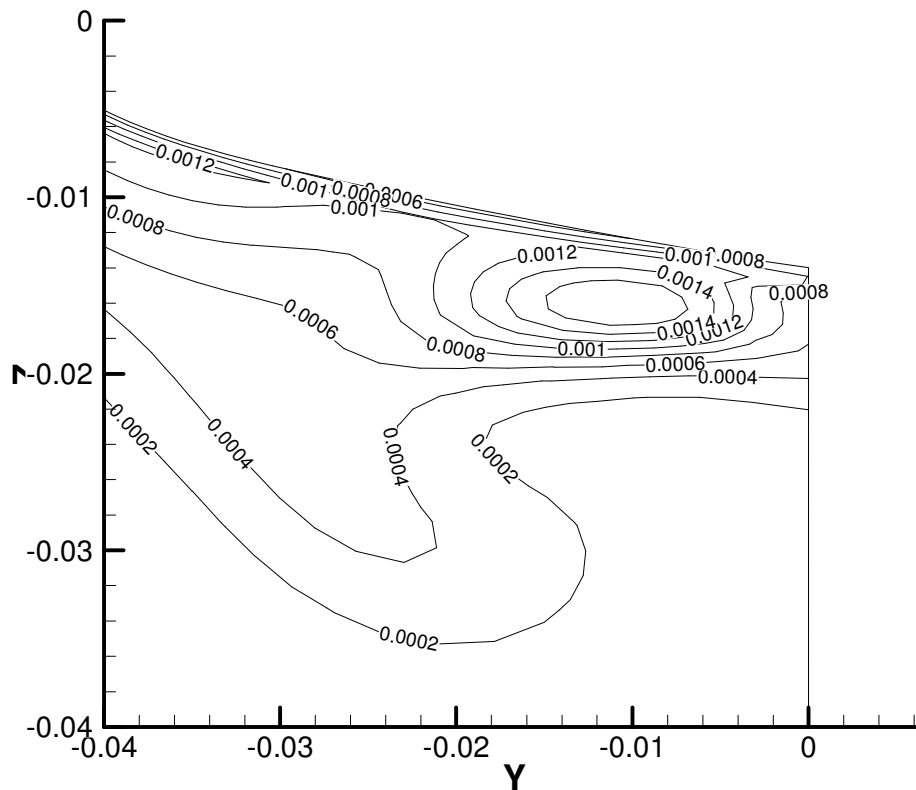
Figure 39 Computed turbulence stress $\overline{uw}$ by RSM

The computed Reynolds stress $\overline{uw}$ by RSM is shown in Figure 40. The magnitude of the predicted $\overline{uw}$ is closer to that obtained by SST k-ω than by the measurement. The range of $\overline{uw}$ by RSM is 0.0-0.0016.

From the comparison of computed results by RSM with the measurement and SST k-ω, it can be concluded that RSM generally overestimates turbulence stress like the SST k-ω turbulent model. The predicted $\overline{uv}$ by RSM is more consistent with data than the SST k-ω model. The over prediction of turbulence quantities by RSM may be due to the wall boundary condition, which is based on shear stress. As RSM is not fully valid for low Reynolds number flows, the benefit and advantage of the RSM over SST k-ω in complicated hydrodynamic problems is not significant. Therefore, in

addressing other ship hydrodynamics problems, only the SST k-ω turbulence model is used.

The predicted axial velocity contour is shown in Figure 40. Comparing it with that from SST k-ω, the effect of RSM on wake distribution is not significant for this hull.
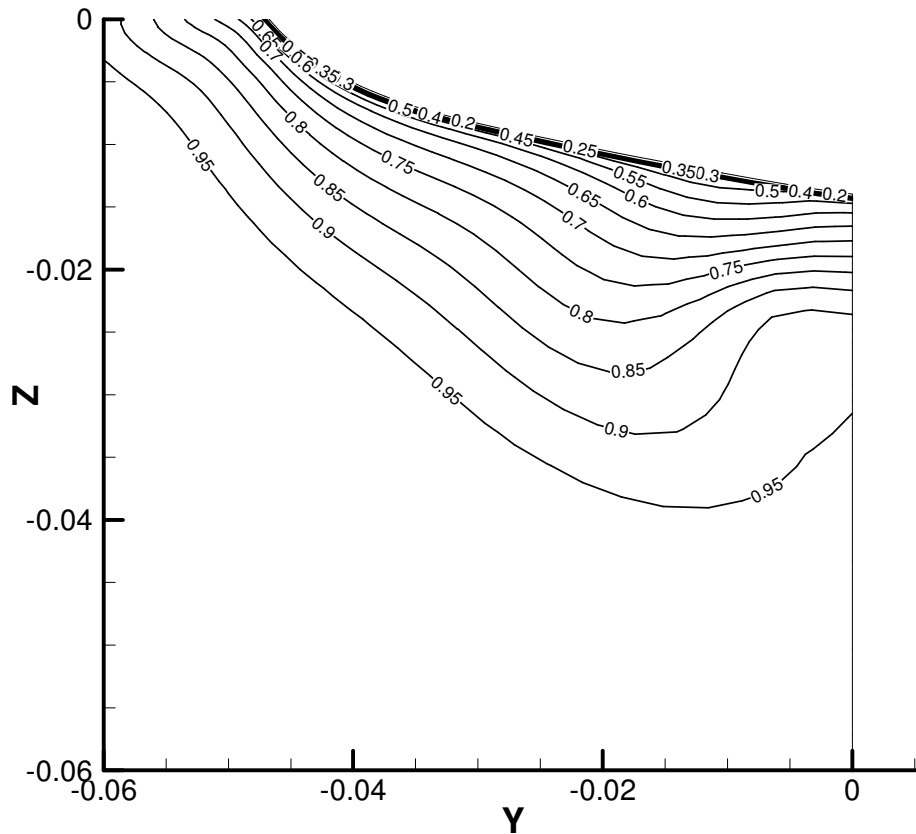
Figure 40 Computed axial velocity contour by RSM

The computed wave pattern by RSM is shown in Figure 41. As expected, there is little change noticed for the wave elevations predicted by the turbulence models RSM and SST k-ω.
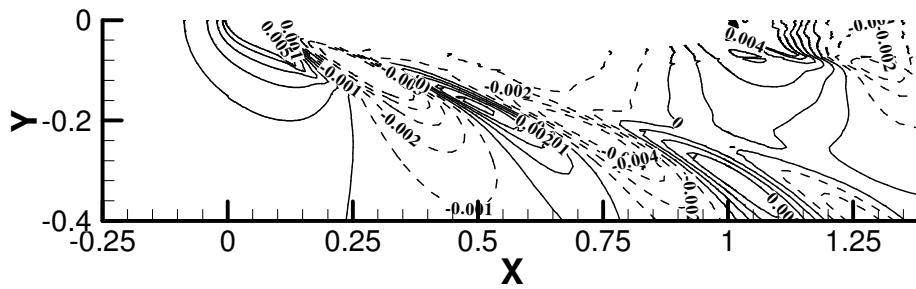
Figure 41 Computed wave height by RSM

The comparison of resistance predicted by turbulence models RSM and SST k-ω is shown in Figure 42. As we can see, the pressure resistance is quite close. The friction resistance by RSM is 1% higher than by SST k-ω due to the slightly larger turbulence predicted by RSM. As less computational time is required by SST k-ω than RSM, SST k-ω turbulence model will be used in the following.
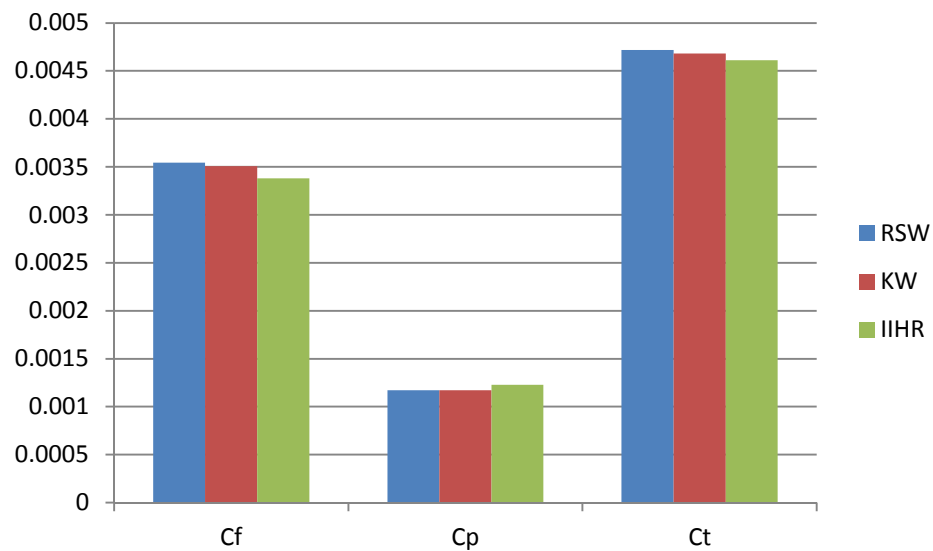
Figure 42 Computed resistance coefficients by RSM and SST k-ω

7 Propulsion

The interaction between ship hull and propeller was traditionally studied by physical self-propulsion tests supplemented with ship resistance and propeller open water tests. The influence of the propeller on the hull and of the hull on the propeller was assessed by the load (thrust or torque)-identity method (LIM). The resulting thrust deduction reflects the ship resistance augmentation due to reduced pressure at the stern by the action of the propeller in accelerating water flowing into it. Two other measures are relevant, namely: effective wake fraction, a measure of averaged axial stream from the hull into the propeller; relative rotative efficiency, used to quantify the contribution of the circumferential stream . One disadvantage of LIM is that the actual change of the field and the integral variables due to interaction are never known and need to be obtained by other tests, such as pressure and velocity measurements.

With the advance of computer and numerical technology, computer simulation provides an alternative solution to the study of interaction of ship hull and propellers. There exist two methods to model propellers. One is body force method in which the propeller is represented by an actuator disk with identity of loads, while in the other method the propeller is meshed geometrically. The current state of the RANSE based full simulation of the propeller hydrodynamics is not yet as practical as the potential theory-based methods, such as panel method or lifting surface theory. Therefore, the body force modelling of the propeller is widely preferred by researchers.

Stern et al [83] calculated and validated body-propeller interaction of a DTNSRDC afterbody model with propeller model 4577 by partially parabolic method and body force approach. The body force is either analytically prescribed through measured loads or obtained iteratively through vortex lattice lifting surface method.

Comparisons show that the computed results are in close agreement with the experimental data available.

Zhang et al [96] studied hull-propeller interaction of Series 60 by RANS and body force methods. The propeller body force is obtained by the lifting line theory. They compared calculation of velocity and pressure fields with the model test data by Toda. Reasonable agreement was obtained.

Chou et al [11] coupled a RANS code UVW with a potential code based on the vortex lattice method to study the numerical self-propulsion of a container ship. The comparison of the computed results with measured data shows that the numerical prediction using body force method is encouraging.

More recently, Simonsen et al [12] coupled CFDSHIP-IOWA with a simplified potential theory-based propeller model by using the body force method. The computations were performed for a Series 60 ship and appended tanker Esso Osaka. The comparison between calculated and measured data shows fair agreement.

All these works couple RANS solver and potential code through body force. The body force was predicted by a potential theory-based propeller performance prediction program. The effective wake (after deducting induced velocity due to propeller's suction), and the input into propeller solver was obtained by RANS calculation. How to remove induced velocity and consider viscous/potential interaction is an issue, which will affect the computed propeller loading (body force) and overall flow field. Therefore, a systematic study of body force effect is required.

In the present study, focus was placed on the influence of body force on the hull-propeller interaction. Research works are aimed to examine the influence of the body force on the flow field by comparing with that without propeller, to study the effect of body force distribution (three different formulations with the same total loads) and finally to check the influence of body force magnitudes ($\pm 5\%$ and $\pm 10\%$).

7.1   Propeller Modelling

An actuator disk representation of propeller is applied. The radial loading distribution is prescribed as below:

$$F_x = C_X \hat{r}(1-\hat{r})^P$$
$$F_\theta = C_\theta \hat{r}(1-\hat{r})^P$$

Where:

$$\hat{r} = \frac{r - r_{hub}}{R - r_{hub}}$$

r is radial coordinate nondimensioned by propeller radius

r_{hub} and R are hub and propeller radius (0.02m and 0.1271m, respectively).

F_x and F_θ are longitudinal and tangential forces acting on propeller

Superscript P is a parameter determining the distribution of the propeller loads. Here, P is 0.3, 0.5 and 0.7 to examine the influence of modelling parameter.

Coefficients Cx and Cθ are determined by thrust and torque

$$\iiint F_X dv = T$$
$$\iiint F_\theta r dv = Q$$

Where T and Q are thrust and torque acting on propeller

To determine propeller loads, normally potential panel methods or lifting surface theories are used. One issue related to these methods is how to find the propeller inflow (longitudinal and circumferential wakes). If nominal wake is applied, propeller effect cannot be taken into account; the loads will be overestimated. If the effective wake is used, propeller induced velocity needs to be removed, otherwise, propeller loads will be underestimated. How to deduct propeller induced velocity and

consider viscous/potential interaction introduces uncertainty into the calculations. In order to eliminate the error due to propeller loads and focus on body force modelling, the propeller loads from the model test are used. For ship speed 1.89m/s (18 Knots in full scale) and propeller revolution 9.65/s, measured KT and KQ are 0.226 and 0.0318, respectively.

7.2   Test Cases

A container model (Hamburg Test Case) was selected for the numerical analysis. The model test data from HSVA is available for validation.

The body plan and profile of bow and stern are shown in Figure 43.
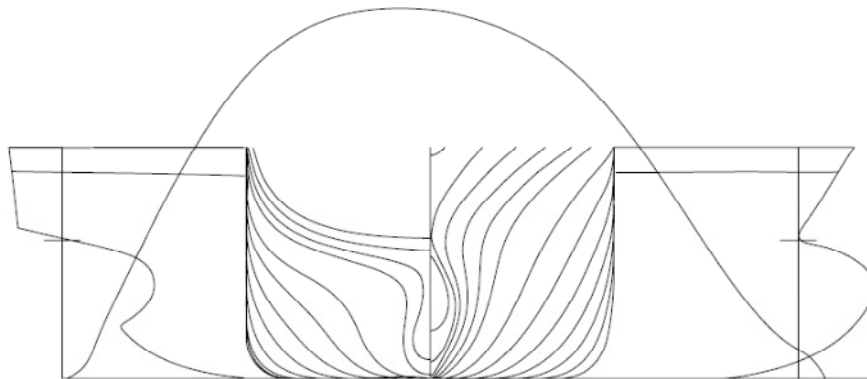
Figure 43 HTC Body plan

The main particular of the vessel is given in Table 8.

Table 8 Main particulars of HTC

Description	Symbol	proto	model	Unit
Scale	□		1 :24	-

Length between perpendiculars	L_{pp}	153.700	6.404	m
Breadth max. moulded	B	27.500	1.1458	m
Draught moulded fore	T_f	10.300	0.4292	m
Draught moulded aft	T_a	10.300	0.4292	m
Displacement volume moulded	$\square$	28342	2.0500	m^3
Wetted surface area bare hull	S_{wa}	5567	9.6640	m^2
Position centre of buoyancy forward of midship	x_B	-0.571	-0.571	$\%L_{pp}$
Block coefficient	C_b	0.650	0.650	-
Length-Breadth ratio	L/B	5.582	5.582	-
Breadth-Draught ratio	B/T	2.673	2.673	-
Length-Draught ratio	L/T	0.822	0.822	-

Four meshes were generated with 0.4, 0.8, 3.1, 6.1M cells respectively. The Y plus values are around 30 for all meshes. The computational results are shown below.

7.3   Propeller Effect

The calculation for the condition without propeller was carried out for mesh 2. The comparison of nominal wake between the calculation and the measurement (HSVA) is given in Figure 44 Computed wake distribution Figure 45 Measured wake distribution .
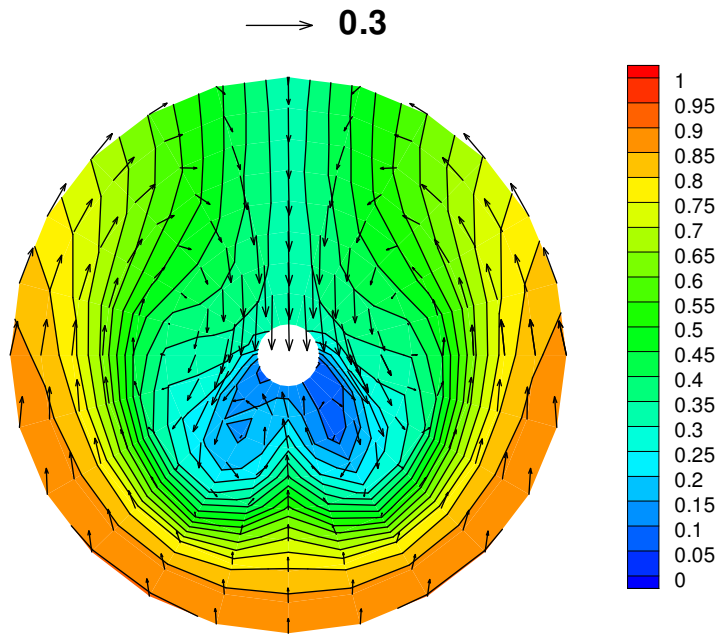
Figure 44 Computed wake distribution
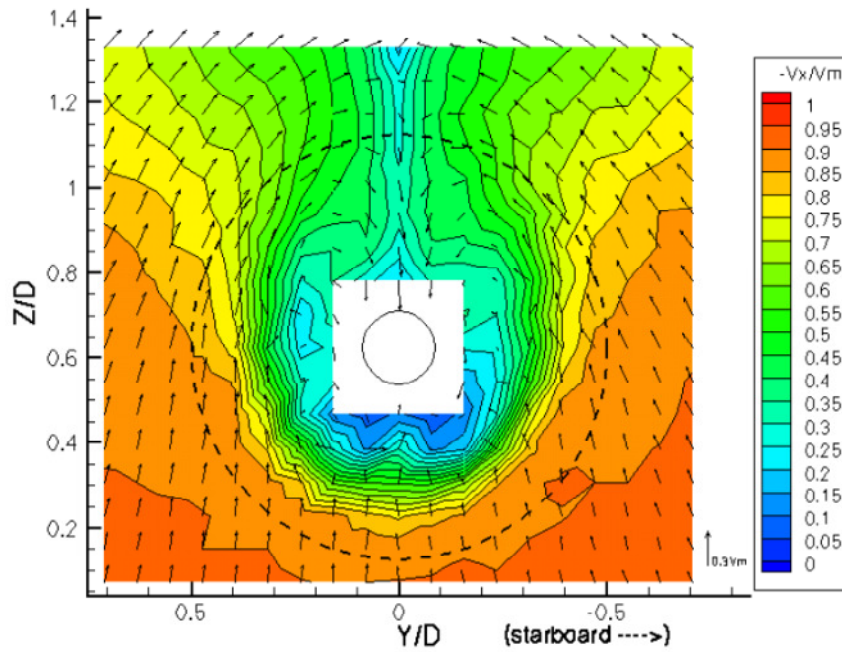
Figure 45 Measured wake distribution

As we can see from the plots, one pair of bilge vortex is formed in the propeller plane. The longitudinal velocity contour appears in the shape of a hook. The size of the hook and the strength of vortex are related to the hull form. It is weak for the present hull form when compared with fuller hull forms, such as tanker. In general, the computed axial velocity contour and cross vector are in close agreement with measurements.

The wake distribution with propeller (P=0.5) from the calculation done by mesh 2 is shown in Figure 46 Computed effective wake (P=0.5).
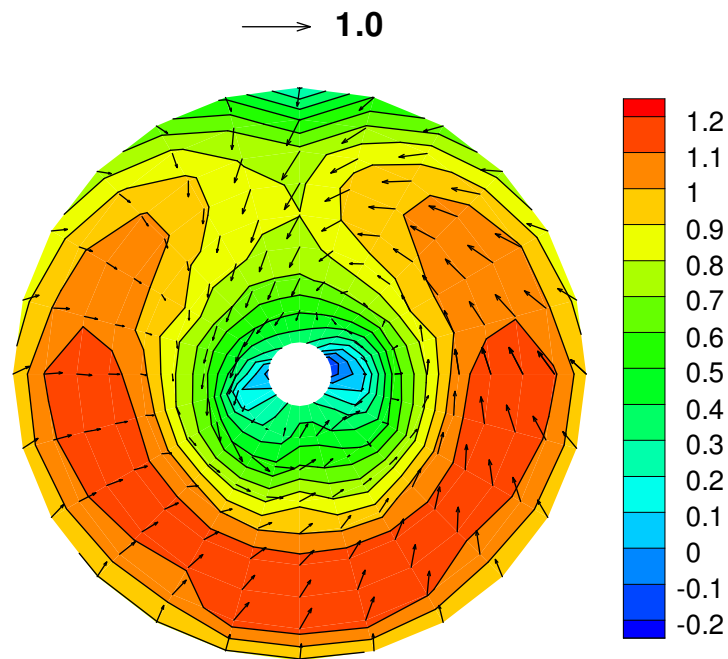
Figure 46 Computed effective wake (P=0.5)

As can be seen clearly, the longitudinal velocity at the propeller plane increases significantly due to the body force or suction effect of propeller. The absolute increase of axial velocity depends on the magnitude of propeller loads. In the present

case, the increase is up to 20%. When compared with velocity contour of the nominal wake, the longitudinal velocity with the propeller is more evenly distributed circumferentially due to its method of load distribution. One worth noticing change is around the bossing, where there is a small longitudinal flow separation due to the acceleration of flow by the propeller. The circumferential velocity is also increasing due to the influence of propeller rotation.

The pressure coefficients are shown in Figures 47-49.

Figure 47 Computed Cp without propeller
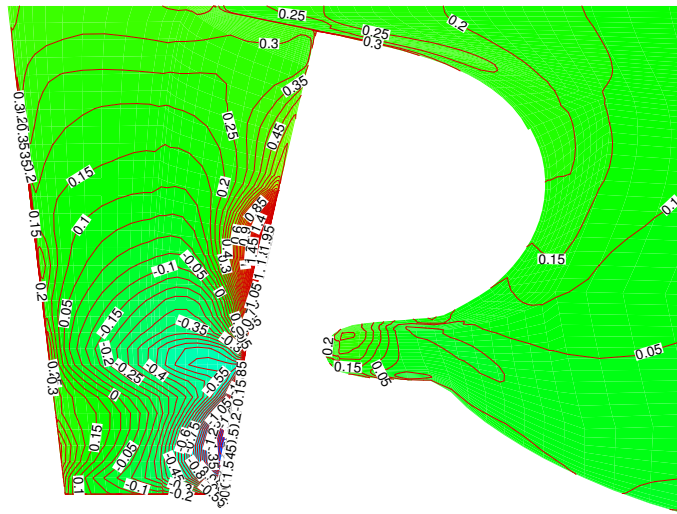
Figure 48 Computed Cp at port with propeller (P=0.5)
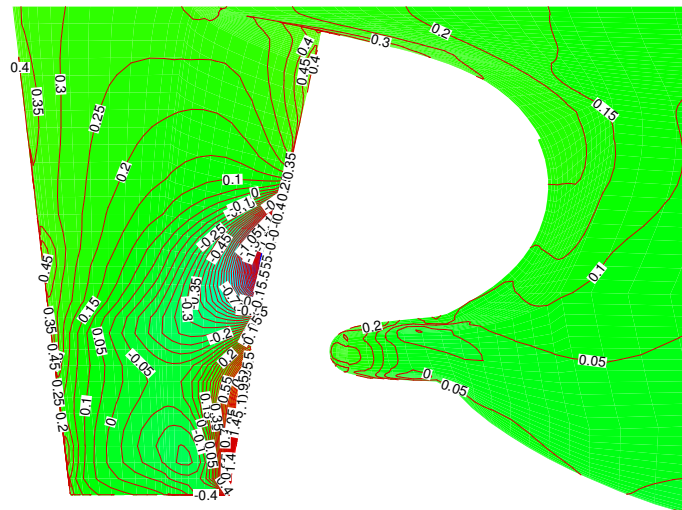
Figure 49 Computed Cp at starboard with propeller (P=0.5)

As can be seen from these plots, there are strong effects of propeller loads on the pressure distribution at starboard and in the port of the hull and in particular in the rudder. Without the propeller, the pressure coefficients would be symmetric around the centre plane. With the propeller, the pressure coefficients are highly asymmetric. On the rudder, the rotational component of propeller loads exerts severe change of hydrodynamic pressure near its leading edge. There are opposing influences of swirling flow on the upper and lower part of the rudder similar to suction and pressure effects of a hydrofoil. The pressure differences at the two sides of the trailing edges are reduced. Differences port and starboard of the hull are not as large as on the rudder.

7.4   Body Force Parameter Effect

For the same loads of propellers, the different distribution of the loads by the body force approach may influence the local flow and overall hydrodynamic performance. Therefore, the effects of body force parameters are studied. The distribution factor is taken to be 0.3, 0.5 and 0.7. Comparative calculations were performed, and the results are shown below.

1.0

Figure 50 Computed effective wake (P=0.3)

1.0
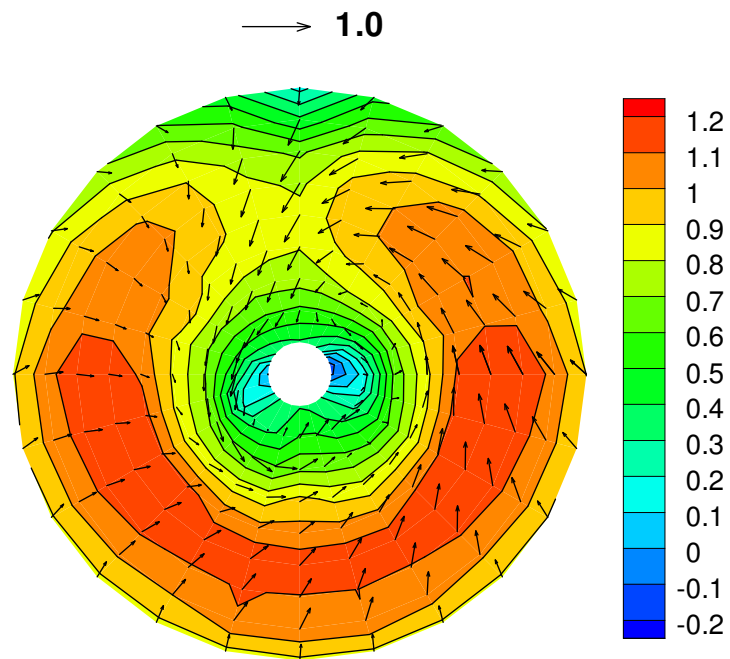
Figure 51 Computed effective wake (P=0.7)

The wake distributions predicted by three modelling parameters are compared in Figure 46 Computed effective wake (P=0.5)and Figure 50 Computed effective wake (P=0.3)-Figure 50 Computed effective wake (P=0.3). With the increase of the modelling parameters, the loads distribution shifts gradually from the tip to the root. As we can see, there are marginal effects for both longitudinal velocity contour and cross vector. However, the change is not significant. Similar conclusions apply to the pressure coefficients as shown in Figure 52 Computed Cp at starboard with propeller (P=0.3)-Figure 55 Computed Cp at port with propeller (P=0.7).
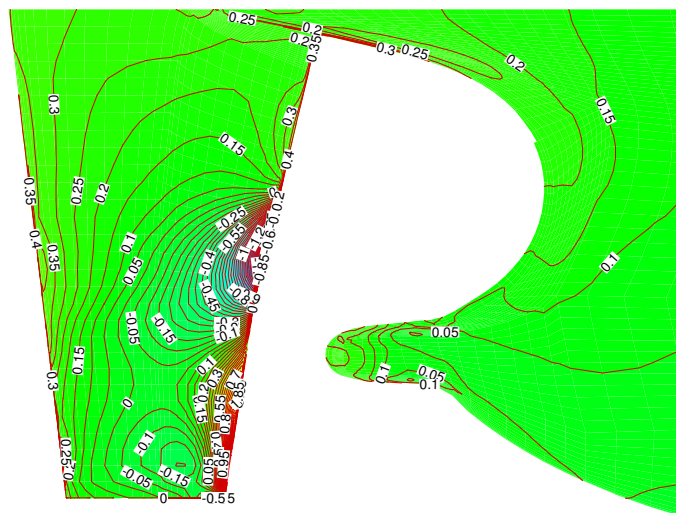
Figure 52 Computed Cp at starboard with propeller (P=0.3)
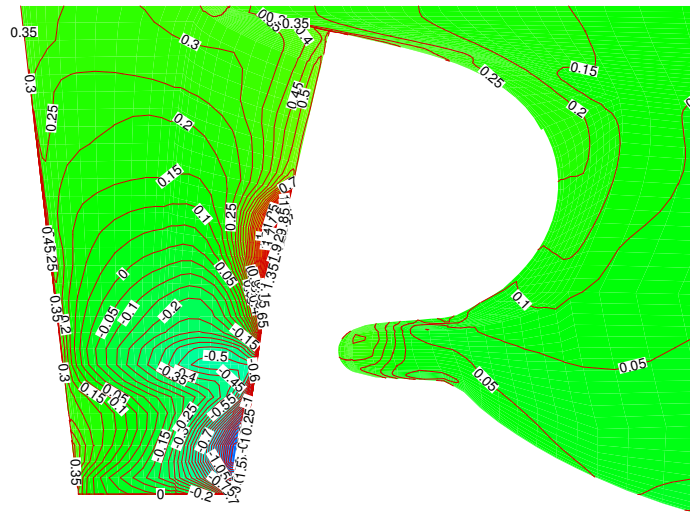
Figure 53 Computed Cp at port with propeller (P=0.3)
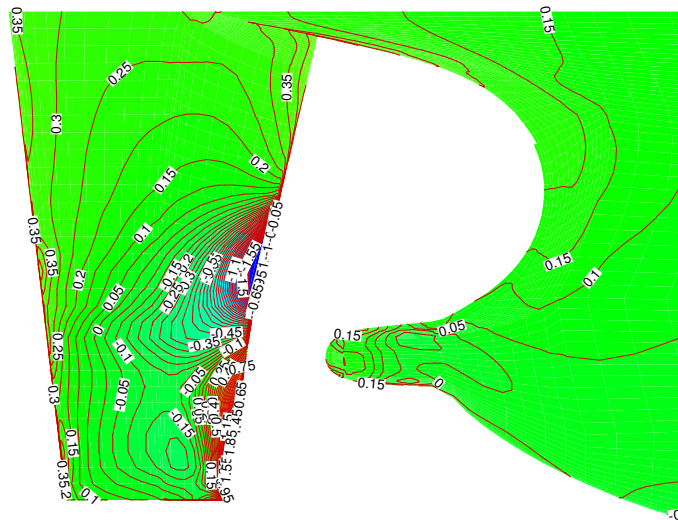
Figure 54 Computed Cp at starboard with propeller (P=0.7)
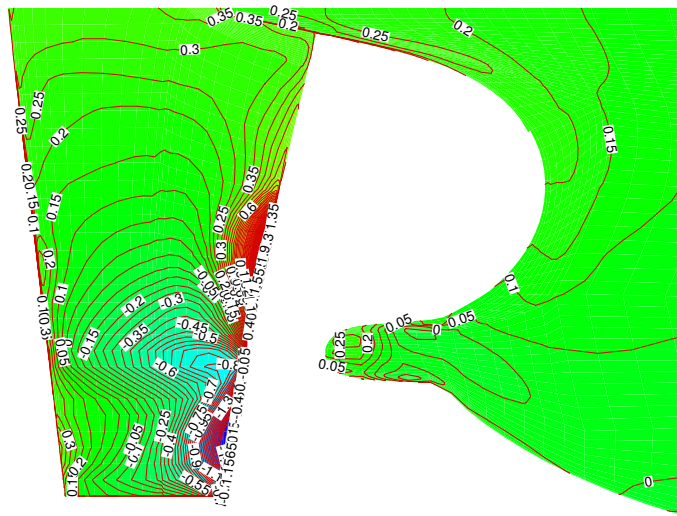
Figure 55 Computed Cp at port with propeller (P=0.7)

Therefore, we can say that the flow field is not significantly affected by the distribution factor as long as the total loads stay the same. This result is important for the successful application of the body force approach.

7.5   Grid Dependence Study

Similar calculations using 4 meshes with increasing resolution were made to study grid effects. Comparisons of flow fields predicted by mesh 1 and 3 are given below.

1.0

Figure 56 Computed effective wake (P=0.5, mesh 1)

1.0

Figure 57 Computed effective wake (P=0.5, mesh 3)

114
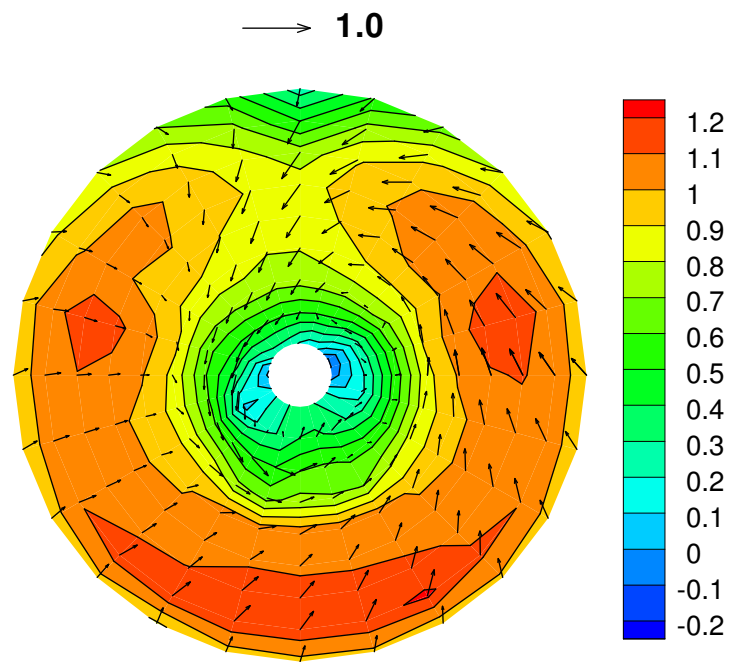
The wake distributions in Figure 56 Computed effective wake (P=0.5, mesh 1)Figure 57 Computed effective wake (P=0.5, mesh 3)show that the results from the coarse mesh exhibit slight numerical diffusion. However, the general flow feature is pretty close. Compared with the change in the computed wake by different modelling parameters, changes by using different meshes are slightly larger.

The pressure coefficients predicted by mesh 1 and 3 are compared in Figure 58 Computed Cp at port with propeller (P=0.5, mesh1) and Figure 61 Computed Cp at starboard with propeller (P=0.5, mesh3). Similar to results of wake distribution, pressure coefficients by coarse mesh suffer from numerical diffusion, missing some local flow structure.

Figure 58 Computed Cp at port with propeller (P=0.5, mesh1)

Figure 59 Computed Cp at port with propeller (P=0.5, mesh3)
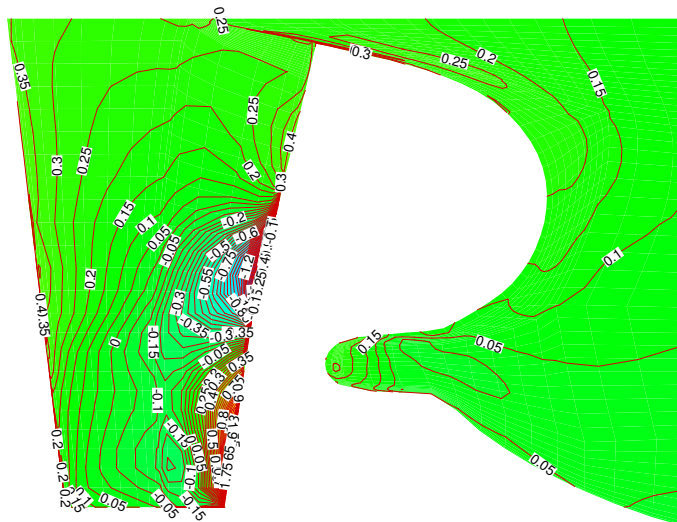
Figure 60 Computed Cp at starboard with propeller (P=0.5, mesh1)
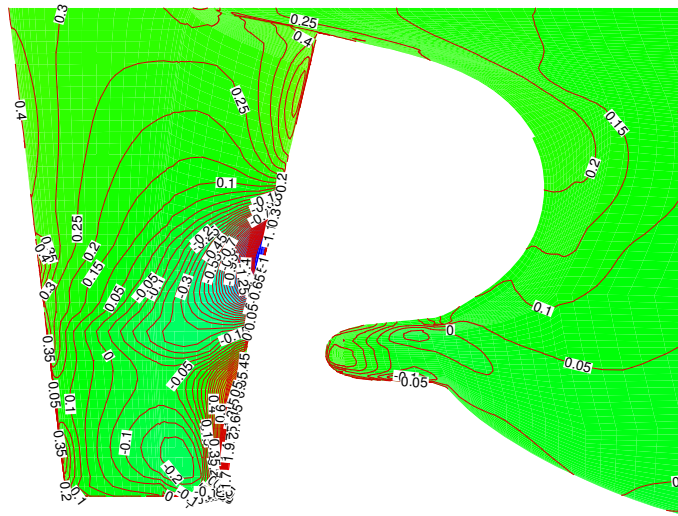
Figure 61 Computed Cp at starboard with propeller (P=0.5, mesh3)

For the study of hull-propeller interaction, grid density near the propeller is more important than its modelling parameters.

7.6   Free Surface Effect

Calculations including free surface effect was also made. The wake distribution is shown below.
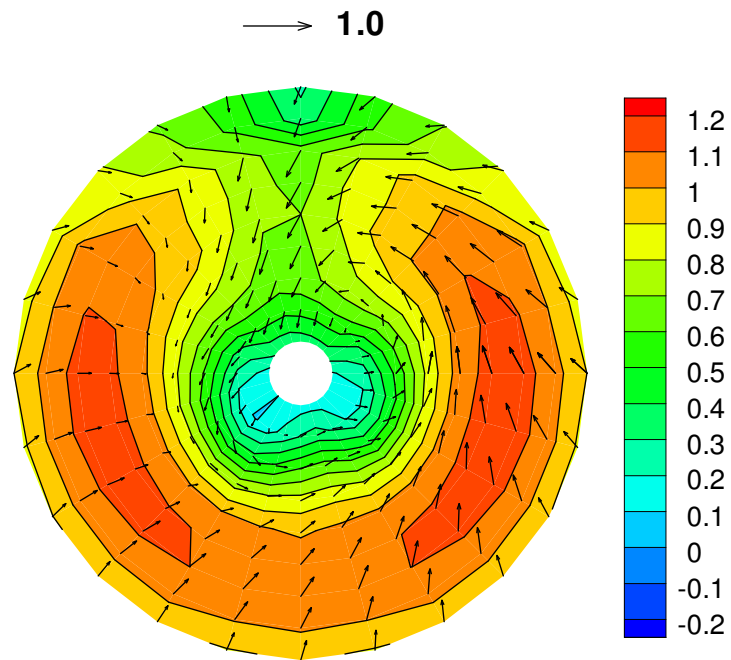
Figure 62 Computed effective wake with free surface

Although overall flow structure is similar to that without free surface, the wake distribution computed with free surface shows that the longitudinal velocity increases near bossing and decreases near high velocity zone. The free surface acts as a buffering zone, reducing the sharpness of the wake distribution.

The wave elevations near the propeller for calculations with and without propeller are compared below.
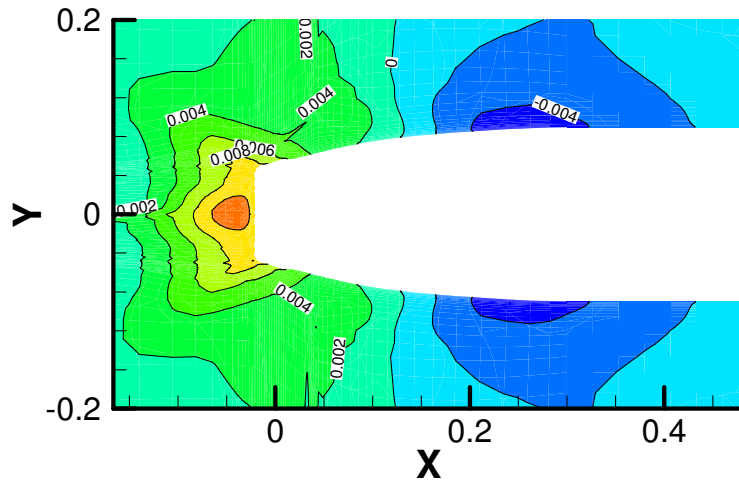
Figure 63 Stern wave pattern with propeller
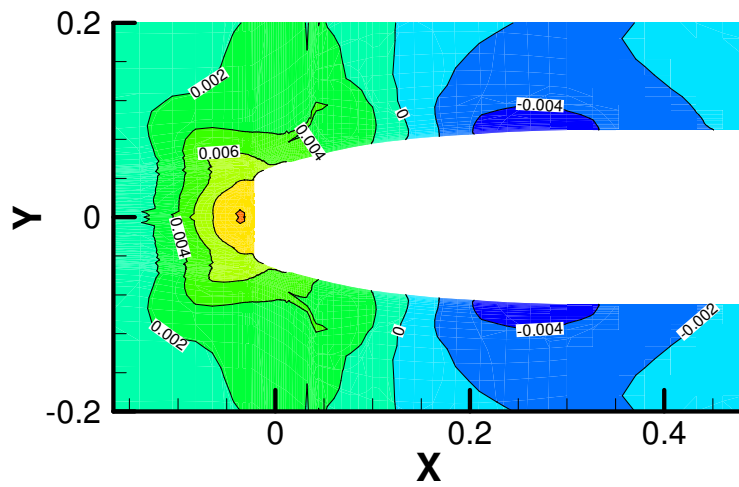
Figure 64 Stern wave pattern without propeller

As we can see from Figure 63 Stern wave pattern with propellerFigure 64 Stern wave pattern without propeller, the wave patterns computed with and without propeller are

pretty close. However, as we expected, there do exist some differences near the propeller. The computed wave crest at the stern with propeller is larger than that without the propeller. Although the propeller is operating under free surface, there is a noticeable effect of pressure disturbance due to the propeller action. However, the influence is limited locally.

7.7   Longitudinal Force

Additional to the field variables, the effects of parameters on the longitudinal force X are examined as shown in Table 9.

Table 9 Comparison of longitudinal force

Computational Condition	X (N)
Mesh 2, no propeller, double model	60.3
Mesh 2, propeller, double model, P=0.3	74.2
Mesh 2, propeller, double model, P=0.5	74.7
Mesh 2, propeller, double model, P=0.7	74.2
Mesh 1, propeller, double model, P=0.5	75.8
Mesh 3, propeller, double model, P=0.5	74.2
Mesh 4, propeller, double model, P=0.5	74.5
Mesh 2, propeller, double model, P=0.5, -10%	73.3
Mesh 2, propeller, double model, P=0.5, -5%	74.0
Mesh 2, propeller, double model, P=0.5, +5%	75.2
Mesh 2, propeller, double model, P=0.5, +10%	76.0

Mesh 2, without propeller, free surface	67.1
Mesh 2, propeller, free surface, P=0.5	82.1
Measurement, without propeller	68.2
Measurement, with propeller	83.6

As we can see from Table 9, the differences of longitudinal force with and without propellers are: 14.4N by the calculations using double model, 15.0N by calculations with free surface, and 15.4N by the model tests. The differences from the double model calculations are smaller than that from measurements and the calculation with free surface due to free surface effects. The results from calculations with free surface and measurements agree well.

The results of the longitudinal forces from three different modelling parameters 0.3, 0.5, and 0.7 are reasonably close. There is no significant effect of the modelling parameters on X force. The differences of the longitudinal forces by the 4 meshes are slightly larger than those using different modelling parameters.

The computed longitudinal forces by the different propeller loads ranges from a decrease of -10% to an increase of 10% varied accordingly but not linearly.

The free surface effect can be roughly estimated from the calculation with and without free surface. These are 6.8N from calculations without the propeller and 7.7N from calculations with the propeller, roughly 11% of the total resistance.

The flat plate drag from ITTC friction line is 50.6N. Therefore, the estimated viscous pressure resistance can be evaluated from double model calculation without the propeller, which is 9.7N. Then the form factor k can be obtained, which is 0.19 for the concerning speed.

7.8   Concluding Remarks

Body force-based propeller modelling was implemented in the simulation of ship propulsion. The test case showed that the flow fields changed significantly due to the suction and swirling action of the propeller when compared with nominal wake. The body force parameter effect on hull-propeller interaction is not large. The computed thrust deductions agree well with the measurements.

8   Manoeuvring

The approach traditionally used by towing tanks for manoeuvrability predictions is based on the calculation of hydrodynamic derivatives of forces and moments with respect to the individual degrees of freedom. These derivatives are then used in manoeuvrability simulation programs to predict the ship performance in real manoeuvres. The derivatives are either found from experiments or are calculated numerically.

Most of numerical studies using RANSE methods follow the same ideas. Forces are calculated in simple modes of motion such as steady drift or steady circulation.

Alessandrini and Delhommeau [1] presented a paper on the calculation of viscous free surface flow past Series 60 in steady oblique motion on the 22nd ONR Symposium. Free surface was captured by a moving grid technique. In their study, a wave-breaking model was introduced. The wave pattern showed excellent agreement with the experiments, particularly for the bow wave. Lateral force was predicted with good accuracy.

Cura Hochbaum [17] presented a paper on numerical simulation of steady yaw motion on the 22nd ONR Symposium. The RANSE code NEPTUN was used, which is based on a multi-block computational method and can be applied to complicated configurations (hull with appendages). Three-dimensional separation and vortex shedding were captured well and the force results were reasonably consistent with the experimental data. Free surface effects were not included in the calculation.

Some more benchmarking computations of manoeuvring motions can be found in recent CFD workshops, namely the SIMMAN (Copenhagen, 2008) and the CFD workshops (Tokyo, 2005 and Gothenburg, 2010).

The calculations of the steady manoeuvring motions, such as steady drift and turning, similar to the physical oblique towing tests and rotating arm tests, can be used to obtain hydrodynamic derivatives with respect to sway and yaw velocity. Another technique, so called the Planar Motion Mechanism (PMM) facility, can be used to obtain hydrodynamic derivatives with respect to velocity and acceleration. In this respect, it is of great interest to simulate oscillatory sway and yaw motions (pure sway and pure yaw) by the RANSE approach. In this study, numerical PMM calculations were performed and the results are presented below.

8.1   Planar Motion Mechanism (PMM) Technique

In order to avoid the large expense of a rotating arm facility, a device known as Planar Motion Mechanism (PMM) has been developed for use in the conventional long and narrow towing tanks to measure the velocity-dependent derivatives, Y_v and N_v, the rotary derivatives Y_r and N_r, as well as the acceleration derivatives $Y_{\dot{v}}$, $N_{\dot{v}}$, $Y_{\dot{r}}$ and $N_{\dot{r}}$.

In pure sway motion, the ship is towed with a constant forward speed, and at the same time, with an oscillatory sway speed, therefore the effects of sway motion on ship hydrodynamics can be recorded.

In pure yaw motion, the ship is towed with constant resultant speed at an oscillatory yaw angle, thus the influence of yaw motion on ship hydrodynamics can be obtained.

In the numerical simulation of manoeuvring motions (Numerical Manoeuvring Tank), calculations of pure sway and pure yaw were carried out using the RANS method as described in the study of ship resistance earlier.

8.1.1 Oscillatory Sway Motion

In pure sway motion, the forward speed u is constant. The sway speed is determined by the amplitude of sway motion as below.

The sway oscillation is of the form:

$$y = A_0 \sin(\omega t)$$

Where: y   Sway displacement at time t

     A_0 Amplitude of sway displacement

     ω Angular frequency of oscillatory sway ($2\pi/T$)

     T   Period of oscillatory sway

Resulting sway velocity and acceleration are:

$$v = A_0 \, \omega \cos(\omega t)$$
$$a = -A_0 \, \omega^2 \sin(\omega t)$$

As the ship is moving with oscillatory sway speed, special treatment is required to deal with the unsteady motion, which could involve the use of a moving mesh as a rigid body, or alternatively, a non-inertial reference frame to avoid the introduction of grid velocity. Both methods were tested and consistent results were obtained, therefore, only one method and results are presented below, which is the non-inertial reference frame method.

The non-inertial force is derived from the acceleration given above. It was added into momentum equations as source term or body force.

The boundary conditions need to be modified to consider the time-dependent sway speed. There is no symmetry condition applied. The inlet and the outer boundary are assigned as velocity inlet. Three components of velocity and wave elevation are prescribed.

8.1.1.1   Test cases

The pure sway model tests were carried out in HSVA multi-purpose deep water towing tank using their PMM facility. The computational parameters used in the numerical simulation are the same as those in model tests, which are given in Table 10.

Table 10 Computational parameters

Motion	T(s)	V_0/U	U(m/s)
Oscillatory sway	10	0.075	1.05

Where: T period of oscillatory sway motion

U ship longitudinal speed

V_0 amplitude of oscillatory sway motion

The Froude number is Fr=0.132.

8.1.1.2   Mesh generation

For manoeuvring simulation, the whole of the hull needs to be meshed and computed. The structured meshes on the starboard were generated first, like those used in the resistance calculation, then the meshes were mirrored to the port side. Meshes with cell number of 3.2M were generated. The Y plus value at the hull surface was around 50.

A sketch of the computational domain and boundary mesh is shown below
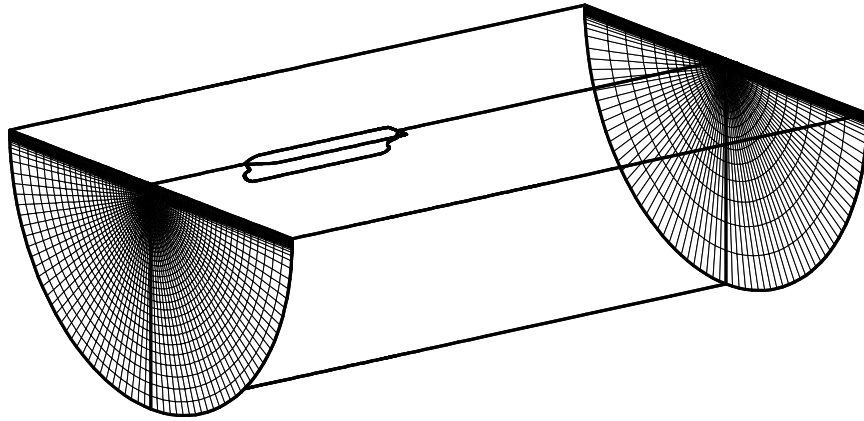
Figure 65 Computational domain

8.1.1.3 Analysis method

The hydrodynamic forces and moments are non-dimensioned with reference to length Lpp, T, B and speed U.

The definition of non-dimensional hydrodynamic forces is shown below:

$$X' = \frac{X}{0.5\rho V_\infty^2 L_{PP}T}$$

$$Y' = \frac{Y}{0.5\rho V_\infty^2 L_{PP}T}$$

$$Z' = \frac{Z}{0.5\rho V_\infty^2 L_{PP}B}$$

$$K' = \frac{K}{0.5\rho V_\infty^2 L_{PP}T^2}$$

$$M' = \frac{M}{0.5\rho V_\infty^2 L_{PP}^2 B}$$

$$N' = \frac{N}{0.5\rho V_\infty^2 L_{PP}^2 T}$$

8.1.1.4   Numerical results of oscillatory sway motion

Unsteady parallel computations of the oscillatory sway motion with specified parameters were carried out. Second order implicit discretisation of time was used. The time step is 0.005s, therefore total time step in one period is 2000. Second order upwinding discretisation of convection was used. It took roughly 3 days to complete the 4 periods of calculation on 16 cores of HPC.

The results of the longitudinal force (X), sway force (Y) and yaw moment (N) for the concerning oscillatory sway motion are given in Figure 66, Figure 67 and Figure 68.
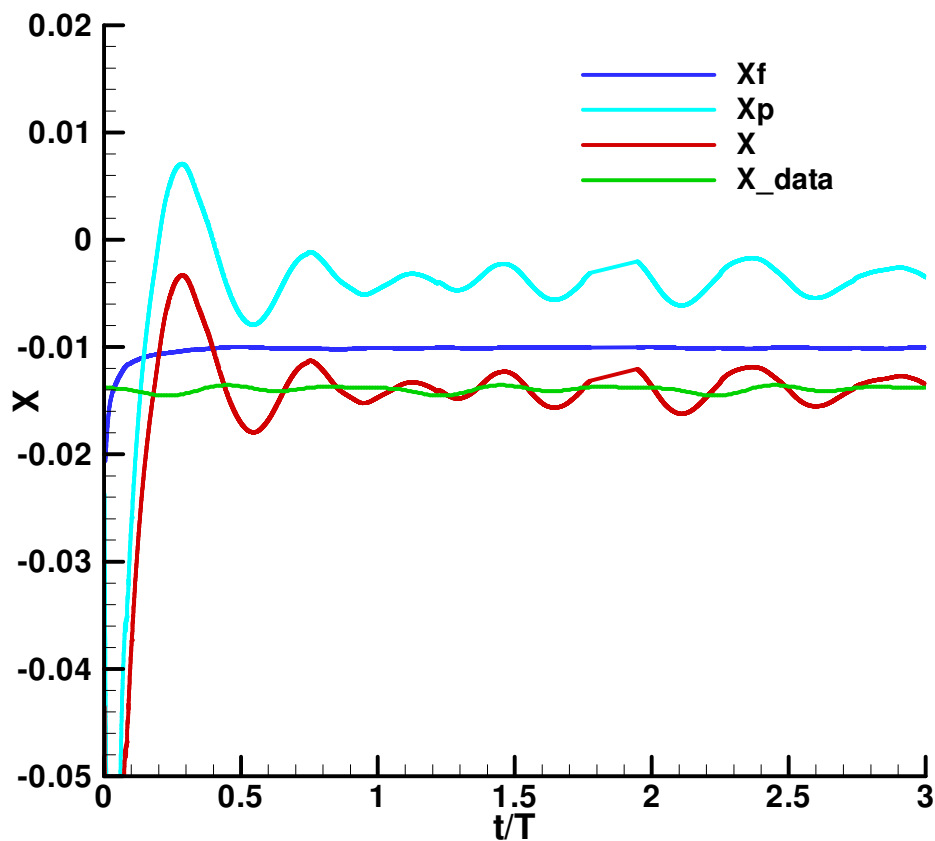
Figure 66 Computed X time history

Where:

       t   time

       X   Total computed longitudinal force

       X_f Friction component of computed X

       X_p Pressure component of computed X

       X_data   Longitudinal force from HSVA model test

As we can see from Figure 66, both the computed and the measured longitudinal forces show an oscillatory feature responding to the oscillatory sway motion. The computed mean longitudinal force is reasonably close to the measured one (roughly -0.014, which is close to data from the resistance test).

It is to be noticed from the plot that the amplitude and phase of oscillation are different in the calculation and the model test. The phase of the oscillation from the model test is constant and the amplitude is much smaller than that from the computation. The oscillatory phenomenon in the computed longitudinal force is due to the interaction of oscillatory sway motion with numerical wave disturbance. Numerical wave disturbance was quite large in the initial stage, and is expected to be diminishing with time slowly.

Among the computed total longitudinal force, friction force is almost unchanged after 0.2 seconds irrespective of oscillatory sway motion. The computed pressure force was oscillating, which is the source of the oscillation in the total longitudinal force.

Both the computed and the measured sway force in Figure 67 show oscillatory feature responding to the oscillatory sway motion. The computed and measured mean sway forces are both zero as there was no steady sway motion.
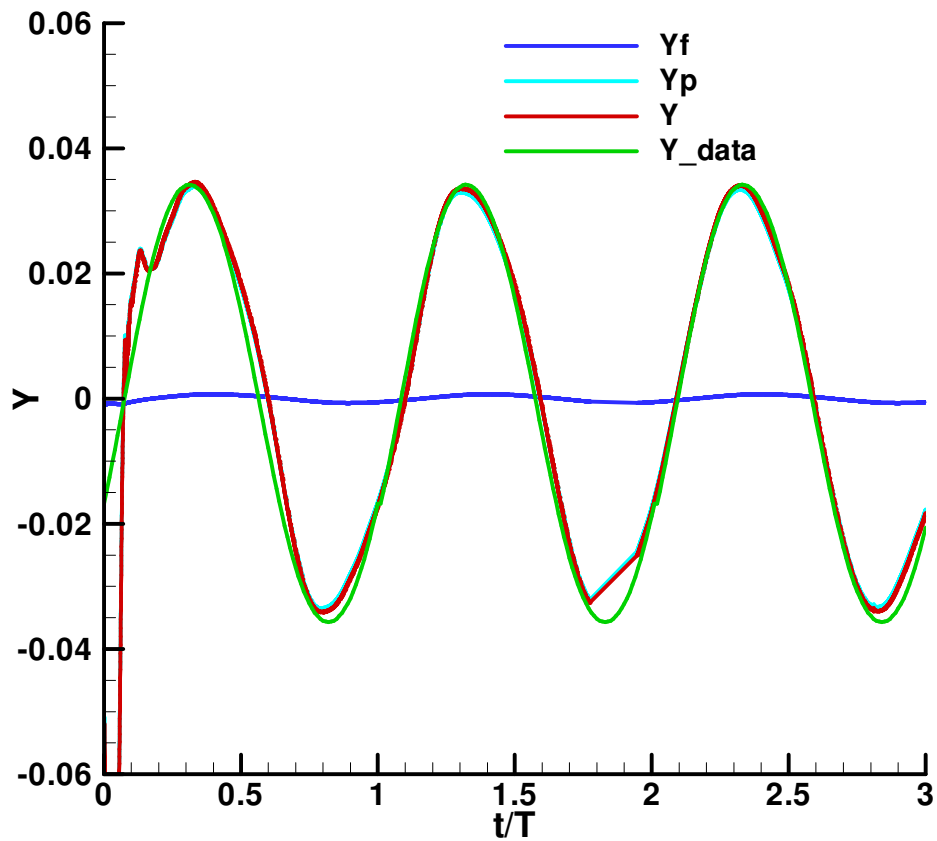
Figure 67 Computed Y time history

Where:

Y   Total computed sway force

Y_f Friction component of computed Y

Y_p Pressure component of computed Y

Y_data   Sway force from HSVA model test

We can see that the amplitude and the phase angle of the oscillation were very close between the calculation and the measurement. The measured amplitude of sway force is 2% larger than the computed one. The agreement between calculation and

experiment is quite satisfactory. Numerical wave disturbance is negligibly small in the computed sway force.

Among the computed total sway force, friction force is small and can be neglected. The computed pressure force was roughly 99% of the total sway force.

As we can see from Figure 67, at time 1.7-1.9, computed results have a discontinuity. After checking with the data file, it was found that series of data of 576 time steps from 1.77-1.94 were not recorded due to server fault. It was back normal after that. Thus the discontinuity should be ignored.

The comparison of yaw moment is shown in Figure 68.

As we can see from Figure 68, the computed and the measured yaw moments show a similar oscillatory feature. The computed and the measured mean yaw moment is zero as there is no steady turning motion.

The amplitude and phase angle of oscillation are very close between the calculation and the model test. The measured yaw moment is 8% smaller than the computed one. Numerical wave disturbance is negligibly small in the computed yaw moment.

Among the computed total yaw moment, friction force is very small and can be neglected. The computed pressure force is roughly 100% of the total yaw moment.
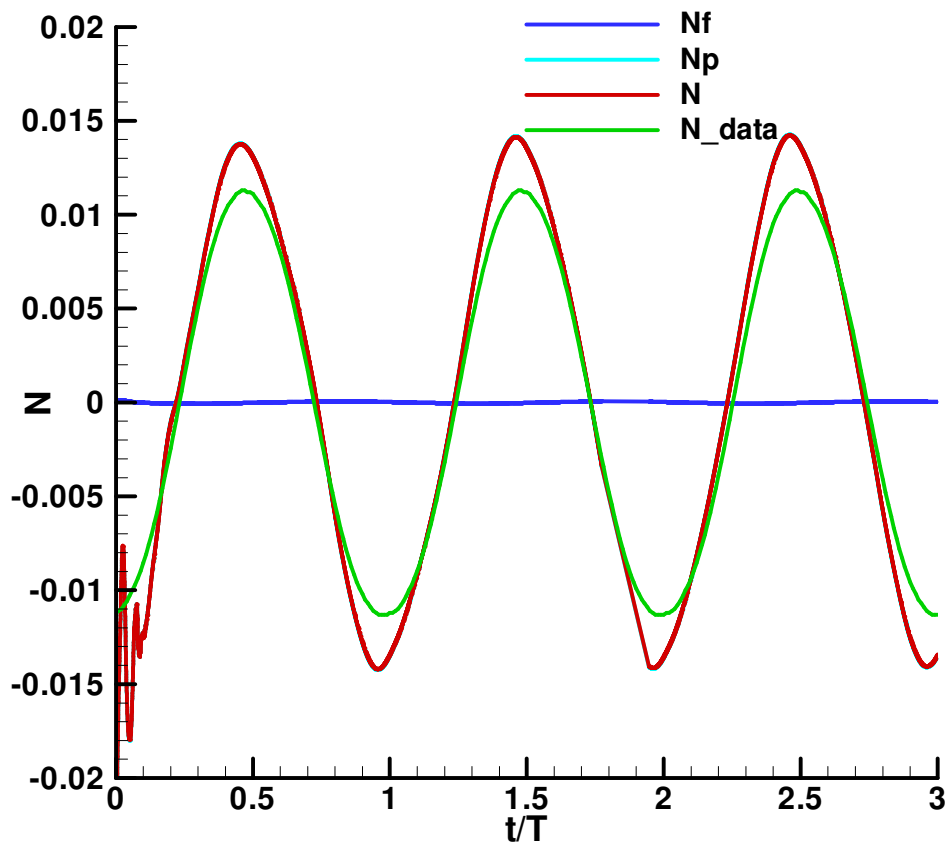
Figure 68 Computed N time history

Where:

    N   Total computed yaw moment

    N_f Friction component of computed N

    N_p Pressure component of computed N

    N_data   yaw moment from HSVA model test

Comparison of manoeuvring forces shows that the sway force and yaw moment are reasonably well predicted. There is little numerical wave disturbance on the manoeuvring forces. The mean longitudinal force is well predicted by RANS. However, oscillation of X force suffers from numerical disturbance. However, as we

are mostly interested in the hydrodynamic coefficients of the sway force and the yaw moment, the accuracy of the RANS prediction is satisfactory.

We can obtain the hydrodynamic derivatives from the time record of the computed force and moment. Two analysis methods were compared, the Fast Fourier Transform (FFT) and least square fit (LST). These two methods give similar results of the zero and the first order harmonics, thus only FFT results are presented in this research below.

8.1.1.5   Calculations of hydrodynamic derivatives

Using time series of the forces from the numerical and the experimental PMM tests, acceleration and velocity dependent components were extracted using FFT. The results were given in Table 11.

Table 11 components of sway force and yaw moment

V_0/U	Method	Acy	Vey	Acn	Ven
0.075	Present	3.01E-02	-1.71E-02	2.42E-03	-1.30E-02
0.075	Data	3.20E-02	-1.52E-02	1.74E-03	-1.10E-02

Where:

Acy   Acceleration dependent first harmonic component of Y

Acn   Acceleration dependent first harmonic component of N

Vey   Velocity dependent first harmonic component of Y

Ven   Velocity dependent first harmonic component of N

As we can see from the table, there is overall reasonably good agreement between the computed and the measured added mass/inertia and damping. There are nonlinear effects on both sway force and yaw moment, however, these are not large due to relatively long period.

From the derived added mass and damping components, hydrodynamic derivatives are obtained as shown below

$$Y_v = \frac{\partial Y}{\partial V} = \frac{Vey}{a\varpi}$$

$$N_v = \frac{\partial N}{\partial V} = \frac{Ven}{a\varpi}$$

$$Y_{\dot{v}} = \frac{\partial Y}{\partial A} = \frac{Acy}{-a\varpi^2}$$

$$N_{\dot{v}} = \frac{\partial N}{\partial A} = \frac{Acn}{-a\varpi^2}$$

Derived hydrodynamic derivatives are listed in Table 12.

Table 12 Hydrodynamic derivatives

V_0/U	Method	Y_v	$Y_{\dot{v}}$	N_v	$N_{\dot{v}}$
0.075	Present	-2.28E-01	1.88E-01	-1.73E-01	1.52E-02
0.075	Data	-2.02E-01	1.99E-01	-1.47E-01	1.09E-02

It can be seen from Table 12 that the computed hydrodynamic derivatives with respect to velocity and acceleration of the sway forces and yaw moments are reasonably consistent with those from measurements.

From Yv and Nv, using linear assumption, the change of the sway forces and yaw moments with yaw angle are derived and compared with steady state measurement (SSM) as shown below.

Table 13 Comparison of forces

Yaw (°)	Method	Y	N
5	Present	1.99E-02	1.51E-02
	data	1.76E-02	1.28E-02
	SSM	1.94E-02	1.21E-02
10	Present	4.02E-02	3.05E-02
	Data	3.56E-02	2.59E-02
	SSM	4.48E-02	2.37E-02

It can be seen from the comparison that the predicted sway forces and yaw moments from the numerical and the measured hydrodynamic derivatives are consistent with those obtained by the steady drift model tests. The predicted sway force is close to the model test at drift angle 5 degrees. However, the difference increases at 10 degrees due to the non-linear effects, where the predicted yaw moment is overestimated. However, results are still acceptable.

8.1.1.6   Comparison with Empirical Formula

Due to high cost involved in physical manoeuvring tests, empirical formulae are widely used for the prediction of ship manoeuvrability. The comparison between predicted hydrodynamic derivatives and empirical methods is described below.

Two well known empirical formulae of hydrodynamic derivatives [16, 46] were applied:

Clarke's empirical formulae:

$$Y_{\dot{V}}' / \pi(T/L)^2 = 1 + 0.16C_B B/T - 5.1(B/L)^2$$

$$N_{\dot{V}}' / \pi(T/L)^2 = 1.1B/L - 0.041B/T$$

$$Y_V' / \pi(T/L)^2 = 1 + 0.40C_B B/T$$

$$N_V' / \pi(T/L)^2 = 1/2 + 2.4T/L$$

Inoue's empirical formulae:

$$Y_V' = -(\pi k/2 + 1.4C_B B/L)$$
$$N_V' = -k$$
$$k = 2T/L$$

The comparisons of hydrodynamic derivatives by PMM and by the empirical methods are given in Table 14.

Table 14 Comparison with empirical methods

	Y_v	$Y_{\dot{v}}$	N_v	$N_{\dot{v}}$
Present	-2.28E-01	1.88E-01	-1.73E-01	1.52E-02
Data	-2.02E-01	1.99E-01	-1.47E-01	1.09E-02
Clarke	-3.52E-01	1.80E-01	-1.39E-01	1.84E-02
Inoue	-3.67E-01		-1.33E-01	

The comparison shows that the derivatives with respect to the acceleration from the empirical formulae are close to those from both the numerical and the physical PMM tests. However, the derivative of sway force with respect to velocity is much overestimated by the empirical approach while the derivative of yaw moment is well predicted by the empirical method.

8.1.1.7   Flow Contour

To examine the velocity distribution in one period, axial velocity contours at x=0.3 were plotted. The time steps selected are 0, T/8, T/4, 3T/8 and T/2 (T is the period of oscillation motion). The results are given in Figure 69 Axial velocity contour at x=0.3.
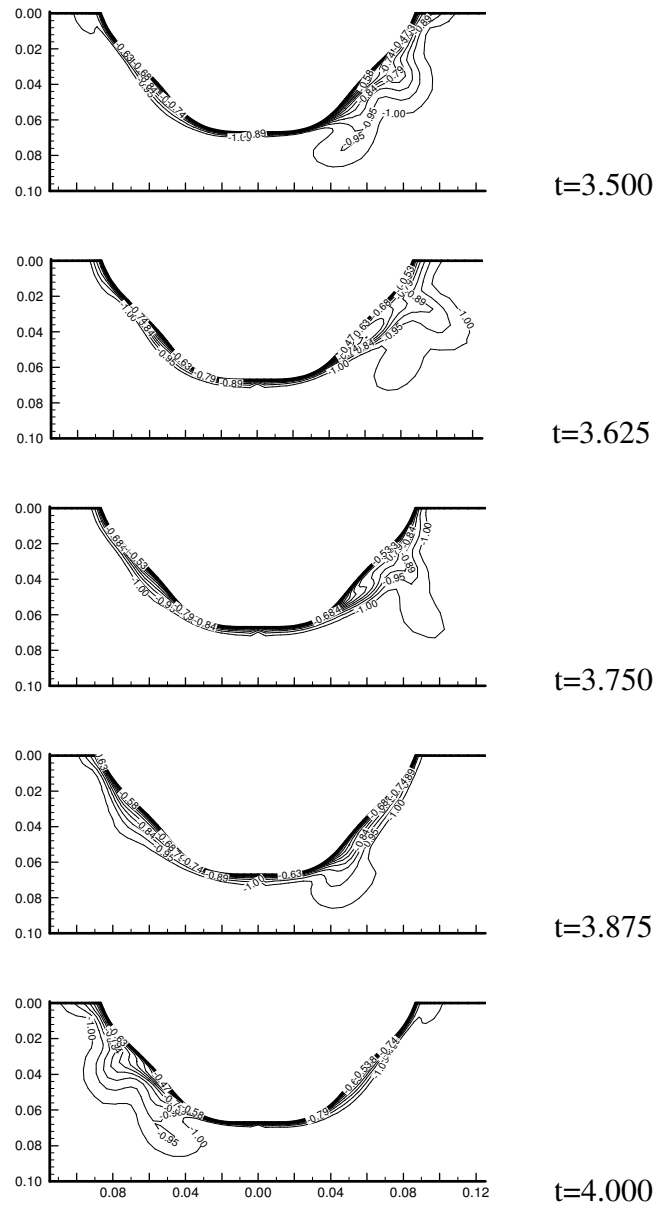
Figure 69 Axial velocity contour at x=0.3

It can be seen that the flow pattern oscillates with oscillatory sway motion. The boundary layer is thin on the weather side and becomes thicker on the leeside. There is a bulge on the leeside, which is due to cross separation. At the bottom of hull, the boundary layer is generally very thin. The sway motion changes the axial velocity distribution periodically.

8.1.2   Oscillatory Yaw

Numerical simulation of the oscillatory yaw
was also made and the results were
compared with model test data.

The pure yaw model tests were carried out in an HSVA multi-purpose deep water
towing tank using their PMM facility. The computational parameters used in the
numerical simulation are the same as those used in the model tests, which are given
in Table 15 Computational parametersbelow.

Table 15 Computational parameters

Motion	T(s)	r_0	U(m/s)
Oscillatory yaw	32	0.2	1.05

Where:

T   Period of oscillatory yaw motion

U   Ship speed

r_0 Non-dimensional amplitude of oscillatory yaw motion (rL/U)

r   Yaw rate

The yaw oscillation is of the form:

$$\psi = \psi_0 \sin(\omega t)$$

Where: ψ   Yaw angle at time t

ψ0   Yaw amplitude

ω   Angular frequency of oscillatory yaw (2π/T)

T   Period of oscillatory yaw

Resulting yaw velocity and acceleration are:

$r = \psi_0 \, \omega \cos(\omega t)$

$r' = -\psi_0 \, \omega^2 \sin(\omega t)$

From the parameters in Table 15, we can obtain:

Angular frequency ω is 0.2/s.

The amplitude of yaw velocity r is $R_0 U/L = 0.032$.

The corresponding ψ_0 is 0.16 or 9.2 degrees.

7.1.2.1   Mesh

The same meshes as that used in oscillatory sway are used.

7.1.2.2   Computational method

For oscillatory yaw motion, both velocity components u and v are oscillating periodically.

$u = U \times \cos(\psi)$

$v = U \times \sin(\psi)$

It is not convenient to use moving reference frame, as the body force and the boundary conditions are all time dependent.

The method of moving meshes as rigid body was adopted. The inlet and outer boundary conditions can be imposed in the absolute coordinate system. The outlet is the hydrostatic pressure boundary.

The time step is 0.005s; total time step in one period is thus about 6400. It took about 3 times in calculation time as it did in the calculation of pure sway.

The comparisons of the computed and the measured longitudinal force, sway force and yaw moment were given in Figure 70 Computed and measured longitudinal forcesFigure 72 Computed and measured yaw moment.
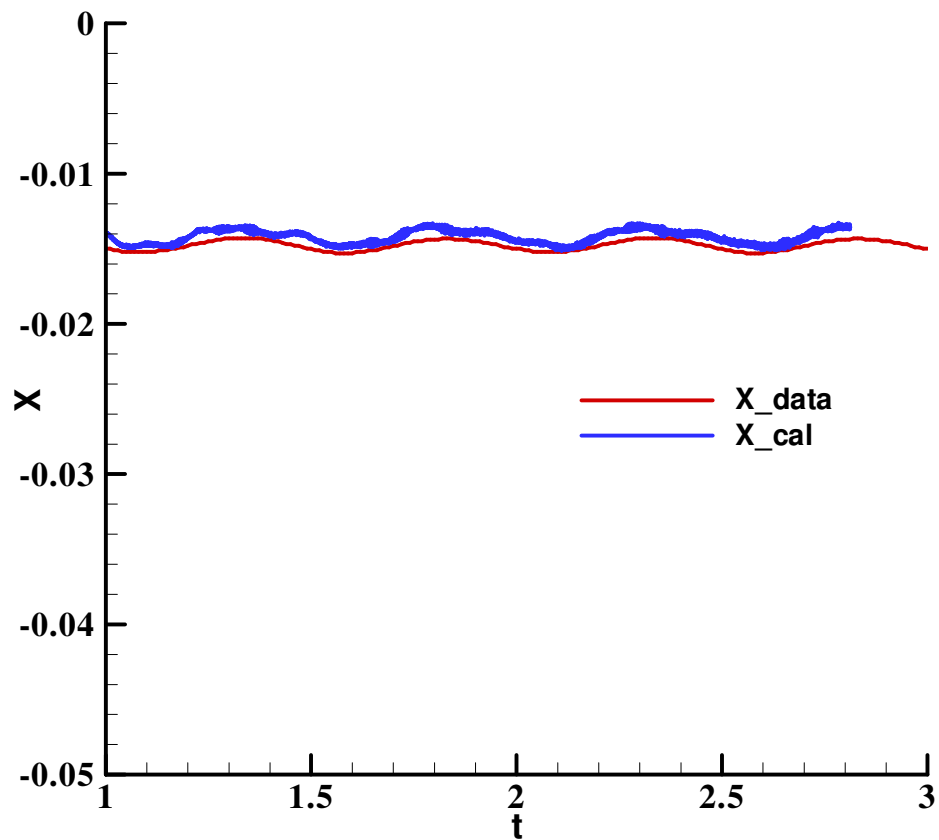
Figure 70 Computed and measured longitudinal forces

Comparisons of the computed and the measured longitudinal forces in Figure 70 show that the results from the calculation have been slightly overestimated. The amplitudes of oscillations are close. It seems that there is a small phase lag in the

calculation. Overall, the agreement between calculation and measurement is acceptable.
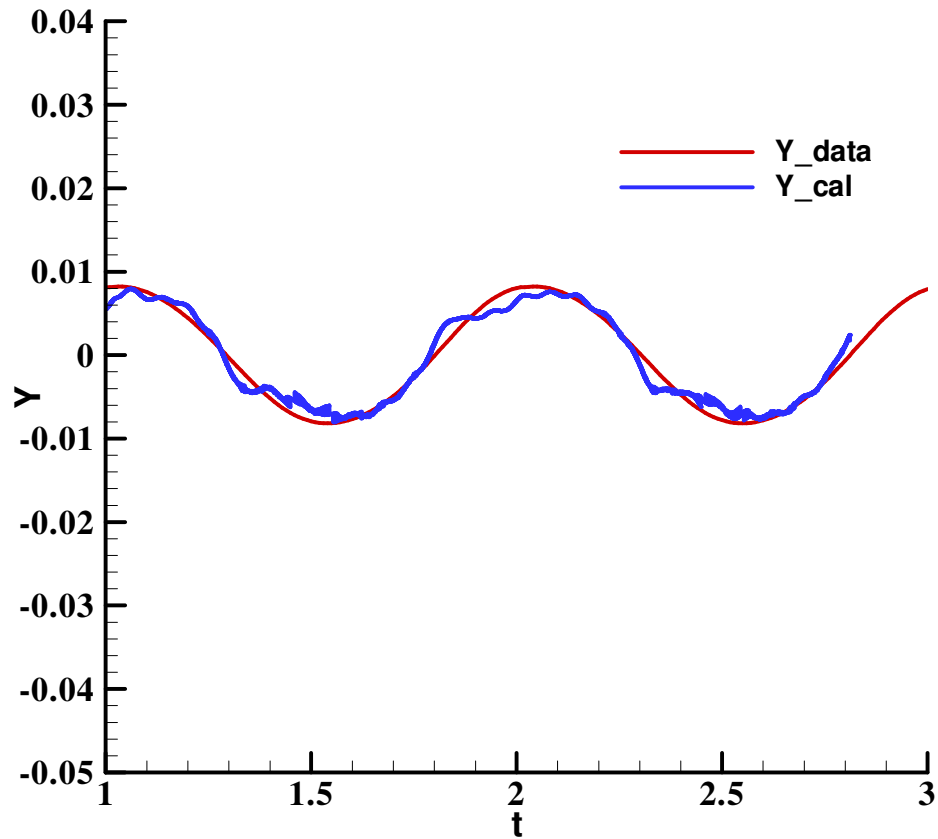
Figure 71 Computed and measured sway forces

Comparison of the computed and the measured sway forces in Figure 71 shows that the results from the calculation and the measurement are consistent. The amplitudes of oscillations are close and the phase angles are the same. However, we notice that the computed sway force exhibits oscillation around the measured value, which might be due to the effects of the vortex shedding at the bow and stern. Overall, agreement between calculation and measurement is acceptable.
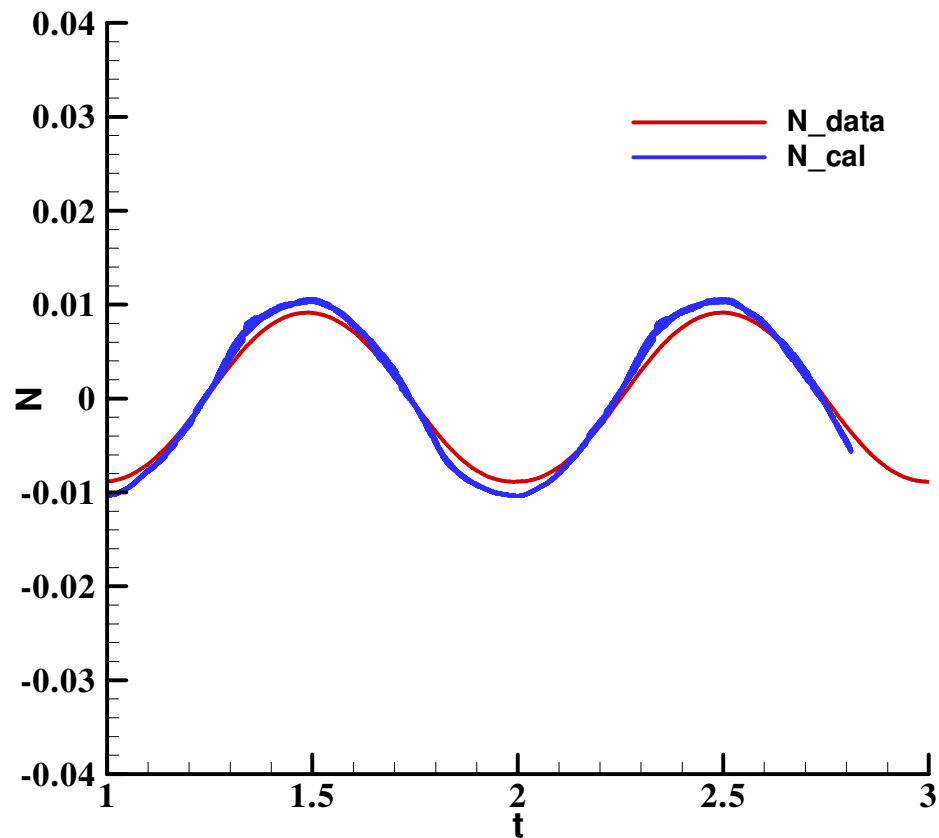
Figure 72 Computed and measured yaw moment

As we can see from the comparison of forces in Figure 72, the oscillatory feature of yaw moment and its motions are consistent between the calculations and the measurements. The period of the computed and the measured yaw moments is the same as that of the oscillatory motion. The phase angles between calculation and data agree well. However, it can be seen that the computed amplitude of the yaw moment is roughly 5% overestimated. As we know, the pressure distribution at the bow and the stern have a large contribution on the yaw moment. At pure yaw motion, the pressure at the bow and the stern changes significantly. On the weather side, pressure is very high and on the leeside it is very low. There is also minor separation on the leeside; therefore, it is difficult to predict the flow around the bow and the stern with yaw. Turbulence model and mesh quality play a significant role. Further studies on

how to improve the accuracy of the yaw moment are needed. From the manoeuvring prediction point of view, the numerical accuracy is acceptable.

8.2 Manoeuvring simulation

Using the hydrodynamic derivatives obtained, standard manoeuvring simulations can be carried out.

As we know, for manoeuvring simulations we need to have the resistance curve, propeller performance and rudder force in addition to the manoeuvring derivatives. These are obtained from either experiments or empirical formulae.

The SSRC in-house manoeuvring software is used for manoeuvring simulation. Simulation of the turning circle was performed with initial forward speeds of 10 and 18 knots. For each speed, three rudder angles are applied, 15, 25 and 35 degrees, respectively.

The time records of trajectory, velocity u, v and yaw rate r were given below.
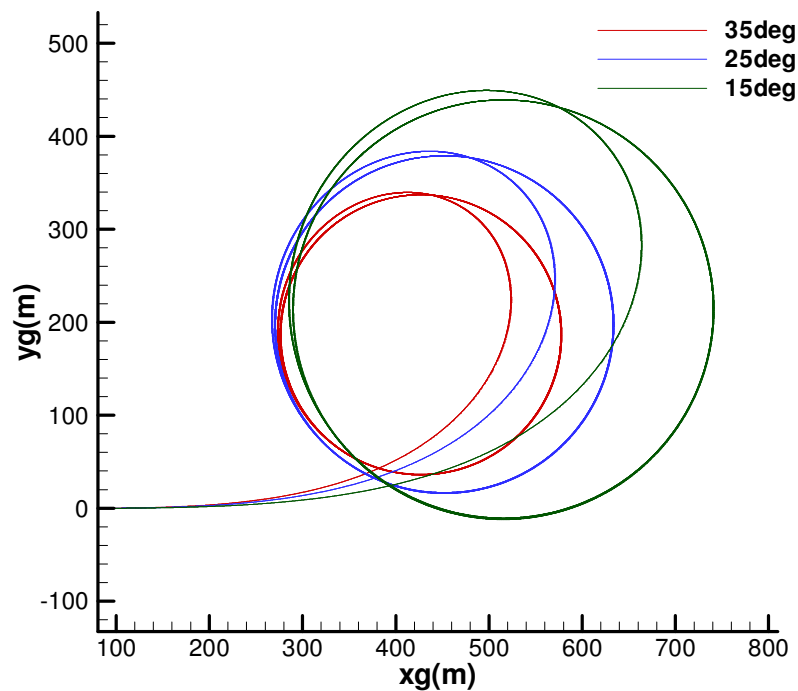
Figure 73 Trajectory of turning circle simulation (18 knots)

Where xg and yg are longitudinal and transverse coordinates of gravity centre.

The results of time record of the trajectories show that the turning circle decreases with an increase in the rudder angles. The steady turning diameters are 451, 364 and 300m for rudder angles 15, 25 and 35 degrees. Non-dimensional diameters/lengths are 2.93, 2.37 and 1.95.
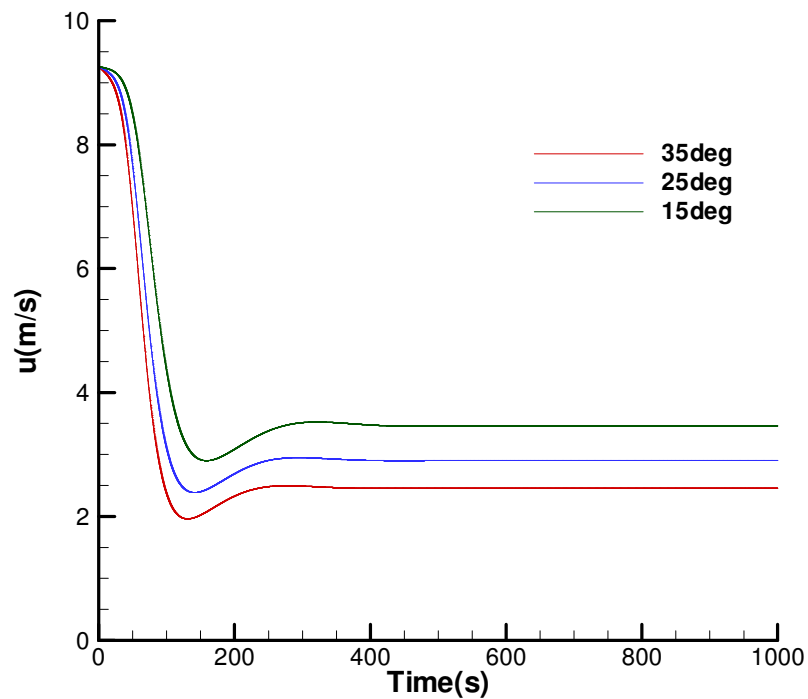
Figure 74 longitudinal velocity u time record (18 knots)

Velocity u in Figure 74 longitudinal velocity u time record (18 knots) shows that there is a significant speed drop when the rudder angle increases from 15 degrees to 35 degrees. However, v velocities do not change much for three rudder angles as show below.
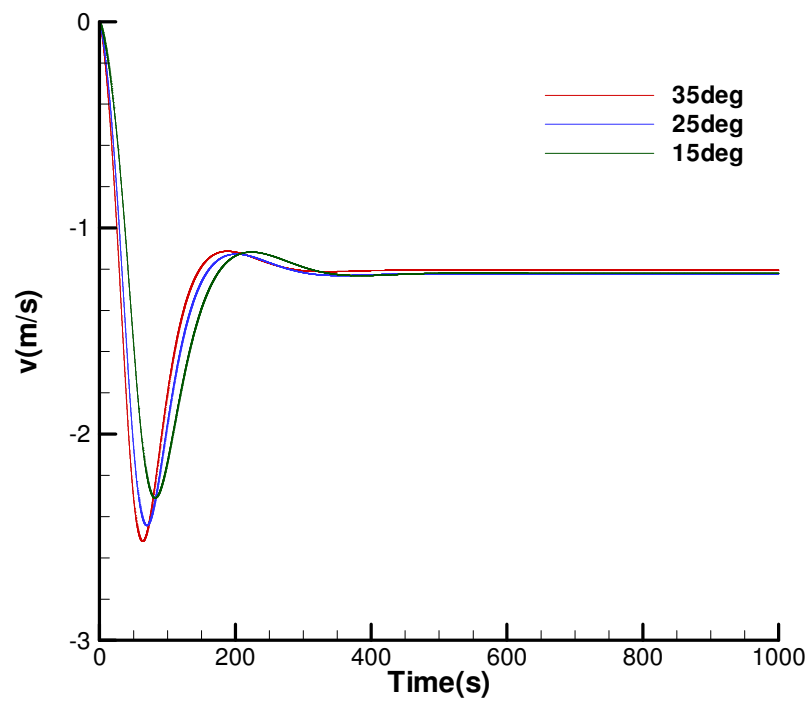
Figure 75 transverse velocity v time record (18 knots)

Turning rates will increase with increase of rudder angles as shown below.
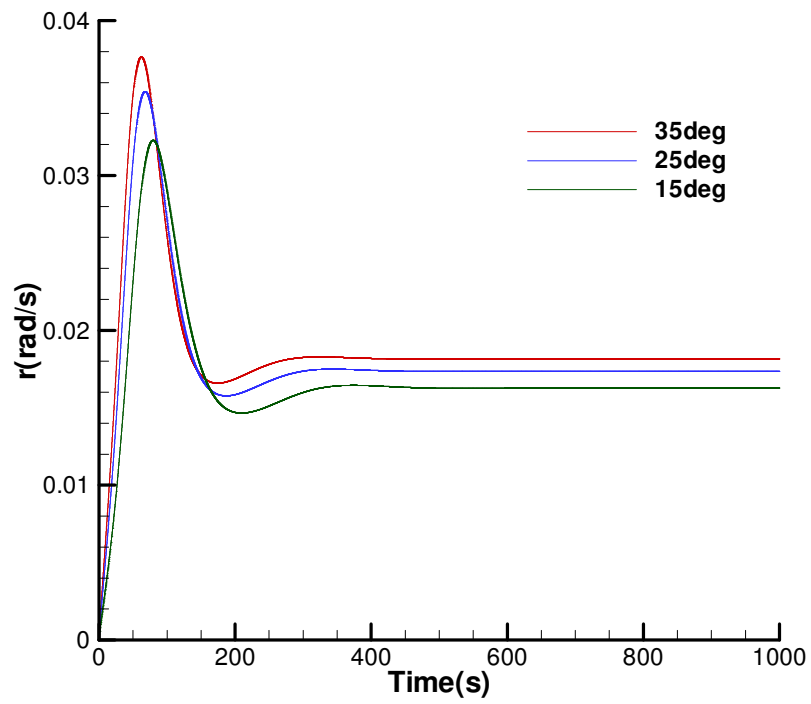
Figure 76 Yaw rate time record (18 knots)

Results with initial forward speed 10 knots are given below. Non-dimensional diameters/lengths are 3.11, 2.48 and 2.05.
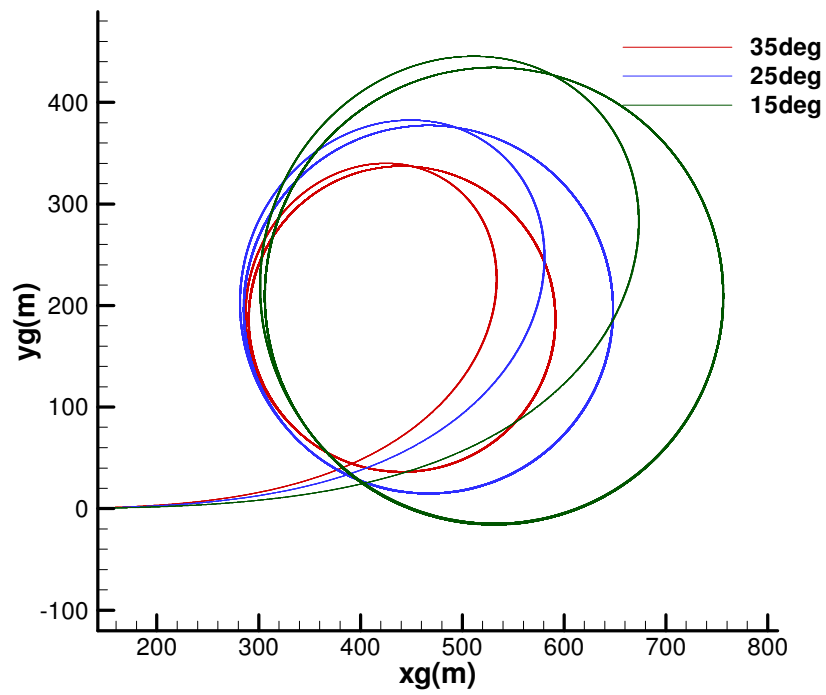
Figure 77 trajectory of turning circle simulation (10 knots)

The predicted longitudinal velocity is shown in Figure 78. Compared with 18 kn, velocity u has similar trends with change of rudder angles. However, the magnitude is reduced proportionally due to the lower initial forward speed.
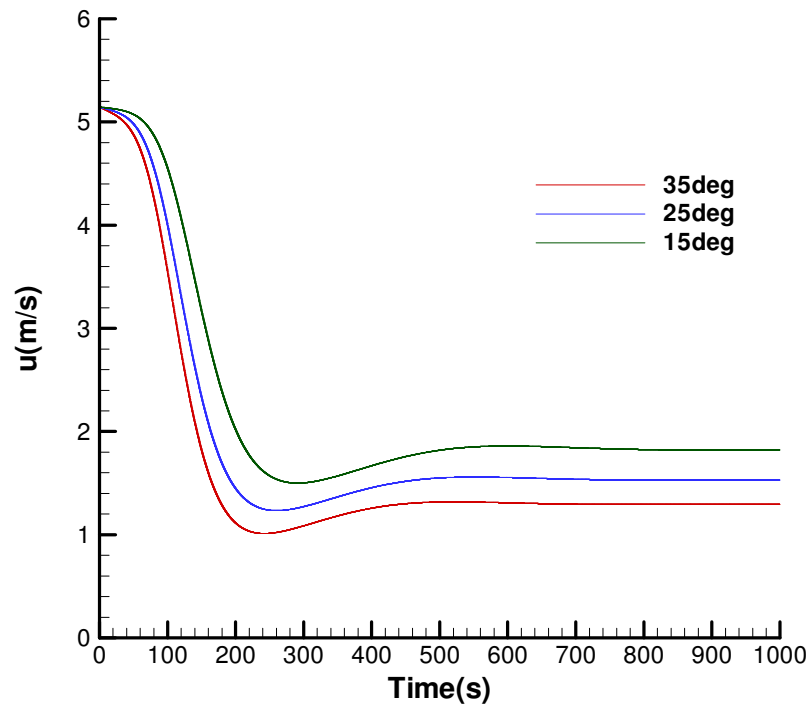
Figure 78 u time record (10 knots)

The predicted sway velocity v is shown in Figure 79. Similar changes of sway velocity are seen as those in higher speed.
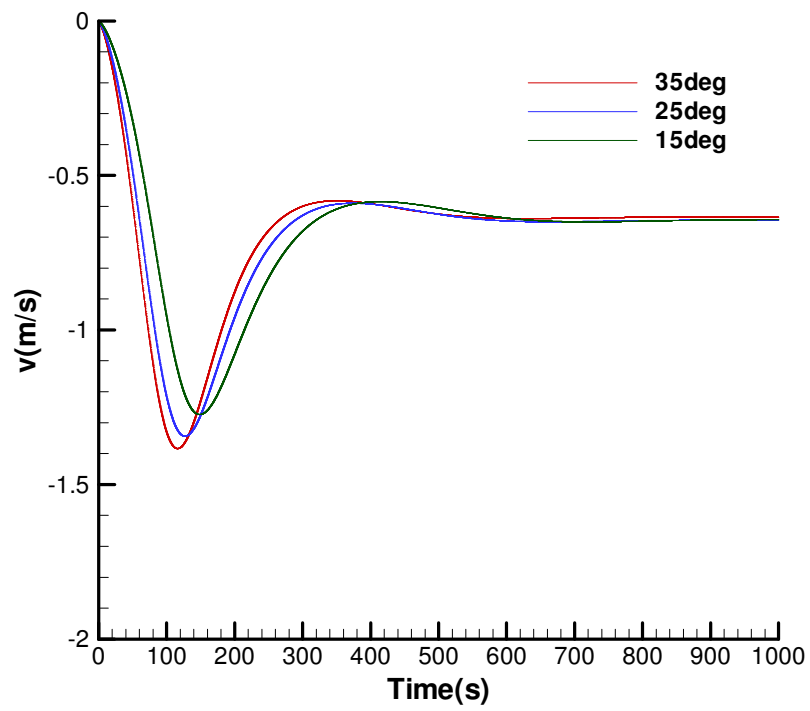
Figure 79 v time record (10 knots)

The predicted yaw rate r at speed 10 knots is shown in Figure 80. Similar speed effects as those observed for yaw rate.
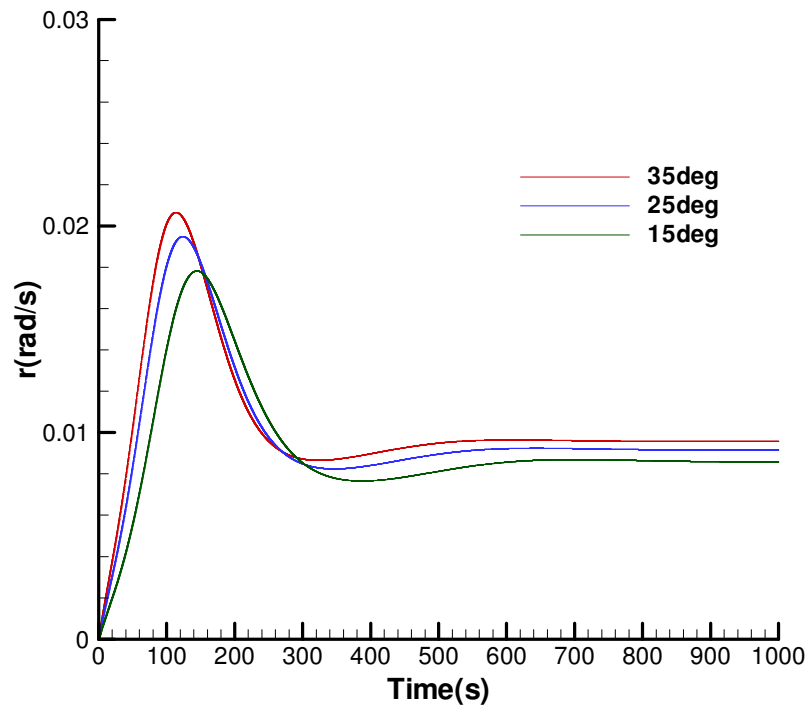
Figure 80 Yaw rate time record (10 knots)

Comparison of steady diameter of the turning circle with MARIN was made in Table 16. As we can see, the results between present calculations and MARIN are consistent for all 3 rudder angles.

Table 16: Comparison of HTC steady turning diameters/ L_{pp}, 10 kn

Rudder angle	MARIN	Present
15°	3.25	3.11
25°	2.38	2.48
35°	1.91	2.05

8.3 Concluding remarks

In summary, numerical simulations of the oscillatory sway/yaw motions corresponding to physical PMM tests were carried out using RANS solver. Based on the computational results, the following remarks can be made:

There is numerical wave disturbance on the computed longitudinal force. Its effects on sway force and yaw moment are not large.

The viscous components of the sway force and the yaw moment are negligibly small compared to the pressure components.

Generally reasonable agreement was achieved between computed and measured manoeuvring forces for consideration of manoeuvring analysis.

9   Seakeeping

Ships sailing in waves are subject to exciting forces due to incident waves. The wave forces/moments will cause the dynamic motion of a ship over her otherwise static or steady course. In addition, the steady motion of the ship interacts with the six degree of freedom (6DOF) motions in the wave, i.e. surge, sway, heave, roll, pitch and yaw. The interaction is normally non-linear and time dependent. It is one of the most tricky hydrodynamic problems to solve.

Figure 81 MARIN model tests of ship motion in wave

The problem is traditionally dealt with through model tests. The waves are generated in the wave basin and the ship motion is recorded in free sailing condition.

Numerically, the seakeeping problem was mostly dealt with by linear potential theory. The method applies a linear superposition of wave diffraction and radiation related terms. It is very efficient and reliable if the non-linear effects are small and damping is known.

With the development of CFD, the application of RANS method on the study of wave effects is gaining increasing attention.

In the pursue of simulation of wave effects by RANS, Ducrozet, et al [23] adopted a HOS scheme in developing the SWENSE approach for the non-linear water wave simulation. The comparison shows that the wave quality is good and the method can be applied for practical purposes. More recently, Blondel et al [7] developed two efficient deterministic prediction models.

Weynouth, et al used CFDSHIP-IOWA0 [27] to study the head sea effects on diffraction problems. Uncertainty studies were carried out and systematic calculations of parametric effects were conducted. The comparisons of results between the RANSE code, strip theory and potential code, with measurements show that the RANSE code performed much better than other codes.

Cura Hochbaum and Vogt studied straight ahead motion in head waves using the HSVA code NEPTUN [19]. The force and the moment results agree well with the experimental data.

Hedeo [33] calculated unsteady surface pressure, added resistance and ship motions of SR2201C model in regular waves and good agreements with the data are obtained.

Guo et al [31] studied added resistance and ship motion of KVLCC2 in head wave in fixed and free conditions by ISIS-CFD. The uncertainty studies of grid resolution and time step are carried out. The numerical results are validated against model tests and good agreements are achieved.

More recent numerical works (Stern, Gao, Alexander etc) were reported in the latest Gothenburg CFD workshop on benchmarking tests of diffraction of DTMB5415 [50].

In this research, focus is laid on the numerical simulation of the wave diffraction and roll decay by the RANS approach.

The incident wave is generated at the inlet by the analytical solution of deep water waves. The velocity components and wave elevation due to the incident wave are superimposed into steady motion. The non-linearity and viscous effects are automatically included in the numerical simulation.

9.1   Diffraction

In this research, the wave diffraction problem is studied using the RANSE approach. A harmonic incident wave is generated at inlet, and the analytical wave parameters are imposed. The description of the numerical wave maker is given below.

9.1.1   Test case

The benchmarking calculations of the wave effects on DTMB5415 were carried out. The model test of wave diffraction was performed by Longo [71]. The same model as in resistance test is used. The main dimensions can be found in the foregoing.

The main description of the tests is given below.

- Bare hull without bilge keel
- Towing condition in head waves
- Sinkage and trim: s = -1.92x10^{-3}, t = -0.136°
- Incident wave length λ = 1.5 LPP
- Wave steepness: Ak = 0.025
- Re= 4.86×10^6
- Fr=0.28

9.1.1.1   Mesh

Meshes with 2.6M cells were generated. The amplitudes of incident and exciting waves are estimated beforehand so that free surface can be effectively resolved. About 50 cells are distributed vertically to ensure the resolution of wave capturing. As the wave length is 1.5L, no special treatment of grid resolution in the longitudinal direction is taken.

9.1.1.2   Digital wave maker

The inlet is located at one ship length in front of the bow where the velocity components and the volume fraction were imposed as below.

- Wave length $\lambda/L = 1.5$
- Wave number $k = 2\pi/\lambda$
- Wave steepness: $Ak = 2\pi A/\lambda = 0.025$
- Where A is wave amplitude
- Wave frequency for deep water $\omega = \sqrt{gk}$
- Model speed V=1.53m/s
- Wave encounter frequency $\omega_e = \omega + kV$
- Period $T = 2\pi/\omega_e$
- Wave elevation at inlet $\zeta = \zeta_a \sin(kx - \omega_e t)$
- X velocity $u = \zeta_a \omega e^{kz} \cos(kx - \omega_e t)$
- Z velocity $w = \zeta_a \omega e^{kz} \sin(kx - \omega_e t)$

The time-dependent velocity and wave elevation are prescribed at the inlet boundary.

The incident wave was generated at time 4L/U after the steady inflow sweeps the whole domain once and the solution is converged.

The outlet is located at two ship lengths behind the stern where the open channel flow is specified. No explicit wave damper is used. The coarse mesh at outlet damps wave numerically.

The method can be used to generate head wave with or without forward speed. However, it cannot generate following waves through specifying inlet boundary conditions. For oblique or beam waves, one of side boundaries in addition to inlet will be used as wave maker where mesh resolution needs to be sufficient to ensure the quality of wave.

9.1.1.3 Result and Analysis

The forces and moment are nondimensioned as follows.

$$CT = Fx / 0.5\rho V^2 S_0$$
$$CH = Fz / 0.5\rho V^2 S_0$$
$$CM = My / 0.5\rho V^2 S_0 L_{PP}$$

Where Fx, Fz and My are total resistance, heave force and pitch moment

S_0 is wetted surface area at rest and V is forward speed of the ship

The computational results are compared with measurements and shown below.

The comparison of surge forces is shown in Figure 82. It can be seen that the computed amplitude of the oscillation of the surge force is consistent with the measurement. However, the computed mean value of surge force is slightly larger than the measured. The phase is very close; both force time records show the same oscillation period and similar behaviour of wave effects.

It is noteworthy that the data of resistance with and without waves (calm water) are the same in the published data. It seems that the measured resistance in head wave is undervalued.
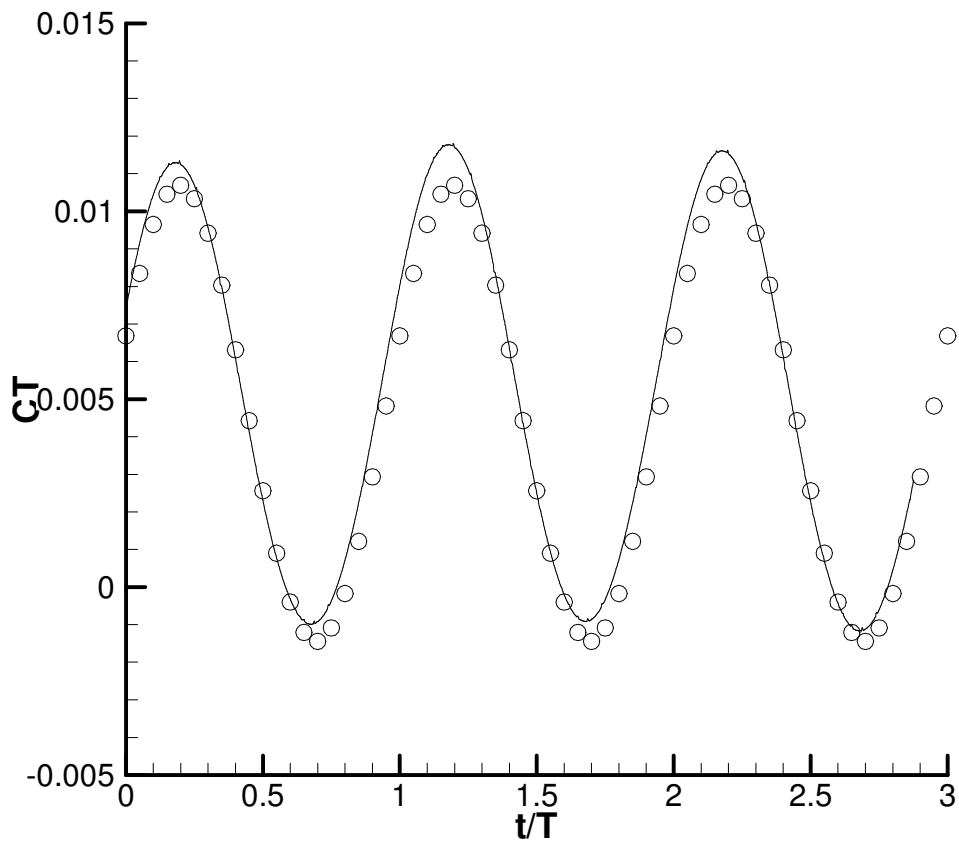
Figure 82 Surge force (Line: present, Symbol: Longo)

The comparison of heave forces is shown in Figure 83. It can be seen that the computed amplitude of the oscillation of the heave force is smaller than the measured force. The differences in the mean values are mainly due to hydrostatic or steady motion effects. The phase angles agree well. Both force time records show the same oscillation period and similar behaviour of wave effects. The difference of amplitude between calculation and measurement needs to be investigated further.
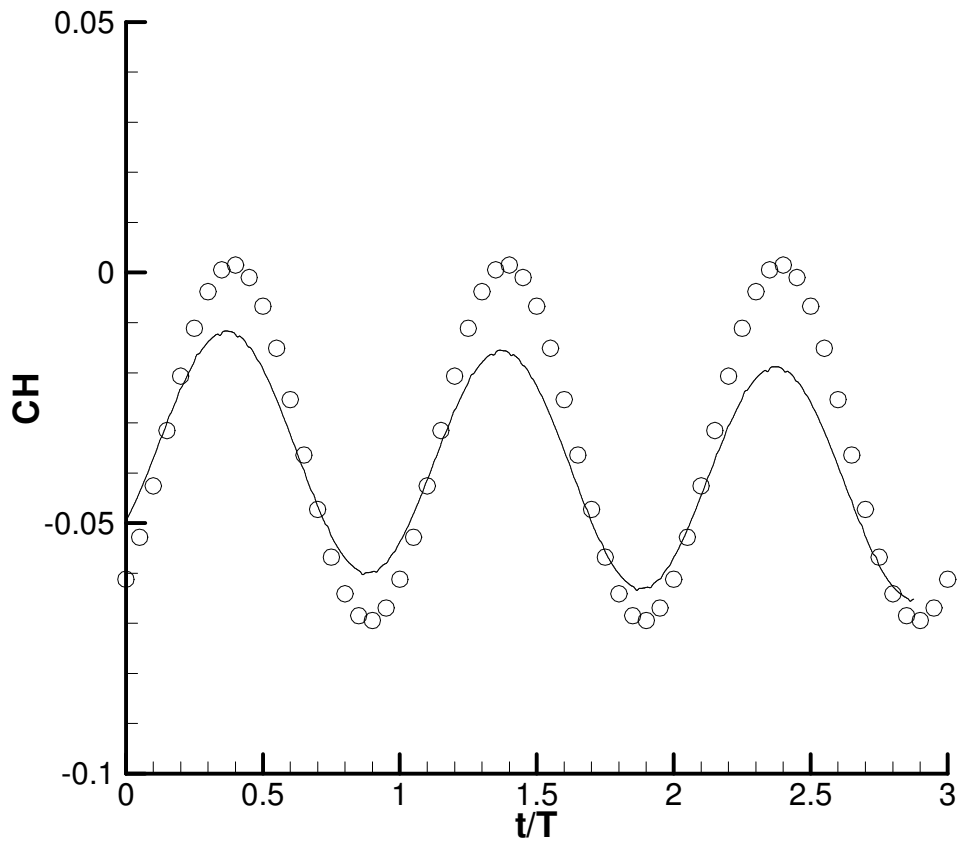
Figure 83 Heave force (Line: present, Symbol: Longo)

A comparison of the pitch moments is shown in Figure 84. It can be seen that computed amplitude of the oscillation of the pitch moment coincides with the measured amplitude. There is a small difference in the mean values, which is mainly due to hydrostatic or steady motion influences. The phase is consistent between calculation and measurement.
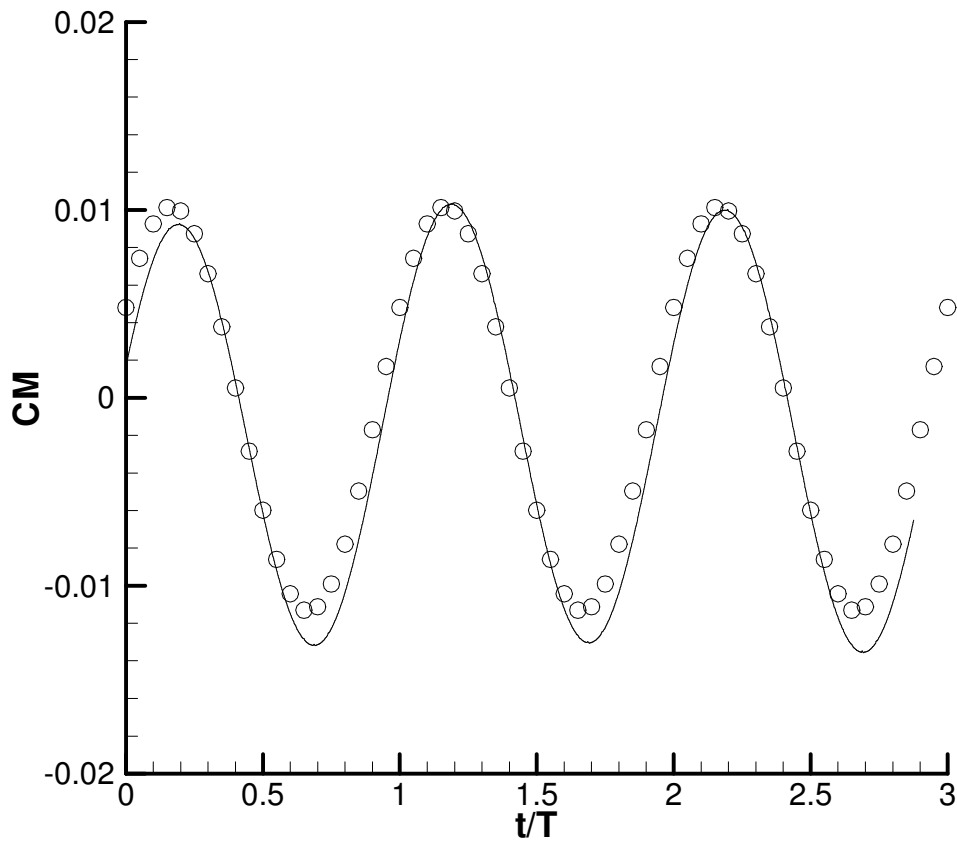
Figure 84 Pitch Moment (Line: present, Symbol: Longo)

For the time record of the forces, Fourier analysis is carried out and the results are summarised in Table 17.

The results of the 0th amplitudes show that the computed forces are slightly larger than the measurements. In general, agreement is acceptable.

The results of amplitudes of 1st harmonic components show that the consistency between the calculation and the measurement depends on the forces. For surge force and pitch moment, the agreements are quite satisfactory; however, for heave force,

the difference is quite large. The reason of the inconsistencies in the heave force needs to be further studied.

The results of 1st harmonic phase show that phase angles of the surge force, heave force and pitch moment are very close between calculation and measurement.

Table 17 Analysis of wave spectrum

Cases	CT		
	0th Amplitude	1st Amplitude	1st Phase□
Present	0.00495	0.00610	-61.2
Longo	0.00462	0.00608	-63.3
E%D	7.1	0.3	-3.3
Cases	CH		
	0th Amplitude	1st Amplitude	1st Phase□
Present	-0.0348	0.0241	-139.2
Longo	-0.0334	0.0357	-140
E%D	4.2	32.5	-0.1
Cases	CM		
	0th Amplitude	1st Amplitude	1st Phase□
Present	-0.00065	0.0112	-59.8
Longo	-0.00061	0.0108	-58.8
E%D	6.5	3.7	-1.70

In order to assess the computed results, a mathematical analysis of wave forces was undertaken as shown below.

The wave elevation at location x is expressed as:

$$\zeta = \zeta_a \cos(kx - \omega_e t)$$

The expression of wave height given above means the crest of incident wave is coincident with FP of the ship (x=0.) at time 0.

The difference of wave height at FP and AP can be obtained as:

$$\delta\zeta = \zeta_{x=0.} - \zeta_{x=L} = \zeta_a \cos(\omega_e t) - \zeta_a \cos(kL - \omega_e t)$$

We can deduce that the maximum difference of wave height occurs when t=0.091s. The corresponding phase angle is 360t/T=30 degrees. If we assume that the maximum resistance and pitch moment due to wave occur when the difference of the wave height at the bow and the stern reaches maximum, the resistance and the pitch moment will have the same phase lag of 30 degrees. The computed phase angle is larger than the value from this analysis.

Similarly, we can obtain the wave height at mid-ship as follows:

$$\zeta_{x=L/2} = \zeta_a \cos(kL/2 - \omega_e t)$$

Hence, we can estimate that the maximum wave height was reached at t=0.36s or an equivalent phase angle of 120 degrees. This leads to the conclusion that the heave force reaches maximum when the wave height at the mid-ship reaches maximum.

Both computed and measured phase angles are 20 degrees larger than in the above rough analysis, which may be due to viscous effects.

9.1.1.4 Comparison of velocity field

Comparisons of velocity contours at longitudinal position x=0.935 at the instant t/T=0.75 are given in Figure 85-Figure 90.

The U contours in Figure 85-Figure 86 show that the overall agreement is acceptable except near the centre plane. It can be seen that the measured U contour is not exactly symmetric about the centre plane, while symmetry conditions are imposed in the calculation.

The thickness and the shape of boundary layer are consistent between calculation and measurement.

Comparing with the U contour in the calm water, the wave effect on the longitudinal velocity is not significant.
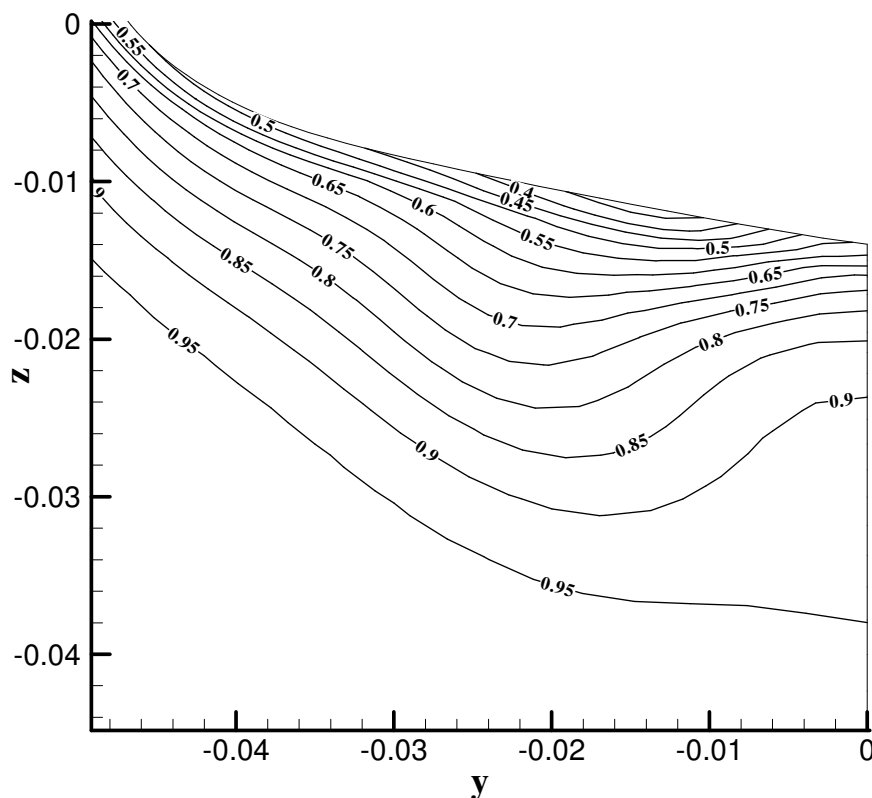
Figure 85 Computed longitudinal velocity contour, t=0.75

Where y and z are lateral and vertical coordinates nondimensioned by ship length.
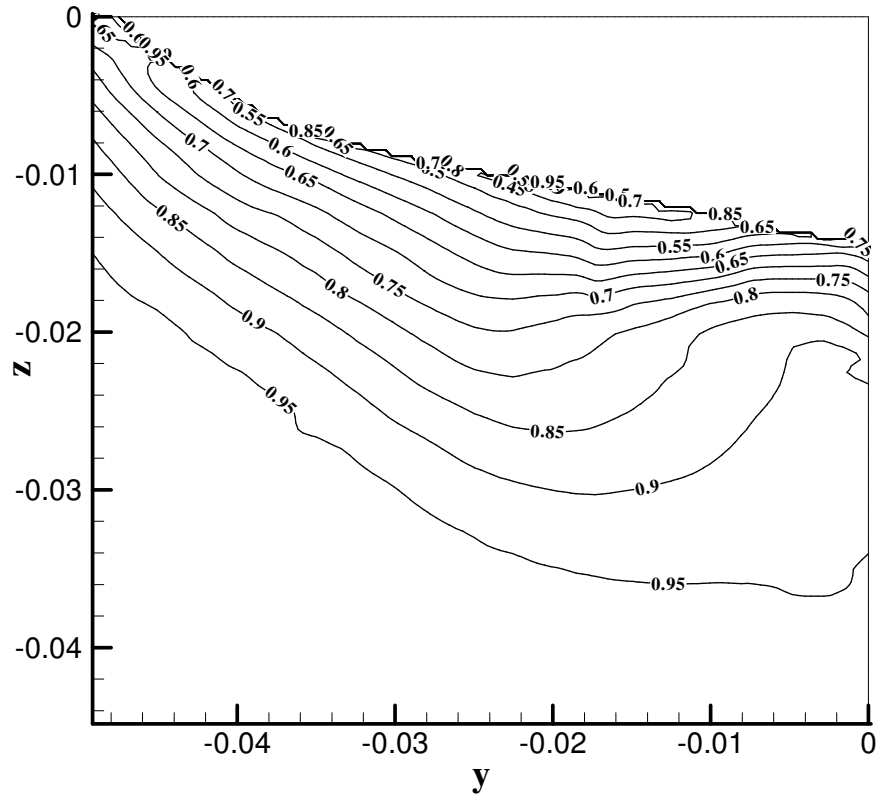
Figure 86 measured longitudinal velocity contour, t=0.75

The comparison of velocity V contours is shown in Figure 87-Figure 88. The ranges of the contours are close from 0-0.03. The lateral velocity is much smaller than the longitudinal velocity due to symmetry condition at the centre plane. As we can see, the overall agreement between calculation and measurement is reasonable. However, it is noticed that the computed results are not as sharp as the data. It seems that the computed results are suffering from numerical diffusion.
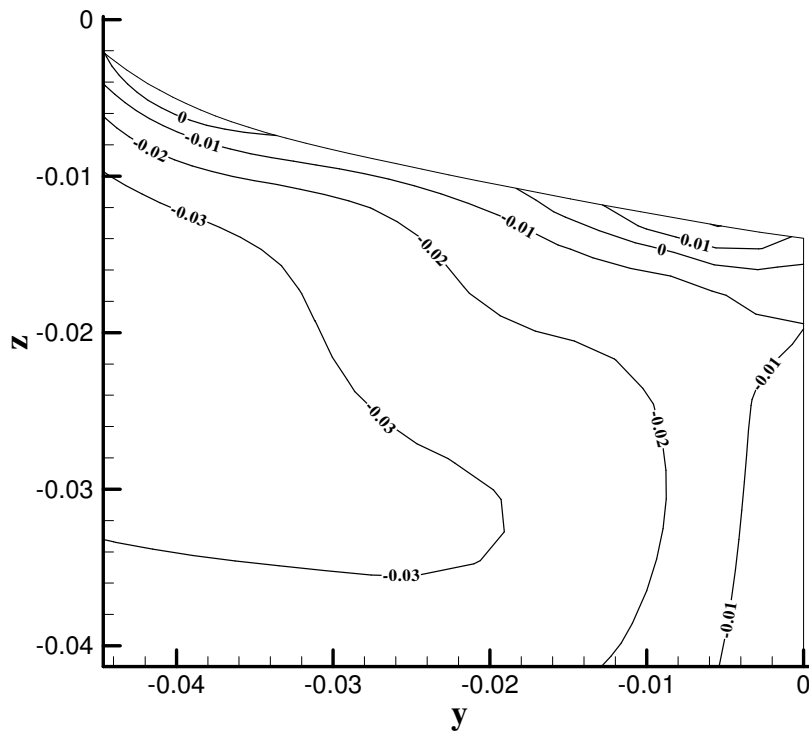
Figure 87 computed lateral V contour
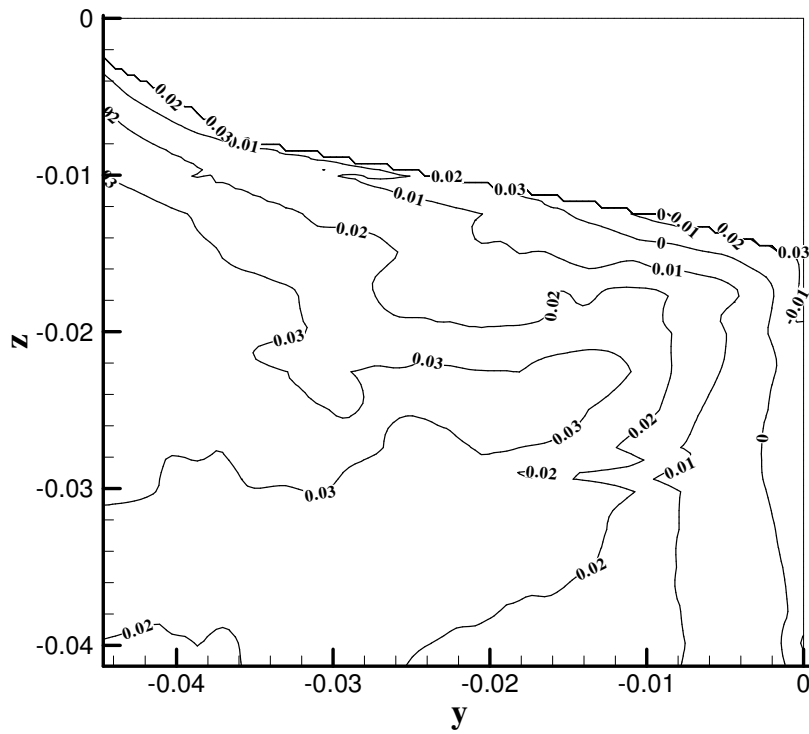
Figure 88 measured lateral V contour, t=0.75

The comparison of velocity W contours is shown in Figure 89-Figure 90. The ranges of w contours are 0-0.14. Velocity component W is larger than component V. As we can see, the overall agreement between calculation and measurement is reasonable. However, like velocity V, the computed results are overly smooth.
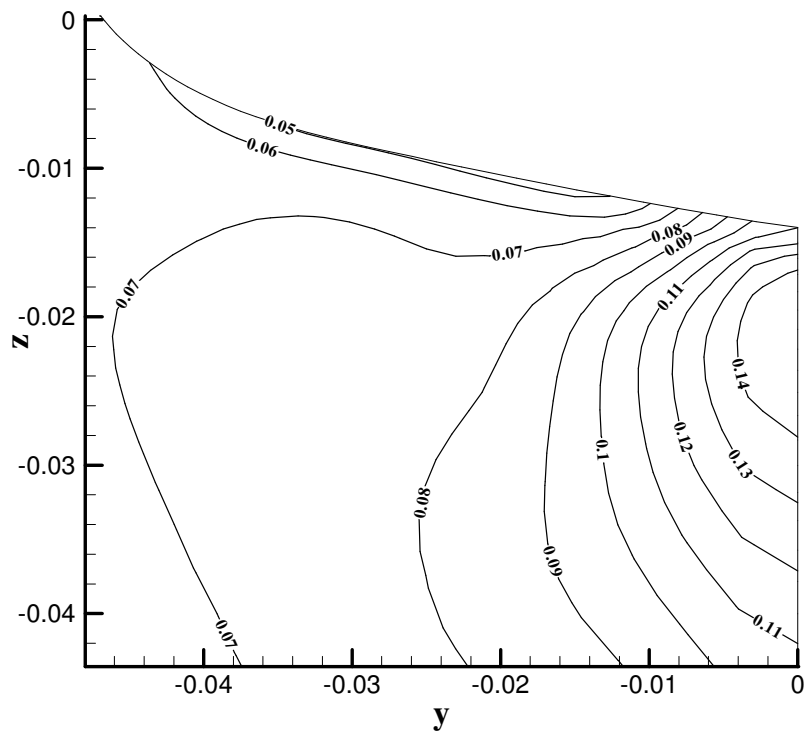
Figure 89 computed vertical velocity W contour

Figure 90 measured vertical velocity W contour, t=0.75

The comparison of wave elevations is shown in Figure 91-Figure 92. The measured bow wave, stern wave and interaction with incident wave are all correctly reproduced in the calculation. However, the agreement of the wave patterns between calculation and measurement is not as good as that in the calm water. Some discrepancies are noticed. It seems a small phase lag exists between the computed and the measured wave pattern.

Figure 91 Computed wave elevation

Where X and Y are longitudinal and lateral coordinates nondimensioned by ship length.
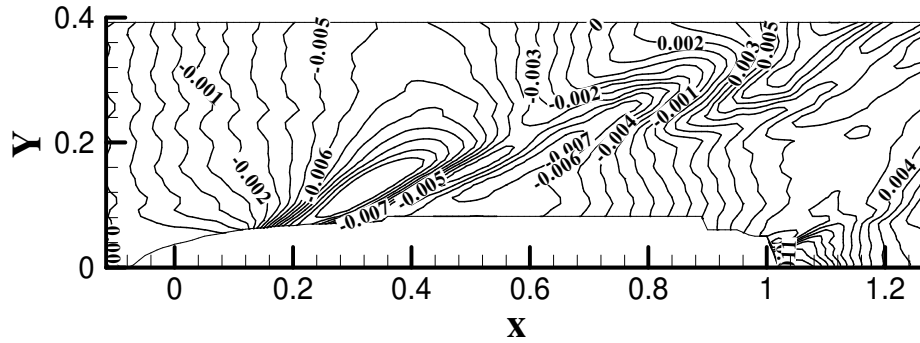
Figure 92 Measured wave elevation

9.1.2 Concluding Remarks

In summary, the numerical simulation of the wave diffraction was performed by the RANS approach. A comparison between the computed and the measured results on the test case DTMB5415 was made. The results of 1st amplitudes show that good agreement was obtained for the surge force and the pitch moment. However, the computed heave amplitude was underestimated.

The results of 1st phases show that the phase angles are close between calculation and measurement.

The difference of 0th amplitude of surge forces is up to 7.1%. The measurement results seem to be undervalued.

Comparisons between velocity contours and wave pattern show that there is overall acceptable agreement between calculation and measurement. However, some discrepancies were observed. It seems that there is a lag in the sampling time between calculation and measurement.

9.2   Roll decay

The roll damping coefficient (and added inertial moment, natural roll frequency) is essential for the accurate prediction of ship roll motion. Traditionally, it is obtained from free roll decay tests (without forward speed). In a free roll decay test, the ship model is released from an initial roll angle and then start to roll freely. The time series of roll angle is recorded and then used for subsequent analysis. From the results of free roll decay tests the natural roll period can be obtained. Roll damping coefficient as well as added inertial moment can be computed.

The free roll test at zero speed is normally conducted in a wave basin. If the influence of the forward speed is to be taken into account, free roll test needs to be performed in a long towing tank.

From the point of view of seakeeping analysis, it is of great interest to simulate free roll test with a forward speed using the RANS approach. In this research, the numerical results of roll decay will be presented. Comparisons between calculation and measurement of roll decay history, velocity distribution and longitudinal force will then be made.

The model tests were carried out by IIHR, University of IOWA [76]. The model used is DTMB5415 as described in the calculation of resistance. The model includes bilge keels. The geometry with the bilge keel is shown in Figure 93.
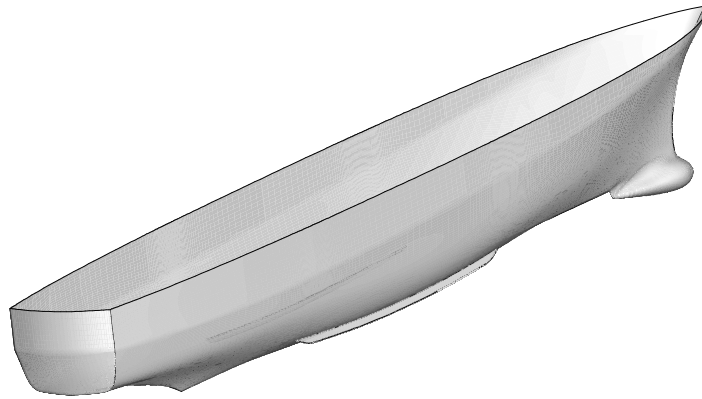
Figure 93 DTMB model with bilge keels

The main description of roll decay test is given below:

- Bare hull with bilge keels

- Towing condition in calm water

- Sinkage: s = 2.93×10^{-4}

- Trim: t = -3.47×10-2°

- The model speed is 1.53m/s

- The Froude number is 0.138

- The Reynolds number is 2.56×106

- The initial roll angle is 10 degrees

9.2.1   Mesh

To ensure the quality of meshes, techniques of multi-block and hybrid grids are employed. In most blocks, high quality structured meshes are generated. In a few blocks with geometric complexity, unstructured meshes are generated.

The total cell number is about 3.5M. There are around 10 cells over the width of each side of the bilge keel. More cells are distributed along the circumferential direction than the calculation without the bilge keel to maintain a reasonable aspect ratio.

The mesh was generated by GAMBIT 2.4.6. A sketch of the front body meshes can be seen in Figure 94.
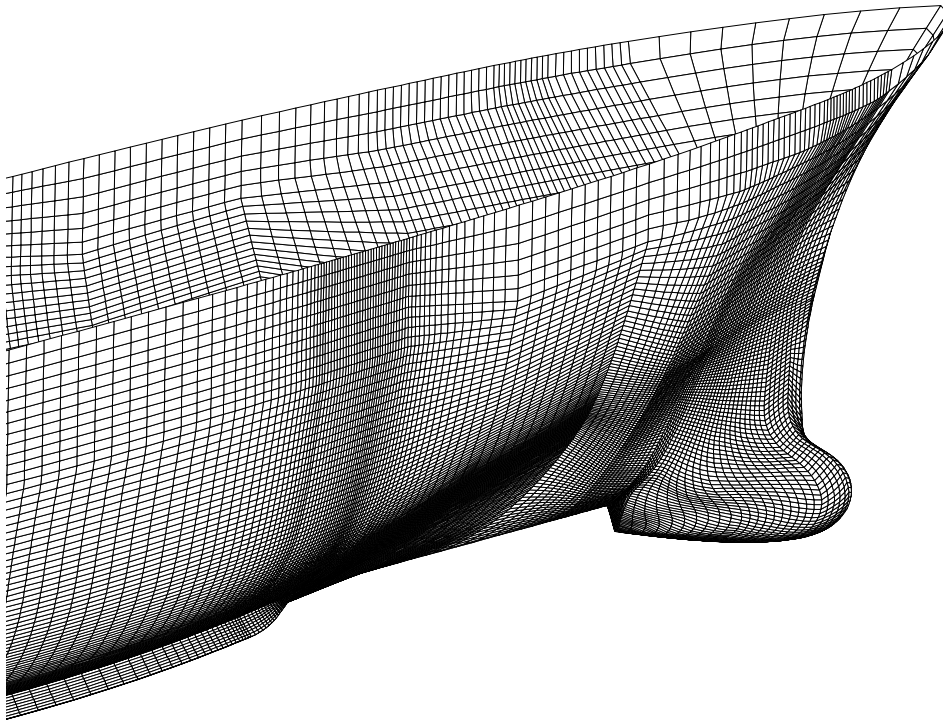
Figure 94 Surface mesh of front body

To simulate free roll motion, a grid interface with the shape of a cylinder around roll axis as shown in Figure 95 was created. Inside the cylinder, the meshes are moving rigidly with the roll motion. Outside the cylinder, the meshes are static so that the external boundary condition can be imposed easily and accurately.
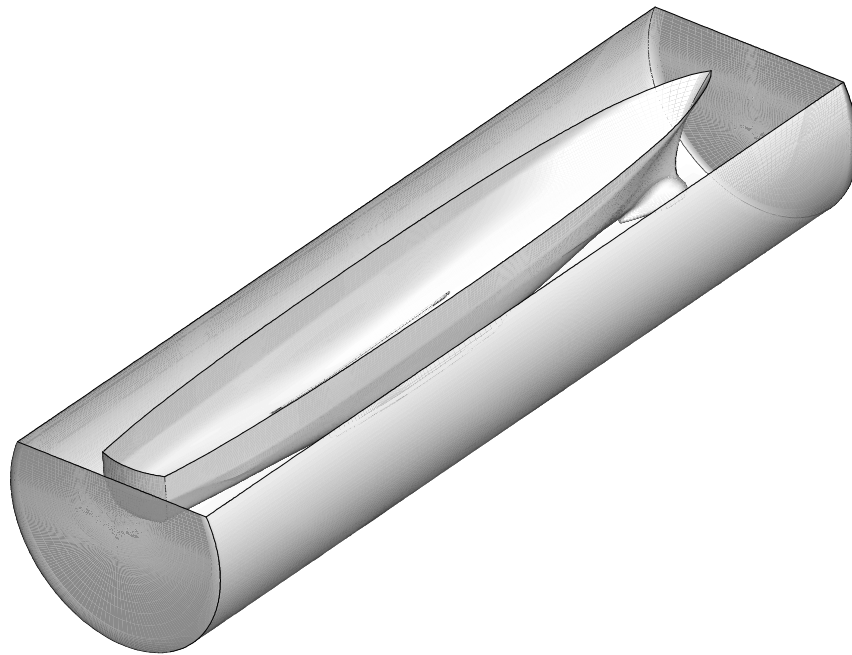
Figure 95 View of grid interface

9.2.2 Calculations of roll decay

The calculation starts from a steady forward speed without roll. After time 12L/U (roughly flow sweeps the whole domain 3 times) and steady solution is converged, free roll motion is then released.

The simulation of roll decay was made using the RANS method. The roll moment was obtained at each time step by integrating the forces on the hull along with the forces on the bilge keel. The total roll moment was then used to solve the roll equation.

The roll equation is written as:

$$I_4 \, d\omega/dt = K - mg \times GM \times \sin(\alpha)$$

Where:

I_4 moment of inertia for roll

K computed hydrodynamic roll moment

$mg \times GM \times \sin(\alpha)$ Righting moment

$I_4 = m(K_{xx}B)^2$

$K_{xx}=0.37$

The roll equation is solved by Crank-Nicolson method as shown below:

$$\omega^{n+1} - \omega^n/\Delta t = (M^{n+1} + M^n)/I_4/2$$

Where

$$M = K - mg \times GM \times \sin(\alpha)$$

The time step is 0.005s. It took about 5 days to run five roll periods on an HPC using 8 cores.

The computational results are presented below and compared with the experimental results available.

The comparison of roll decay time records is given in Figure 96.

It can be seen that the computed roll decay is generally consistent with the measured one. In the first 3 periods of roll decay, the agreement of phase angle is satisfactory. With time, accumulation of phase difference is noticeable.

The computed roll amplitudes are slightly higher than the measured results. After three periods, the amplitudes become close but the phase difference grows larger.

A difference in time histories of roll decay between calculation and measurement is noticed. As there is transverse flow separation from the oscillatory roll motion, the error in roll moment may be attributed to the turbulence model.
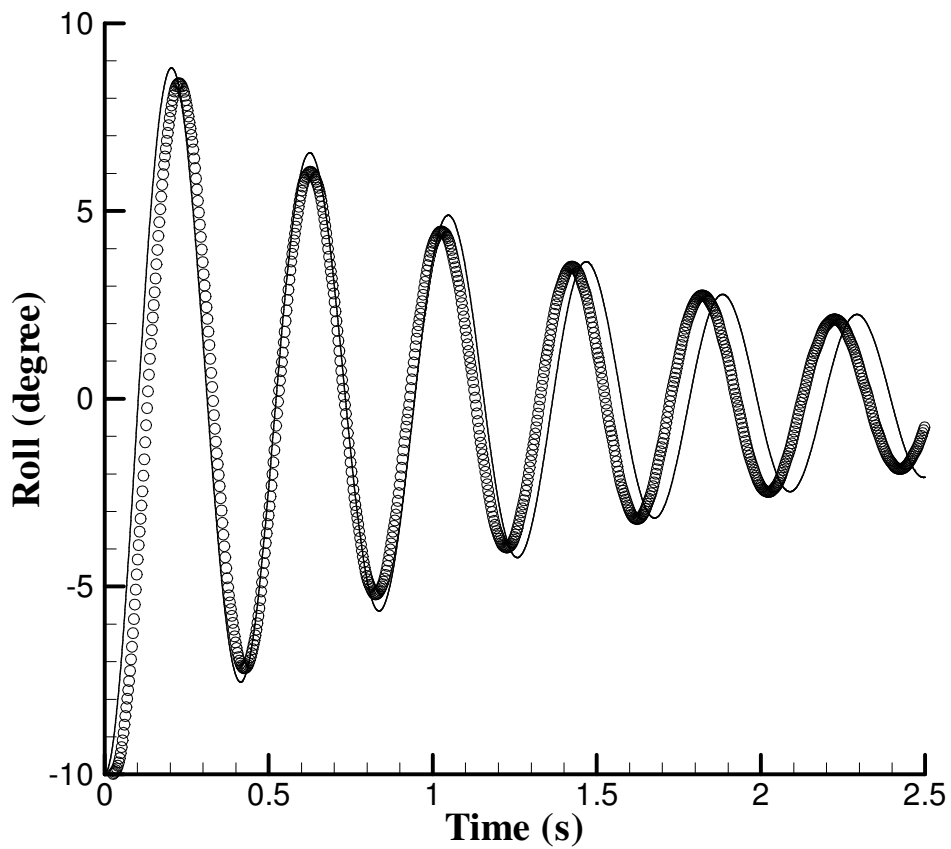
Figure 96 Roll decay record (Line: present, Symbol: Longo)

Comparison of the velocity components at the start of second period at x/Lpp=0.675 are given in Figure 97-103.

It can be seen from Figure 97-Figure 98 that the computed axial velocity contour agrees well with the measured data. The shape of contour is clearly deformed due to the presence of the bilge keel. The cross-vortices are generated at the leeside of bilge keel, thus significantly changing the longitudinal velocity. The computed velocity contour is smooth; however, the measured results show some disturbance (noise).
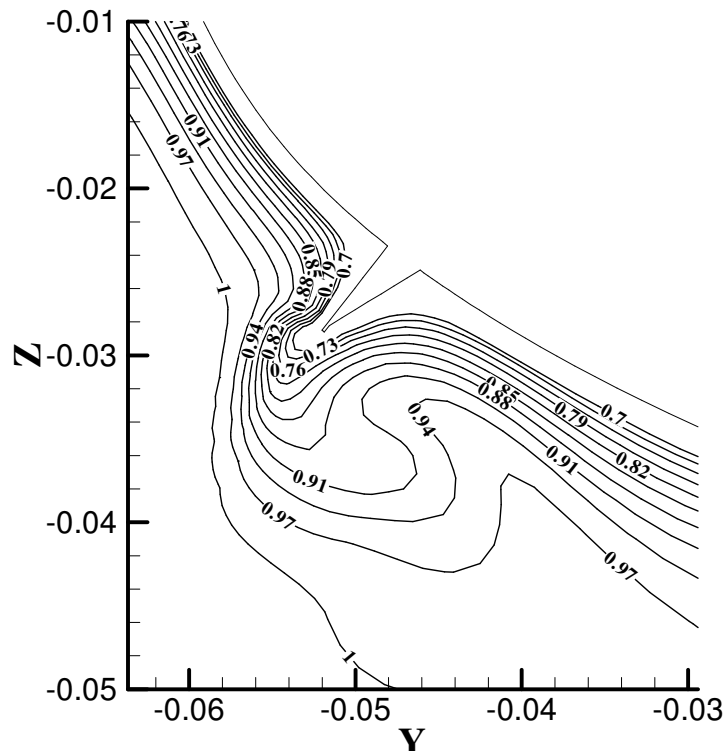
Figure 97 Computed longitudinal velicty U contour

Where Y and Z are lateral and vertical coordinates nondimensioned by ship length

Figure 98 Measured longitudinal velocity U contour

A comparison of velocity v contours in Figure 99-Figure 100 shows that areas of negative and positive V velocity are close in calculation and measurement. However, a few contour levels in the data are missing in the calculations. It is hard to conclude that whether the difference is due to the numerical diffusion in the calculation or the noise of data sampling from the measurement.

Figure 99 Computed lateral velocity V contour
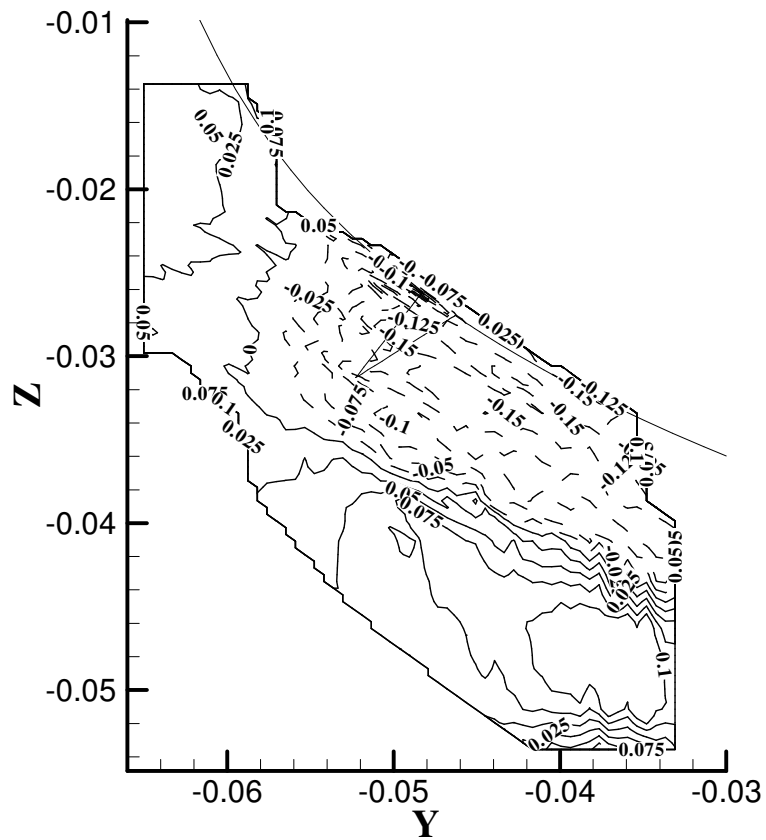
Figure 100 Measured lateral velocity V contour

Comparison of w velocity contours is given in Figure 101-Figure 102. There is good overall agreement between calculations and measurements. Three separate patches of the contour are close in the simulation and data. Again, a difference can be noticed concerning the smoothness of the computed and the measured contours.

179
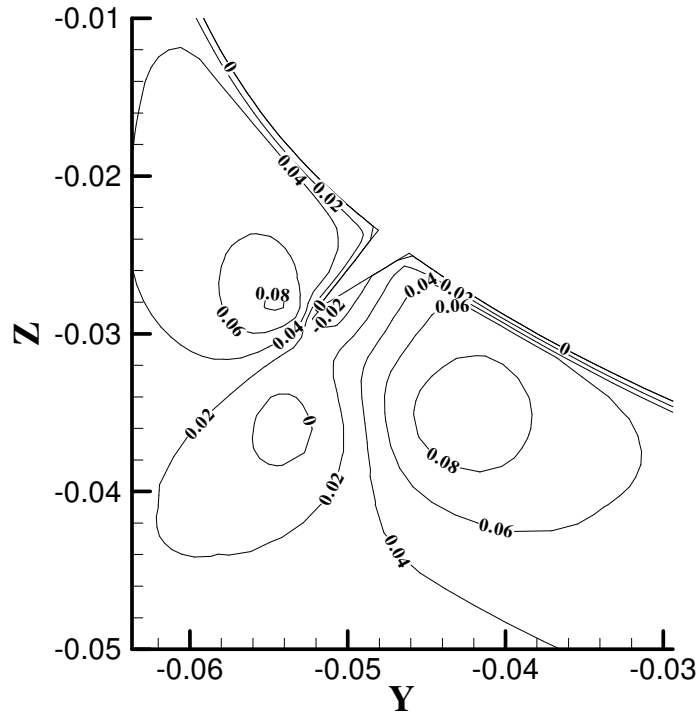
Figure 101 Computed vertical velocity W contour
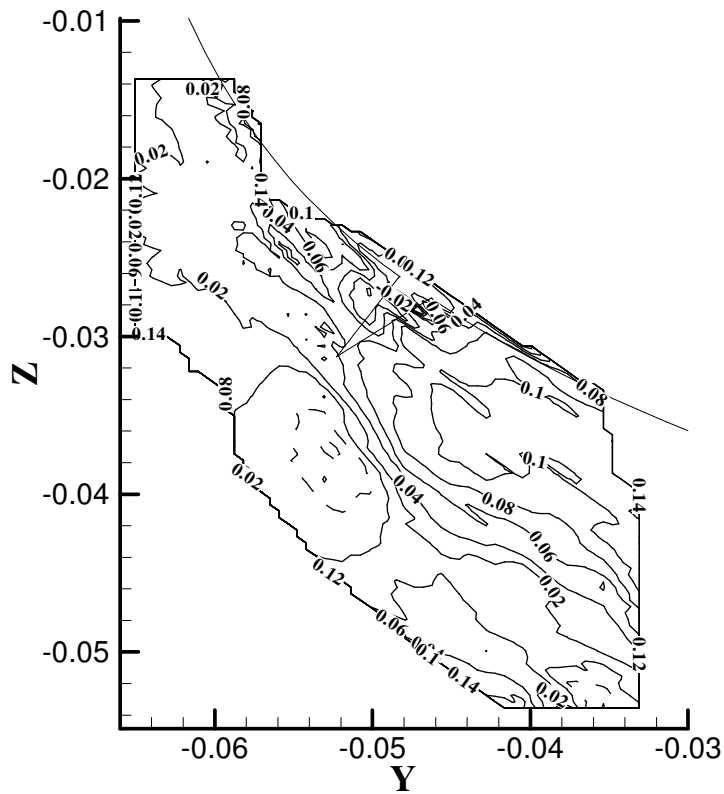
Figure 102 Measured vertical velocity W contour

A comparison of longitudinal forces is shown in Figure 103. As can be seen from the plot, the measured surge force is oscillating violently around the computed one. The computed longitudinal force is smooth and shows limited roll effects. The main part of surge force is from steady forward resistance. However, the data is highly scattered and the amplitude of oscillation is very high. We cannot draw any conclusions of the roll effect on the longitudinal force from the measured data. A proper data filter is needed. The computed force is consistent with the mean value from the measured data.
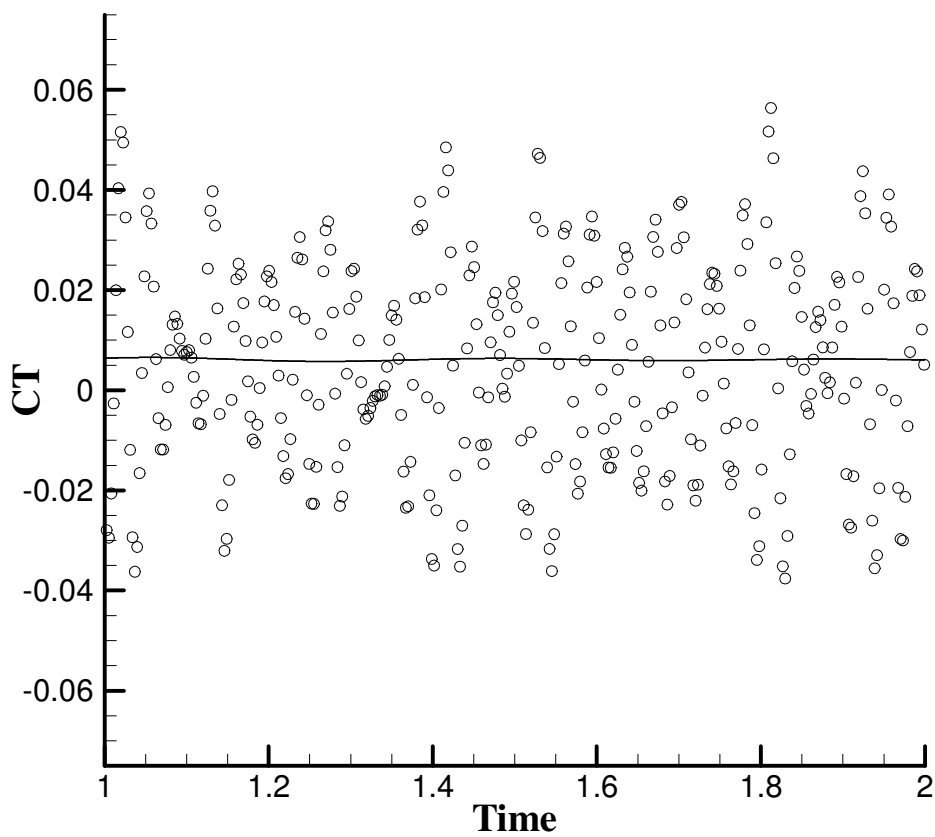
Figure 103 Resistance coefficient (line: calculation, dot: model test)

9.2.3   Roll Coefficients

With the predicted roll moment history, we can derive the natural roll period and the coefficients of the roll motion, i.e. the added moment of inertial and damping moment coefficients.

The equation of roll motion can be written as shown below:

$$(I + I_{44})\frac{\partial^2 \theta}{\partial t^2} + B_{44}\frac{\partial \theta}{\partial t} + Mg \times \overline{GM} \times \sin(\theta) = 0.$$

For small roll motion amplitudes, the equation can be approximated as:

$$(I + I_{44})\frac{\partial^2 \theta}{\partial t^2} + B_{44}\frac{\partial \theta}{\partial t} + Mg \times \overline{GM} \times \theta = 0.$$

The equation can be rearranged as:

$$\frac{\partial^2 \theta}{\partial t^2} + 2\zeta\omega_0 \frac{\partial \theta}{\partial t} + \omega_0^2 \theta = 0.$$

Where

$$\omega_0 = \sqrt{\frac{Mg \times \overline{GM}}{I + I_{44}}}$$

$$\zeta = \frac{B_{44}}{2(I + I_{44})\omega_0}$$

The solution of the equation can be found as shown below:

$$\theta = e^{-\zeta\omega_0 t}(A\cos(\omega_d t) + B\sin(\omega_d t))$$

Where

$$A = \theta_{t=0.}$$

$$B = \frac{\zeta \omega_0 \theta_{t=0.}}{\omega_d}$$

$$\omega_d = \omega_0 \sqrt{1 - \zeta^2}$$

The following observation can be made from the relationship of roll angle:

Natural roll angular frequency ω_0 is a function of righting moment and moment of inertia. The larger the added and hull moment of inertia is, the smaller the angular frequency or the larger the roll period, i.e. slower roll motion. Meanwhile, the larger the righting moment i.e. GM is, the higher the angular frequency is. The roll motion is fast.

The natural damped roll angular frequency ω_d is a function of the un-damped angular frequency ω_0 and the dimensionless damping coefficient. It is linearly proportional with the angular frequency ω_0 and inversely proportional with the damping coefficient. The larger the damping is, the smaller the damped roll angular frequency ω_d, i.e. the slower the roll motion is.

The decay of roll is dependent on both the damping and the natural angular frequency: the larger the damping is, the slower the roll decay is; the larger the natural angular frequency is, the quicker the roll decay is. But the decay in one period is only dependent on the damping coefficient.

There are two orthogonal components in roll motion. The phase angle is determined by the damping coefficient. The larger the damping is, the larger the phase angle is.

We can easily find mass moment of the added inertia and damping by applying the relationship of roll angle at the two instants.

In this research, we adopted a reliable method to obtain roll coefficients, i.e. Least Squares Fit.

From the equation of roll motion, roll speed and acceleration are obtained by the central difference scheme:

$$\frac{\partial^2 \theta}{\partial t^2} = \frac{\theta(t_{i+1}) + \theta(t_{i-1}) - 2\theta(t_i)}{\Delta t^2}$$

$$\frac{\partial \theta}{\partial t} = \frac{\theta(t_{i+1}) - \theta(t_{i-1})}{2\Delta t}$$

Using the input of GM, the ship radius of gyration and the computed roll decay time series, we can obtain the added inertia and damping of the ship by LSF. The results are given below:

$A_{44}=0.54$

$B_{44}=0.84$

The added inertial and damping coefficients are obtained in a dimensionless form as shown below.

$$a_\phi = \frac{a_\phi}{\rho \cdot \nabla \cdot B^2}$$

$$b_\phi = \frac{b_\phi}{\rho \cdot \nabla \cdot B^2 \sqrt{\dfrac{2 \cdot g}{B}}}$$

The hydrodynamic coefficients a44 and b44 are 0.039 and 0.0087, respectively.

To compare the hydrodynamic coefficients computed by roll decay and forced roll oscillation, the numerical simulation of forced roll motion was made. The amplitude of roll motion is 10 degrees and frequency is 0.595, which are the same as that from roll decay. The total, hydrostatic and hydrodynamic roll moments were calculated. The hydrodynamic roll moment is used to obtain added inertial and damping moments, which are 1.47 and 0.54 respectively. The amplitudes of roll velocity and acceleration are 0.65m/s and 2.44m/s^2, which give the added inertia and damping of

the ship 0.6 and 0.83. The hydrodynamic coefficients a44 and b44 are 0.043 and 0.0086 respectively from forced roll oscillation. Thus, the added inertial coefficient from forced roll motion is 10% higher than from roll decay while damping coefficient is close.

9.2.4   Concluding Remarks

In summary, the numerical simulation of free roll decay with a forward speed was achieved using the RANS approach. The RANS solver is coupled with a program of roll motion. The computed results of the test case DTMB5415 with a bilge keel were compared with measured data.

Computed roll decay time record is consistent with measurement. Overall, computed velocity field agrees reasonably well with data. The computed results are overly smooth. Contrary to this, the measured results are overly noisy.

The measured longitudinal force oscillates near the computed results. The computed longitudinal force shows limited roll effects. The scattering of measurement data is mainly due to noise and not roll motion effects. It can be concluded that free roll decay can be simulated with reasonable accuracy using a RANS solver.

10   Flooding Hydrodynamics

Flooding of a damaged ship is a unique hydrodynamic phenomenon. Water will continuously ingress and egress into the compartment through damaged openings, depending on the hydrostatic head, sloshing and incident waves. Consequently, there is steadily transfer of mass, momentum and energy between fluids in and out of the ship. Moreover, sloshing of water in the damaged compartment (s) occurs and tends to be highly nonlinear particularly in case of resonant motions. The complicated interactions of flooding, sloshing and ship motion make it extremely hard to express the flooding physics by empirical or analytical formulae. The water motion in the compartment may become totally out of phase with the exciting motion and the "accepted law" of added mass and damping may no longer apply. There is little knowledge on how pertinent parameters of flooding such as ship loading, opening configuration, environment, amplitude and frequency of ship motions affects flooding hydrodynamics.

The investigation into damage ship flooding in Ship Stability Research Centre (SSRC) started in the early 1990s using mainly experimental approaches. Different types of model test technologies were developed, including forced and free roll simulators [63].

Extensive measurements of ship hydrodynamics of roll motions at intact and damaged conditions were carried out. A large amount of data was accumulated for the understanding of the physics in damaged ship flooding and for the validation of the numerical results.

On the numerical side, there were few RANS simulations published. Woodburn et al [93] developed a coupled ship dynamics (NEREID) /Computational fluid Dynamics

(CFD) model (CFX) for assessing the survivability of a damaged Ro-Ro ferry. A series of parametric studies to study damaged Ro-Ro survivability were carried out. The predicted mass of water on deck as well as ship roll, heave and pitch were compared. The results were broadly in line with expectations or consistent with data.

The primary objective of the present work is to develop a reliable numerical approach to tackle the problem. The numerical method will be based on the solution of RANS equations. The mathematical and numerical formulations are the same as those described in the previous chapters. The main task of this research is to study the influence of flooding and sloshing on the damping moment coefficient and the added moment of inertia of roll motion with the view to improving the accuracy of numerical predictions.

The work in this section will be divided into two parts. The first is the simulation of forced roll motion of an intact ship, the second is of a damaged ship.

Details of the test cases, computational results and validation are given below.

10.1   Test case

Forced roll simulations in intact and damaged conditions were carried out using numerical Planar Motion Mechanism (PMM). The test case selected for validation is the Burgundy model in forced roll motion. There are well documented experimental data of the model available in SSRC.

The main parameters of the model are given in Table 18. The sketch of the damage model is given in Figure 104.

Table 18 Principal Dimensions of Burgundy model

Dimension	Full Scale intact	Full Scale damage	40th Scale intact	40th Scale damaged

Length (m)	60.00	60.00	1.50	1.50
Breadth (m)	27.80	27.80	0.695	0.695
Depth (m)	16.00	16.00	0.40	0.40
Draught (m)	6.25	6.25	0.15625	0.15625
KMT (m)	13.701	13.701	0.3425	0.3425
GMT (m)	0.809	-	0.0202	-
KGT (m)	12.892	-	0.3223	-
Length of Damage (m)	19.20	19.20	0.48	0.48
FW Displacement (tonnes / Kg)	9795.2	6660.7	153.05	104.07
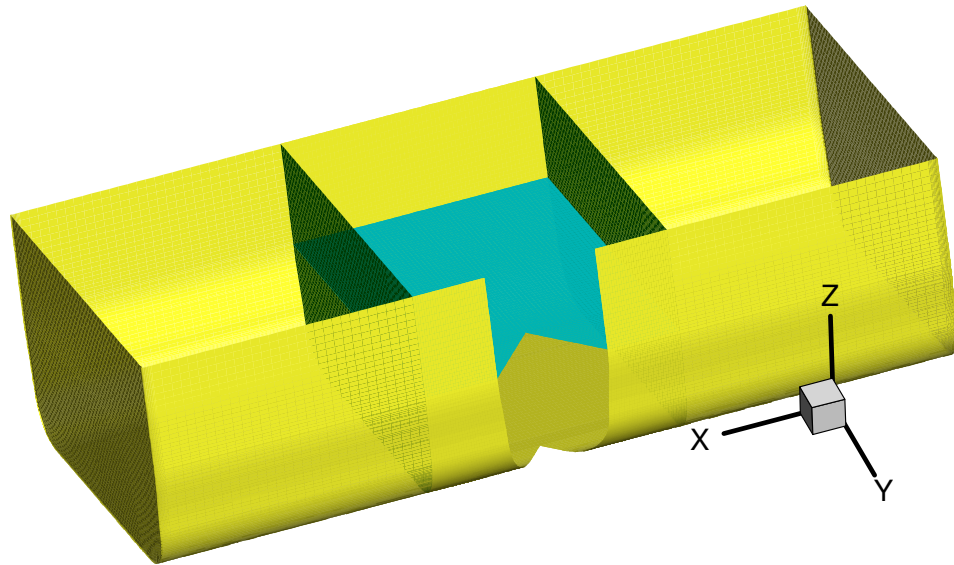
Figure 104 Sketch of SSRC Burgundy 2D model for damage survivability test

The geometry and parameters used in the numerical simulations are the same as those used in the model tests.

10.2 Description of Forced Roll Motion

The numerical forced roll motion of the Burgundy model is realised by a Planar Motion Mechanism (PMM). The PMM controller prescribes the roll angle as function of time as shown below:

$$\theta = \theta_A \sin(2\pi f t)$$

Where:

      t   Time

θ   Roll angle at time t

θ_A Roll amplitude

f   Roll frequency

The roll was designated as the rotation around the ship longitudinal axis. At time t=0, the initial roll angle is 0 degrees. Roll motion starts from a free floating position.

The roll amplitude is 10 degrees. The frequency is in the range of 0.2-2.0 Hz.

From roll angle time series, we can obtain roll velocity and acceleration:

$$r = 2\pi f \theta_A \cos(2\pi ft)$$

$$\dot{r} = -(2\pi f)^2 \theta_A \sin(2\pi ft)$$

Where:

r   Roll speed

$\dot{r}$ Roll acceleration

The amplitude of roll speed increases linearly with increasing roll frequency. The amplitude of roll acceleration increases squarely with the increase of roll frequency. There are 90 degrees of phase difference between roll velocity and roll acceleration. At phase angle zero degrees, roll velocity is maximum, however, roll acceleration is zero, where we would expect damping moment to be the largest and added moment of inertia to be zero. At phase angle 90 degrees (maximum roll angle), roll velocity is zero but roll acceleration is the largest, the added moment of inertia would be largest and damping moment would be zero.

10.3 Mesh

Mesh with cells 2.5M was generated for the simulation. The techniques of mesh generation are similar to that in the calculation of roll decay of DTMB 5415. An interface was created to separate inside grids, which will move at the roll velocity as rigid body with outside grids, which will be static.

For intact condition, the compartment is not meshed. For damaged condition, both compartment and deck are meshed.

The hull surface mesh of damage case is shown in Figure 105.
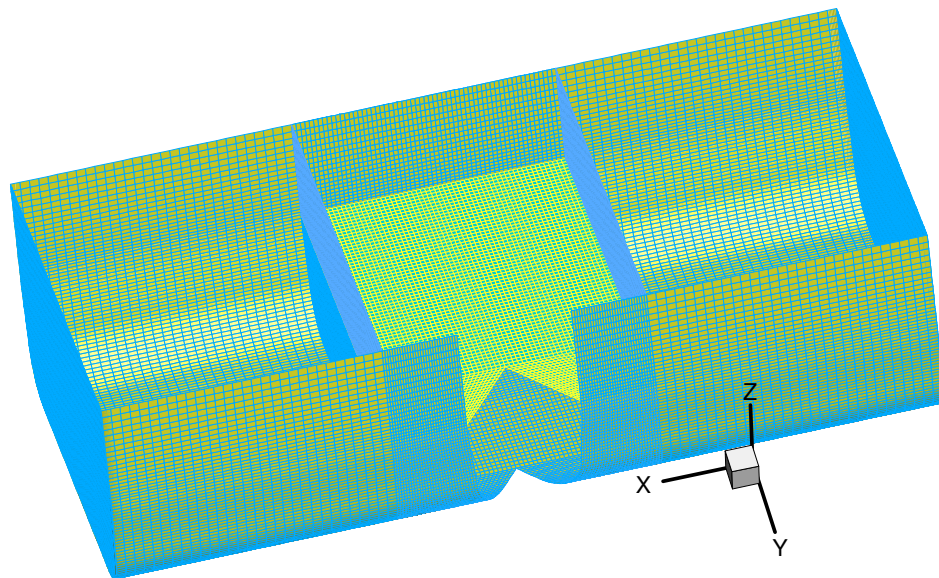
Figure 105 Surface mesh

10.4 The calculation of forced roll motion

The technique of grid interface was applied. Inner grids moves at the roll velocity while the external grids remain still. The frequency of the forced roll motion is from 0.2-1.8Hz. The time step is 0.005s for low frequency; roughly 1000 time steps in one

period. The time step is 0.003s for high frequency; roughly 200 time steps in one period. It took about 2 days for the calculation of each frequency.

The computed pressure and the friction forces (moments) were exported for analysis. The total forces and moments acting on the hull are the summation of those due to pressure and friction. The computed roll moments are traditionally separated into hydrostatic and hydrodynamic. As we know, hydrostatic roll moment is roll angle dependent and is the integration of moment due to hydrostatic pressure over the hull surface. The hydrodynamic component is roll velocity and acceleration dependent and is derived by subtracting the hydrostatic moment from the total moment. Hydrodynamic moment due to acceleration has a 90 degrees phase difference with that due to roll velocity, while it is 180 degrees phase difference with the hydrostatic moment. To separate the contribution of hydrodynamic roll moments with respect to velocity and acceleration, we need to remove the hydrostatic component from the total roll moment accurately and then apply orthogonal manipulation.

The hydrodynamic roll moment due to velocity is expressed as the product of the damping moment coefficient and roll velocity, while that due to acceleration is expressed as the product of added moment of inertia coefficient and acceleration.

The added moment of inertia and damping moment can be obtained by the FFT analysis or the least square fit (LSF). In this research, both methods were used. The results are consistent for both, therefore only the results by least square fit are presented next.

The method of evaluating roll damping moment and added moment of inertia by LSF is described next.

$$Kt=Kf+Kp$$

Where

Kt total roll moment (Nm)

Kf   roll moment due to friction

Kp   roll moment due to pressure

The total roll moment can also be written as:

Kt=Ks+Kd

Where

Ks   hydrostatic roll moment

Kd   hydrodynamic roll moment

Here, we separate hydrodynamic roll moment into two parts as shown below:

Kd=Ka+Kv

Where

Ka   hydrodynamic roll moment due to acceleration

Kv   hydrodynamic roll moment due to velocity

We have the following expression for two orthogonal components:

$$Ka = A \cdot \ddot{x}(t)$$

$$Kv = B \cdot \dot{x}(t)$$

Where

A   Added moment of inertia coefficient

B   Damping moment coefficient

The hydrodynamic roll moment can be written as:

$$Kd(t) = A \cdot \ddot{x}(t) + B \cdot \dot{x}(t)$$

The least squares fit will find values for A and B, which minimises the squared error between the computed and the estimated forcing functions.

That is, to minimize

$$\varepsilon^2 = \left[Kd(t) - A \cdot \ddot{x}(t) - B \cdot \dot{x}(t)\right]^2$$

To proceed with the method ε is differentiated with respect to A and B. Equating the derivatives to zero gives the system of equations of A and B from which we obtain the added moment of inertia and damping moment coefficients for each frequency. The method will be used in the data processing of numerical simulation. The results are presented below.

10.5   Natural roll period

The hydrodynamic roll moment is frequency dependent. When the exciting frequency is approaching the natural frequency, the phenomena of resonance will occur.

The natural period of roll motion is obtained as shown next:

The equation of roll motion is

$$I\frac{d^2\phi}{dt^2} + M = 0.$$

Where

     I   mass moment of inertia about roll axis

     M   righting moment

     ϕ Roll angle

$$I = \frac{\Delta}{g} k^2$$

Where

k   The radius of gyration of mass about the roll axis

Δ The displacement

For a small angle of inclination, $M = \Delta \overline{GZ} = \Delta \overline{GM} \sin \phi = \Delta \overline{GM} \phi$

Therefore, we have $\dfrac{d^2\phi}{dt^2} + \dfrac{g\overline{GM}}{k^2}\phi = 0.$

For the above harmonic motion the roll period is

$$T_\phi = \frac{2\pi k}{\sqrt{g\overline{GM}}}$$

Using parameters of the model, we can obtain the natural period of roll motion, which is about 1.3s or the corresponding frequency 0.78 Hz.

10.6   Intact condition

To study the effects of flooding, calculations of forced roll motion in intact conditions are made first.

The roll amplitude in the intact condition is 10 degrees. The frequency is 0.2-1.8Hz. The results are given below.

The computed forces at frequency 0.2Hz are given in Figure 106.
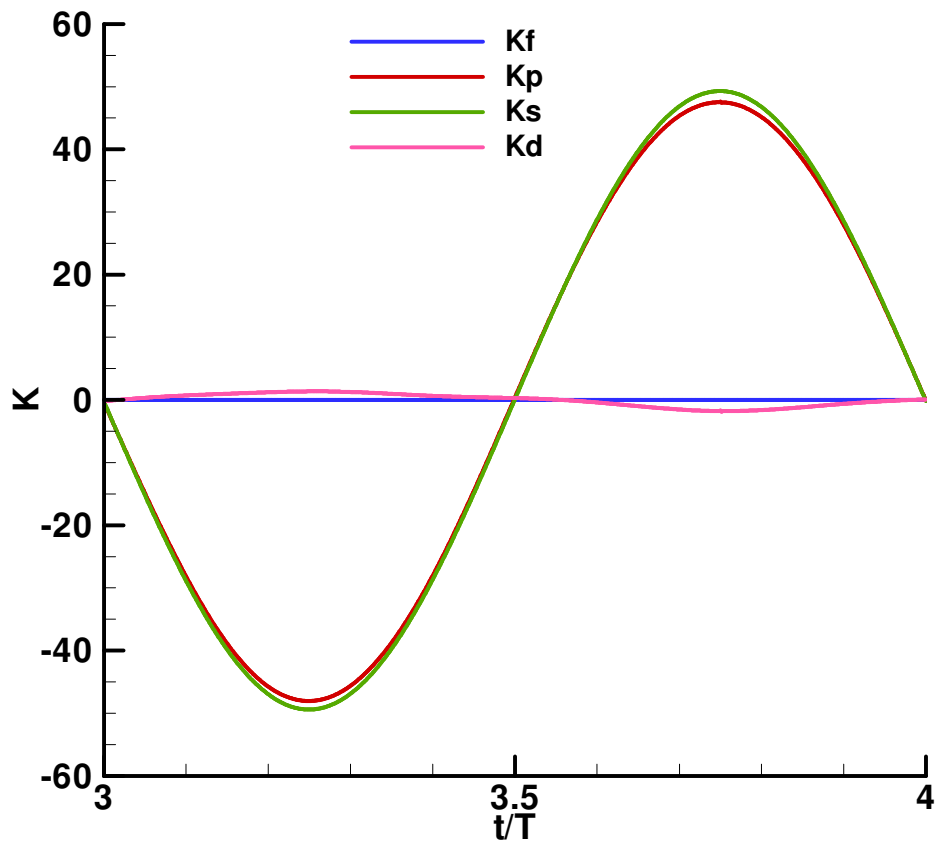
Figure 106 Computed roll moment (f=0.2)

Where

    K   roll moment (Nm)

    Kf   roll moment due to friction

    Kp   roll moment due to pressure

    Ks   hydrostatic roll moment

    Kd   hydrodynamic roll moment

In the plot above, the x axis shows the non-dimensioned time by period, while the y axis shows the roll moment in Nm. The hydrodynamic roll moments due to acceleration and velocity are not plotted separately as these can be easily estimated.

As we can see from Figure 106, there are two components in the total roll moment. The first is due to friction, which is negligibly small. The second is due to pressure, which is the main part of roll moment.

The total roll moment is separated into two parts. One is the motion dependent part (hydrodynamics) and the other is the displacement-dependent part (hydrostatics). The hydrostatic part is calculated by integrating roll moment due to hydrostatic pressure. The hydrodynamic part is extracted by subtracting the hydrostatic component from the total roll moment and is treated in the method described above.

At frequency 0.2, which is equivalent to a period of 5 seconds, the hydrodynamic roll moment is very small, about 1.3Nm compared with 50Nm of hydrostatic part. It is essential to accurately calculate the hydrostatic contribution in order to obtain the correct hydrodynamic roll moment. In small roll angles, it can be computed as shown below:

$$Ks = Mg \times KM \times \sin(\theta)$$

At low frequencies, there is 180 degrees phase difference between the hydrodynamic moment and the hydrostatic one. As we know, hydrodynamic roll moment is divided into two components. One is velocity dependent, or the damping moment part; while the other is acceleration dependent or the added moment of inertia part. The added inertial part is 180 degrees out of phase with the hydrostatic part. The damping moment is 90 degrees out of phase with the added moment of inertia. Therefore, at frequency 0.2, the damping component (roughly the value of hydrodynamic moment at t/T=3.0) is small and the added inertial part is large in the hydrodynamic roll moment.

The general observation of roll moment at low frequencies is that damping is negligibly small. The hydrodynamic roll moment is almost totally added moment of inertia.

The results of roll moment at frequency 0.4 are given in Figure 107.
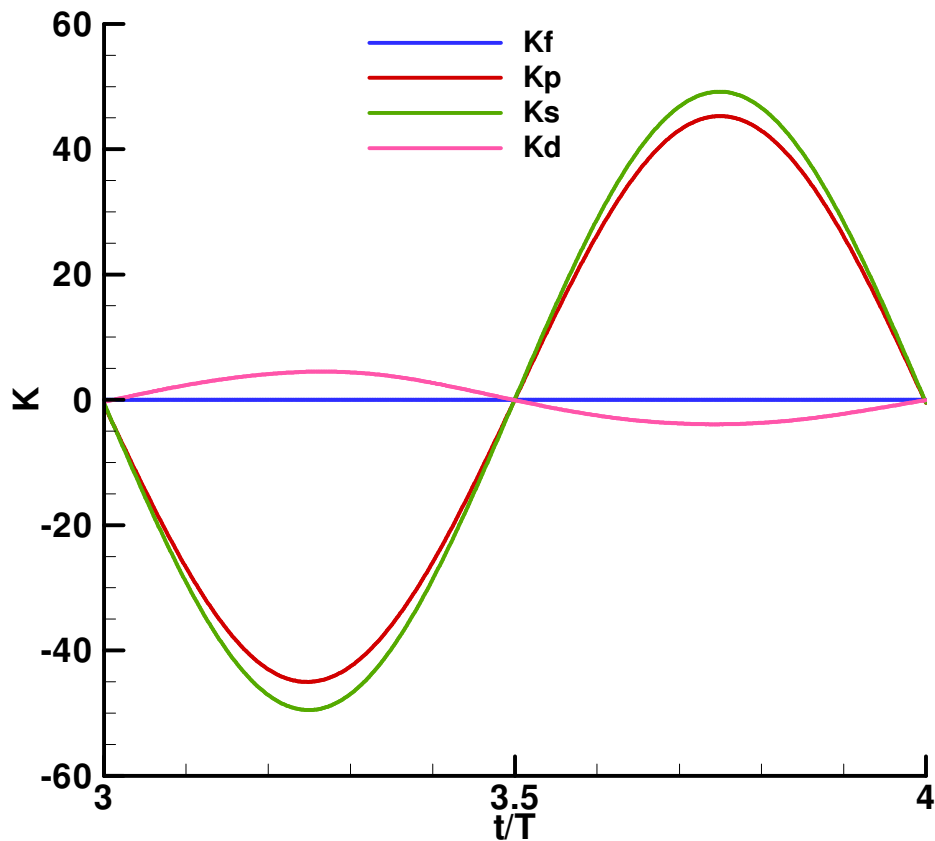
Figure 107 Computed roll moment at (f= 0.4)

At frequency 0.4, which is equivalent to a period of 2.5 seconds, the hydrodynamic roll moment is increasing with increasing frequency. The amplitude is 4.5Nm. There is a slight increase of phase difference. Damping component at this frequency is small. The added inertial moment is the main part in the hydrodynamic roll moment.

As we know, roll acceleration and velocity increases squarely and linearly with frequency, respectively. The hydrodynamic roll moment at frequency 0.4 is nearly 3.4 times of that at frequency 0.2, which is slightly less than implied by the square law.

The results of roll moment at frequency 0.6 are given in Figure 108.
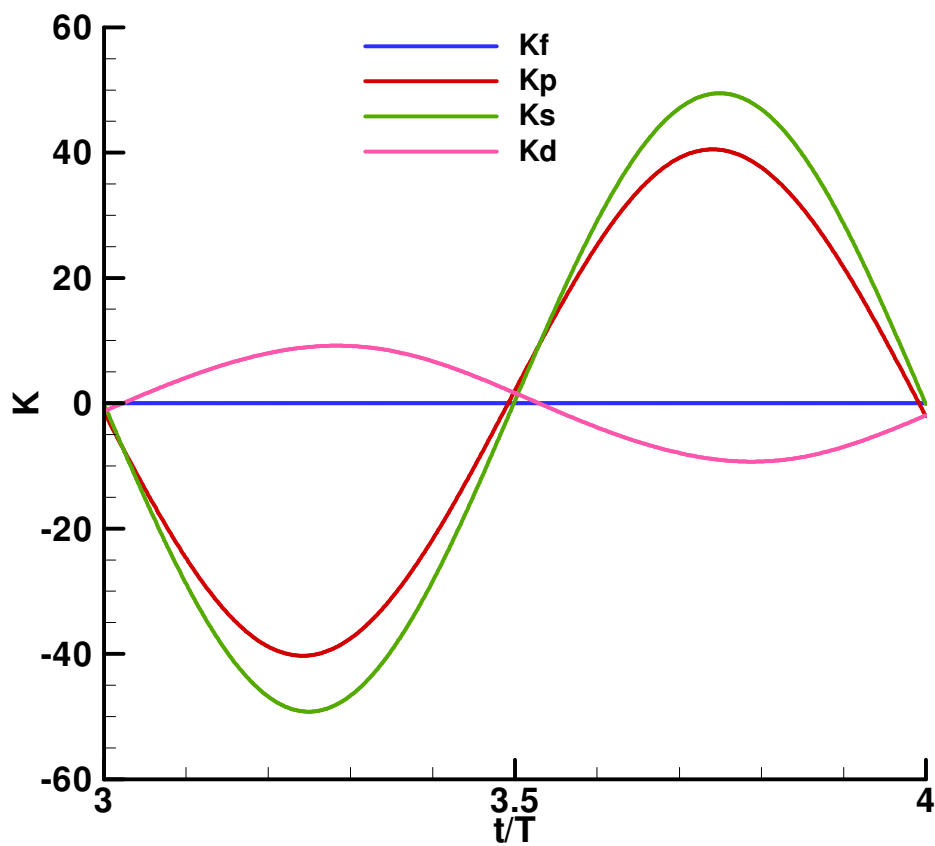
Figure 108 Computed roll moment at f=0.6

At frequency 0.6, equivalent to a period of 1.67 seconds, the hydrodynamic roll moment increases further with the increaseing frequency. The amplitude is 9.2Nm. The phase angle between the hydrostatic and the hydrodynamic moments is becoming larger. Damping component increases. The added inertial moment is the main part of the hydrodynamic roll moment at this frequency.

The hydrodynamic roll moment at frequency 0.6 is nearly 7 times that at frequency 0.2, which is slightly less than 3 squared.

The results of roll moment at frequency 0.8 are given in Figure 108.
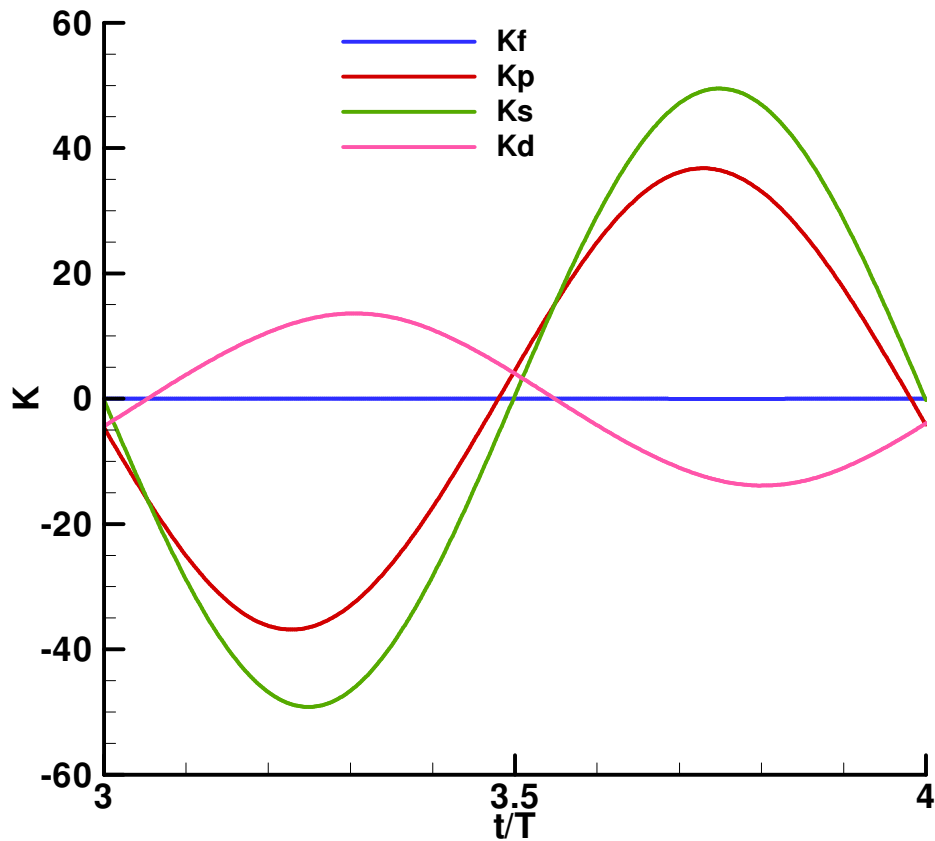
Figure 109 Computed roll moment at f=0.8

At frequency 0.8 (near natural roll frequency), which is equivalent to a period of 1.25 seconds, the hydrodynamic roll moment increases further with the increase in frequency. The amplitude is 13.7Nm. The phase angle between the hydrostatic and the hydrodynamic moments becomes larger. Damping component increases. The added inertial moment is roughly 70% of the hydrodynamic roll moment at this frequency.

The hydrodynamic roll moment at frequency 0.8 is nearly 10 times of that at frequency 0.2; lower than 4 squared.
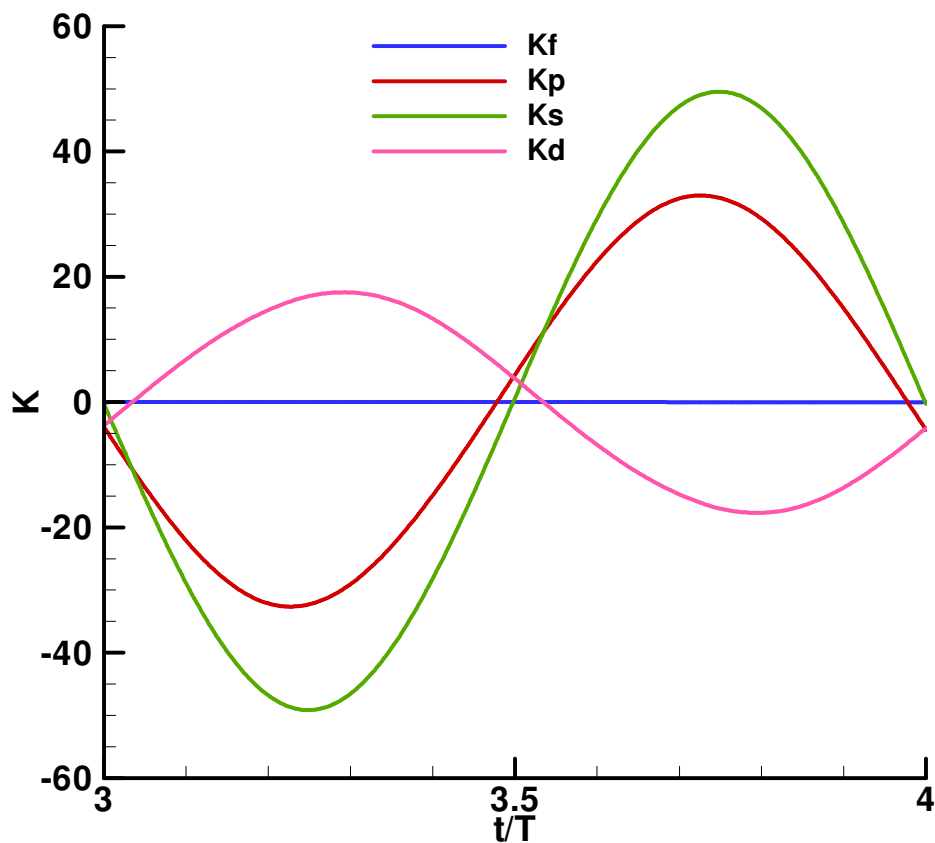
Figure 110 Computed roll moment at f=1.0

The results of roll moment at frequency 1.0 are given in Figure 108.

At frequency 1.0 (higher than natural roll frequency), equivalent to a period of 1.0 second, the hydrodynamic roll moment increases further with the increase in frequency. The amplitude is 17.6Nm. The phase angle between the hydrostatic and the hydrodynamic moments is not increasing any more but slightly decreasing. The damping component is also decreasing. The added inertia moment is 75% of the hydrodynamic roll moment at this frequency.

The hydrodynamic roll moment at frequency 1.0 is nearly 13 times of that at frequency 0.2, which is about half of 5 squared.
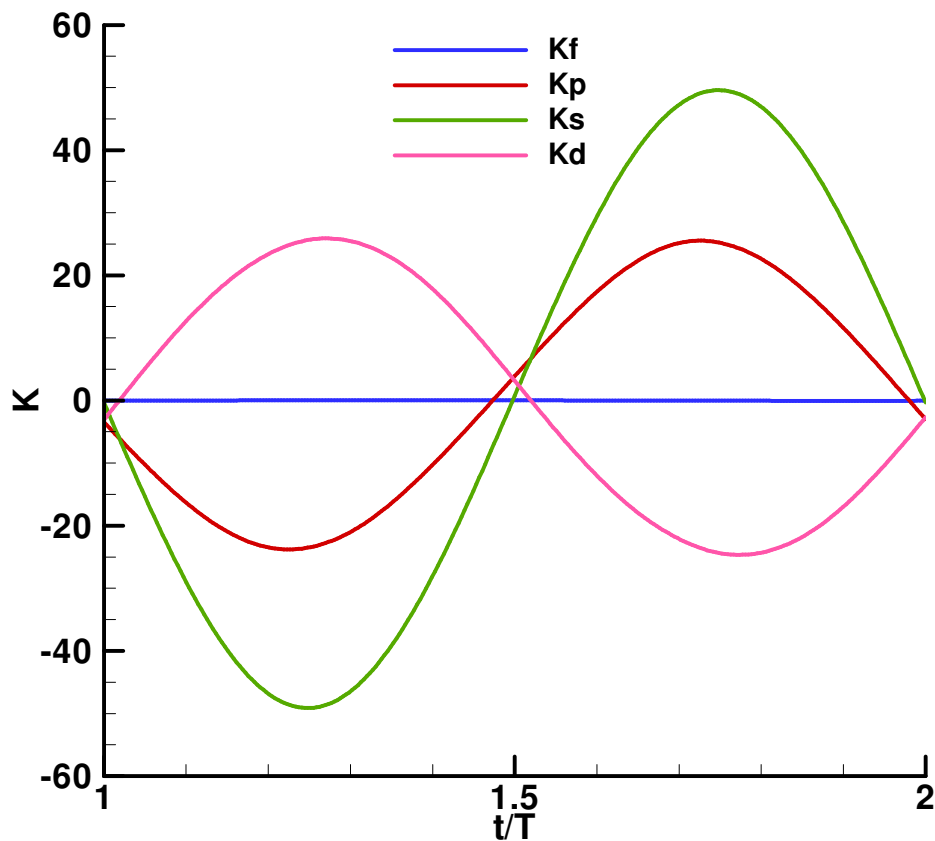
Figure 111 Computed roll moment at f=1.2

The results of roll moment at frequency 1.2 are given in Figure 10811.

At frequency 1.2, equivalent to a period of 0.83 seconds, the hydrodynamic roll moment increases further with the increase in frequency. The amplitude is 25.1Nm. The phase angle between the hydrostatic and the hydrodynamic moments is becoming smaller. Damping component is decreasing. The added inertial moment is about 80% of the hydrodynamic roll moment at this frequency.

The hydrodynamic roll moment at frequency 1.2 is nearly 18 times of that at frequency 0.2, which is just half of square of 6.
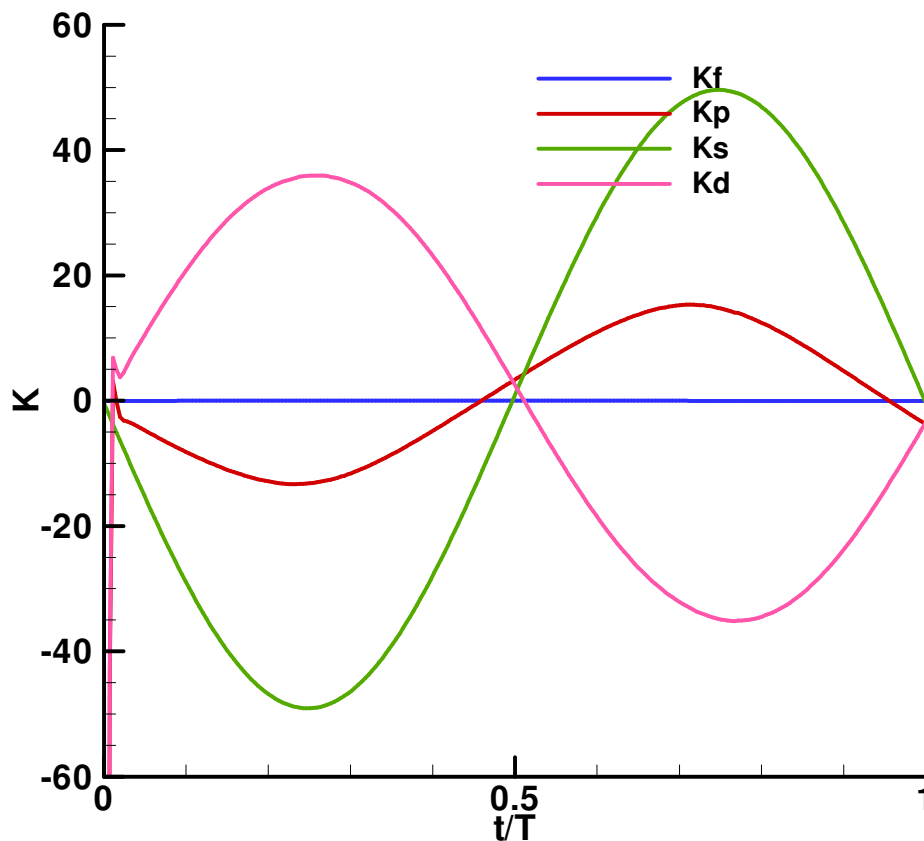
Figure 112 Computed roll moment at f=1.4

The results of roll moment at frequency 1.4 are given in Figure 108.

At frequency 1.4, equivalent to a period of 0.71 seconds, the hydrodynamic roll moment increases further with the increase in frequency. The amplitude is 35.5Nm. The phase angle between the hydrostatic and the hydrodynamic moments is becoming smaller. Damping component is decreasing. The added inertial moment is 85% of the hydrodynamic roll moment at this frequency.

At high frequency, added inertial moment is dominant. Damping component is relatively small.
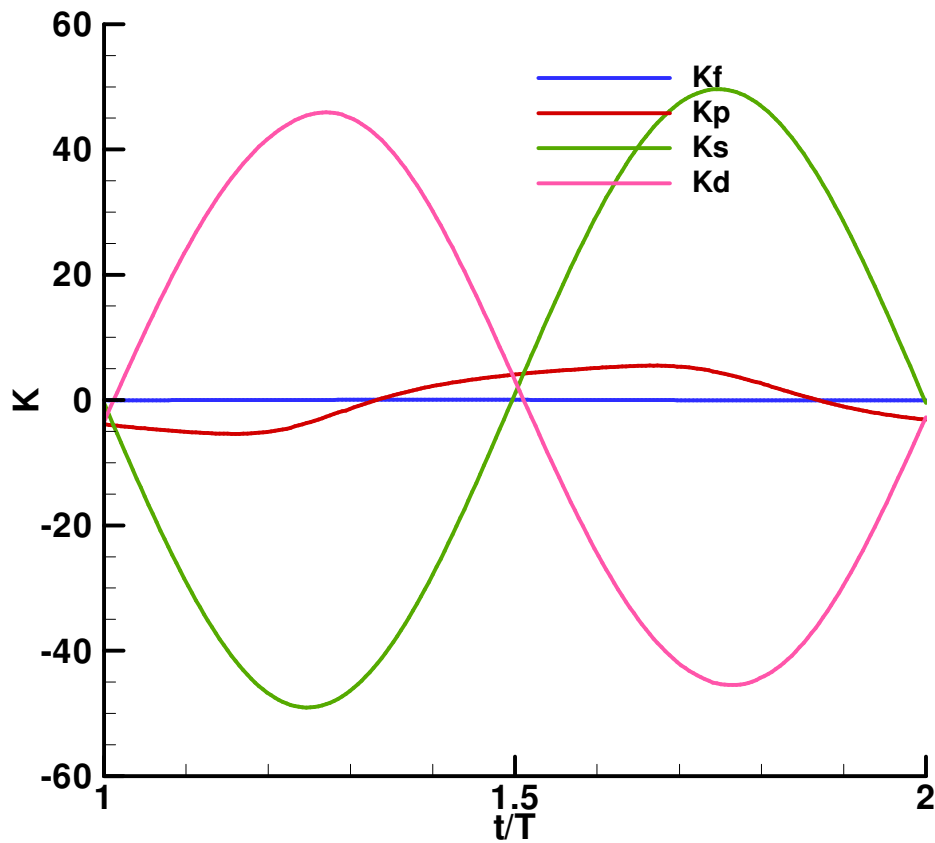
Figure 113 Computed roll moment at f=1.6

The results of roll moment at frequency 1.6 are given in Figure 113 Computed roll moment at f=1.6.

At frequency 1.6, equivalent to a period of 0.67 second, the hydrodynamic roll moment increases further with the increase in frequency. The amplitude is 46.0Nm. The phase angle between the hydrostatic and the hydrodynamic moments is nearly 180 degrees. Damping component is decreasing. The added inertial moment is the main part of the hydrodynamic roll moment.

The magnitude of total hydrodynamic roll moment is close to the hydrostatic roll moment. The total fluid moment is nearly zero. The ship is rotating in the water with little fluid resistance, thus very light, similar to being in the air. This is the unique feature of roll motion at high frequency.
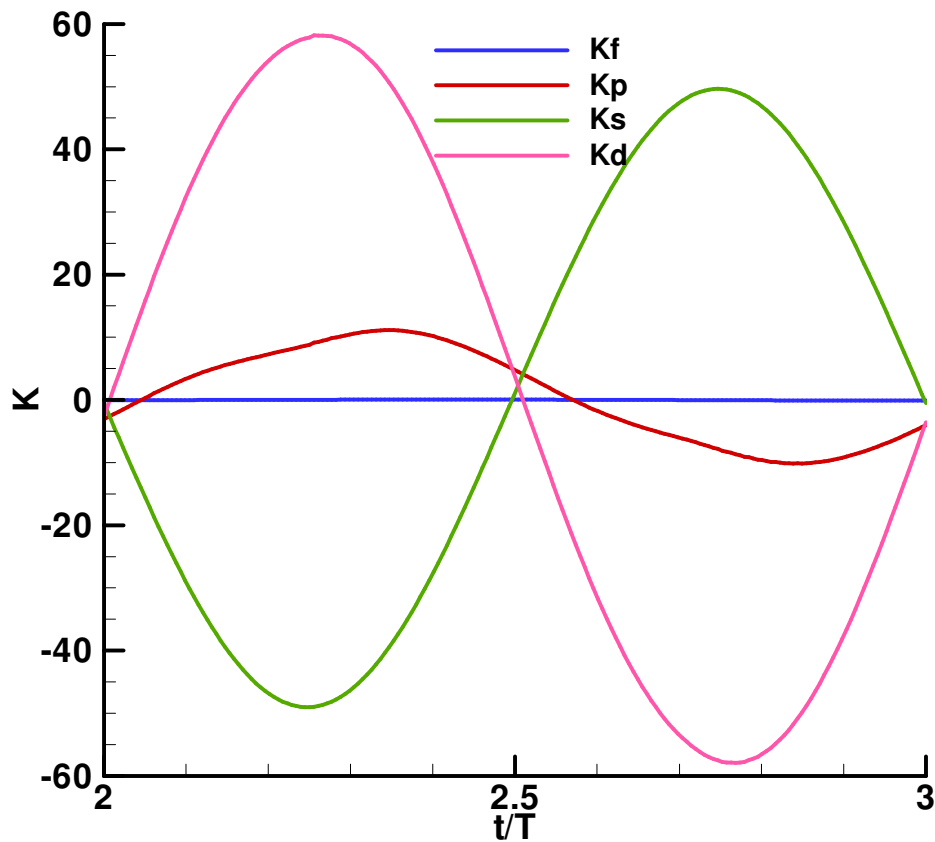
Figure 114 Computed roll moment at f=1.8

At frequency 1.8, equivalent to a period of 0.56 second, the hydrodynamic roll moment as shown in Figure 114 increases further with the increase in frequency. The amplitude is 58.0Nm. The hydrodynamic roll moment is larger than the hydrostatic part. The phase angle between the hydrostatic and the hydrodynamic moments is nearly 180 degrees. The damping component is decreasing. The added inertia moment is the main part of the hydrodynamic roll moment.

The magnitude of the total hydrodynamic roll moment is larger than the hydrostatic roll moment. The total fluid moment is in phase with the roll motion, thus accelerating the roll motion. This is the feature of hydrodynamic roll moment at very high frequencies.

10.7   Hydrodynamic coefficients

Comparisons of hydrodynamic roll moments, added inertia and damping moments can be seen in Figure 115.

It can be seen that the added moment of inertia is the main part of the hydrodynamic roll moment and increases with increasing frequency almost squarely.

The damping part increases at low frequency but reaches its maximum near frequency 0.8 (natural roll frequency). Then, the damping moment starts to decrease. As we know, the amplitude of the angular velocity increases linearly with frequency. The damping moment is not proportional to the angular velocity.
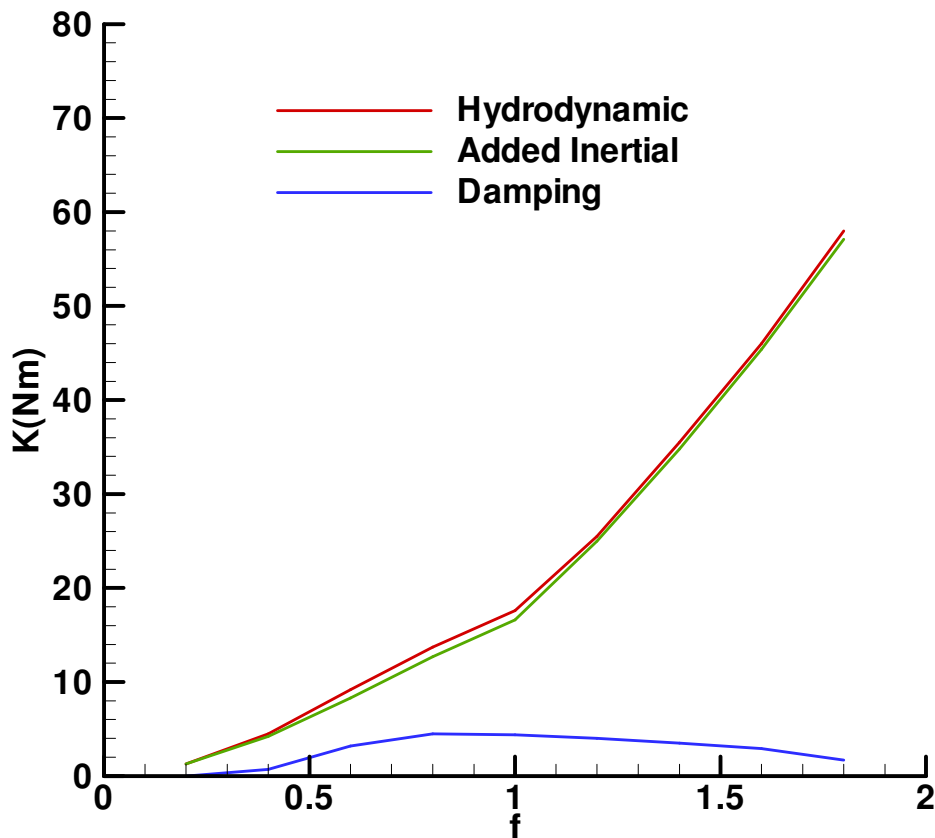
Figure 115 Comparison of components of roll moment

The coefficients of added inertia moment a_ϕ and damping moment b_ϕ are derived by dividing accelerations and angular velocity as described above and are non-dimensioned as shown below.

$$A_{44} = \frac{a_\phi}{\rho \cdot \nabla \cdot B^2}$$

$$B_{44} = \frac{b_\phi}{\rho \cdot \nabla \cdot B^2 \sqrt{\dfrac{2 \cdot g}{B}}}$$

The hydrodynamic coefficients were compared with SSRC model tests in Figure 116 Comparison of damping coefficients-Figure 117 Comparison of added moment of inertia coefficients.
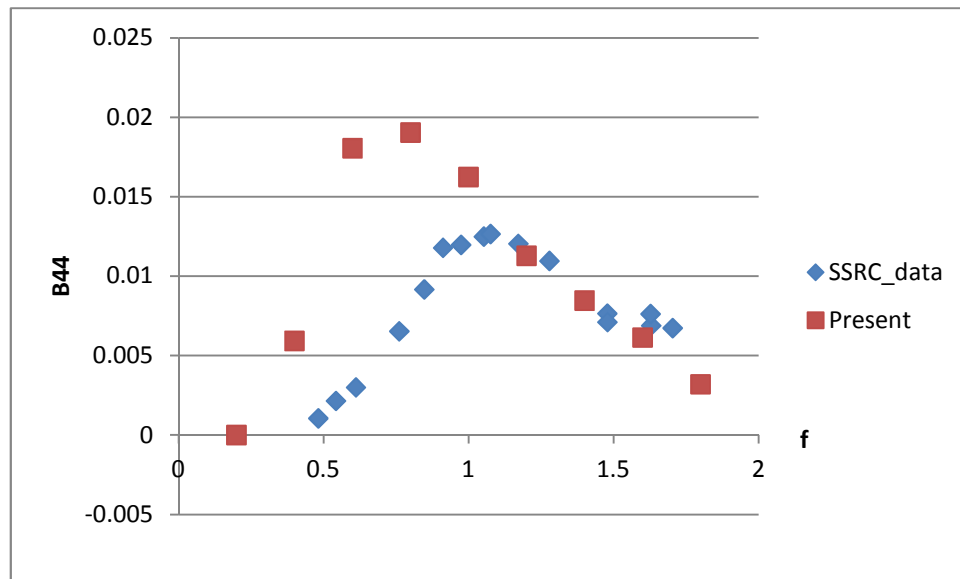
Figure 116 Comparison of damping coefficients

A comparison of damping coefficients shows that the agreement between the coefficients is good at higher frequencies. At low frequencies, the measured damping is lower than our present calculations.

At low frequencies, the uncertainty in the measurements is large. A small phase angle error could result in a large error of the damping coefficients. The measured damping is negative at the lowest frequency. This might be due to an error in post processing.
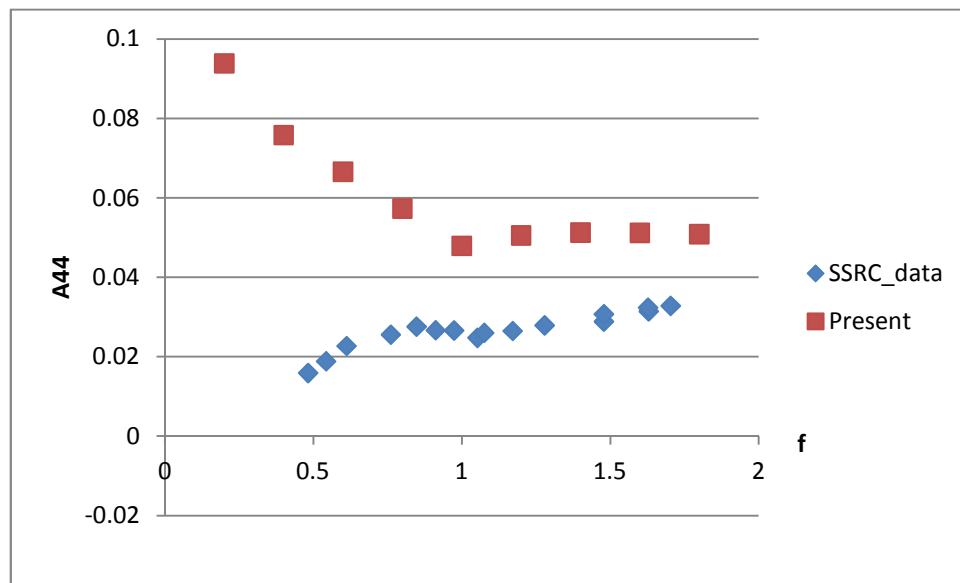
Figure 117 Comparison of added moment of inertia coefficients

The comparison of added inertial coefficients in Figure 117 shows that the trend at low frequency is not consistent. The added inertial coefficients from measurement are negative at low frequencies, then gradually increasing until it becomes flat at higher frequencies. The computed added inertial coefficients are high at low frequency and decrease until it becomes flat at higher frequencies.

The computed A44 is higher than the measured at high frequencies. The difference of A44 in the calculations and measurements may be due to the hydrostatic force. It seems that there is an underestimation of hydrostatic forces in the model test, which results in the negative A44 at low frequencies and lower value at high frequencies.

The computed wave pattern is shown below.

The wave pattern shows clearly that wave chains are generated on both sides of oscillatory hull. The wave length depends on the oscillation frequency. In the case of frequency 1.0Hz, wave length is $gT^2/2\pi$, i.e. 1.56m from deep water linear wave theory, which is close to the present numerical simulation. The wave height is related to the roll amplitude and frequency. At this frequency, wave height is about 1cm and increases with any increase in roll amplitude and frequency.

It should be mentioned that the side boundary of the computational domain is located at y=±5.0m (model is 1.5m long) where open channel flow conditions of pressure outlet are imposed that allows wave to transmit freely.
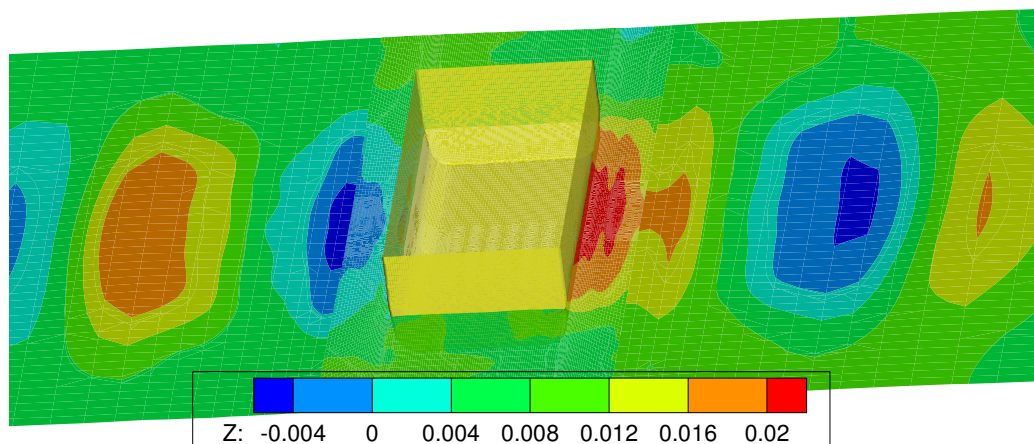
Figure 118 Wave pattern (Z: nondimensional wave height)

10.8   Forced roll in damaged condition

It is hardly possible to measure the roll moments acting on the external hull surface and the internal tank separately. In order to study the flooding and damage effects on roll hydrodynamics, the roll moment on the external hull surface and internal compartments need to be obtained. This can only be achieved by numerical simulation.

The simulations of forced roll in damage conditions were performed using the RANS approach. Similar setup and computational methods were used as in the intact condition. In the calculations, the time histories of the roll moments on the outer surface of the hull, internal compartment and deck are all computed and results are exported for comparison with those from the intact condition.

Similar to the intact condition, the hydrodynamic roll moment is extracted from the total moment by removing hydrostatic moments. The computed roll moments on the hull surface and in the compartment are presented separately as shown below.

The results of roll moments at a frequency of 0.2 are shown in Figure 119-Figure 120. The deck is dry at roll angle 10 degrees. The roll moments on the deck and upper compartment are zero, therefore only the results of roll moments in the lower compartment and the hull outer surface are presented. As can be seen from Figure 119-Figure 120, the hydrostatic roll moment at upright position (roll angle is zero) is not zero on the hull surface and the compartment (roll angle 0 degree) due to the damaged opening. However, the sum of the hydrostatic roll moment on the hull and the compartment is zero at the upright position.

At a frequency of 0.2, the hydrodynamic roll moments on both the hull and the compartment are very small. Damping component is almost zero. The added inertial moment is the main part of the hydrodynamic roll moment at this frequency. The phase difference between the hydrostatic roll moments on the hull and the compartment is 180 degrees. The total hydrostatic roll moment was reduced when compared with that from the intact condition due to flooding of the compartment.

The motion of the water in the tank is a typical sloshing problem. At frequency 0.2Hz, the sloshing effect is small, thus the hydrodynamic roll moment due to sloshing is small.
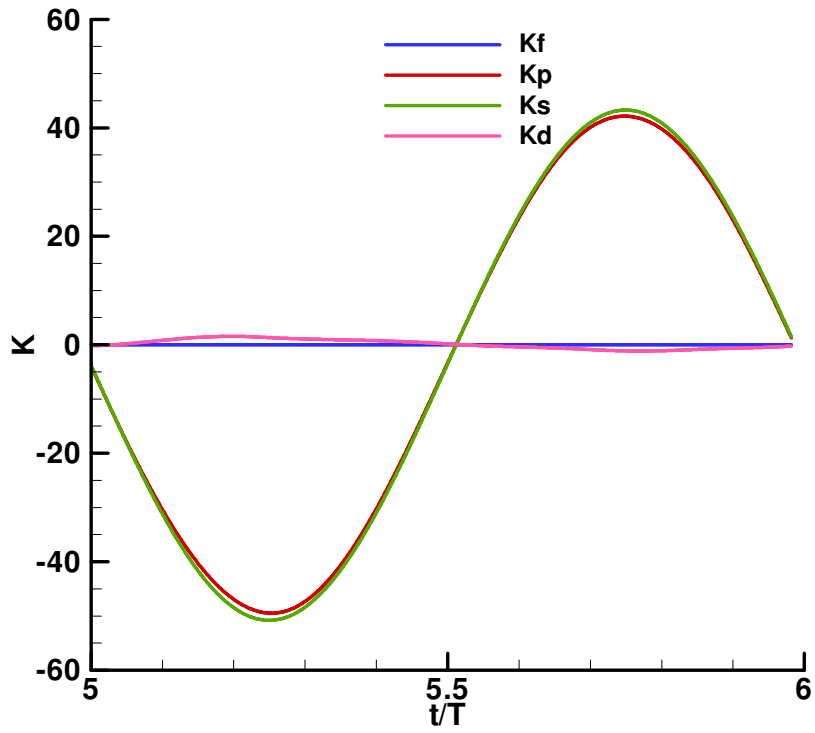
Figure 119 Computed roll moment on hull (f=0.2)
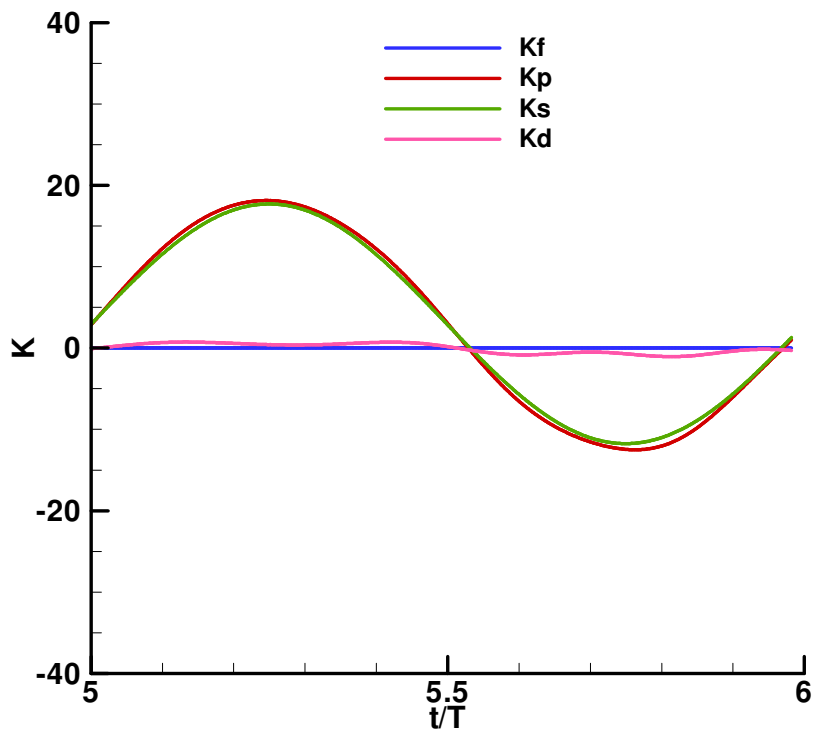
Figure 120 Computed roll moment on compartment (f=0.2)

The computed roll moments at frequency 0.4 are shown in Figure 121-Figure 122.

At a frequency of 0.4, the hydrodynamic roll moments on both the hull and the compartment increase gradually. However, compared with the hydrostatic roll moment, hydrodynamic moments are much smaller on the hull surface and in the compartment.

The damping component on the hull is almost zero similar to that in the intact condition. However, it is more notable in the compartment. The sloshing of water in the tank significantly increases damping in the compartments. The total damping effect at this frequency is from the compartment.

The added inertial moment on the hull surface is the main part of the hydrodynamic roll moment with a nearly opposite phase to the hydrostatic roll moment at this frequency. However, it is only slightly larger than the damping moment in the

213

compartment. The added inertial moment in the compartment is slightly smaller than that on the hull surface.

The hydrodynamic roll moment on the hull surface has a phase close to that in the compartment.

The total hydrostatic roll moment was reduced; however, the total hydrodynamic roll moment was increased in the damage condition at this frequency. Both damping and added inertial increased compared with the intact condition.
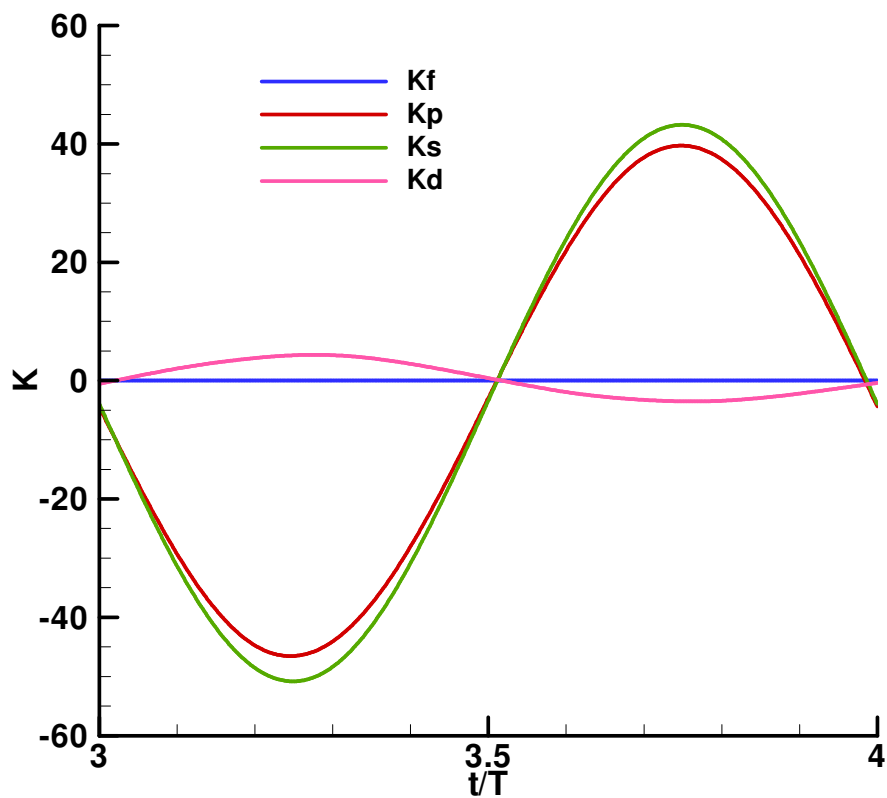
Figure 121 Computed roll moment on hull (f=0.4)
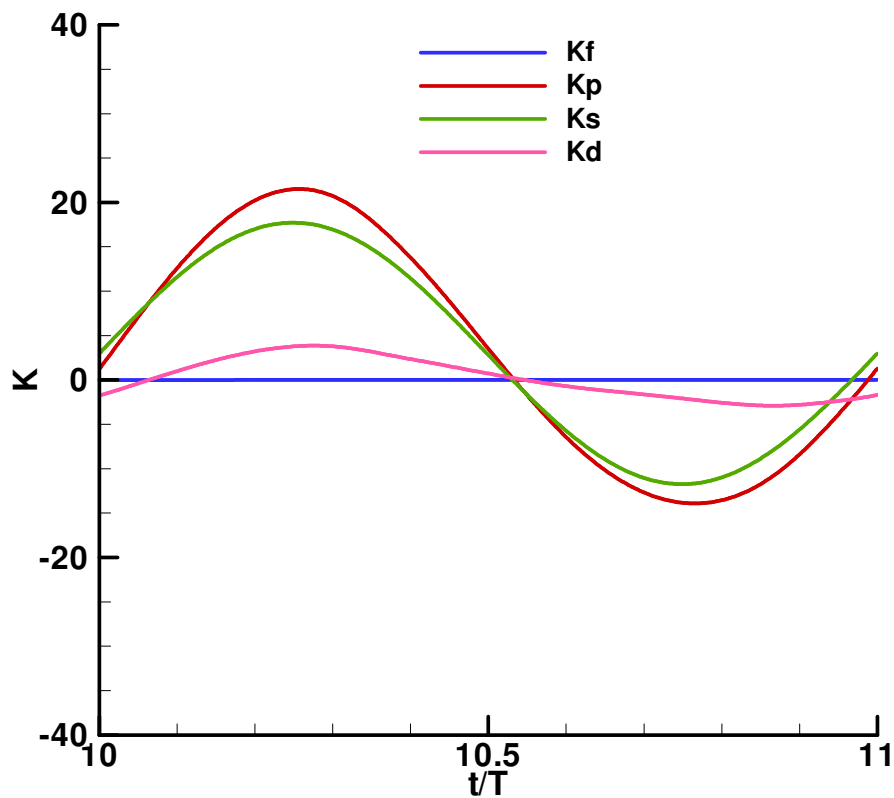
Figure 122 Computed roll moment on compartment (f=0.4)

The computed roll moments at frequency 0.6 are shown in Figure 121-124.

At frequency 0.6, the hydrodynamic roll moment on both the hull and the compartment increase gradually. Compared with the hydrostatic roll moment, the hydrodynamic moments are smaller on the hull surface and 50% smaller in the compartment.

The damping component on the hull is similar to that in the intact condition. However, it is more noticeable in the compartment. The sloshing of water in the tank increases damping remarkably with the increase of frequency. The damping moment in the compartment is larger than that acting on the hull.

The added inertial moment on the hull surface is the main part of hydrodynamic roll moment with nearly opposite phase to the hydrostatic roll moment at this frequency. However, it is only slightly larger than the damping moment in the compartment. The added inertial moment in the compartment is slightly smaller than that on the hull surface.

The phase angle between the hydrodynamic and the hydrostatic roll moment on the hull surface increased to about 18+180 degrees due to the increase in the damping effects; while it is about 40 degrees in the compartment due to the significant increase in damping.

The history of the hydrodynamic roll moment in the compartment is exhibiting some low frequency oscillation due to sloshing; while the outer surface of the hull is similar to that as in the intact condition. The effect of flooding on the hydrodynamic roll moment on the outer hull surface is not large.
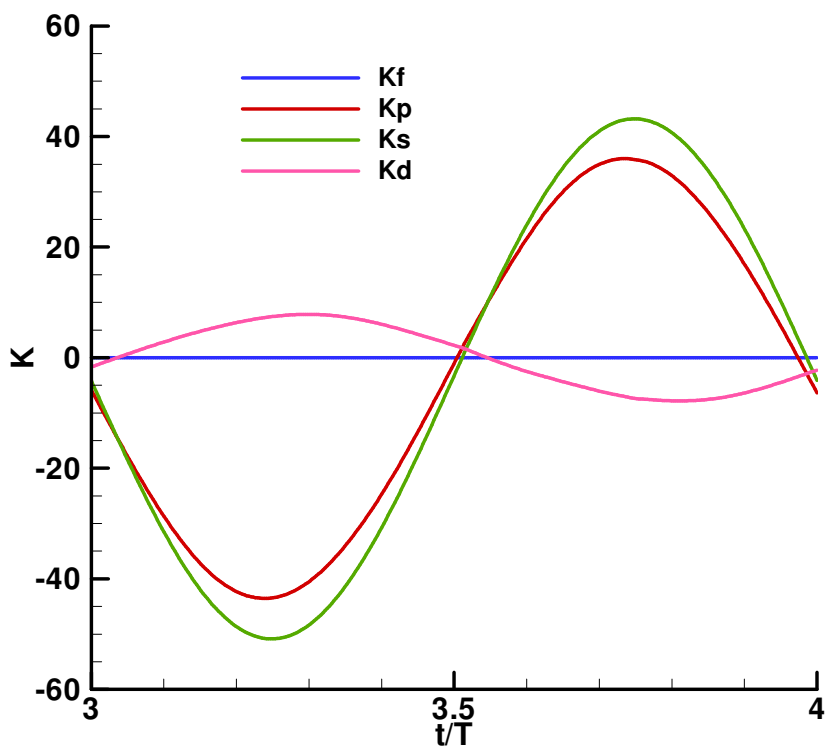
Figure 123 Computed roll moment on hull (f=0.6)
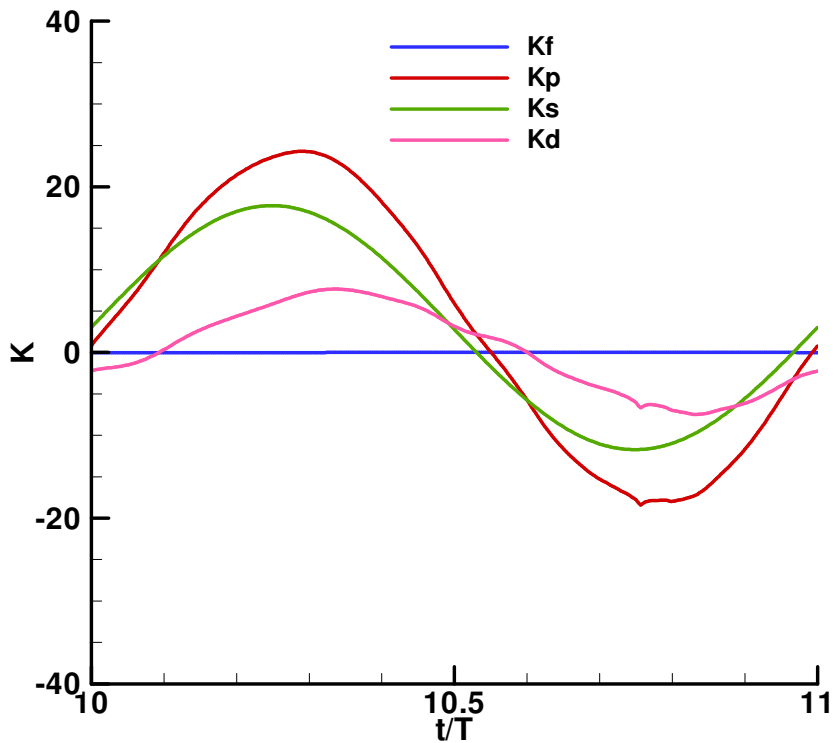
Figure 124 Computed roll moment on compartment (f=0.6)

The computed roll moments at a frequency of 0.8 are shown in Figure 125 Computed roll moment on hull (f=0.8)Figure 126.

At a frequency of 0.8 (near natural roll frequency), the hydrodynamic roll moment on the hull increased gradually, similar to that in the intact condition. However, it increased significantly in the compartment. Compared with the hydrostatic roll moment, the hydrodynamic moment on hull surface is about 30%; however, it is up to 90% in the compartment.

The damping component on the hull is small, similar to that in the intact condition. However, it increases notably in the compartment. The damping moment in the compartment is roughly three times larger than that on the hull. The sloshing of water in the tank increases damping in the compartment significantly. Total damping effect at this frequency is from the compartment.

The phase angle between the hydrodynamic and the hydrostatic roll moment on the hull surface is reducing to about 10+180 degrees due to the increased inertial moment; while it is about 90 degrees in the compartment due to significant increase in damping. The added mass in the compartment is negative.

There are high frequency components in the hydrodynamic roll moment in the compartment due to sloshing generated. At this frequency, the method to separate hydrodynamic moment into damping and added inertial moments is not appropriate due to high non-linearity.

The effect of sloshing at this frequency on the total hydrodynamic effect is the largest due to resonance.
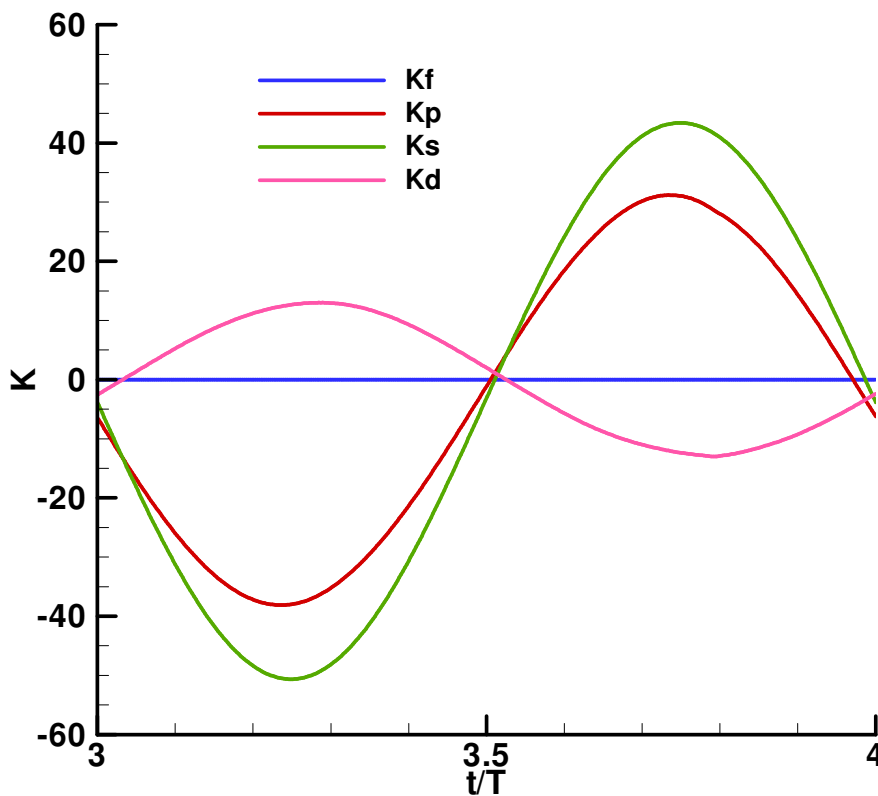
Figure 125 Computed roll moment on hull (f=0.8)
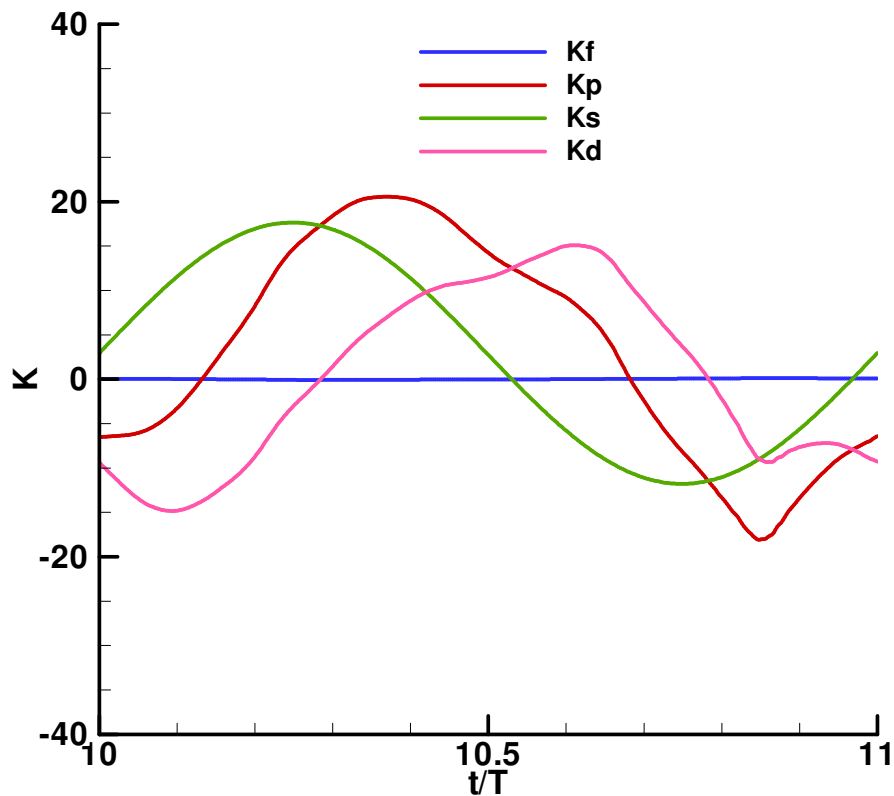
Figure 126 Computed roll moment on compartment (f=0.8)

The computed roll moments at a frequency of 1.0 are shown in Figure 127-Figure 128.

At a frequency of 1.0 (above natural roll frequency), the hydrodynamic roll moment on the hull increased gradually, similar to that in the intact condition. However, it decreases slightly in the compartment. Compared with the hydrostatic roll moment, hydrodynamic moment on the hull surface is about 40%. It is reduced to 75% in the compartment.

The damping component on the hull is small, similar to that in the intact condition. However, it is quite large in the compartment. The damping moment in the compartment is as large as that on the hull. The sloshing of water in the tank and the flooding at the opening contribute to the damping in the compartment. Most damping effect at this frequency is from the compartment.

The phase angle between the hydrodynamic and the hydrostatic roll moment on the hull surface is reducing to about 5+180 degrees due to the increases in added mass; while it is about 140 degrees in the compartment due to significant damping increase and negative added mass.

There are high frequency components in the hydrodynamic roll moment in the compartment due to short wave and sloshing generated. At this frequency, the method to separate hydrodynamic moment into damping and added inertial moments linearly is not appropriate but only an equivalent method.

The effect of sloshing at this frequency on total hydrodynamics is large.

.
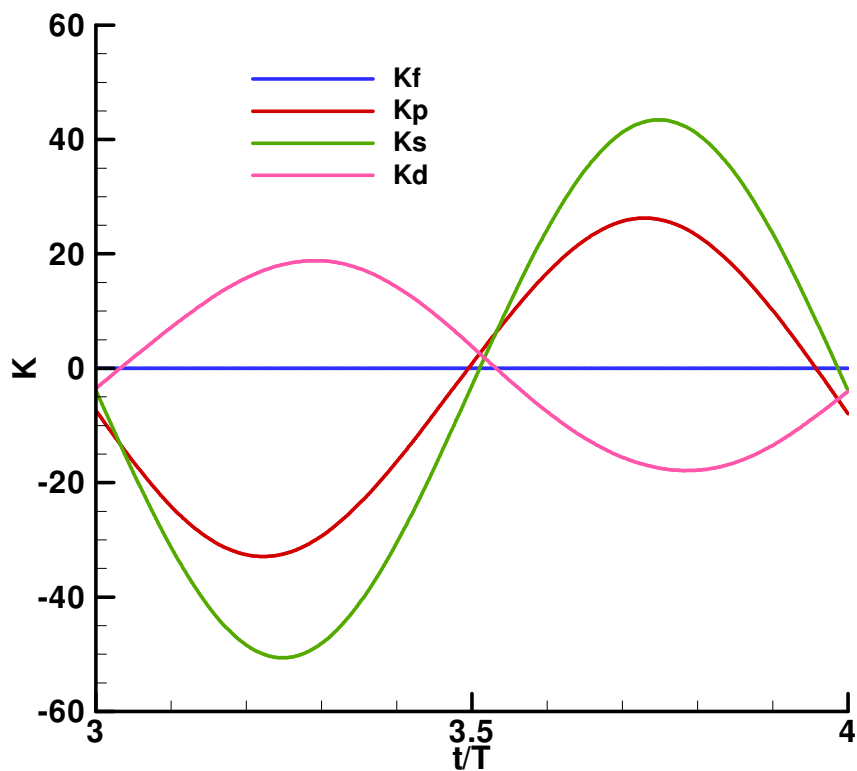
Figure 127 Computed roll moment on hull (f=1.0)
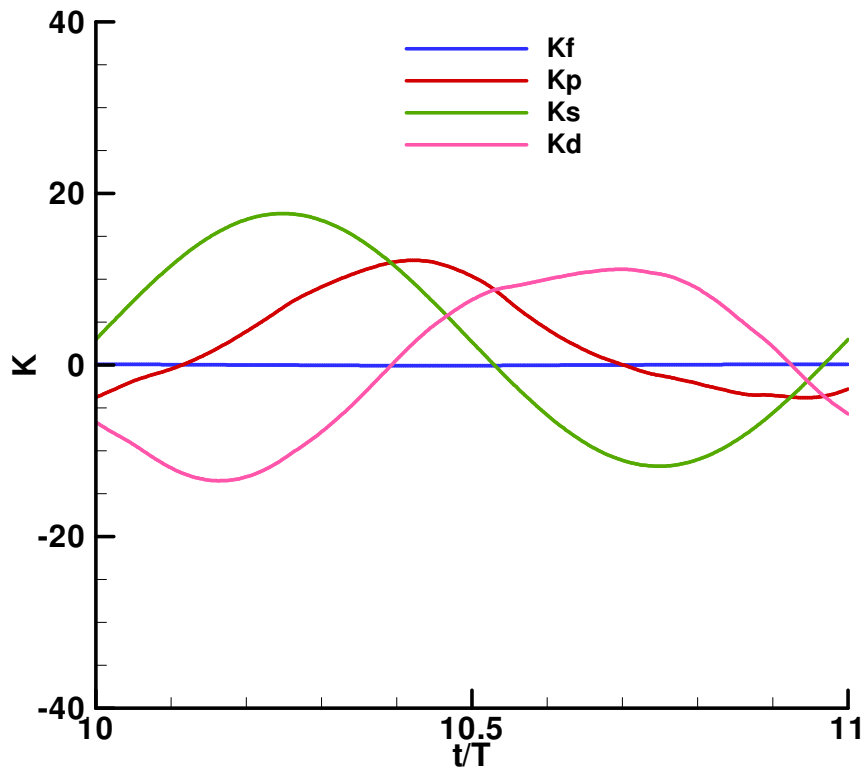
Figure 128 Computed roll moment on compartment (f=1.0)

The computed roll moments at frequency 1.2 are shown in Figure 129-Figure 130.

At a frequency of 1.2, the hydrodynamic roll moment on hull increases continuously, similar to that in the intact condition. However, it decreases slightly in the compartment. Compared with the hydrostatic roll moment, the hydrodynamic moment on the hull surface is about 50%. It is reduced to 35% in the compartment.

The damping component on the hull is small, similar to that in the intact condition, and is reduced gradually in the compartment. The damping moment in the compartment is as large as that on the hull. The sloshing of water in the tank dominates damping in the compartment. Most damping effect at this frequency is from the compartment.

The phase angle between hydrodynamic and hydrostatic roll moment on hull surface is reducing to about 180 degrees due to increasingly added mass; while it is about 160 degrees in the compartment due to damping and negatively added mass.

At this frequency, high frequency effects are decreasing on the hydrodynamic roll moment in the compartment. The method used to separate hydrodynamic moment into damping and added inertial moments can be used, however, added inertial is negative due to sloshing effects.

The effect of flooding and sloshing at this frequency on total hydrodynamics is large.

.
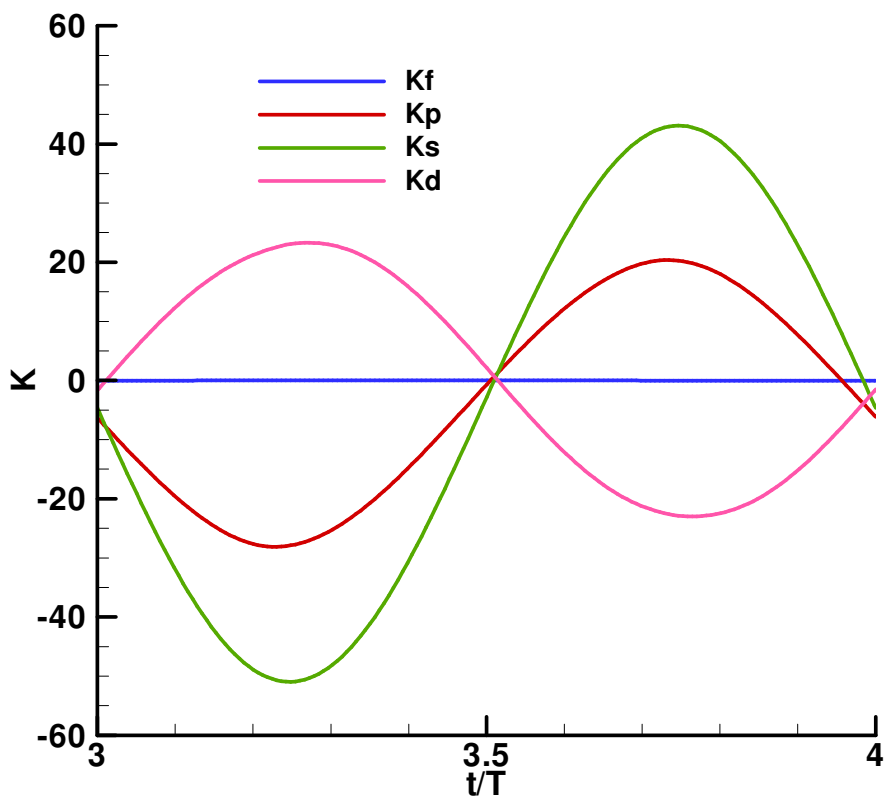
Figure 129 Computed roll moment on hull (f=1.2)
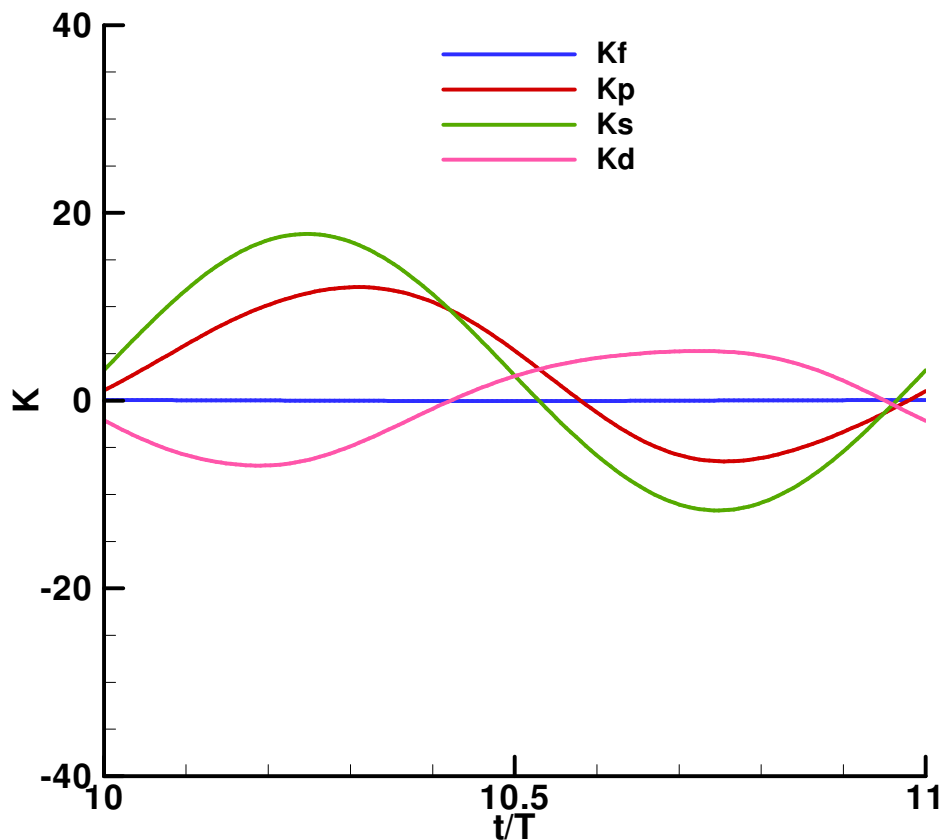
Figure 130 Computed roll moment on compartment (f=1.2)

The computed roll moments at a frequency of 1.4 are shown in Figure 131-Figure 132.

At a frequency of 1.4, the hydrodynamic roll moment on the hull is increasing continuously similar to that in the intact condition. However, it is small in the compartment. Compared with hydrostatic roll moment, the hydrodynamic moment on hull surface is about 60%. It is reduced to 25% in the compartment.

The damping component on hull is small similar to that in the intact condition, and reduced gradually in the compartment. The damping moment in the compartment is smaller than that on the hull. The effects of sloshing of water in tank and flooding at opening on damping are reducing in the compartment at very high frequency. Most of the damping effect at this frequency is from the hull surface.

The phase angle between hydrodynamic and hydrostatic roll moment on hull surface reduced to about 180 degrees due to the increased added mass; while it is resumed to nearly zero degrees in the compartment. The added mass in the compartment is almost zero. The moment acting on the compartment is mainly due to the hydrostatic contribution.

At this frequency, high frequency effects are visible on the hydrodynamic roll moment in the compartment. However, both damping and added inertial are small due to the higher frequency. It seems that there is less time to generate non-linear wave in the compartment at high frequency.

The effect of flooding and sloshing at this frequency on total hydrodynamics is decreasing..
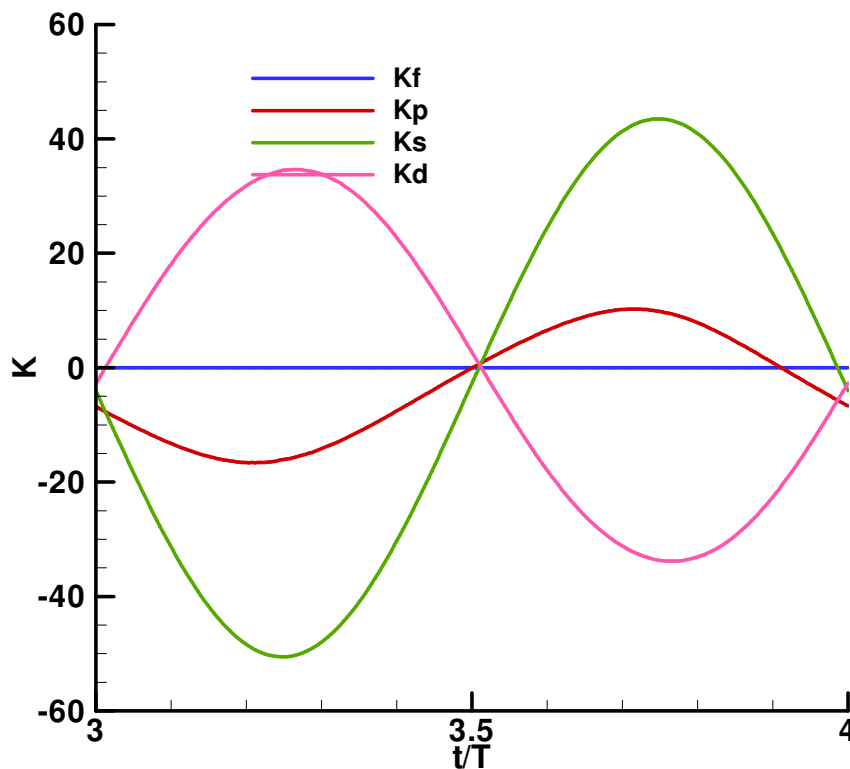
Figure 131 Computed roll moment on hull (f=1.4)
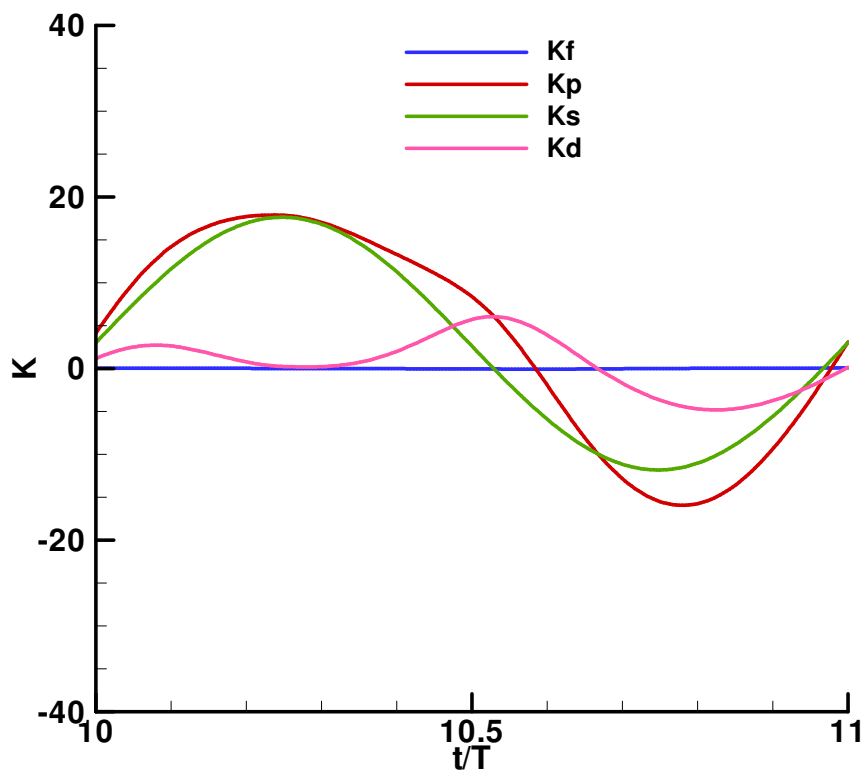
Figure 132 Computed roll moment on compartment (f=1.4)

The computed roll moments at a frequency of 1.6 are shown in Figure 133-Figure 134.

At a frequency of 1.6, the hydrodynamic roll moment on hull is increasing continuously, similar to that in the intact condition. It increases slightly in the compartment. Compared with the hydrostatic roll moment, the hydrodynamic moment on the hull surface is about 90%. It is roughly 30% in the compartment.

The damping component on the hull is small similar to that in the intact condition. And it is low in the compartment. The damping moment in the compartment is smaller than that on the hull. The effects of sloshing of water in the tank on damping are reduced further in the compartment. Most of the damping effect at this frequency is from the hull.

The phase angle between hydrodynamic and hydrostatic roll moment on hull surface is reduced to about 180 degrees due to the increased added mass; while it resumes to

nearly zero degrees in the compartment. The added mass in the compartment is back to positive but small compared with that on the hull.

At this frequency, high frequency effects are weak on the hydrodynamic roll moment in the compartment. There is less time to generate non-linear wave in the compartment and the wave pattern in the compartment is frozen or move like a solid without deformation.
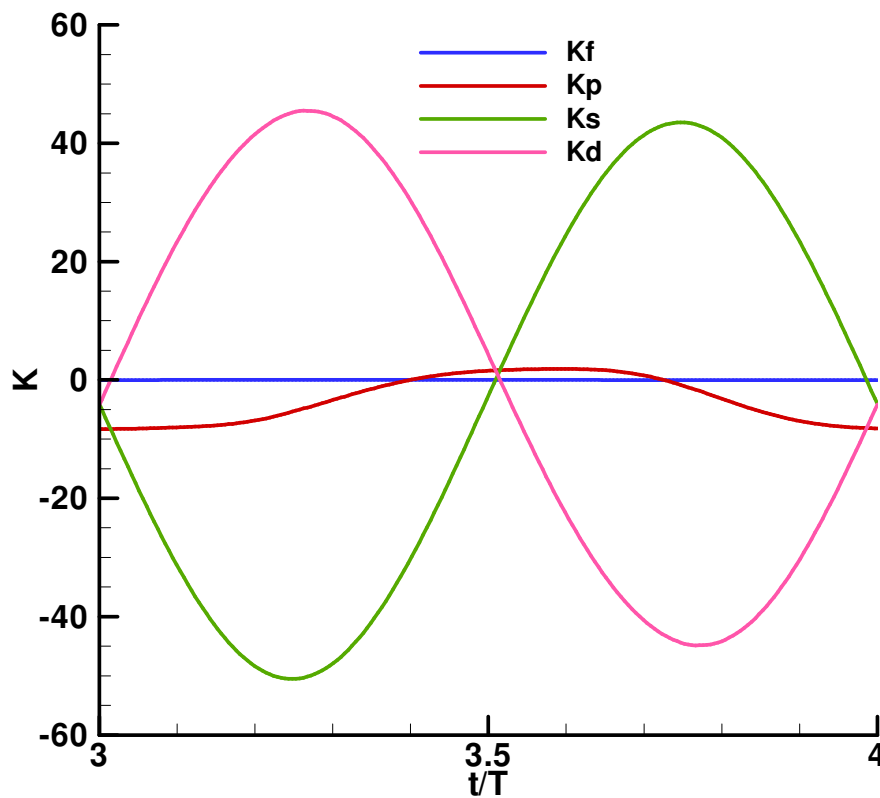
Figure 133 Computed roll moment on hull (f=1.6)
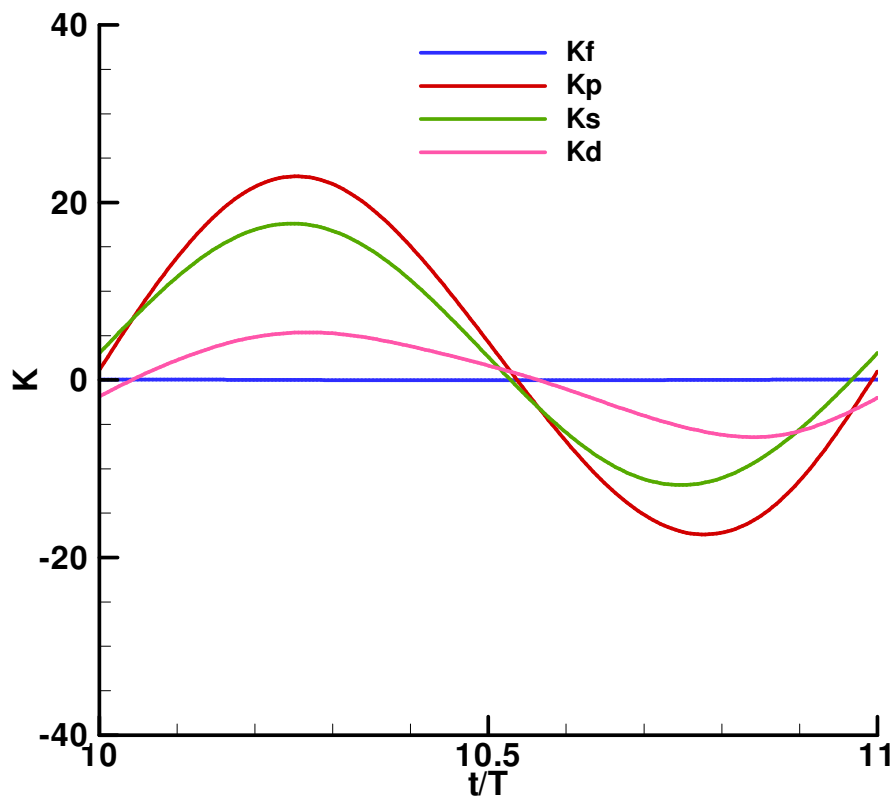
Figure 134 Computed roll moment on compartment (f=1.6)

The computed roll moments at a frequency of 1.8 are shown in Figure 135-Figure 136.

At a frequency of 1.8, the hydrodynamic roll moment on hull increases similar to that in the intact condition. It increases slightly in the compartment. Compared with the hydrostatic roll moment, the hydrodynamic moment on the hull surface is larger. It is roughly 60% in the compartment.

The damping component on hull is small, similar to that in the intact condition. And it is low in the compartment. The damping moment in the compartment is smaller than that on the hull. The effects of the sloshing of water in the tank and the flooding at the opening on damping are dying in the compartment. Most damping effect at this frequency is from the hull.

The phase angle between hydrodynamic and hydrostatic roll moment on hull surface is reduced to about 180 degrees due to the increased added mass; while it is increasing slightly in the compartment.

At this frequency, high frequency effects are weak on the hydrodynamic roll moment in the compartment.
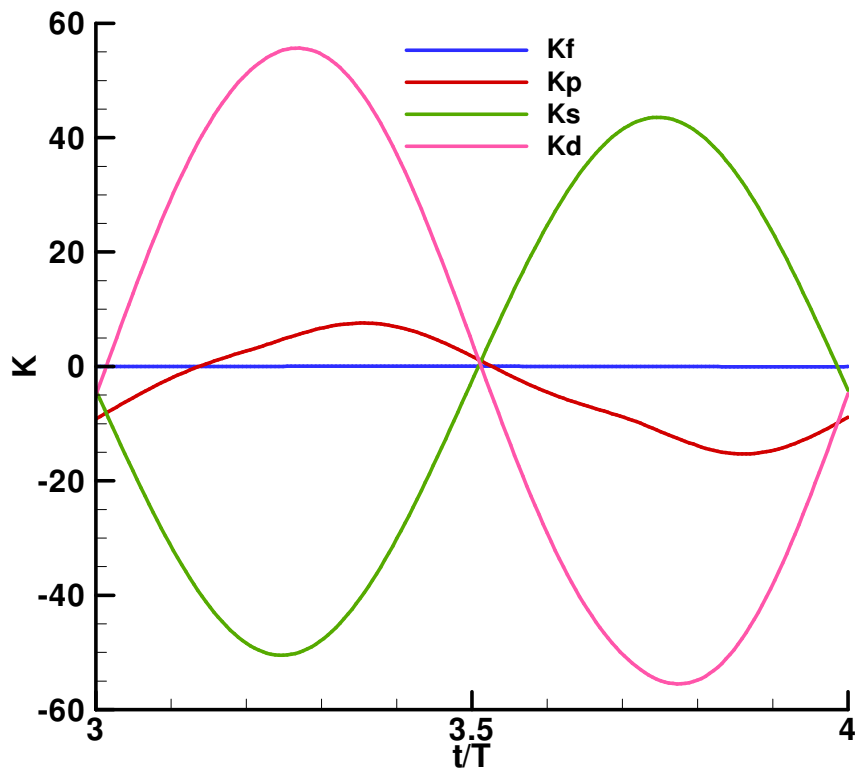
Figure 135 Computed roll moment on hull (f=1.8)
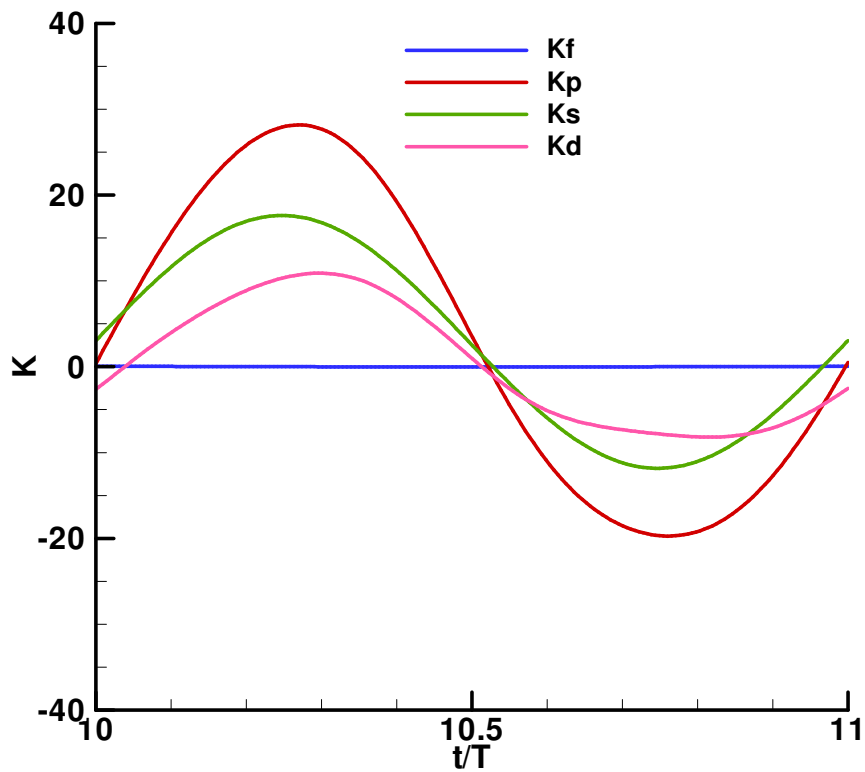
Figure 136 Computed roll moment on compartment (f=1.8)

The computed roll moments at a frequency of 2.0 are shown in Figure 137-Figure 138.

At a frequency of 2.0, the hydrodynamic roll moment on hull increases similar to that in the intact condition. It increases further in the compartment. Compared with the hydrostatic roll moment, the hydrodynamic moment on the hull surface is much larger. It is roughly 90% in the compartment.

The damping component on hull is small similar to that in the intact condition. And it is also low in the compartment. The damping moment in the compartment is smaller than that on the hull. The effects of the sloshing of water in the tank on damping are decreasing in the compartment. Most damping effect at this frequency is from the hull.

The phase angle between hydrodynamic and hydrostatic roll moment on hull surface is reducing to about 180 degrees due to the increased added mass; while it is quite small in the compartment.

At this frequency, high frequency effects are weak on hydrodynamic roll moment in the compartment.
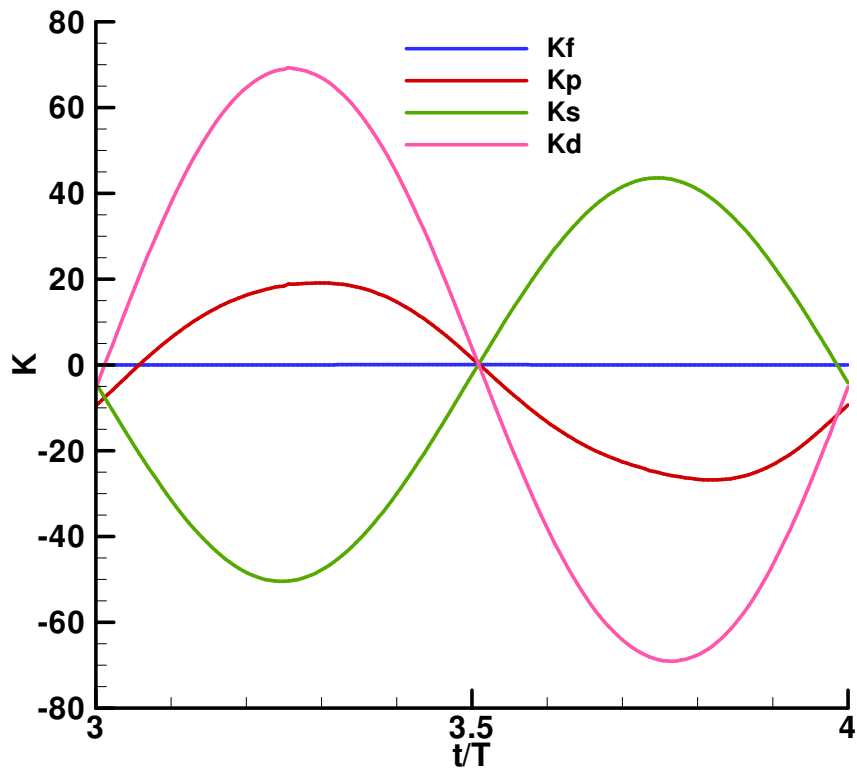
Figure 137 Computed roll moment on hull (f=2.0)
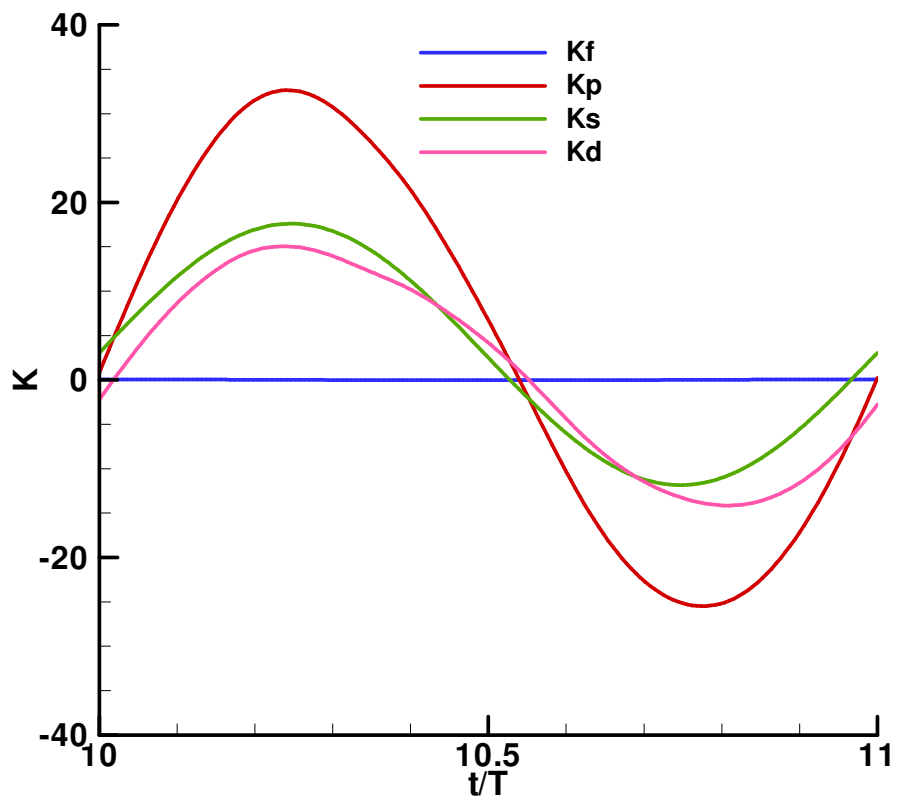
Figure 138 Computed roll moment on compartment (f=2.0)

The flow pattern at damage condition is shown below.
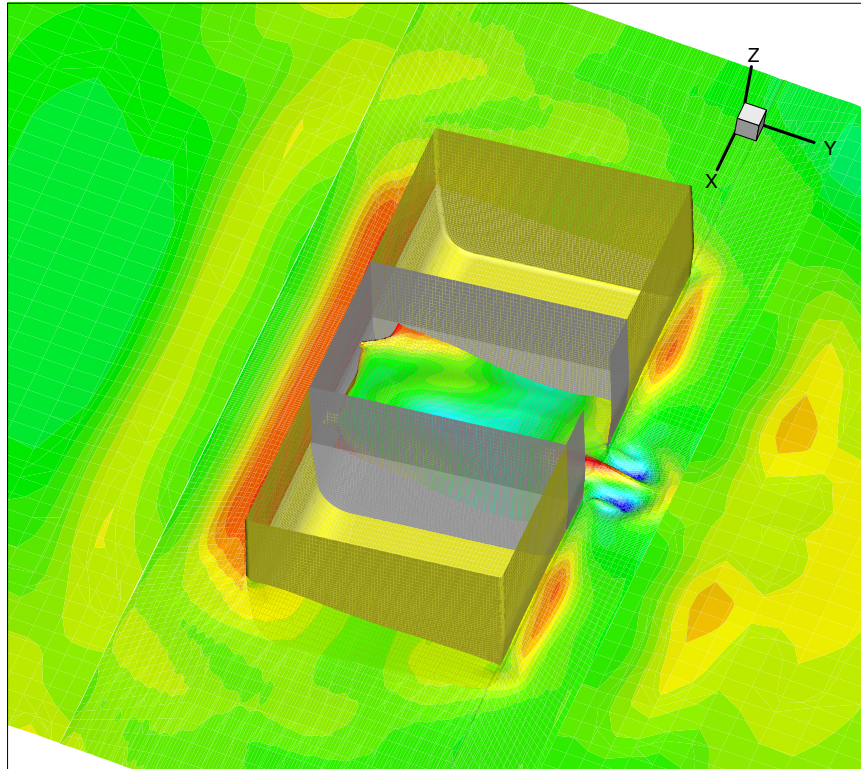
Figure 139 Instant flooding of water in tank (f=1.0)

It is clear that the effect of flooding on the hydrodynamic moment acting on the hull is limited to a small area surrounding the opening. The effect becomes relatively larger in the compartment. The amount of sloshing in the tank depends on the frequency. Around a frequency of 0.8, sloshing is excessive and there is significant influence of sloshing on the roll moment. The phase of hydrodynamic roll moment in the tank changes largely from being in the same phase as hydrostatic force to the opposite phase, then return to in phase. Therefore, it is difficult to find a universal expression of added mass and damping in the damage condition. They should be obtained based on a case-by-case analysis.

Although the method of separating hydrodynamic roll moment into damping and added inertial is not theoretically valid in the damaged condition, it can be seen as an equivalent approach.

The hydrodynamic coefficients were obtained by the least square fitting and given in the Figure below.
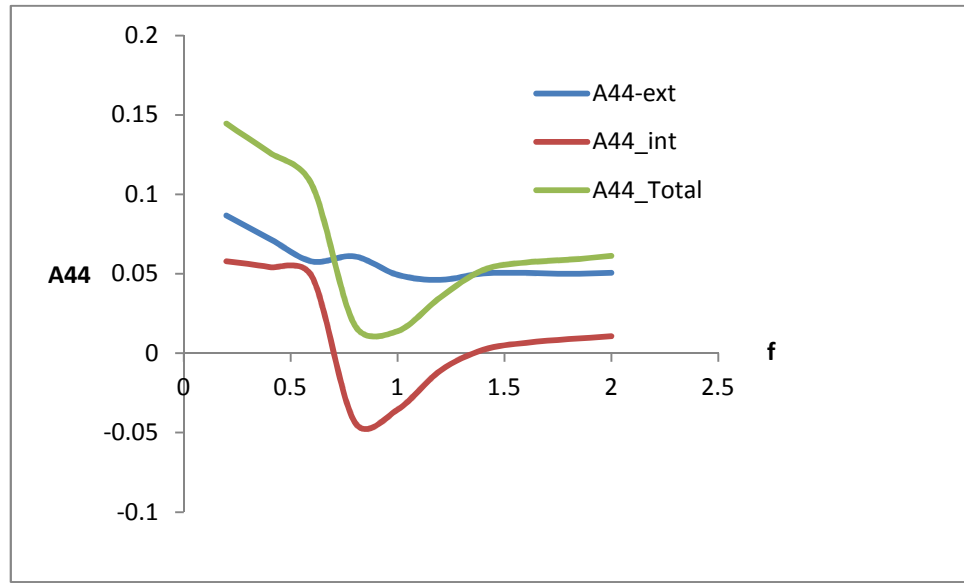
Figure 140 Added moment of inertia coefficients
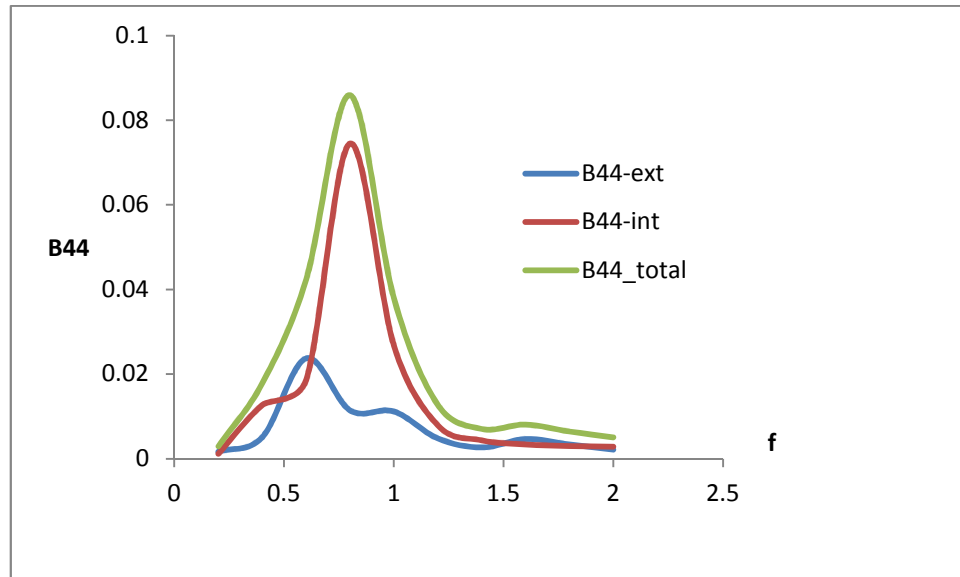
Figure 141 Damping moment coefficients

As we can see, the total added inertial coefficients include the contributions from the hull and the compartment. The A44 on hull (A44-ext) is consistent with that in the intact condition. Some deviations occur near a frequency of 0.8, at which sloshing and flooding are violent.

The A44 in the compartment changes largely depending on the frequency. At a frequency of 0.5-0.8, A44 drops rapidly to negative values. The sloshing in the tank carries the liquid to the other end of the tank and causes large non-linear roll moment. With the increases in frequency, the A44 return to positive values and shows similar features as that acting on the hull.

The total damping includes contributions from the hull and the compartment. The B44 on the hull (B44-ext) is consistent with that in the intact condition but the peak is slightly lower. Flooding at critical frequency tends to reduce damping slightly.

B44 in the compartment changes significantly with frequency. At a frequency of 0.8 (natural roll frequency), B44 reaches its maximum value. Then, damping coefficient decreases gradually at higher frequencies. The damping in the compartment is much larger than that on the hull near natural roll frequency (roughly 5 times as large as

that in intact condition and with a phase lag). The main reason of large damping in the compartment near natural roll frequency is the violent sloshing of water in the tank. The nonlinear effects are becoming strong and wave pattern develops from standing wave to significant surge. At roll angle zero where roll acceleration is zero and velocity is the largest, the surge is not symmetric about centre plane but lies at the one side of the tank, which results in huge roll moment or roll damping. Therefore, the total damping has the same trend as that in the compartment. Thus for the prediction of seakeeping behaviour of a damaged ship, the damping in the compartment needs to be treated with special care.

10.9   Sway force

The sway force due to roll motion at a frequency of 1.0 is shown below.

It can be seen that the sway force due to friction is nearly zero. The main part is due to pressure. Hydrostatic sway force oscillates with the roll motion. It is positive on the hull and negative in the compartment due to the effects of the opening. The net hydrostatic sway force is zero.

The hydrodynamic sway force on the hull is nearly harmonic but not in the compartment due to the effects of sloshing and flooding. The net total sway force is not zero in one period. Thus, there is a sway motion in free running condition.
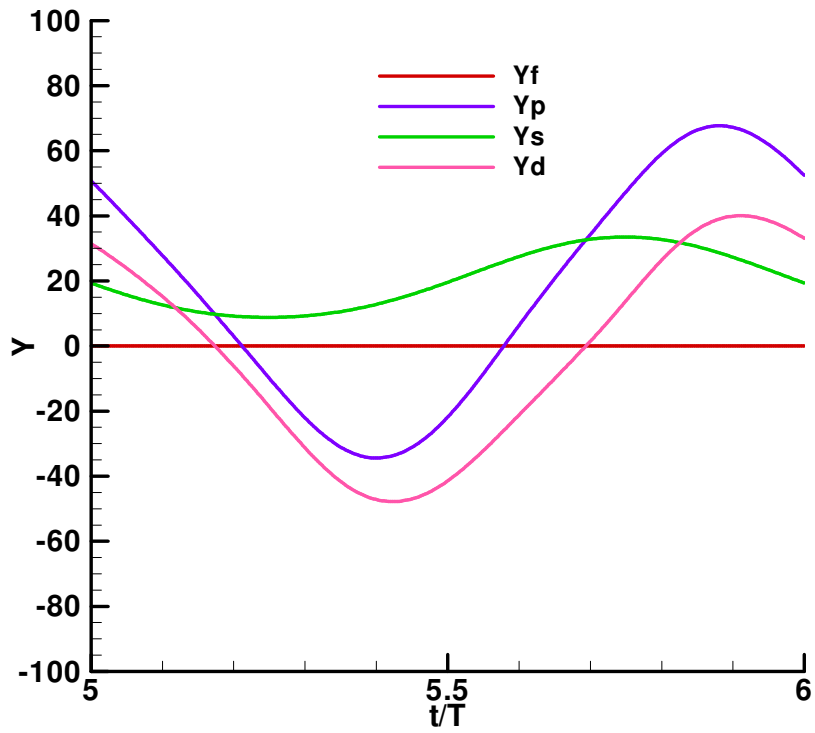
Figure 142 Sway force Y on hull (f=1.0)

Where

Y   Sway force (N)

Yf   Sway force due to friction

Yp   Sway force due to pressure

Ys   hydrostatic sway force

Yd   hydrodynamic sway force
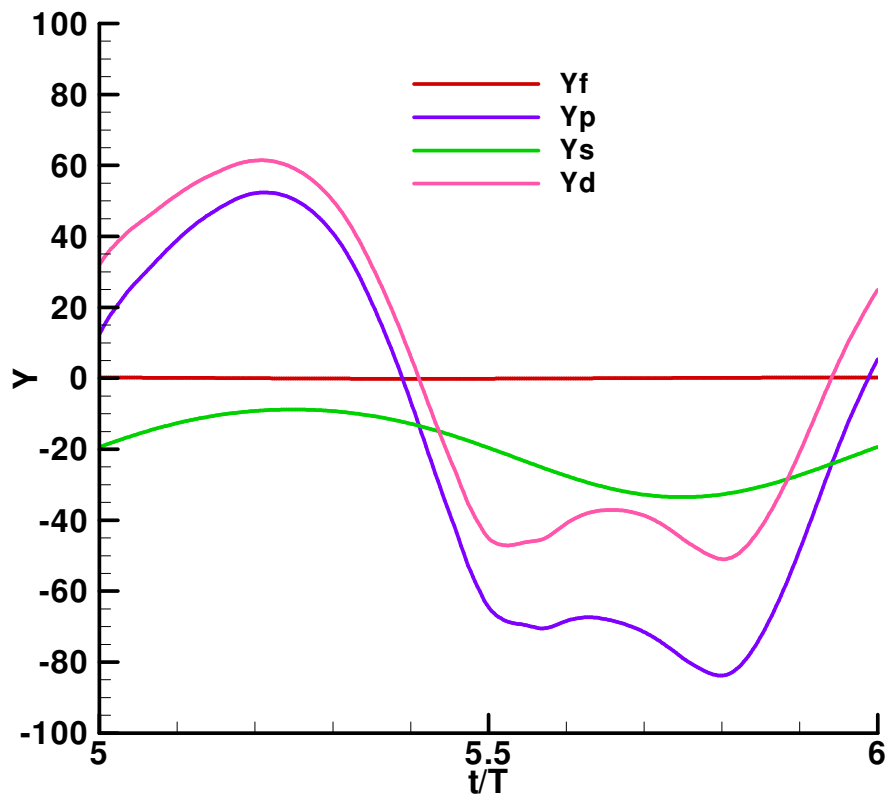
Figure 143 Sway force Y in compartment (f=1.0)
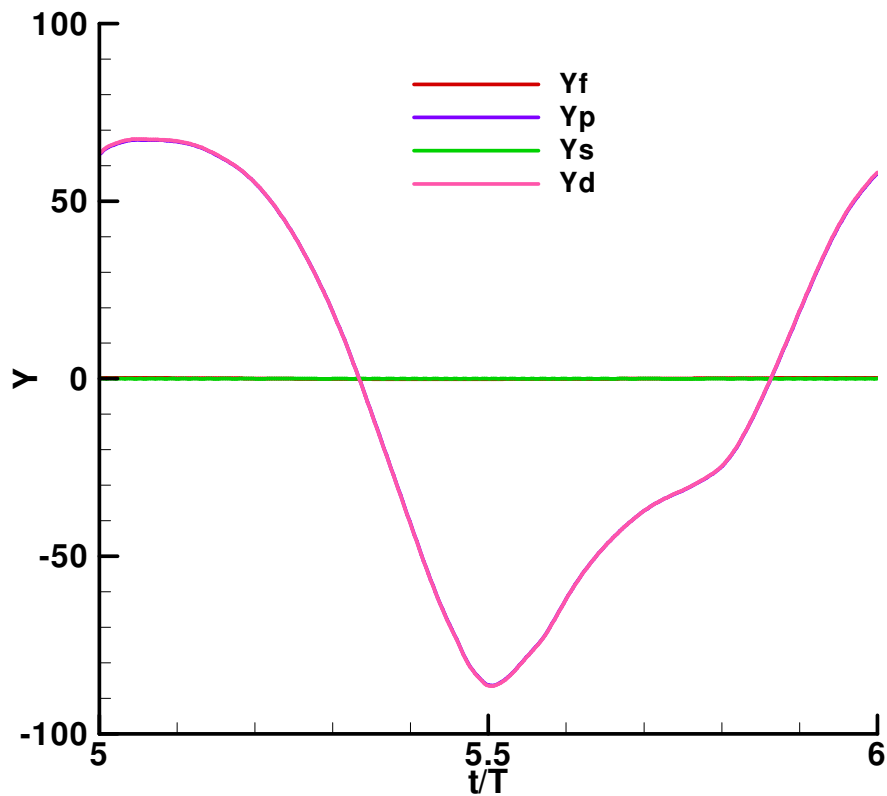
Figure 144 Total sway force Y (f=1.0)

The mass in the tank, on the deck and the flow rate at the opening are shown Figure
145. As we can see, the mass in the tank oscillates with the roll motion. The water
flows in and out of the compartment through the damage opening due to the
difference of the hydrostatic head. The velocity of water flooding at the opening can
be monitored by the flow rate at the opening. The mass in the tank and the flow rate
are frequency dependent. At low frequencies, change of the mass in the tank is larger
due to having more time to ingress and egress. At high frequencies, the mass in the
tank is nearly constant due to having less time available.
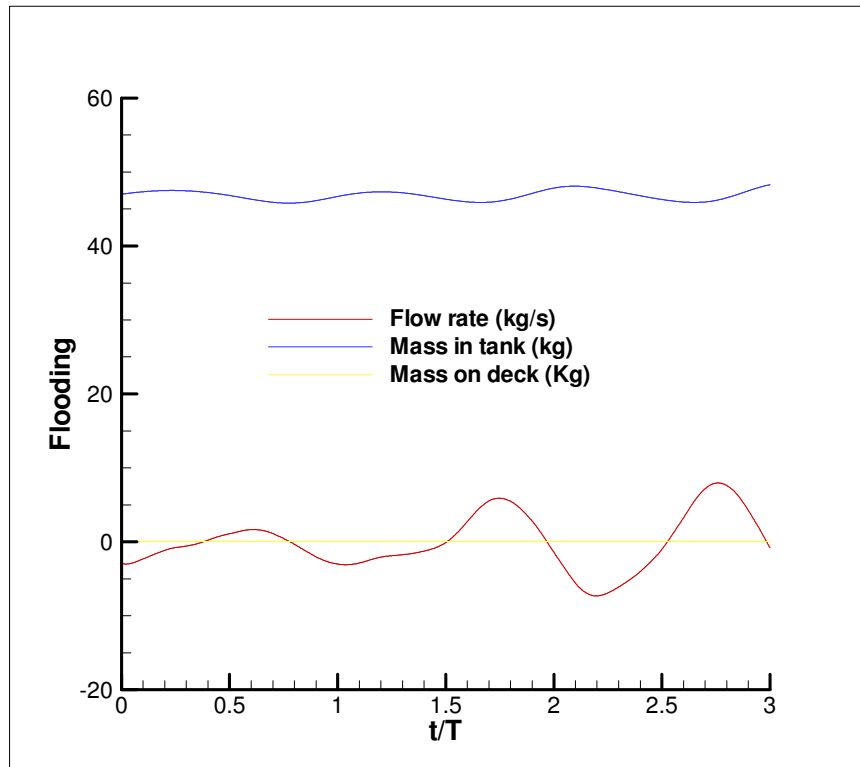
Figure 145 Flooding tracker

10.10   Concluding Remarks

In summary, the numerical simulations of the forced roll motion (numerical rolling tank) were carried out and the results are validated.

The numerical simulation shows that it is quite convenient to setup simulation of forced roll motion such as roll axis (which has limitation in model tests due to space), roll frequency and amplitude, damage opening etc. There is a lot of information available for the analysis of damaged ship flooding, such as mass on deck, water in tank, loads on hull or compartments and so on. The effect of friction on the roll moment and the sway force is small. Damaged ship flooding and sloshing changes the roll moment and the sway force significantly, especially near the natural roll frequency.

Hydrostatic roll moment is large and needs to be removed accurately. The added inertial force is sensitive to the hydrostatic roll moment. The hydrodynamic roll moment increases with increasing frequency. The added inertial moment increases with the frequency almost squared; however, damping decreases at higher frequencies. The non-dimensional added inertial coefficient decreases until it becomes flat at high frequencies. The non-dimensional damping coefficient increases at low frequency regions and decreases at high frequencies.

The damage flooding and sloshing in the compartment have a huge effect on the hydrodynamic roll moment near the critical roll frequency. The added inertial moment in the compartment is negative near the natural roll frequency and will affect the period of roll motion in damaged conditions. The damping in the compartment is the dominating part and should be used with reliable knowledge. It will influence the roll decay and roll motion significantly.

11   Discussion

In accordance with the aims of this research, the benchmarking and validation studies of ship hydrodynamics using RANSE approach covering ship resistance, propulsion, manoeuvring, seakeeping and ship stability have been carried out. Based on the work fulfilled in this research, the following remarks can be made:

- The numerical towing tank is a green facility to evaluate the performance of ship hydrodynamics with little cost and great potential. The computed results indicate that the numerical accuracy is sensitive to the grid resolution and turbulence model. For a medium sized grid density up to 2m cells with 50 grid points in a wave length, 20 grid points in a wave envelop and 20 grid points in a boundary layer, it takes 3 days to run a steady numerical simulation using 8 nodes. The computational time is still long. Generally we can expect an accuracy of ship hydrodynamics within 3-5%. To increase the grid resolution will improve the numerical accuracy, however, the availability of computer resource still restricts the grid size. For a simulation with 10m cells, it takes about 30 days to run a unsteady calculation using 8 cores, which severely affects the productivity of CFD. Additionally, the flow problem with vortex demands even finer meshes or flow adaptive grids to resolute delicate flow phenomena, which is still not realistic. Moreover, the Reynolds-Averaged turbulence model capable to capture the physics of swirling flow is still deficient, which is reflected in the accuracy of present numerical simulations. Therefore, the difficulty encountered with grid density and turbulence model will still exist for some time. In this work, these difficulties are partly overcome by utilizing High Performance Cluster (HPC) and the comparison of the state of the art of most popular turbulence models. A number of recommendations deriving from the above for further researches on are given below:
  - Grid sensitivity study on the generation, size and strength of vortex; identify the variation of the pressure near bow and stern

- Turbulence model effect on numerical results quantify the change of pressure and turbulence viscosity in the area of flow separation
- The optimisation of time and quality of grid generation, as this is still a challenge for problems with appendages

The key contribution of the present research can be summarised below:

- Establishment of the integrated numerical facilities, including deep water towing tank, planar motion mechanism, wave maker and roll tank.
- The development of user codes including parallel computing to enable the application and maximise the benefit of commercial software.
- Verification and validation of numerical simulations from field variables, particularly turbulence quantities to the integrated variables, and demonstration of the current state of the art of turbulence models and numerical ship hydrodynamics.
- The original work of separation of forces acting on the damaged compartment and hull to quantify the effects of sloshing, flooding on roll damping.
- The nonlinearlity and viscous effects are inherently taken into account and the accuracy of numerical results are accredited by using RANSE approach, which are the main advantages over traditional approaches; The information from the analysis of classical ship hydrodynamics enables a holistic approach for explanation of flow phenomena, analysis of hydrodynamic loads and optimization of design.

12   Conclusions

RANS-based CFD approach was used to study the classic ship hydrodynamic problems including ship resistance, propulsion, manoeuvring, seakeeping and damaged ship flooding. Grid sensitivity studies were carried out and the effects of turbulence models were investigated. The computed results were validated against the model test data.

Based on the computational results, the following conclusions can be drawn:

Ship Resistance: the numerical results of velocity field, wave elevation and resistance coefficients predicted by the k-ω turbulence model agree well with the model test. There was no significant improvement seen in using the RSM turbulence model. Grid uncertainty studies show that the resistance coefficients converge monotonically with the grid by the present methods of calculation, and the Richardson extrapolation can be applied. The results of computed far field wave pattern indicate that the wave was damped and mesh resolution needs to be increased there. The predicted turbulent Reynolds stresses have close contours with those from the measurements; however, numerical results generally overestimate the turbulence intensity.

Ship Propulsion: body force-based propeller modelling was implemented. The test case showed that the flow fields changed significantly due to the suction and swirling action of the propeller when compared with nominal wake. The body force parameter effect on hull-propeller interaction is not large. The computed thrust deductions agree well with the measurements.

Ship Manoeuvring: numerical PMM simulations of pure sway and yaw motions were performed. The numerical results of sway force and yaw moment were consistent

with model tests. Among them, the friction components were negligible and pressure forces were dominant. The computed longitudinal force exhibits numerical wave disturbance. The computed yaw moment were generally overestimated. The separation and the vortex of flow in manoeuvring motion could influence the performance of the current turbulence models.

Seakeeping: incident wave were generated by numerical wave maker at the inlet. The calculations of wave diffraction and roll decay were conducted. The predicted surge, sway forces and yaw moment with incident wave showed overall good agreements of 0th amplitudes and phase angles with the model test data. The computed 1st amplitudes of the surge force and the pitch moment agreed well with measurements; however, the computed heave force showed large deviation, which needs to be investigated further.

The computed roll angle in the simulation of roll decay coincided reasonably well with measurement of amplitude and phase angle. The predicted velocity contours had similar shapes as the model test, however, exhibited numerical diffusion.

Damaged flooding: the numerical roll tank was established to study the hydrodynamic coefficients of roll motion in intact and damage conditions. The hydrostatic roll moment was removed synchronically. The damping and added inertial components were extracted from the hydrodynamic roll moment by least square estimator. The results were compared with model test available. It showed that the hydrostatic force needed to be exactly removed to obtain the correctly added inertial. Both damping and added inertial moments were frequency sensitive. Damping coefficients increased with frequency and reached a maximum near the natural roll frequency of 0.78 and then decreased gradually. Near the natural roll frequency, the damage effects on the hydrodynamic roll moment were the largest. The added inertial coefficients decreased with the increases in frequency and then recovered near the natural roll frequency. It was nearly flat at high frequencies, i.e. the added inertial moment was proportional to the square of frequency. Both sloshing in tank and flooding at opening changed total roll moment significantly.

Overall, the accuracy of the RANS calculations on the classic hydrodynamic problems is encouraging. The computational time is still long; it is however improving with the emergence of HPC cluster. Although these problems can be resolved numerically by CFD, more studies on turbulence and grid effects are needed before applying CFD on the designing of the ships and to optimise ship performances.

Publications

1   Qiuxin Gao, Wei Jin and Dracos Vassalos "The Calculations of Propeller Induced Velocity by RANS and Momentum Theory", Journal of Marine Science and Technology, Accepted

2   Qiuxin Gao, and Dracos Vassalos "Numerical Study of Damage Ship Hydrodynamics", Journal of Ocean Engineering, Submitted

3   Qiuxin Gao and Dracos Vassalos, "Numerical Study of Hydrodynamic Coefficients by RANS", STAB, 2012, Athens, Greece

4   Qiuxin Gao and Dracos Vassalos, "The Numerical Study of Robotic Fish Hydrodynamics", International Conference of Maritime Technology, 2012, Harbin, China

5   Wei Jin, Qiuxin Gao and Dracos Vassalos, "Numerical Simulation of Large Marine Diesel Engine Combustion by RANS Method", International Conference of Maritime Technology, 2012, Harbin, China

6   Qiuxin Gao and Dracos Vassalos, "Numerical Study of Intact and Damage Roll Decay", 12th International Ship Stability Workshop, Washington D.C., June 12-15, 2011

7   Zhiliang Gao, Qiuxin Gao and Dracos Vassalos, "Numerical Study of Damaged Ship Motion in Waves", 12th International Ship Stability Workshop, Washington D.C., June 12-15, 2011

8   Qiuxin Gao, Zhiliang Gao and Dracos Vassalos, "Numerical Study of Damage Ship Flooding", 4th INT. DESIGN FOR SAFETY CONFERENCE, Trieste, 18-20 October 2010

9   Qiuxin Gao, Zhiliang Gao and Dracos Vassalos, "Numerical Study of Damage Ship Flooding", 4th INT. DESIGN FOR SAFETY CONFERENCE, Trieste, 18-20 October 2010

10   Q. Gao, W. Jin, D. Vassalos, "Computation of wave diffraction by RANS approach", Workshop in Ship Hydrodynamics, December 8-10, 2010, Gothenburg

11   Q. Gao, W. Jin, D. Vassalos, "Simulation of roll decay by RANS approach", Workshop in Ship Hydrodynamics, December 8-10, 2010, Gothenburg

12   Q. Gao, D. Vassalos, "Study of Froude and Hughes methods by numerical towing tank", THE WILLIAM FROUDE CONFERENCE - "Advances in Theoretical and Applied Hydrodynamics, Past and Future, 24-25 November 2010, Portsmouth, UK

13   Wei Jin, Qiuxin Gao, Dracos Vassalos, "The Numerical Study of Propeller Performance Using RANS", Marine Technology Postgraduate Conference, 10th - 11th June 2010, Newcastle, UK

14   Q. Gao, D. Vassalos, "The Study of Hull-Propeller Interaction by RANSE", The 6th International Workshop on Ship Hydrodynamics, IWSH, January 9-12, 2010, Harbin, China

15   Zhiliang Gao, Dracos Vassalos and Qiuxin Gao , "Numerical simulation of water flooding into a damaged vessel's compartment by the volume of fluid method", Ocean Engineering 37 (2010) 1428–1442

16   Q. Gao, D. Vassalos "Simulation of wave effect on ship hydrodynamics by RANSE", STAB, St Petersburg, June, 2009

17   Zhiliang Gao, Dracos Vassalos and Qiuxin Gao , "A Multiphase CFD Method for Prediction of Floodwater Dynamics" , 10th International Conference on Stability of Ships and Ocean Vehicles, St Petersburg, 2009

18   Q. Gao, D. Vassalos, "Computational Hydrodynamic Derivatives by Numerical PMM", RINA MARINE-CFD, Southampton, 26 March 2008

19   Q. Gao, D. Vassalos "Computational hydrodynamic derivative", ISOPE-2007 Lisbon Paper No 2007-JSC-152

20   Q. Gao, V. Shiganov, D. Vassalos "Numerical Simulation of Yaw Effect", 4th International Conference on Marine Hydrodynamics, Mar. 2005, Southampton

21   Q. Gao, "Numerical Simulation of Damage Ship Flooding", 7th Numerical Towing Tank Symposium, Hamburg, Oct. 2004

22   Q. Gao, Dracos Vassalos "Numerical Simulation of Free Surface Flow around KCS", International Symposium on Naval Architecture and Ocean Engineering, Shanghai, Sep. 2003

23   Qiuxin Gao, "Numerical Simulation of Free Surface Flow around DTMB 5415", Journal of Ship Mechanics, 2002 Vol.6 No.4

24   Qiuxin Gao, "Numerical simulation of free surface flow around ship hull", Journal of Ship Mechanics, 2002 Vol.6 No.3

25   Qiuxin Gao, "CFD simulation of water ingress into damaged ship", Journal of ship mechanics, 2001 Vol.5 No.3

26   Qiuxin Gao, Zhou Liandi, "Numerical simulation of scale effect on ship stern flow and hydrodynamics performance", Journal of Hydrodynamics, Ser. B, 1995, Vol.7, No.3, 56-64

27   Qiuxin Gao, Zhou Liandi, "The numerical calculation for stern flow of three dimensional surface ship with multi-propellers in operation", Journal of Hydrodynamics, Ser.B 10, No.1, 75-85,1998

28   Qiuxin Gao, Zhou Liandi, "Numerical Simulation of interaction between ship stern flow and Multi-Propellers", Shipbuilding of China, No.140, 1998, 16-24,

29   Q. Gao, "A numerical study on ship self-propulsion factors", Proceeding of IWSH'99, Vol. 23 Sep. 1,1999

30   Q. Gao, Zhou Liandi, "Ship stern flow solver by 3-D unsteady RANS Equation", Proc. International Conference on Hydrodynamics, Wuxi, China, 1994, 179-183

References

1   Alessandrini, B. and Delhommeau, G. (1998). "Viscous Free Surface Flow Past a Ship in Drift and in Rotating Motion," 22nd Symposium on Naval Hydrodynamics, Washington D. C., USA.

2   Andrillon, Y., Alessandrini, B., "A 2D+T VOF Fully Coupled Formulation for Calculation of Breaking Free Surface Flow", Twenty Fourth Symposium on Naval Hydrodynamics, Fukuoka, Japan, 2002.

3   Aulisa, E., Manservisi, S., and Scardovelli, R., "A Mixed Marker and Volume-of-fluid Method for the Reconstruction and Advection of Interfaces in two-phase and Free-boundary Flow", Journal of Computational Physics, 188:611-639, 2003.

4   Avanzini, G., Benedetti, L., Olivieri, A., Palini, M., and Penna, R., "Studio sperimentale del campo fluidodinamico intorno ad una carena dislocante veloce. Parte III: rilievo del campo di velocità triassiali a Fr=0.28 mediante tubi di pitot," Rapporto Tecnico (in Italian)

5   Baldwin, B.S., and Lomax, H., "Thin Layer Approximation and Algebraic Model for Separated Turbulent Flows," AIAA Paper 78-257, Huntsville, AL, 1978.

6   Bidoae, R., Ciobotaru, R.M., and Raad, P.E., "An Eulerian-Lagrangian Marker and Micro Cell Simulation Method for Fluid Interaction with Solid/Porous

Bodies", in IUTAM-Symposium on Integrated Modeling of Fully Coupled Fluid-Structure Interactions Using Analysis, Computations and Experiments, 1 June-6 June, 2003.

7   Blondel E., Bonnefoy F., Ferrant P., "Deterministic non-linear wave prediction using probe data", Journal of Ocean Engineering, 37, 2010.

8   Bosch, J.J. van den, and Vugts, J.H., "Roll Damping by free Surface Tanks", Shipbuilding Laboratory of the Technical University of Delft, Report No. 83S, 1966.

9   Bourlioux, "A Coupled Level Set Volume-of-fluid Solver for Tracking Material Surfaces. In Proc. Int. Symp. Comput. Fluid Dyn. 6th Lake Tahoe, Pages 15-25, 1995.

10 Boussinesq, J., "Theorie de l'Ecoulement Tourbillant," Mem. Presentes par Divers Savants Acad Sci. Inst. Fr., Vol. 23, pp. 46-50.,1877.

11 Chou S.K., Chau S.W., Chen W.C. and Hsin J.Y., Computation of ship flow around commercial hull forms with free surface or propeller effects, Proceedings, Workshop on Numerical Ship Hydrodynamics, Gothenburg, Sweden, 2000

12 Claus D. Simonsen and Frederick Stern, RANS Maneuvering Simulation of Esso Osaka with rudder and a Body-Force Propeller, Journal of Ship Research, Vol. 49, No.2, June 2005, pp98-120

13 Cebeci, T., and Smith, A.M.O., "Analysis of Turbulent Boundary Layers", Ser. In Appl. Math & Mech., Vol. XV, Academic Press, 1974.

14 Chen, S., Johnson, D.B., and Raad, P.E., "The surface marker and micro cell method", Int. Journal Numerical Methods Fluids, 25:749-778,1997.

15 Chen, S., Johnson, D.B., and Raad, P.E., "Velocity Boundary Condition for the Simulation of free surface flow", Journal Computational Physics 116:262-276,1995.

16 Ckarje, D., Gedling, P. and Hine, G.(1982). "The application of Manoeuvring Criteria in Hull Design Using Linear Theory," The Royal Institution of Naval Architects

17 Cura Hochbaum, A. (1998). "Computation of the Turbulent Flow around a Ship Model in Steady Turn and in Steady Oblique Motion," 22nd Symposium on Naval Hydrodynamics, Washington D. C., USA,

18 Cura Hochbaum A. and Vogt M. "Flow and Resitance Prediction for a Container Ship". A Workshop on numerical Ship Hydrodynamics, Chalmers University of Technology Gothemburg, 2000

19 Cura Hochbaum and M.Vogt: "Towards the Simulation of Seakeeping and Manoeuvring based on the Computation of the Free Surface Viscous Ship Flow", 24th Symposium on Naval Hydrodynamics, 2003

20 Daalen, E.F.G. van, Doeveren, A.G. van, Dressen, P.C.M, and Visser C.M, "Two–dimensional Free Surface Anti-roll Tank Simulations with a Volume of Fluid based Navier-Stokes Solver", Maritime Research Institute Netherlands, Report No. 15306-1-OE, October, 1999

21 Deng, G. B., Queutey, P., and Visonneau, M., "Navier-Stokes Computations of Ship Stern Flows: a Detailed Comparative Study of Turbulence Models and Discretization Scheme", Proceedings, 6th Symposium on Numerical Ship Hydrodynamics, Iowa City, Iowa, 1993.

22 Deng, G. B., A. Leroyer, E. Guilmineau, P. Queutey, M. Visonneau and J. Wackers, "VERIFICATION AND VALIDATION FOR UNSTEADY COMPUTATION", CFD workshop 2010, Gothenburg

23 Ducrozet G, F.Bonnefoy, D. Le Touze & P. Ferrant : "Development of a Fully Nonlinear Water Wave Simulator based on Higher Order Spectral Theory", 20th Workshop on Water Waves and Floating Bodies, Norway, 2005

24 F. R. Menter, "Two Equation Eddy Viscosity Turbulence Models for Engineering Applications", AIAA Journal 32, 1598-1605 1994

25 Farmer J, Martinelli L, and Jameson A., "Multi-grid Solutions of the Euler and Navier-Stokes Equations for a Series 60, CB=0.60 Ship Hull for Froude Numbers 0.16, 0.22 and 0.316", Proceedings, CFD Workshop, Ship Research Institute, Japan, 1994.

26 Fujisawa, J., Ukon, Y., Kume, K., and Takeshi, H., "Local Velocity Field Measurements around the KCS Model (SRI M.S.No.631) in the SRI 400m Towing Tank," Ship Performance Division Report No. 00-003-02, The Ship Research Institute of Japan, April 27, 2000. SPD Report No. 00-003-02 Tsukada, Y., Hori, T., Ukon, Y., Kume, K., and Takeshi, H., SPD Report No. 00-004-01, 2000.

27 Gabriel David Weymouth, Robert Vance Wilson and Frederick Stern: "RANS Computational Fluid Dynamics Predictions of Pitch and Heave Motions in Head Seas", Journal of Ship Research, Vol. 49 No.2, June 2005, pp. 80-97

28 Gentaz, L., A. Drouet, P.-E. Guillerm, R. Luquet, C. Monroy, O. Payen, G. Reliquet, B. Alessandrini, P. Ferrant, E. Jacquin, "THE SWENSE FUNCTIONAL DECOMPOSITION METHOD", CFD workshop 2010, Gothenburg

29 Gingold, R.A., and Monaghan, J.J., "Smoothed Particle Hydrodynamics: Theory and Application to Non-Spherical Stars", Monthly Notices of the Royal Astronomical Society, 181:375-389,1977.

30 Gordon, W. N. and Hall, C.A., "Construction of Curvilinear Coordinate Systems and Application to Mesh Generation", International Journal of Numerical Methods in Engineering, Volume 7, pages 461-477, 1973.

31 Guo B.J., Steen S. and Deng G.B. , "Seakeeping prediction of KVLCC2 in head waves with RANS", Applied Ocean Research, Vol. 35, page 56-67, 2012.

32 Harlow, F. H. and Welch, J. E., "Numerical calculation of time-dependent viscous incompressible flow of fluid with free surface", Los Alamos scientific laboratory, University of California, Los Alamos, New Mexico, The Physics of Fluids, Volume 8, Number 12,2182-2189, 1965.

33 Hedio O, "Comparison of CFD simulations with experimental data for a tanker model advancing in waves", International Journal of Naval Architecture and Ocean Engineering, 2011, 3:1-8.

34 Hino, T. (2005, ed.), "Proceedings of the CFD Workshop Tokyo 2005", NMRI Report (Test case 4).

35 Hirt, C. W., and Nichols, B. D., "Volume of Fluid (VOF) Method for Dynamics of Free Boundary", Los Alamos scientific laboratory, University of California, Los Alamos, New Mexico 87545, Journal of Computational Physics 39, 201-225(1981)

36 Hirt, C.W., Cook, J.L. and Butler, T.D., "A Lagrangian Method for Calculating the Dynamics of an Incompressible Fluid with Free Surface," Journal of Computational Physics 5, 103,1970.

37 Irvine, M., Longo, J., Stern, F. (2004), "Towing Tank Tests for Surface Combatant for Free Roll Decay and Coupled Pitch and Heave Motions," Proc. 25th ONR Symposium on Naval Hydrodynamics, St Johns, Canada.

38 ITTC quality manual, 7.5-03, 2002

39 Kajitani, H., and Miyata, H., "The Summary of the Cooperative Experiment on Wigley Parabolic Model in Japan", 1983.

40 Kara, F., "Time domain hydrodynamic and hydro-elastic analysis of floating bodies with forward speed", PHD thesis, 2000.

41 Kim, Y, "A numerical study on sloshing flows coupled with ship motion", Journal of Ship Research 46, 1,52-62, 2002.

42 Kim, Y. H. and Jenkins, D., "Trim and Sinkage Effect on Wave Resistance with Series 60 CB=0.6", DTNSRDC Report /SPD-1013-01, Sept. 1981

43 Kodama, Y., Takeshi, H., Hinatsu, M., Hino T., Uto, S., Hirata, N., and Murashige, S., "Proceedings of CFD workshop", Ship Research Institute, Tokyo, Japan, 1994.

44 Kolmogorov, A.N., "Equations of Turbulent Motion of an Incompressible Fluid," Izvestia Academy of Sciences, USSR, Physics, Vol. 6, Nos. 1 and 2, pp. 56-58, 1942.

45 Kume, K., Ukon, Y., Fujisawa, J., Hori, T., Tsukada, Y., and Takeshi, H., "Uncertainty Analysis for the KCS Model (SRI M.S.No.631) Test in the SRI 400m Towing Tank," Ship Performance Division Report No. 00-008-01, The Ship Research Institute of Japan, June 1, 2000.

46 Inoue, S., Hirano, M. and Kijima, K.(1981). "Hydrodynamic Derivatives on Ship Manoeuvring," International Shipbuilding Progress Vol. 28, No. 321.

47 Larsson, L., "SSPA-ITTC Workshop on Ship Boundary Layers", SSPA Report 90, Gothenburg, Sweden, 1981.

48 Larsson, L., Patel, V. C. and Dyne, G., SSPA-CTH-IIHR Workshop on Viscous Flow, Flowtech Research Report 2, Flowtech Int. AB, Gothenburg, Sweden, 1991.

49 Larsson, L., Stern, F., and Bertram, V., "Gothenburg 2000 - a Workshop on Numerical Hydrodynamics", Department of Naval Architecture and Ocean Engineering, Chalmers University of Technology, Gothenburg, Sweden, 2002.

50 Larsson, L., etc "Gothenburg 2010 - a Workshop on Numerical Hydrodynamics", Department of Naval Architecture and Ocean Engineering, Chalmers University of Technology, Gothenburg, Sweden, 2010.

51 Launder, B.E., and Spalding, D.B., "The Numerical Computation of Turbulent Flows", Computer Methods in Applied Mechanics and Engineering, 3:269-289, 1974.

52 Launder, B.E., Reece, G.J., and Rodi, W., "Progress in the Development of a Reynolds-Stress Turbulence Closure," Journal of Fluid Mechanics, Vol.68, Pt. 3, pp.537-556, 1975.

53 Lee, J., Lee, S.J., and Van, S.H., "Wind Tunnel Test on a Double Deck Shaped Ship Model," 3rd International Conference on Hydrodynamics, Seoul, Korea, 1998.

54 Leonard, B.P., and Mokhtari, S., "UNLTA-SHARP Non-oscillatory Schemes for High Speed Steady Multidimensional Flows." NASA TM 1-2568 (ICOMP-90-12, NASA Lewis Research Center, 1990.

55 Lilly, D.K., "On the Application of the Eddy Viscosity Concept in the Inertial Subrange of Turbulence". National Center for Atmospheric Research Manuscript 123, 1966

56 Local flow measurements (Mean velocity and cross flow vectors). Olivieri et al (2001).

57 Longo, J. F. and Stern, F., "Yaw Effect on Model Scale Ship Flows", Proceedings 21st ONR Symposium on Naval Hydrodynamics.

58 Longo, J., "Scale Effects on Near-Field Wave Patterns," M.Sc. thesis, Department of Mechanical Engineering, The University of Iowa, Iowa City, IA, 1990.

59 Longo, J., Shao, J., Irvine, M., and Stern, F. (2007), "Phase-Averaged PIV for the Nominal Wake of a Surface Ship in Regular Head Waves," ASME J. Fluids Eng, Vol. 129, pp. 524-540.

60 Longo, J., Stern, F., and Toda, Y., "Mean-Flow Measurements in the Boundary Layer and Wake and Wave Field of a Series 60 CB=0.60 Ship Model - Part 2: Scale Effects on Near-Field Wave Patterns and Comparisons with Inviscid Theory," Journal of Ship Research, Vol. 37, No. 1, pp. 16-24, 1993.

61 Lucy, L. B., The Astronomical Journal, 82, 1013,1977.

62 M. Manzke, T. Rung, "Resistance Prediction and Seakeeping Analysis with FreSCo+", A workshop on Numerical Ship Hydrodynamics, Gothenburg, 2010.

63 Mirfield, M., "Burgundy 2-D forced motion experiment", SSRC internal report, 2001.

64 Monaghan, J. J., "Simulating Free Surface Flows with SPH, Journal of Computational Physics", 110, 399-406, 1994.

65 Ogiwara, S., and Kajitani, H., "Pressure Distribution on the Hull Surface of Series 60 (Cb=0.60) Model", Proceedings CFD Workshop Tokyo, Vol. 1, pp. 350-358, 1994.

66 Olivieri, A., Pistani, F., Mascio, A.D., and Penna, R., INSEAN, "Breaking Waves Generated by a Fast Displacement Ship Model", 24th Symposium on Naval Hydrodynamics, 2003.

67 Olivieri, A., Pistani. F., Avanaini, A., Stern, F., and Penna, R. (2001), "Towing Tank Experiments of Resistance, Sinkage and Trim, Boundary Layer, Wake, and Free Surface Flow Around a Naval Combatant INSEAN 2340 Model," Iowa Institute of Hydraulic Research, The University of Iowa, IIHR Report No. 421, 56 pp.

68 Olivieri, A., Palini, M., and Penna, R., "Studio sperimentale del campo fluidodinamico intorno ad una carena dislocante veloce. Parte II: rilievo della formazione ondosa a Fr=0.28 e Fr=0.41," Rapporto Tecnico INSEAN (in Italian), 1998.

69 Osher, S., and Sethian, J., "Front Propagating with Curvature Dependent Speed: Algorithms based on Hamilton-Jacobi Formulations. Journal of Computational Physics, 79: 12-49, 1988.

70 Patankar, S.V., and Spalding, D.B., "A Calculation Procedure for Heat, Mass and Momentum Transfer in Three-dimensional Parabolic Flows", International Journal of Heat and Mass Transfer, 15:1787-1806, 1972.

71 Longo et al, "PIV-measured nominal wake in regular head waves (Mean velocity, turbulent kinetic energy, and Reynolds stresses)". (2007).

72 Prandtl, L. (1904).*Über Flüssigkeitsbewegung bei sehr kleiner Reibung*. Verh. III. Intern. Math. Kongr., Heidelberg, 1904, S. 484-491

73 Olivieri et al, "Resistance, sinkage, trim, and wave profiles". (2001).

74 Rhie, C.M., and Chow, W.L., "Numerical Study of the Turbulent Flow past an Airfoil with Trailing Edge Separation", AIAA Journal, 1525-1432, Nov. 1983.

75 Rognebakke, O. F., and Faltinsen, O. M., "Coupling of Sloshing and Ship Motions", Journal of Ship Research, Volume 47 Number 3 pp 208 – 221, 2003.

76 Roll decay (Motion, free surface, mean velocities). Irvine et al (2004).

77 Sato, Y., Miyata, H., and Sato, T., "CFD simulation of 3-dimensional motion of a ship in waves: application to an advancing ship in regular heading waves", Journal of Marine Science and Technology, 4: 108-116, 1999.

78 Smagorinsky, J., "General Circulation Experiments with the primitive equations. I. The Basic Experiment", Monthly Weather Review. 91:99-164, 1963.

79 SNAME, "Principles of Naval Architecture"

80 Sotiropoulos, F., and Abdallah, S., " A Primitive Variable Method for the Computation of Ship Stern & Wake Flows," Ship Viscous Flow, Proceedings of

1990 SSPA-CTH-IIHR Workshop, Flowtech International Research Report, No 2, Gothenburg, Sweden, (L. Larsson, V. C. Patel, G. Dyne, Eds.), 1991.

81 Sotiropoulos, F., and Patel, V. C., "Second Moment Modeling for Ship Stern and Wake Flows", Proceedings CFD Workshop, Ship Research Institute, Tokyo, Japan, 1994.

82 Spalart, P., and Allmaras, S., "A one-equation turbulence model for aerodynamic flows", Technical Report AIAA-92-0439, American Institute of Aeronautics and Astronautics, 1992.

83 Stern F, Kim H. T., Patel V. C. And Chen H.C., A Viscous Flow Approach to the Computation of Propeller-Hull Interaction, Journal of Ship Research, VOL. 32, No. 4, Dec. 1988, PP246-262

84 Stern, F., Paterson, E.G., and Tahara, Y., "CFDSHIP-IOWA: Computational Fluid Dynamics Method for Surface-ship Boundary Layers, Wake and Wave Fields", IIHR Report No. 381, Iowa Institute of Hydraulic Research, Iowa, July, 1996.

85 Subramani, A., Paterson, E.G., and Stern, F., "CFD Calculation of Sinkage and Trim," Journal of Ship Research, Vol. 44, Number 1, March 2000, pp. 59-82

86 Tahara, Y., and Stern, F., "A Large Domain Approach for Calculating Ship Boundary Layers and Wakes for Non-zero Froude Number", Proceedings, CFD Workshop, Ship Research Institute, Japan, 1994.

87 Thompson, J.F., "Numerical Grid Generation", North Holland, 1985.

88 Toda, Y., Stern, F., and Longo, J., "Mean-Flow Measurements in the Boundary Layer and Wake and Wave Field of a Series 60 CB=0.6 Ship Model for Froude Numbers 0.16 and 0.316," IIHR Report No. 352, 188 pp., 1991.

89 Toda, Y., Stern, F., and Longo, J., "Mean-Flow Measurements in the Boundary Layer and Wake and Wave Field of a Series 60 CB=0.6 Ship Model - Part 1:

Froude Numbers 0.16 and 0.316," Journal of Ship Research, Vol. 36, No. 4, pp. 360-377, 1992.

90 Van Daalen, E.F.G., Kleefsman, K.M.T., Gerrits, J., Luth, H.R., and Veldman, A.E.P., "Anti-roll Tank Simulation with a Volume of Fluid (VOF) Based Navier-Stokes Solver", 23rd Symposium on Naval Hydrodynamics, 2001.

91 Van, S.H., Kim, W.J., Kim, D.H., Yim, G.T., Lee, C.J., and Eom, J.Y., "Measurement of Flows Around a 3600TEU Container Ship Model," Proceedings of the Annual Autumn Meeting, SNAK, Seoul, pp. 300-304 (in Korean), 1997.

92 Van, S.H., Kim, W.J., Yim, G.T., Kim, D.H., and Lee, C.J., "Experimental Investigation of the Flow Characteristics Around Practical Hull Forms," Proceedings 3rd Osaka Colloquium on Advanced CFD Applications to Ship Flow and Hull Form Design, Osaka, Japan, 1998.

93 Woodburn, P., Fundamentals of damaged ship survivability, W.S.Atkins Consultants Ltd. Report, 2000.

94 Yamaguchi, S. and Shinkai, A., "An Advanced Adaptive Control System for Activated Anti-roll Tank", International Journal of Offshore and Polar Engineering, Vol.5, No. 1, pp. 17-22, 1995.

95 Youngs, D. L., "Time-Dependent Multi-Material Flow with Large Fluid Distortion". In K. W. Morton and M. J. Baines, editors, Numerical Methods for Fluid Dynamics. Academic Press, 1982.

96 Zhang DH, Broberg L, Larsson L, and Dyne G, A method for computing stern flows with an operating propeller, Transaction of the Royal Institution of Naval Architects, 1992, PP245-259

97 Zhong, Z., Falzarano, J.M., and Fithen, R.M., "A Numerical Study of U-tube Passive Anti-roll Tanks", Proceeding of the International Symposium of Offshore and Polar Engineering (ISOPE), Vol.3, pp.504-512, 1998.